*Author:*
**Zhou, Yan**

*Title:*
**Thermal/Mechanical/Structural Properties of Polycrystalline Diamond and Novel Layered Materials for Electronic Devices**

# Thermal/Mechanical/Structural Properties of Polycrystalline Diamond and Novel Layered Materials for Electronic Devices


Yan Zhou

*A thesis submitted to the University of Bristol in accordance with the requirements for award of the degree of Doctor of Philosophy at the*

*H. H. Wills Physics Laboratory*

*School of Physics, Faculty of Science*

*May 2018*

*Main text word count: ~62,000*

# Declaration of authorship

I declare that the work in this dissertation was carried out in accordance with the requirements of the University's Regulations and Code of Practice for Research Degree Programmes and that it has not been submitted for any other academic award. Except where indicated by specific reference in the text, the work is the candidate's own work. Work done in collaboration with, or with the assistance of, others, is indicated as such. Any views expressed in the dissertation are those of the author.

Signed: ……

Date: ……

# Abstract

Under the ever-increasing requirements of higher power and higher radio-frequency in future power electronics and telecommunication applications, the thermal management of gallium nitride (GaN) based devices becomes crucial, this can be significantly improved by integrating high thermal conductivity diamond into the devices to enhance the extraction of waste heat. An important consideration is the thermal boundary resistance (TBR) of the GaN/diamond interface, which forms a bottleneck for heat transport. For incorporation as a substrate, the thermal properties of this interface and of the polycrystalline diamond (PCD) grown onto GaN using various controlled barrier layers under different growth conditions are investigated and systematically compared; SiN barrier layers were found normally producing lower TBR with a smoother interface formed. For integration of PCD as a top-side heat spreader onto AlGaN/GaN-on-Si HEMT, its thermal performance was systematically evaluated by time-domain thermoreflectance and ANSYS simulation; at best a 15% reduction in peak temperature was obtained when only the source-drain opening of a passivated AlGaN/GaN-on-Si HEMT is overgrown with PCD.

Meanwhile, next generation higher compacted electronics for future communications or computing require sub-10-nm or even atomic dimension scaling, incorporation of a new two-dimensional (2D) materials channel then has emerged as a highly attractive solution to address this challenge. Gallium telluride (GaTe) is a 2D layered material that recently raised considerable interests due to its unique optoelectronic properties but is still under extensive exploration of its fundamental properties for potential applications. The pressure-dependent solid-state properties of GaTe multilayers up to 46 GPa were firstly investigated. A strong Raman mode anisotropic splitting started at ~6.5 GPa originating from phase transition was first-time revealed and understood through first-principles calculations. Then the thermal properties of free-standing GaTe multilayers were studied mainly by micro-Raman opto-thermography, displaying an anisotropic and very low thermal conductivities along the in-plane armchair and zigzag orientations. Moreover, the mechanical properties of both $SiO_2$/Si substrates supported and free-standing GaTe multilayers were investigated mainly through nanoindentation. Concurrence of multiple pop-ins and load-drops in the loading curve were found, likely originating from interlayer sliding within the GaTe multilayer. These pressure-tuned behaviors, thermal and mechanical properties of GaTe multilayers enable new insights for investigating and manipulating the anisotropic solid-state properties of potential device applications and other low symmetry layered materials.

*To my dear family and friends*

致 我的家人和朋友们

*"We don't get a chance to do that many things, and everyone should be really excellent.*

*Because this is our life."*

**Steve Jobs** (1955-2011)

# Acknowledgements

First, I would like to thank my supervisor, Prof. Martin Kuball, who supported and advised me throughout my PhD study. Then, I would like to acknowledge Dr. James Pomeroy, Dr. Julian Anaya and Dr. Huarui Sun who mentored me in thermal theory, characterization, simulation and writing, Dr. Dong Liu who helped me the skills in nanoindentation based mechanical analysis, and Dr. Yong Xie who helped me in the fabrication skills of layered materials. Finally, I want to acknowledge the collaboration work with Mr. Rajesh Rameneti and Prof. Ken Hannen in University of Hasselt, Qorvo Company, Mr. Qinghua Zhao in Northwestern Polytechnical University and Dr. Jianbo Liang in Osaka City University. I would also warmly thank everyone in the Centre of Device Thermography and Reliability Group, Materials and Devices for Energy and Communication Group for making the laboratory a stimulating environment to work in.

A special thank you to my dear family and friends for supporting me.

# Table of Contents

# List of Figures

# List of Tables

# List of Abbreviations

| | |
|---|---|
| **2D** | Two-Dimensional |
| **2DEG** | Two-Dimensional Electron Gas |
| **3D** | Three-Dimensional |
| **CCD** | Charge Coupled Device |
| **CVD** | Chemical Vapour Deposition |
| **CMOS** | Complementary Metal-oxide-semiconductor |
| **DFT** | Density Functional Theory |
| **DFPT** | Density Functional Perturbation Theory |
| **DOS** | Density of States |
| **FCC** | Face Centred Cubic |
| **FEM** | Finite Element Model |
| **FET** | Field-effect Transistor |
| **GaN** | Gallium Nitride |
| **HEMT** | High Electron Mobility Transistor |
| **IFCs** | Interatomic Force Constants |
| **IR** | Infrared |
| **LED** | Light-Emitting Diode |
| **LD** | Load Drop |
| **MOCVD** | Metal-organic Chemical Vapour Deposition |
| **MOSFET** | Metal-oxide-semiconductor Field-effect Transistor |
| **NA** | Numerical Aperture |
| **PCD** | Polycrystalline Diamond |
| **PI** | Pop-in |
| **PO** | Push-out |

| | |
|---|---|
| **RF** | Radio Frequency |
| **SCD** | Single-crystal Diamond |
| **SEM** | Scanning Electron Microscopy |
| **TBR** | Thermal Boundary Resistance |
| **$TBR_{eff}$** | Effective Thermal Boundary Resistance |
| **TDTR** | Time Domain Thermoreflectance |
| **TEM** | Transimittance Electron Microscopy |
| **USPEX** | Universal Structure Predictor: Evolutionary Xtallography |
| **UV** | Ultraviolet |
| **VASP** | Vienna ab initio Simulation Package |
| **vdW** | van der Waals |
| **XRD** | X-ray Diffraction |

# List of Publications

## Journal papers

1. **Yan Zhou**, Oliver Lord, Tao Fan, James Pomeroy, Qinghua Zhao, Xingyu Guo, Yong Xie, Hui Cai, Bin Chen, Sefaattin Tongay, Wanqi Jie, Vladislav A. Blatov, Tao Wang, Qingfeng Zeng, and Martin Kuball. "Anisotropic Raman Mode Splitting and Reversible Phase Transition in Multilayered Gallium Telluride." In preparation for submission to Nature.

2. **Yan Zhou**, Dong Liu, Qinghua Zhao, Yong Xie, Filip Gucmann, Hui Cai, Bin Chen, Sefaattin Tongay, Wanqi Jie, Tao Wang, and Martin Kuball. "Interlayer Sliding Induced Concurrence of Pop-ins and Load-drops in Nanoindented Gallium Telluride Multilayers." In preparation for submission to ACS Nano.

3. Jianbo Liang[a], **Yan Zhou**[a], Manikant Singh, Filip Gucmann, James Pomeroy, Martin Kuball, and Naoteru Shigekawa. "Annealing on interfacial structure and residual stress in diamond substrates bonded to Si substrates by wafer bonding." Submitted to ACS Applied Materials & Interfaces ([a]contributed equally).

4. Jianbo Liang[a], **Yan Zhou**[a], Manikant Singh, Filip Gucmann, James Pomeroy, Martin Kuball, and Naoteru Shigekawa. "Thermal annealing driven interlayer thinning and stress change crossover in GaN epitaxial layers bonded to Si by surface activated bonding." Journal of Applied Physics, under review ([a]contributed equally).

5. **Yan Zhou**, Rajesh Ramaneti, Julian Anaya, Svetlana Korneychuk, Joff Derluyn, Huarui Sun, James Pomeroy, Johan Verbeeck, Ken Haenen, and Martin Kuball. "Thermal characterization of polycrystalline diamond thin film heat spreaders grown on GaN-on-Si HEMT." ***Applied Physics Letters 111, no. 4 (2017): 041901***

6. **Yan Zhou**, Julian Anaya, James Pomeroy, Huarui Sun, Xing Gu, Andy Xie, Edward Beam, Michael Becker, Timothy A. Grotjohn, Cathy Lee, and Martin Kuball. "Barrier layer optimization for enhanced GaN-on-diamond device cooling." ***ACS Applied Materials & Interfaces 9, no. 39(2017):34416-34422***

7. Le Zhang, Xiaojie Lou, Dong Wang, **Yan Zhou**, Yang Yang, Martin Kuball, Michael A. Carpenter, and Xiaobing Ren. "Glass-Glass Transitions by Means of an Acceptor-

Donor Percolating Electric-Dipole Network." ***Physical Review Applied 8, no. 5 (2017): 054018.***

# Presentations

1. Oral: **Yan Zhou**, Rajesh Ramaneti, Julian Anaya, Svetlana Korneychuk, Joff Derluyn, Huarui Sun, James Pomeroy, Johan Verbeeck, Ken Haenen, and Martin Kuball. "Thermal Properties of Diamond Thin Film Heat Spreaders Grown on GaN HEMTs." MRS 2016 Spring Meeting, Phoenix US, April, 2016.
2. Poster: **Yan Zhou**, James Pomeroy, Rajesh Ramaneti, Svetlana Korneychuk, Joff Derluyn, Johan Verbeeck, Ken Haenen, and Martin Kuball. "Thermal Characterization of Polycrystalline Diamond Thin Film Heat Spreaders Grown on GaN HEMTs." UKNC Conference, Manchester, January, 2018.
3. Poster: **Yan Zhou**, Rajesh Ramaneti, James Pomeroy, Julian Anaya, Svetlana Korneychuk, Joff Derluyn, Huarui Sun, Johan Verbeeck, Ken Haenen, and Martin Kuball. "Influence of Growth Temperature on the Thermal Properties of Diamond Thin Film Heat Spreaders Grown on GaN HEMTs." 2017 XXII-SBDD Conference, Hasselt Belgium, March, 2017.
4. Poster: **Yan Zhou**, Oliver Lord, James Pomeroy, Tao Fan, Xingyu Guo, Qinghua Zhao, Yong Xie, Elisha Mercado, Changhao Yang, Tao Wang, Wanqi Jie, Qingfeng Zeng, and Martin Kuball. "Pressure-dependent Optical Properties of Gallium Telluride." High Pressure Research Forum, Bristol UK, May, 2017
5. Oral: Rajesh Ramaneti, Svetlana Korneychuk, **Yan Zhou**, Julian Anaya, Paulius Pobedinskas, Joff Derluyn, Johan Verbeeck, Martin Kuball, Ken Haenen. "Interface and Thermal Characterisation of Diamond on CMOS Devices-CVD Diamond on HEMT." MRS 2017 Spring Meeting, Phoenix US, April, 2017.
6. Oral: Svetlana Korneychuk, Rajesh Ramaneti, Johan Verbeeck, **Yan Zhou**, Julian Anaya, Paulius Pobedinskas, Joff Derluyn, Huarui Sun, James Pomeroy, Ken Haenen, Martin Kuball. "Bandgap Measurements of Diamond Materials with EELS Using Electron Bessel Beams." 2017 XXII-SBDD Conference, Hasselt Belgium, March, 2017.
7. Oral: M. Kuball, J. W. Pomeroy, J. Anaya, R. B. Simon, H. Sun, **Y. Zhou**, and D. Liu, "GaN-Diamond RF Electronics - Challenges and Successes" (invited), International Conference on Electronic Materials, Singapore, July 2016.
8. Oral: Rajesh Ramaneti, Svetlana Korneychuk, **Yan Zhou**, Christine Korner, Peter Verhoeven, Xianjie Liu, Julian Anaya, Paulius Pobedinskas, Joff Derluyn, Mats Fahlman, Johan Verbeeck, Martin Kuball, and Ken Haenen. "Diamond on HEMT: Maskless Patterning and Selective Diamond Growth on Passivation Dielectrics." MRS 2016 Spring Meeting, Phoenix US, April, 2016.

# Chapter 1.

# Introduction

The semiconductor transistor invented and revolutionized continually since 1947[1] has completely substituted the bulky and unreliable valve transistors. This led to integrated circuits and a miniaturization of devices, and transistors therefore have become the essential component for a wide variety of electronics in our daily lives from smartphones and computers to those in defense such as satellites and radars. Without a continued and massive effort invested in semiconductor physics from both academic and industrial research, there will be no further rapid increase in the capability, efficiency and reliability of these semiconductor electronics over the next decades. This is critical as we can foresee increased requirements in the data capacity and speed, with a recent example of the emerging 5G mobile phone communications. This will promote ongoing research interests into novel device design and new semiconductor materials.

## 1.1 A brief history for high electron mobility transistors

Semiconductor technology has experienced a sustaining revolution since the invention of the first semiconductor transistor by Shockley, Bardeen and Brattain from Bell Labs in 1947.[1] Along this development, the semiconductor material for a transistor has evolved from germanium based to Si, which is proved better as it can overcome the two main shortages of germanium, i.e., being easier in the high purity growth and not rather temperature sensitive as germanium in devices. In the later, as another important purpose for transistors had been for radio frequency (RF) applications, it required transistors can be operated at higher frequencies than the present Si based devices. Therefore, compound semiconductors such as gallium arsenide (GaAs) were started to being explored as they have higher electron mobility than Si, although growing them to the required quality were technically challengeable. The first AlGaAs/GaAs heterostructure based high electron mobility transistor (HEMT) was invented in 1980 by Mimura, which extended the operation frequency beyond the previous limit.[2] In a

HEMT, close to the interface of AlGaAs/GaAs heterostructure, a highly mobile region of electrons named the two-dimensional electron gas (2DEG) which could offer higher electron mobility was formed. With the further increasing demand to operate these devices at even higher power density, higher voltage and higher temperature, another III-V compound semiconductor, namely gallium nitride (GaN), was put forward which could be highly useful for electronics to be operated at higher frequencies, voltages and power densities, due to its distinguished material properties such as wide direct bandgap, high breakdown field and high electron saturation velocity. In 1969, the first single crystal GaN was grown and characterized with promising electrical properties by Maruska and Tietjen.[3] GaN has then became the focus of research community, however, the growth of high quality GaN has proven to be technically very challenging and cost intensive, resulting in its progress being hindered until the first GaN based blue light emitting diode (LED) demonstrated in 1991 by Nakamura[4] and, independently, Akasaki and Amano,[5] in which reasonable quality GaN layers were successfully grown on the sapphire substrates (a widely used low-cost substrate). Intrigued by the improved GaN growth technology, naturally, the first AlGaN/GaN HEMT grown on sapphire was demonstrated by Khan et al. in 1993.[6] But the GaN layer suffered from high defect density and the sapphire had rather low thermal conductivity which had hindered the achievable performance of GaN-on-sapphire HEMTs. Subsequently, another wide bandgap compound semiconductor, silicon carbide (SiC), which has a higher thermal conductivity (360-490 W/mK) and a similar lattice constant to that of GaN started to be used as substrate to grow GaN on (the SiC itself was also developed for transistors[7]). The first AlGaN/GaN HEMT grown on SiC substrate was demonstrated by Binari et al. in 1997.[8] This GaN-on-SiC HEMT enabled operation at higher temperature and power density than that of sapphire. Meanwhile, to integrate GaN with present CMOS logic and into the existing Si infrastructure which would be cost efficient and available for large-area devices, growth of GaN on a Si substrate emerged as new interest area. However the lattice constant and the coefficient of thermal expansion of Si is highly mismatched compared to those of GaN. In 2001, the first AlGaN/GaN HEMT grown on Si through thick strain relief layer was reported by Chumbes *et al.*[9] Currently the GaN-on-Si devices are still under intensive research and 8-inch GaN-on-Si wafers have been commercially available. Today, the research focus in GaN based power switching and RF electronics is on pushing the limit of GaN towards applications of much higher power densities, higher frequencies and higher voltages.

### 1.2 Challenges and improvements in AlGaN/GaN based devices and 2D devices

Similar to all other emerging technologies, early stage GaN-based devices faced significant reliability challenges. In 1998, reduced device performance was demonstrated due to self-heating (Joule heating) during operation which limited the lifetime of AlGaN/GaN HEMTs.[10] To minimize the performance degradation, it was found channel temperature in the

devices needed to be minimized.[11,12] The channel temperature of AlGaN/GaN HEMTs was first measured using a high resolution micro-Raman thermography technique under steady-state DC operation,[13] which was similar as that previously performed on Si MOSFETs.[14] The temperature rise within the HEMTs was found to be inhomogeneous (much more inhomogeneous than in Si devices due to the higher thermal conductivity of GaN and SiC than for Si), with a peak temperature occurring close to the drain side of the gate foot. This peak temperature region only extended to few 100s nm laterally, and coincided with the location where the highest electric field generated in the device. Therefore, this region was thought to be the origin site for degradation, making the accurate characterization of this peak temperature very critical for the reliability evaluation of devices. Other thermal characterization techniques have also been applied to measure the thermal properties of HEMTs, such as infrared (IR) imaging which can map the overall temperature distribution across the channel,[15] time-resolved micro-Raman thermography that can be used to measure the temperature rise in the channel under electrical pulsing,[16] thermoreflectance,[17] micro/nano-thermometers,[18,19] and photoluminescence.[15,20-22] Micro-Raman thermography can offer a high lateral and temporal resolution of about 500 nm and 10 ns, respectively, with an accuracy of few K in temperature, but the measured temperature by this technique is a volumetric depth average temperature through the entire GaN layer in the devices; in fact, presently no technique can directly characterize the peak temperature in a HEMT as the hot spot region due to self-heating is often buried under the metallic gate and field plates which can block the laser passing through. Therefore, finite element model (FEM) based numerical thermal transport simulations were combined with the experiments to estimate the peak temperature according to the measured average temperature and other known materials properties of the HEMT structure.[20] It should also be noted that micro-Raman thermography cannot be applied to measure Raman inactive surfaces directly, such as the metal part of gate/source/drain in a HEMT; alternatively, diamond or $TiO_2$ micro-particle or Si nanowire deposited on top of the contacts have been applied to acquire their temperature.[18,19,23]

As the peak temperature rise accelerates the device to failure, thermal management of minimizing this temperature is becoming more and more important to ensure the reliability of working HEMTs and enhance their potential performance. It was proposed that the high peak temperature was mainly due to the ineffective vertical heat transport in the devices. Typically, the heat was removed through the substrate of a HEMT, using a heat sink that can be either actively or passively cooled. As a result, to remove the heat efficiently, the thermal conductivity of the substrate is required to be as high as possible. In recent years, diamond, the known material in nature with the highest thermal conductivity of ~2200 W/mK, was integrated into the GaN technology as a substrate to form a GaN-on-diamond HEMT.[24] Compared to the high cost single-crystal diamond (SCD), chemical vapor deposition (CVD) grown polycrystalline diamond (PCD) was used, which can also achieve a high thermal

conductivity close to that of SCD. However, the thermal conductivity of CVD grown PCD is strongly affected by its complicated crystalline structure, which has been extensively investigated[25] but not yet been fully understood. In addition, due to the mismatch of lattice constant and thermal expansion coefficient between GaN and foreign substrate usually introduces a large strain, and the need to seed diamond nanoparticles as well as protect GaN from the harsh diamond growth environment, a transition layer is normally grown in between. This transition layer typically consists of materials with very low thermal conductivity and is usually very thin. There is typically a significant thermal resistance formed at this interface, often termed as thermal boundary resistance (TBR), which acts as a thermal bottleneck for the heat transport from the channel region towards the heat sink. Minimizing this TBR while maintaining the reliable mechanical properties of the interfaces and the interlayers is vital for efficient thermal management and device structure optimization. Currently by fabricating test structures on the wafer or device structures with heater contacts, the TBR can be characterized by micro-Raman thermography and extracted through fitting the measured temperature profile using FEM simulations.[26,27] Although it has many advantages, the measurement time of micro-Raman thermography is normally long, therefore a faster technique named time-domain thermoreflectance has recently been applied to measure the thermal resistance within the layer stack of the GaN-based devices successfully, such as GaN-on-diamond,[28,29] and GaN-on-SiC.[30] Meanwhile, nanocrystalline diamond heat spreaders was also being designed to be grown on top of the HEMTs to assist conducting away the heat generated under the gate from the topside.[31-37] Although this approach has met with limit success and even contradicted findings, this strategy does need a comprehensive evaluation about its potential especially in experiments.

Increased data rates for communications or computing furthermore requires our electronics to become smaller and smaller, i.e. the so-called Moore's law which predicted decades ago that the size of semiconductor devices halves every few years. Therefore next generation electronics require sub-10-nm or even atomic dimension scaling to extend Moore's law which is very difficult based on present channel materials and devices. Incorporation of new two-dimensional (2D) materials channel is a highly attractive solution to address this challenge.[38,39] Since the last decade, tremendous advances have been made in the preparation of 2D materials through mechanical exfoliation or chemical synthesis.[40] In particular, 2D heterojunctions are just beginning to emerge as the building blocks for future electronics, such as power efficient ultra-fast RF transistors.[41] To ensure continued progress of this field, new 2D materials with distinguished new properties must be considered. Among the large 2D family, an emerging group with low in-plane structural symmetry, (Ga, In) chalcogenides, of extremely high photoresponsivity ($10^4$ A/W) and highly in-plane anisotropic properties, has emerged as having outstanding potential for new generation transformative high performance optoelectronic, phase-switch and memory devices, but little physics is known about these

novel phenomena and no devices have been demonstrated to date despite the rising interest. In contrast to graphene, these materials have an actual bandgap which enable proper bandgap engineering to manipulate their anisotropic properties for the design of more 2D materials based functional devices.

## 1.3 The structure of this work

The main aim of this work focuses on investigating the thermal properties of novel materials used for electronic devices and improving the device thermal managements, including polycrystalline diamond integrated AlGaN/GaN devices with various thermal designs, and a novel nanoscale 2D layered materials of gallium telluride (GaTe) multilayers. The phase transitions of GaTe ultrathin flakes using high-pressure techniques and its mechanical properties will also be characterized and discussed. Chapter 2 presents the detailed material properties of GaN, diamond and layered materials especially GaTe as well as theoretical background. Chapter 3 provides an overview of the experimental characterization techniques used in this work. Chapter 4 describes the thermal properties of GaN-on-diamond devices using different barrier layer materials and growth recipes for polycrystalline diamond, and thermal optimization of devices by reducing the TBR at the GaN/diamond interfaces are demonstrated. In Chapter 5, thermal characterization of growing polycrystalline diamond heat spreaders on topside of GaN HEMTs are described, also, thermal benefits and thermal optimization using experimental parameters via finite-element modelling of this GaN-on-Si HEMTs based topside diamond heat spreading strategy are introduced. Chapter 6 focuses on the high-pressure experimental characterization and physical understanding of strain induced phase transitions in 2D GaTe ultrathin layered materials, using multiple experimental characterization techniques including diamond anvil cell, micro-Raman and synchrotron XRD combined with theoretical first-principles calculations. Chapter 7 explores the thermal properties and mechanical properties (especially in-plane anisotropic properties) of free-standing 2D GaTe multilayered materials, via micro-Raman opto-thermography and nanoindentation techniques, respectively. Finally, Chapter 8 summarizes the overall conclusions of the work presented in this thesis and provides future directions that this work could further take.

# Chapter 2.

# Properties of Materials and Devices

This chapter introduces the basic properties of the semiconductor GaN, polycrystalline diamond and layered materials in particular GaTe which is investigated in this study. The following aspects are discussed: crystal structure, basic physical properties, electron and phonon transport characteristics; the main growth methods; principles of the AlGaN/GaN high electron mobility transistors (HEMTs). Theoretical background of the experimental characterization techniques are also discussed.

## 2.1 Properties of GaN semiconductors and HEMT devices

### 2.1.1 Crystal structure

GaN, can crystallize into two solid-state phases, i.e., the thermodynamically stable wurtzite structures ($\alpha$-type) and the metastable zincblende structures ($\beta$-type),[42] the former was investigated solely in this work. Projections of the GaN wurtzite structure in top-view and side-view orientations are shown in Figure 2.1, where the *x*- and *y*-axis are parallel to the basal plane and the *z*-axis is parallel to the [0001] direction, i.e., the crystal *c*-axis. From the top-view (basal plane) projection in Figure 2.1(a), the hexagonal symmetry is clearly apparent, consisting of two interpenetrating hexagonal close-packed sublattices of Ga and N atoms respectively. Figure 2.1(b) illustrates that the closest-packed planes of N and Ga atoms are stacked in the sequence (ABAB…) along the [0001] direction. The alternating stacked planes of Ga and N atoms can be termed as Ga- and N-planes or faces respectively in wurtzite GaN. Notably, the crystallographic [0001] and [000$\bar{1}$] directions are non-equivalent. Therefore, the growth of a GaN epilayer on a substrate can lead to a Ga- and N-face terminated surfaces, respectively, with different surface properties. MOCVD grown GaN epilayers typically have a Ga-face polarity terminated surface which is required for 2DEG formation in AlGaN/GaN devices. A schematic of the primitive unit cell of the wurtzite structure is depicted in Figure 2.2. There are four atoms per primitive unit cell, with each

Ga(N) atom tetrahedrally bonded to the four neighboring N(Ga) atoms. Due to the N atoms having a larger electronegativity the bonding is partially ionic, with more electron density or negative charge accumulated on the N atom (anion) than the Ga atom (cation), resulting in an intrinsic non-zero dipole movement i.e. a spontaneous polarization along the *c*-axis. Also, due to the lack of inversion symmetry, wurtzite GaN exhibits piezoelectric polarization. The primitive cell can be defined by the following three parameters, i.e., *a* (3.19 Å), *c* (5.19 Å), and *u* (0.376 Å),[43,44] corresponding to the distance between the two neighboring Ga or N atoms in the (0001) plane, the height of the unit cell, and the length of the shortest Ga-N bond along the [0001] direction respectively, as labelled in Figure 2.2(a). The symmetry of wurtzite GaN belongs to the space group $C_{6v}^4$ (or $P6_3mc$).[45] Figure 2.2(b) shows the first Brillouin zone of wurtzite structure, which is a hexagonal prism Wigner-Seitz cell expressed in reciprocal space.[45] $\boldsymbol{k}$ represents the wavevector in the reciprocal lattice space and is Fourier transformed from the vectors of real space in the unit cell. The center of the Brillouin zone is indicated by $\boldsymbol{k} = 0$, defined as $\boldsymbol{\Gamma}$. Other important high symmetry points and directions ($k_x$, $k_y$, $k_z$,) are also labelled using the conventional coordinate notation in the $\boldsymbol{k}$–space.

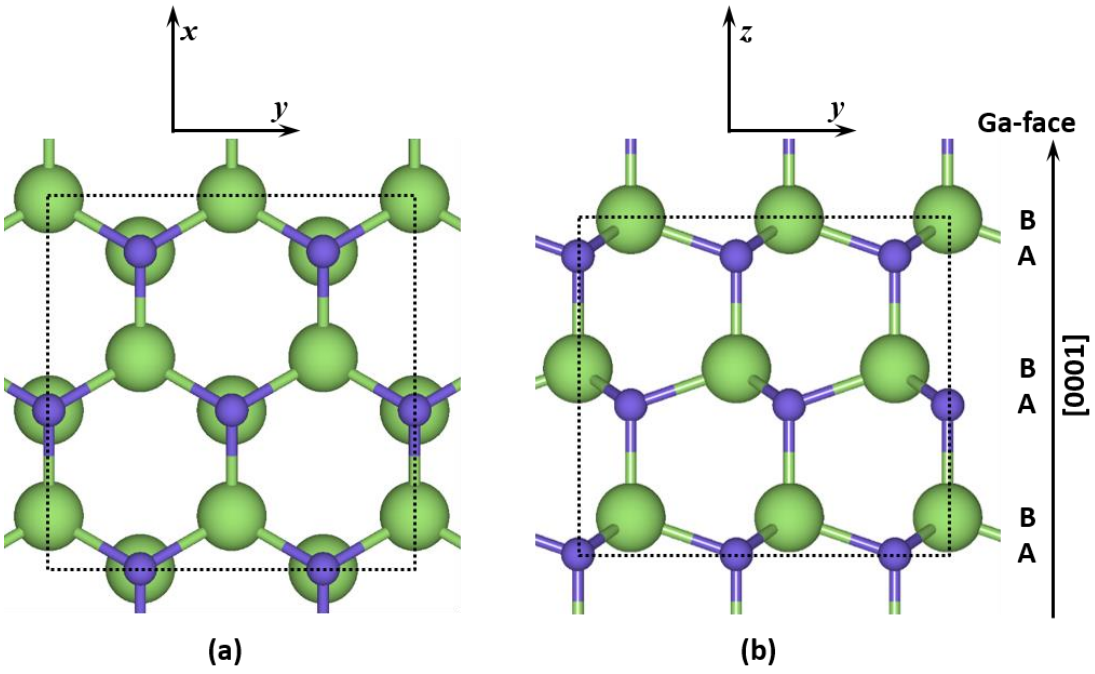


Figure 2.1. Wurtzite crystal structure of GaN. (a) Top-view; (b) side-view. The small purple and larger green circles represent the nitrogen anion and gallium cation, respectively. The x-axis and y-axis lie in the basal plane.

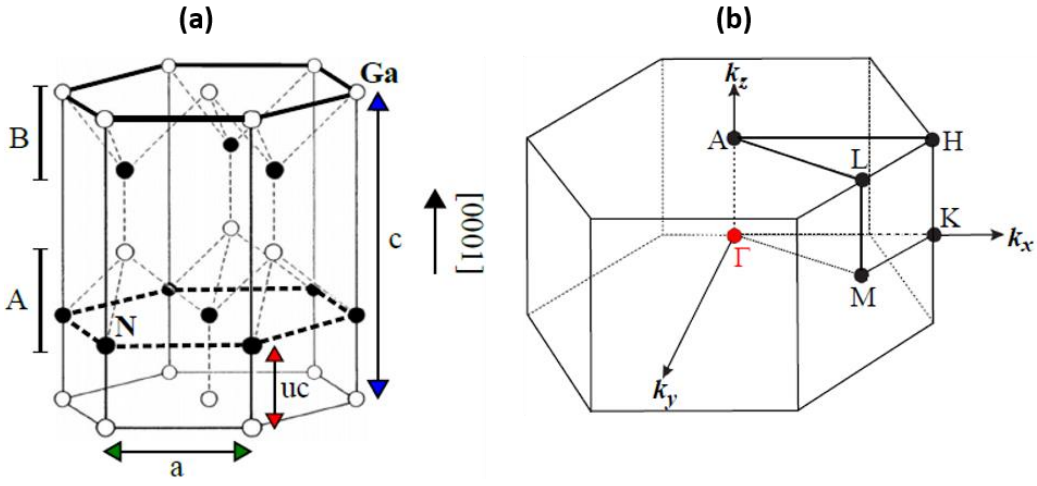


Figure 2.2. A schematic of the primitive unit cell of the wurtzite GaN structure in (a) real space, showing the Ga-plane (solid line) and N-plane (dashed line), and (b) in reciprocal space, showing high symmetry points and directions, where *k* denotes the wavevector. (Adapted from Morkoc *et al.*[45])

### 2.1.2 Electronic band structure

To gain insight into the charge carrier behavior within the wurtzite GaN crystal, electronic band structure is indispensable to analyze the relationship between the energy of discrete energy bands and wavevector ***k***. The electronic band structure is usually calculated using density-functional theory (DFT), which is derived by solving the single-electron Schrödinger equation for an electron in a lattice-periodic potential and will be discussed in Section 2.4.4. The DFT calculated electronic band structure of wurtzite GaN is shown in Figure 2.3. According to the valence band maximum and conduction band minimum, the wurtzite GaN displays a direct bandgap of 3.4 eV located at the **Γ**-point, making it an ideal candidate for high temperature and high voltage applications. Notably, there is a particular feature in the band structure of wurtzite GaN that the uppermost valence band splits into three sub-bands at the **Γ**-point; this multiband character is due to the presence of a crystal field and the influence of spin-orbit interactions (while the conduction band is non-degenerate at the **Γ**-point, so no splitting occurs). As the curvature of the band structure determines the effective mass ($m^*$) of the charge carriers (expressed as $m_e^*$ and $m_h^*$ for electrons and holes which are calculated from conduction band and valence band respectively), the three uppermost valence bands at the **Γ**-point in wurtzite GaN are therefore commonly denoted as the heavy hole (hh), light hole (lh) and crystal-field (ch) split bands. The effective mass of electrons and holes differ along different ***k*** directions (e.g., parallel or perpendicular to the *c*-axis) due to the anisotropy of bands, as shown in Table 2.1. Moreover, the effective mass can significantly

affect the carrier mobility, which is an intrinsic parameter which defines how fast an electron or hole can move through a metal or semiconductor under the bias of an external electric field. The carrier mobility is normally expressed as $\mu = q\tau / m^*$ where $\tau$ represents the scattering time and is affected greatly by carrier concentration, temperature, impurities and defects. The typical mobility for electrons and holes in wurtzite GaN are ~1000 and 200 $cm^2V^{-1}s^{-1}$, respectively.

Table 2.1. Effective masses for electrons ($m_e^*$) and holes in the heavy hole ($m_{hh}^*$), light hole ($m_{lh}^*$) and crystal-split ($m_{ch}^*$) bands with momenta parallel (∥) and perpendicular (⊥) to the c-axis, expressed in units of free electron mass ($m_0$).[46]

| | $m_e^*$ ($m_0$) | $m_{hh}^*$ ($m_0$) | $m_{lh}^*$ ($m_0$) | $m_{ch}^*$ ($m_0$) |
|---|---|---|---|---|
| ∥ | 0.17 | 2.03 | 1.25 | 0.15 |
| ⊥ | 0.19 | 0.33 | 0.34 | 1.22 |

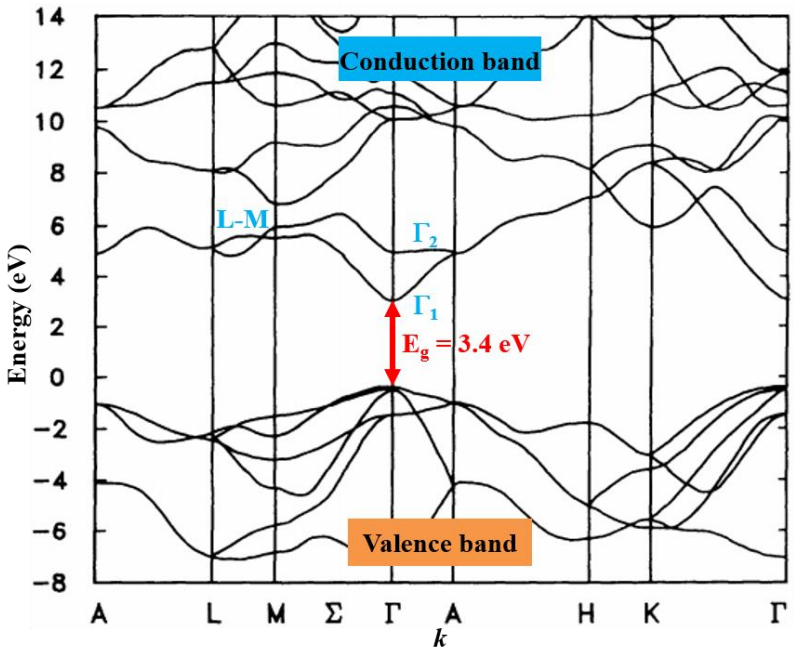


Figure 2.3. Electronic band structure of GaN calculated using DFT based self-consistent linear muffin-tin orbital (LMTO) method within the local-density approximation (LDA), with the direct bandgap, conduction band and valence band indicated. Adapted from Perlin *et al.*[47]

### 2.1.3 Phonon modes and phonon dispersion

The uniform displacement of atoms away from their equilibrium positions within the crystal can lead to propagating lattice vibrations. Each quantum mechanical description of a lattice vibration is called a phonon mode. If a primitive cell has N atoms, there are 3N phonon branches, of which 3 are acoustical and (3N-3) are optical phonon modes. The in-phase and out-of-phase atomic displacements within the primitive cell corresponds to acoustical phonons and optical phonons, respectively. As the wurtzite GaN has 4 atoms per unit cell, there are 3 acoustical and 9 optical phonon modes. The atomic motions associated with different phonon modes of a crystal can be characterized by their displacement vectors. Therein phonon symmetry can be determined by the effects of crystal symmetry operations on these vectors,[48] which is systematically illustrated in group theory. The mathematical method to describe symmetry operations of any crystal is group theory, in which, the set of symmetry operations of a molecular are classified as a point group, while the set of symmetry operations of an infinite crystal are described as a space group. The wurtzite structure belongs to the $C_{6v}^4$ space group, with two formula units in the primitive cell and all atoms occupying the $C_{3v}$ sites. In this notation, $C_6$ denotes that the crystal has a 6-fold rotational axis and $v$ denotes that the mirror planes are parallel to the rotational axis. For wurtzite GaN, eight of the phonon modes ($2A_1+2B_1+2E_1+2E_2$) at the $\Gamma$-point of the first Brillouin zone have been predicted by group theory, among which, one of the $E_1$ and $A_1$ modes correspond to acoustical phonons, while the remaining ($A_1+2B_1+E_1+2E_2$) modes belong to optical phonons. These optical phonon modes are illustrated in Figure 2.4 using an atomic displacement vector description. Phonon mode symmetry is labelled according to the irreducible denotations of their related crystallographic space group and point group. Here, the denotations *A* and *B* represent lattice vibrations along one axis parallel to the *c*-axis, symmetric and antisymmetric distributing with respect to their corresponding six-fold rotation axis, respectively; while the denotation *E* represents lattice vibration within a plane perpendicular to the *c*-axis.[49] The $E_2$ and $B_1$ modes split into a *high* and *low* frequency mode (denoted in superscripts as indicated in Figure 2.4); this is because of the shear and compressive strain associated with their characteristic atomic displacements. The $A_1$ and $E_1$ modes are polar because their associated atomic motions generate a net displacement of charge and hence an electric dipole moment within the primitive unit cell. These polar modes can be split into longitudinal optical (LO) or transverse optical (TO), according to the macroscopic electric field they generate parallel or perpendicular to their propagation direction, respectively. LO-TO phonon frequency splitting is a characteristic of ionic bonding existing in crystals. As the electric field generated by the LO component is along the direction of their propagation, this adds an additional restoring force to the lattice vibration, raising the LO mode to a higher frequency than the TO mode (see Table 2.2 for GaN phonon frequencies).

Table 2.2. Optical phonon frequencies of GaN at the Brillouin zone center.[50]

| | Frequency($cm^{-1}$) | |
|---|---|---|
| Mode | Exp. | Calc. |
| $E_1(LO)$ | 741 | 739 |
| $A_1(LO)$ | 734 | 734 |
| $E_2^{high}$ | 565 | 568 |
| $B_1^{high}$ | - | 728 |
| $E_1(TO)$ | 559 | 554 |
| $A_1(TO)$ | 531 | 546 |
| $B_1^{low}$ | - | 319 |
| $E_2^{low}$ | 153 | 144 |

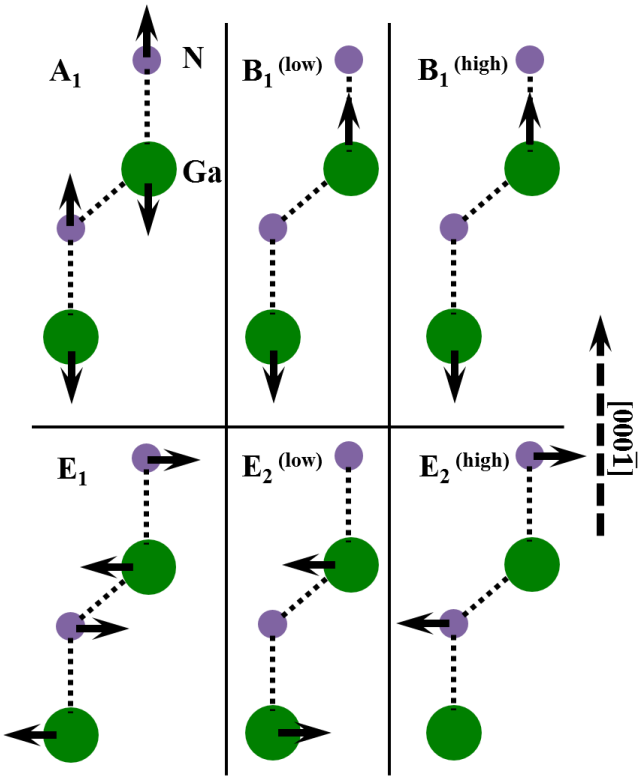


Figure 2.4. Schematic of atomic displacements for different optical phonon modes within wurtzite GaN. (Adapted from Harima *et al.*[51])

Optical phonon modes at Brillouin zone center can be determined by Raman scattering measurements if they are Raman active modes, or by lattice dynamic calculations such as using density functional perturbation theory (DFPT) method to calculate a phonon dispersion curve, which describes the variation of frequency with wavevector for lattice vibrations in crystals. These phonon dispersion curves can also be experimentally measured by inelastic neutron[52] or X-ray scattering[53]. Figure 2.5 displays the calculated phonon dispersion curve for GaN, with the frequencies plotted with respect to wavevector along the high symmetry directions indicated in the Brillouin zone diagram (see Figure 2.2(b)). The optical modes are indicated at the **Γ**-point; the acoustical modes at **Γ**-point correspond to a uniform translation of the entire crystal and have zero frequency. In the curve, the phonon frequency is given in $cm^{-1}$ (1/λ), the wavenumber unit commonly used in spectroscopy (1 $cm^{-1}$=0.124 meV=30 GHz).

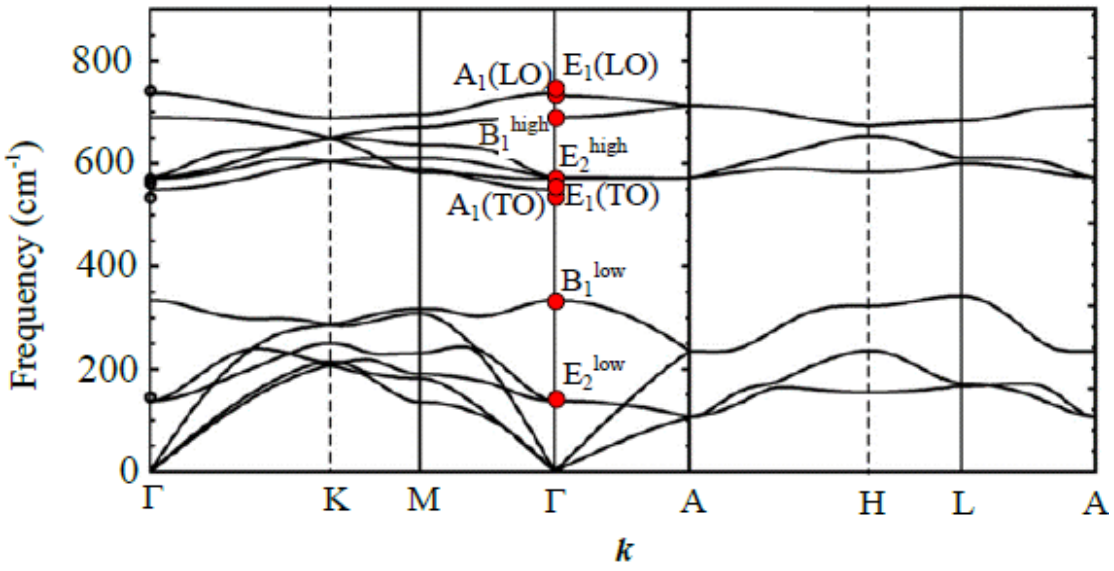


Figure 2.5. Phonon dispersion curve of wurtzite GaN calculated using the first-principles method. (Adapted from Bungaro *et al.*[54])

### 2.1.4 Thermal conductivity

Heat transfer ability at the macroscopic scale is characterized using thermal-energy related properties such as the thermal conductivity, in turn these properties are correlated to atomic-level properties and process, mainly through microscale energy carriers e.g., phonon, electron and hole, fluid particle, photon. In non-metal crystals like GaN, the main heat carriers are phonons. The total thermal conductivity ($\kappa$) of a crystal involves contributions from a lattice (phonon, $\kappa_l$) and an electrical (electron, $\kappa_e$) component, which is described by:[55]

$$\kappa = \kappa_l + \kappa_e = \frac{1}{3} C_v v l + \frac{\pi^2}{3} \left(\frac{k_B}{e}\right)^2 \sigma_e T, \quad (2.1)$$

where $C_v$, and $v$ are the molar heat capacity at constant volume, and the phonon group velocity, respectively; $l$ is the phonon mean free path (MFP) which can be further expressed as $l = v\tau_p$ where $\tau_p$ is the effective phonon scattering time, and $e$, $\sigma_e$, $T$ are the electron charge, electrical conductivity, and temperature, respectively. In metals, $\kappa_e$ is dominant owning to the large concentration of free carriers. Both electrical and thermal transport involves the free electrons in the metal and free electrons can be accelerated to a higher drift velocity with a higher energy by the electric field. Hot electrons at higher energy states can carry more thermal energy than cold electrons. The Wiedemann-Franz law ($\kappa_e = L\sigma_e T$) is traditionally used to calculate the contribution of electrons to the thermal conductivity on the basis of $\sigma_e$, where $L$ is Lorenz number and $L_0 = (\pi^2/3)(k_B/e)^2$ is normally applied for metals. While for semiconductors, various doping levels results in much smaller $\sigma_e$, and smaller $\kappa_e$. Therefore, in terms of GaN and other semiconductors such as diamond, Si and SiC, heat is mainly transferred through the lattice vibrations in the temperature range of electronic device applications,[55] making $\kappa_e$ negligible compared to $\kappa_l$. Therefore, $\kappa_l$, defined as $\kappa$ from now on in the text, will be discussed primarily in this work.

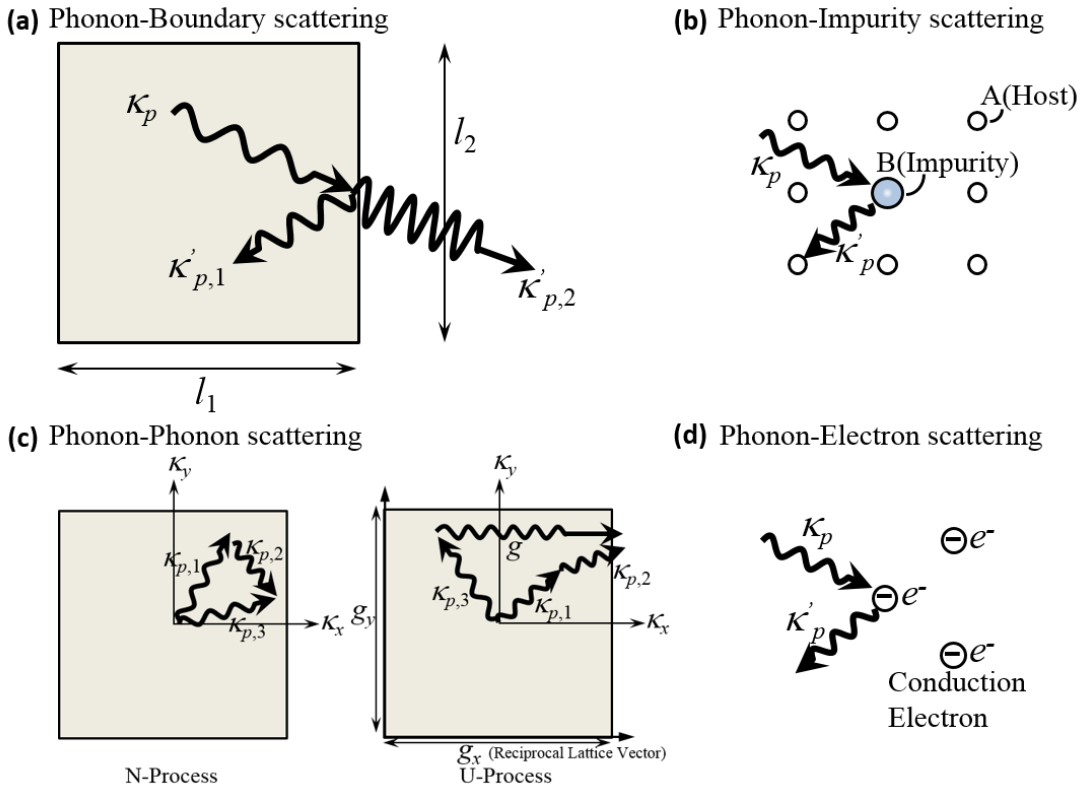


Figure 2.6. Phonon scattering mechanism by (a), (b), (c), (d). (Adapted from Kaviany *et al.*[56])

Phonons can be scattered by various mechanisms in an imperfect crystal which shortens the average distance they can travel through the lattice, i.e. lower their MFP, and the contribution of different mechanisms on phonon scattering has a dependence on temperature. Typically, phonon scattering factors include crystalline boundaries, lattice defects, impurities, electrons and other phonons. Contributions from various scattering factors can be combined and understood by Matthiessen rule in the form of scattering time ($\tau$),

$$\frac{1}{\tau_p} = \sum_j \frac{1}{\tau_{p,j}}. \tag{2.2}$$

The mean phonon scattering time caused by crystal boundaries, (crystal size or grain size, as shown in Figure 2.6(a)) $\tau_{p,b}$ is based on diffusive boundary absorption/emission, and is given as,

$$\tau_{p,b} = L/v_{p,\mathrm{A}}, \tag{2.3a}$$

$$L = \frac{2}{\sqrt{\pi}}\sqrt{l_1 l_2}, \tag{2.3b}$$

where $L$ is the travel length of the phonon before the boundary absorption/emission, $v_{p,\mathrm{A}}$ is the single phonon speed, and $l_1$ and $l_2$ are crystal linear dimensions. It is noted that when below 10 K, scattering from the crystal boundaries dominates because of the finite size of the crystal[55] especially in micro- and nanoparticles. Eq. 2.3 indicates that thermal conductivity of an ultrathin GaN film may be significantly different to its bulk value due to the phonon transport hindered by increased boundary scattering, this is especially true when its thickness close to a value of the dominant phonon MFP. As displayed in Figure 2.7, the phonon MFP that can have a significant contribution to the thermal conductivity of pure GaN mainly ranges from 20 nm to 2 μm at room temperature, and ranges from few nanometers to 1 μm for defects involved GaN. This illustrates why GaN films thinner than 1 μm present a relatively small thermal conductivity when compared to bulk GaN due to the suppression of long MFP phonons.[29,37,57]

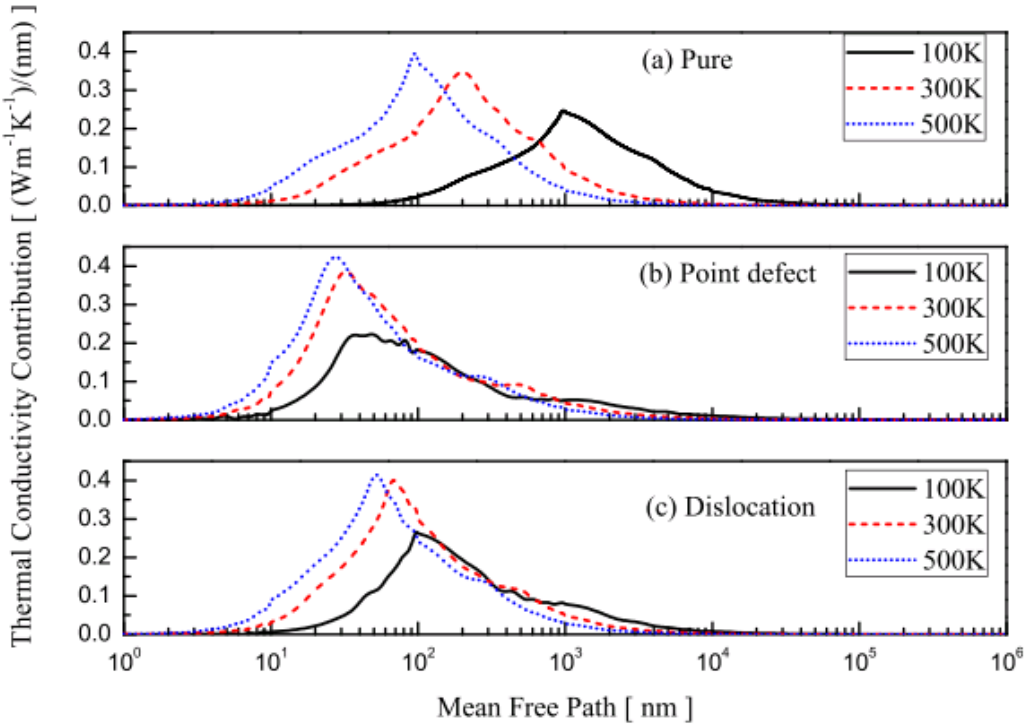


Figure 2.7. Thermal conductivity contribution with respect to phonon MFP for (a) pure wurtzite GaN and consideration of (b) point defects, (c) dislocations at different temperatures.(Adapted from Ma *et al.*[58])

The impurity or imperfections (Figure 2.6(b)) can also result in strong phonon scattering ($\tau_{p,i}$) which is similar to the Rayleigh scattering of the transverse electromagnetic waves, and is normally written as:

$$\tau_{p,i} = \frac{4\pi v_{p,\mathrm{A}}^3}{V_\mathrm{c} \sum_i x_i (1-\frac{M_i}{M})^2} \omega^{-4}, \tag{2.4}$$

where $V_\mathrm{c}$ is unit-cell volume, $x_i$ is mass fraction of impurity atom $i$, and $M_i$ is the molecular weight of the impurity $i$ in its host atomic position. The crystal lattice can be distorted by point defects such as impurities/dopants, vacancies, and isotopes because of their different mass when compare to that of the host atoms, therefore resulting in strong phonon scattering. In addition, these point defects can change the bonding between atoms. By increasing the doping density from $10^{17}$ to $10^{18}$ cm$^{-3}$, a factor of two decrease in the thermal conductivity of wurtzite GaN has been observed by Florescu *et al.*[59] Linear defects i.e. dislocations also scatter phonons because the cores and the surrounding strain fields of these dislocations can change the crystal density and phonon group velocity, respectively. Florescu *et al.* had demonstrated[55,60] a correlation that low threading dislocation density within the wurtzite films lead to a high thermal conductivity at 300 K, while Zou *et al.*[61] showed theoretically that the

thermal conductivity of GaN films decreased when the dislocation density was over $10^{10}$ $cm^{-2}$. It is also noted that in nanometer-thick GaN films, the thermal conductivity may be different along the in-plane (parallel to the *c*-axis) and cross-plane (perpendicular to the *c*-axis) directions; this is because defects and other imperfections will concentrate in a smaller volume which can result in stronger and anisotropic phonon scattering. For GaN films with a typical thickness of ~1-2 μm in electronic device epitaxy at room temperature and above, isotropic thermal conductivities are assumed and have been confirmed by first-principles calculations where the thermal conductivity anisotropy was found to be only ~1% at 300 K.[62]

Inter-phonon scattering is the most significant scattering mechanism at higher temperature and is highly temperature dependent. In principle, inter-scattering between phonons can induce a local strain that changes the phonon velocity. Three-phonon processes are normally exploited to describe the phonon-phonon scattering and can be further divided into normal (N) and Umklapp (U) processes. This scattering mechanism is more complicated and has different behaviors for low temperature and high temperature conditions, as well as for longitudinal and transverse polarizations. A simple vision to distinguish these complicated mechanisms is illustrated in Equation 2.5 and Figure 2.6(c); in a N-process, the phonon momentum of the system is conserved, i.e., after the collision of phonon $\boldsymbol{k}_{p,1}$ and $\boldsymbol{k}_{p,2}$, the momentum of phonon $\boldsymbol{k}_{p,3}$ is within the first Brillouin zone, therefore, the thermal energy carried by the phonon $\boldsymbol{k}_{p,3}$ is in the same direction as that before the collision, i.e., the heat flow is unchanged in the N-process, suggesting a zero thermal resistance and an infinite thermal conductivity of the crystal. Whereas in an U-process, the momentum balance allows for the phonon $\boldsymbol{k}'_{p,3}$ flipping into the adjacent Brillouin zone, which is related to phonon $\boldsymbol{k}_{p,3}$ by $\boldsymbol{g}$, therefore, the crystal momentum is not conserved and there is a change in thermal resistance. Moreover, although the thermal resistances of the crystal do not change in a N-process, this mechanism still plays an important role because it alters energy and momentum from weakly-scattered to strongly-scattered phonons, therein strengthening the Umklapp scattering process simultaneously in which the phonon momentum is not conserved.[55] The high-temperature behavior is dominated by phonon-phonon scattering and has a $T^{-1}$ behavior i.e. slack relation.

$$k_{p,1} + k_{p,2} = k_{p,3}; \tag{2.5a}$$

$$k_{p,1} + k_{p,2} = k'_{p,3} \pm g = k_{p,3}. \tag{2.5b}$$

The effect of electron scattering on phonons (see the schematic in Figure 2.6(d)) is characterized by the phonon-electron relaxation time which is established from a maximum phonon frequency based momentum balance analysis and expressed as,

$$\frac{1}{\tau_{p,\mathrm{e}}} = \frac{3v_{p,\mathrm{A}}^2}{\mu_\mathrm{e}^2}\frac{\sigma_\mathrm{e}}{C_{\mathrm{V},p}T} = \frac{\sigma_\mathrm{e}v_{p,\mathrm{A}}^2}{\mu_\mathrm{e}^2 n_\mathrm{c} k_\mathrm{B} T \alpha_1}\left(\frac{T_\mathrm{D}}{T}\right)^{3/2}; \tag{2.6a}$$

$$\alpha_1 = 4^3\left(\frac{\pi V_a}{6}\right)^{1/2}\left(\frac{m_{\mathrm{e,e}}v_{p,\mathrm{A}}}{h}\right)^{3/2}, \tag{2.6b}$$

where $\sigma_\mathrm{e}$ and $\mu_\mathrm{e}$ are the electrical conductivity and mobility, and $C_{\mathrm{V},p}$ is the specific heat of the phonons allowed to interact with conduction-band electrons, while $V_a$ is the volume per atom and $n_\mathrm{c}$ is the number of unit cells per volume, $h$ the Planck constant, $T_\mathrm{D}$ the Debye temperature. Due to the low electron carrier concentration in the non-channel region of the GaN film, the strength of this complicated term is normally negligible.

The theoretical limit for the thermal conductivity of bulk GaN can be as high as 400 W/mK for isotropically pure undoped GaN;[63] however, due to the existence of dislocations, impurities and other point defects in the lattice, natural GaN epilayers on non-native substrates normally can only achieve thermal conductivities around 160 W/mK.[57,64] The temperature dependence of the GaN thermal conductivity strongly depends on the relative strength of phonon scattering by other phonons, dislocations and point defects due to the different temperature dependencies of these mechanisms. The reported temperature dependence of GaN thermal conductivity varies widely from $T^{-0.5}$ to $T^{-1.4}$ in the literature.[57,65] Therefore, it is necessary to have an accurate GaN thermal conductivity and know its temperature dependence when performing thermal simulations of GaN-based devices. This is because the simulated peak channel temperature rise is impacted greatly by these parameters.

### 2.1.5 Growth

In contrast to most common semiconductors like Si, GaAs or CdTe, which can be grown in bulk using the conventional Bridgeman and Czochralski methods through the outgrowth of melted raw materials on a seed crystal, the III-nitrides have high equilibrium $N_2$ pressures at their melting temperatures which cause them to decompose through $N_2$ desorption below their melting points. Therefore, the aforementioned bulk growth methods are not applicable to grow the III-nitrides. As only a thin (~1 μm-thick) high quality III-nitride layer is required for the device structure fabrication, heteroepitaxy deposition of a thin layer grown on a substrate is the typical method for the growth of III-nitrides. There are two most common techniques used for the epitaxy growth of GaN films on foreign substrates: Metal Organic Chemical Vapor Deposition (MOCVD) and Molecular Beam Epitaxy (MBE). The MOCVD technique, also termed as Metal Organic Vapor Phase Epitaxy (MOVPE), works by passing target chemical elements contained in precursor gases over a heated substrate where they can react. The substrate is normally heated to a typical temperature of around 1000 $^\mathrm{o}$C when used for GaN deposition. The precursor gases used for GaN growth are trimethylgallium ($Ga(CH_3)_3$) and ammonia ($NH_3$), and undergo the following reaction:

$$Ga(CH_3)_3 + NH_3 = GaN + 3CH_4. \quad (2.7)$$

The reaction products are then deposited onto the substrate and grown in a pseudomorphic way, forming a thin GaN layer, while the volatile by-product $CH_4$ desorbs from the substrate surface[66]. The ternary alloy AlGaN can be deposited by using a controlled mixture of trimethylgallium and trimethylaluminium. The MBE growth technique is performed by heating the metallic Ga source material (until it sublimates) in an effusion (or Knudsen) cell to form a collimated molecular beam. This beam is then directed onto a heated substrate surface and reacts with a nitrogen source under ultra-high vacuum (UHV) conditions, forming the GaN layer. The nitrogen normally reaches the substrate surface by passing through a small opening of the Knudsen cell.[66] The reactive nitrogen source can be but is not limited to $N_2$ or $NH_3$ gases,[67] in a radio frequency (RF) plasma[68] or electron cyclotron resonance (ECR) plasma. The beam flux can be controlled by adjusting the Knudsen cell temperature and can be completely turned off by placing a shutter over the Knudsen cell opening. The GaN layer quality during growth can be monitored *in-situ* by using electron or ion probes due to the UHV environment. However, MOCVD poses an advantage over MBE because of its lower cost and faster growth rate.[69]

The selection of substrate for GaN deposition is very important for the quality of the GaN epitaxial layer and the intended application of the sample after growth. The quality of the GaN epilayer is strongly dependent on the mismatch of its lattice and thermal expansion coefficient with the substrate. In this work, AlGaN/GaN deposited on Si and SiC substrates were studied and will be focused on in the following. The lattice mismatch ($f$) is defined in the following equation:

$$f = \frac{a_{(\text{substrate})} - a_{(\text{GaN})}}{a_{(\text{GaN})}}, \quad (2.8)$$

where $a_{(\text{substrate})}$ and $a_{(\text{GaN})}$ are the relaxed lattice constant of the substrate and the GaN, respectively. Under this mismatch, a tensile ($f$>0) or compressive ($f$<0) stress will be imposed on the GaN lattice, as it expands or compresses to match the lattice parameters of the substrate. If the stress is large enough, significant strain or deformation will be introduced, which can induce defects and even cracking in the GaN epilayer. This occurs when its thickness reaches a critical value. The lattice mismatch is 17% between GaN and Si while it is 3.5% between GaN and 6H-SiC, making GaN grown on SiC less strained than grown on Si substrate. The difference in the coefficient of thermal expansion (CTE) between the substrate and the growth material can also introduce large strain, this can be described by:

$$\text{CTE} = \frac{l_f - l_0}{l_0(T_f - T_0)}, \quad (2.9)$$

where $l_f$ and $l_0$ are the lengths of the material at a final temperature, $T_f$ and initial temperature, $T_0$, respectively. The CTE is a measure of the change in crystal length when undergoing a small change in temperature. The CTE has a different temperature dependence for GaN, Si and SiC. The relatively large CTE difference between GaN and sapphire substrate can cause a large residue stress >1 GPa in the GaN layer when cooled down from the growth temperature (~1000 $^oC$), therefore, defect deformation and possible cracking can occur in the GaN layer.[70] In order to mitigate the stress induced in GaN by the lattice mismatch and temperature dependence mismatch of the CTE, an alternative approach is to grow a transition layer in between GaN and different substrates. For example, in the case of direct growth of GaN on a SiC substrate, large tensile stress[71] is caused in the GaN layer which can lead to cracking when grown to a critical thickness. This stress can be reduced by growing an optimized thin AlN layer[26] (a few tens of nanometer thick) between these materials. This is because a compressive stress results in the GaN layer due to the lattice mismatch between GaN and AlN, which counteracts with the tensile stress.[71] In the case of GaN grown on a Si substrate, a larger tensile stress is induced due to their larger lattice mismatch and results in a much lower critical thickness for cracking. Therefore, the aforementioned thin AlN layer is not enough to prevent cracking in 1-2 μm-thick GaN epilayers.[72] To solve this problem, thick transition layers (on the order of a few hundred nanometers[37] to a few micrometers) are introduced between the thin AlN layer (grown on the Si substrate) and the GaN layer. Examples include using linearly-graded[73,74] or step-graded[75,76] AlGaN layers, in which the Al composition from the AlN layer to the GaN layer is decreased linearly or stepwise with thickness, respectively. Moreover, AlN/GaN and AlGaN/GaN superlattices have been explored, in which periodically alternating nanometer-thick layers of each material are grown between the AlN layer and GaN layer. Therefore, the slow Al composition transition from 100% in AlN to 0% in GaN mitigates the stress propagation and increases the counteracting compressive stress to the crack-inducing tensile stress.[77]

The thermal conductivity of the substrate is also an important consideration for device applications to ensure efficient dissipation of heat generated from the hottest region of the operating device to the substrate. The thermal conductivity of single-crystal 6H-SiC substrates (~360-490 W/mK depending on the anisotropic direction) is much larger than that of Si substrates (120-150 W/mK depending on the doping concentration). In thermal performance, the SiC substrates are more suitable than the Si substrates for high power device applications because it can withstand higher power density operation under similar temperature rise conditions. However, the relative cost of the SiC substrate must be considered and needs to be reduced considerably to be a viable substitute for device applications.

### 2.1.6 AlGaN/GaN high electron mobility transistors (HEMTs)

Because of its numerous advantageous properties such as a very high breakdown voltage ($3\times10^6$ V/cm), a high peak velocity ($3\times10^7$ cm/s), a high saturation ($1.5\times10^7$ cm/s) electron velocity,[78] and stability, GaN has been an excellent base material for high power semiconductor materials. AlGaN/GaN high electron mobility transistors (HEMTs), first demonstrated by Khan in 1993 for high power microwave-frequency operation,[6] have achieved promising performance within recent years and this will be focused on in this section. GaN HEMTs have provided excellent electrical performance characteristics, such as high operating voltage, operating frequency and output power density, enabling more compact and efficient high-power, high-frequency and high-temperature electronic devices.[79] Their characteristics, factors that affect their performance, and their applications in power devices will be discussed.

The AlGaN/GaN heterostructure is the fundamental operating part of a GaN HEMT. GaN HEMTs are based on conduction through a layer of high density ($10^{13}$ $cm^{-2}$)[80] two dimensional electron gas (2DEG) formed at the AlGaN/GaN interface, as shown in a schematic in Figure 2.8. The origin of 2DEG formation without any doping will be discussed in the following section. In AlGaN/GaN device fabrication, both GaN and AlGaN are grown along the [0001] direction, i.e. the N-face of AlGaN is grown on the Ga-face of GaN, at this sharp interface the 2DEG is formed. In this case the spontaneous polarization ($\boldsymbol{P_{sp}}$) in both layers is along the [000$\bar{1}$] direction towards the substrate, as indicated in Figure 2.8. AlGaN has a larger $\boldsymbol{P_{sp}}$ than GaN. Owning to the lattice mismatch between GaN and AlGaN, the AlGaN is in biaxial tensile strain, leading to a piezoelectric polarization ($\boldsymbol{P_{pz}}$) formed in the same direction as the spontaneous polarization.[81] The GaN also has $\boldsymbol{P_{pz}}$ but is much smaller than the polarization in the AlGaN layer and is therefore often neglected. A net charge is then induced at the AlGaN/GaN interface by the net polarization within the heterostructure, which can be expressed as:

$$\sigma_{\mathrm{P}} = (P_{\mathrm{sp}} + P_{\mathrm{pz}})_{\mathrm{AlGaN}} - (P_{\mathrm{sp}})_{\mathrm{GaN}}. \tag{2.10}$$

In which $\sigma_{\mathrm{P}}$ is positive, however, due to its nature, there is also a negative charge ($-\sigma_{\mathrm{P}}$) induced by polarization located at the AlGaN surface, to ensure charge neutrality within the AlGaN layer (see Figure 2.8), therefore as Ibbetson pointed out that the dipole ($\pm\sigma_{\mathrm{P}}$) induced by the polarization makes no net contribution to the total space charge and alone cannot contribute to the formation of the 2DEG.[80] As there is no doping in AlGaN, this implies that the 2DEG charge ($\sigma_{\mathrm{2DEG}}$) originates from the ionized donor-like states at the AlGaN surface ($+\sigma_{\mathrm{surface}}$) which move to the AlGaN/GaN interface under the polarization field to compensate the $+\sigma_{\mathrm{P}}$, accumulating at the GaN side. A high electron-density sheet ($\sigma_{\mathrm{2DEG}}$) is then formed until the overall charge neutrality is reached. This requires that $\sigma_{\mathrm{2DEG}} + \sigma_{\mathrm{surface}} = 0$. The 2DEG

is confined in a triangular-shaped quantum well at the GaN side of the interface and parallel to the interface in depth.

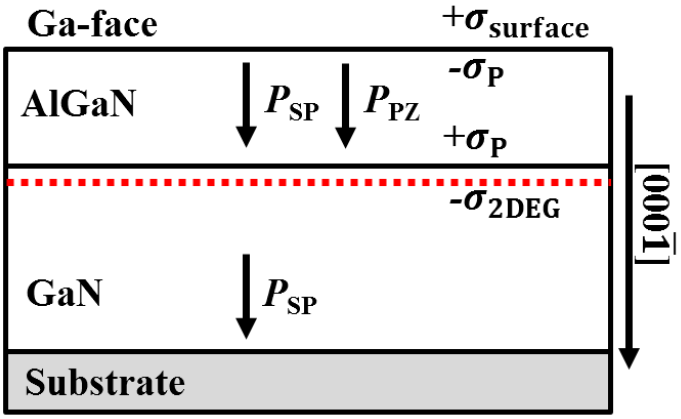


Figure 2.8. Schematic of polarizations and polarization-induced charges in an AlGaN/GaN heterostructure.

The detailed formation mechanism of the 2DEG at the interface of an AlGaN/GaN heterostructure can be well understood by assumption of the donor states existed at the AlGaN surface, as illustrated in Figure 2.9. Assuming an undoped AlGaN layer with surface donor states is under the same tensile strain as that grown on GaN, when the AlGaN layer is thick enough, its Fermi level will be able to reach the donor state level ($E_S$), and the electrons will be excited into the conductive band and swept from the surface of the AlGaN layer toward the interface under the force of the polarization-induced electric field, resulting in the energy band bending toward the interface. Once this AlGaN layer contacts with a GaN layer to form an AlGaN/GaN heterostructure, electrons will flow into the GaN side and the Fermi level of the AlGaN will drop until being aligned well with that of the GaN layer. Finally the electrons will accumulate at the interface of an AlGaN/GaN heterostructure and form the 2DEG. In else, an extra electric field between the 2DEG and the ionized surface donor states will generate and point from the interface to the surface of AlGaN layer thus reduce the polarization field in the AlGaN layer.

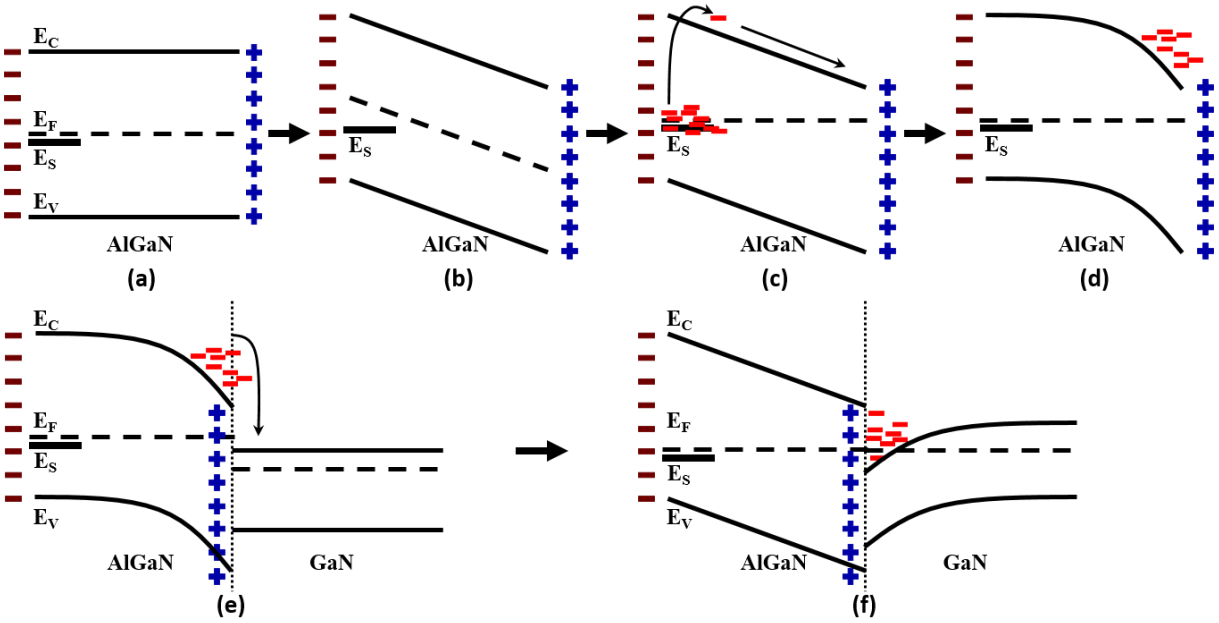


Figure 2.9. Schematic of 2DEG formation in an AlGaN/GaN heterostructure. (a) Energy band of an undoped freestanding AlGaN film (taking surface donor states into account, $E_S$, and assuming that the AlGaN layer is under the same tensile strain as that when grown on GaN); (b) energy band tilt under the polarization-induced electric field; (c) electrons from the ionized surface donor states are stimulated into the conductive band and move under the polarization induced electric field; (d) electrons moving from the surface of AlGaN layer into the interface induced energy band bending; (e) when an undoped AlGaN layer (with surface donor states) contacts a GaN layer, electrons will flow into the GaN side; (f) the electrons accumulates at the interface of an AlGaN/GaN heterostructure and finally form the 2DEG.

The 2DEG can only form when the AlGaN layer is grown over a critical thickness ($t_c$) of about 35 Å.[80] This can be explained using the band diagram of the AlGaN/GaN heterostructure with conditions of the AlGaN layer below and above $d_c$, respectively, as shown in Figure 2.10. For a deep enough surface donor state ($E_D$), when the AlGaN is less than $d_c$, $E_D$ will lie below the Fermi level ($E_F$) and no electrons will be able to flow to the AlGaN/GaN interface to form a 2DEG due to charge neutrality.[80] In this case, a polarization dipole induced uniform electric field is formed in the AlGaN layer, and can cause the energy difference ($E_F$-$E_D$) to decrease with increasing AlGaN layer thickness. Once $d_c$ is achieved, $E_D$ will equal $E_F$ and electrons will become energetically available to transfer from the donor states at the AlGaN layer surface into the conduction band at the AlGaN/GaN interface, forming the 2DEG and leaving behind a positive charge at the surface.[80,82] The electron transfer increases with the AlGaN layer thickness, and $E_F$ is be pinned at $E_D$, until all the surface donor states are emptied. The surface donor states are reported to be 1.6 eV below the

conduction band minimum and are attributed to oxygen impurities residing at the AlGaN surface.[82]

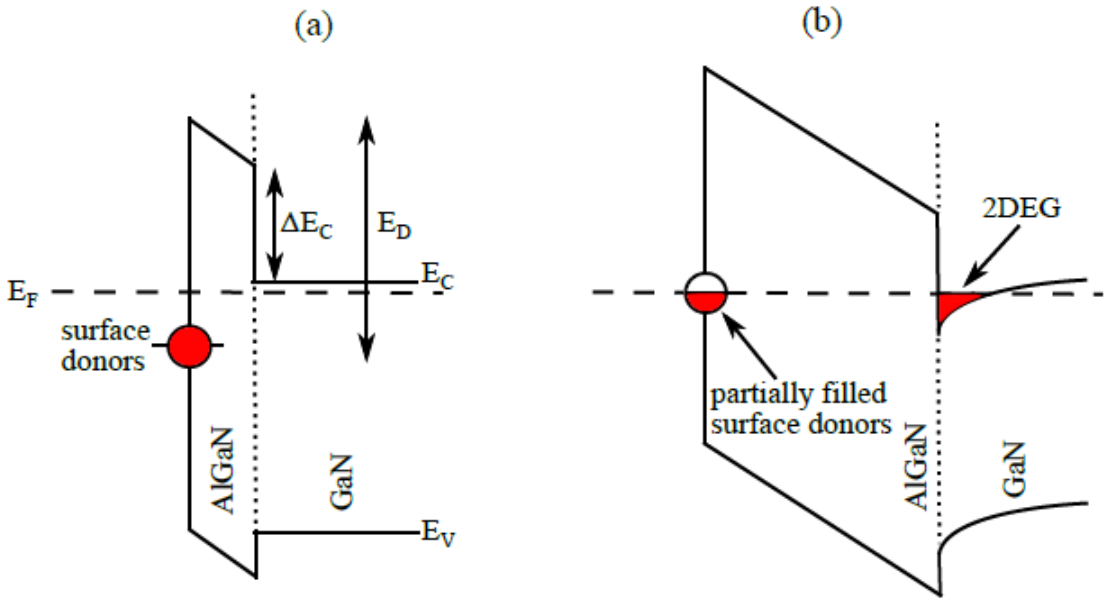


Figure 2.10. Schematic of the band diagram for the AlGaN/GaN heterostructure with the thickness of AlGaN layer (a) less than and (b) greater than the critical thickness for the formation of the 2DEG. (Adapted from Ibbetson *et al.*[80])

A simplified cross-sectional structure of a high-power AlGaN/GaN HEMT is shown in Figure 2.11, consisting of two ohmic contacts serving as source and drain which are electrically connected to the 2DEG and a Schottky contact as gate between the ohmic contacts. Also, a passivation layer, which is usually made of $Si_3N_4$, is deposited over the entire surface area of the device which can improve the electrical performance.[83] By applying a positive drain bias with respect to the grounded source ($V_{DS}$), a drain current ($I_{DS}$) flows through the 2DEG between the two ohmic contacts (termed as channel region). When a negative bias is applied to the gate contact relative to the source contact ($V_{GS}$), this counteracts the polarization field in the AlGaN layer causing a local depletion of the 2DEG underneath the gate. $I_{DS}$ reduces continually with the increase of $V_{GS}$. When $I_{DS}$=0, the 2DEG is fully depleted underneath the gate, and this critical voltage is termed the pinch-off voltage. The minimum $V_{GS}$ to allow $I_{DS}$ to flow is termed threshold voltage, $V_{th}$. Therefore, the current flow in the HEMT can be effectively controlled by the gate voltage, which forms the basis of transistor operation. Moreover, a localised peak electric field usually occurs at the drain side of the gate edge in a HEMT when it is biased under conditions of ON-state[84] or pinch-off[85] operation, a metallic extension of the source or gate contact named field plate (FP), as

schematically illustrated in Figure 2.11, is then normally incorporated to reduce this peak value.[86]

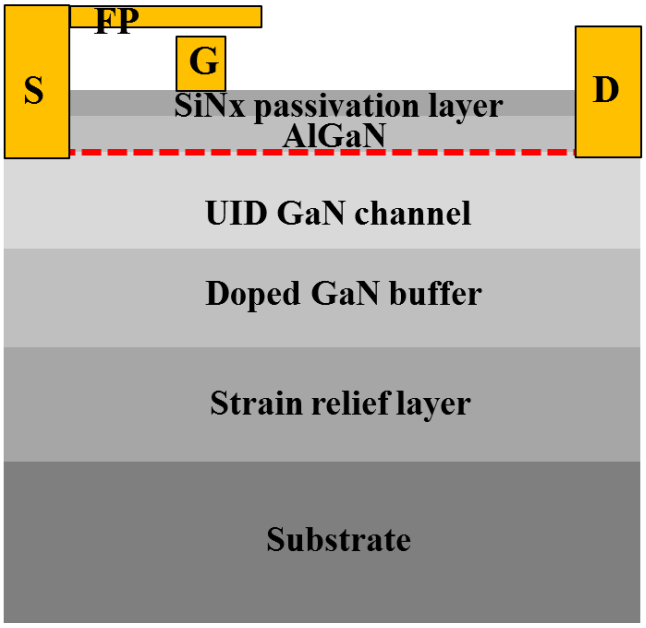


Figure 2.11. Schematic cross-section of a high-power HEMT with the 2DEG layer indicated, where S, D, G and FP corresponds to the source, drain, gate and field plate, respectively.

The typical current-voltage (I-V) characteristics of a high-power AlGaN/GaN HEMT are shown in Figure 2.12. Current density, defined as $I_{DS}$ per gate width (A/mm), is often exploited instead of absolute current to enable comparison between devices of different gate sizes. In the device structure, gate width corresponds to the longest gate dimension (i.e., the direction perpendicular to the page in Figure 2.11). Consider firstly the case of $V_{GS}$=0, $I_{DS}$ increases linearly with $V_{DS}$ until reaching a knee voltage ($V_{knee}$), after which $I_{DS}$ saturates, termed as $I_{max}$. This is because, upon increasing the drain bias, the gate becomes progressively negatively biased with respect to the channel voltage underneath the gate, until depletion of the 2DEG at the point of $V_{knee}$, resulting in a saturated $I_{max}$. Similarly, loading of a more negative bias will reduce the $V_{knee}$ and $I_{max}$, as illustrated in Figure 2.12. It is also noted that $I_{DS}$ (or $I_{max}$) decreases instead of remaining as a plateau when $V_{DS}$ is further increased over the $V_{knee}$ point; this is caused by the self-heating of the device and the accompanied reduction in electron mobility. AlGaN/GaN HEMTs can be normally-ON or normally-OFF.

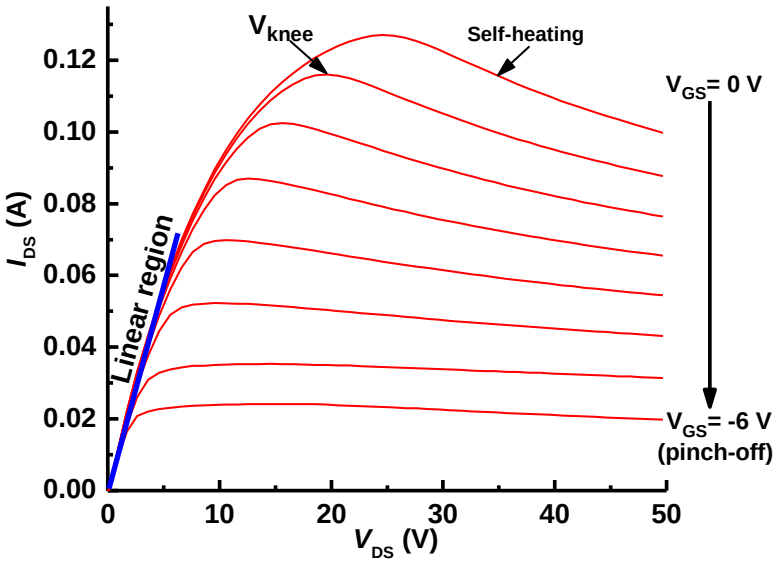


Figure 2.12. $I_{DS}$-$V_{DS}$ characteristics of a high-power AlGaN/GaN-on-Si HEMT at different $V_{GS}$.

## 2.2 Properties of diamond

Owing to many attractive properties such as a high refractive index and dispersion (being applied for commercial jewelry), and the highest hardness of any known bulk materials (being used as drilling and cutting tools), diamond has been a material of choice in a wide range of applications. Recently, due to its extremely high thermal conductivity, diamond demonstrates its potential as a highly efficient heat spreading material, especially for microelectronic applications and optic-electrical devices.

### 2.2.1 Crystal structure

As a metastable allotrope of carbon, the diamond crystal structure consists of 8 carbon atoms in the unit cell which are tetrahedrally bonded with $sp^3$ hybrid bonds ($\sigma$-bonds), and arranged in a variation of the face-centered cubic (FCC) lattice, as depicted in Figure 2.13. Associated with every lattice site in the primitive cell, Yu *et al.*[48] put forward that the diamond structure can be simply understood as being constructed by two FCC sublattices, and with only one atom locating on every lattice site; then along the [111] direction, one sublattice is displaced relative to the other sublattice by one quarter of the body diagonal of the primitive cell. As a result, in the finally constructed crystal structure, each atom is surrounded and bonded by four nearest neighbour atoms forming a tetrahedron. In detail, the angle between these bonds is 109.5°, and the bond length is 1.54 Å, therein a lattice constant ($a$) of 3.56 Å is results. Other group IV elements (e.g., Si, Ge, Sn) also construct in the diamond crystal structure. If the two atoms in the primitive cell are different, a zincblende structure is obtained, such as GaAs, CdTe *et al.*, compound semiconductors. The symmetry of the

diamond structure can be described by the *Fd-3m* space group. The corresponding first Brillouin zone and some high symmetry points are illustrated in Figure 2.13(c and d).

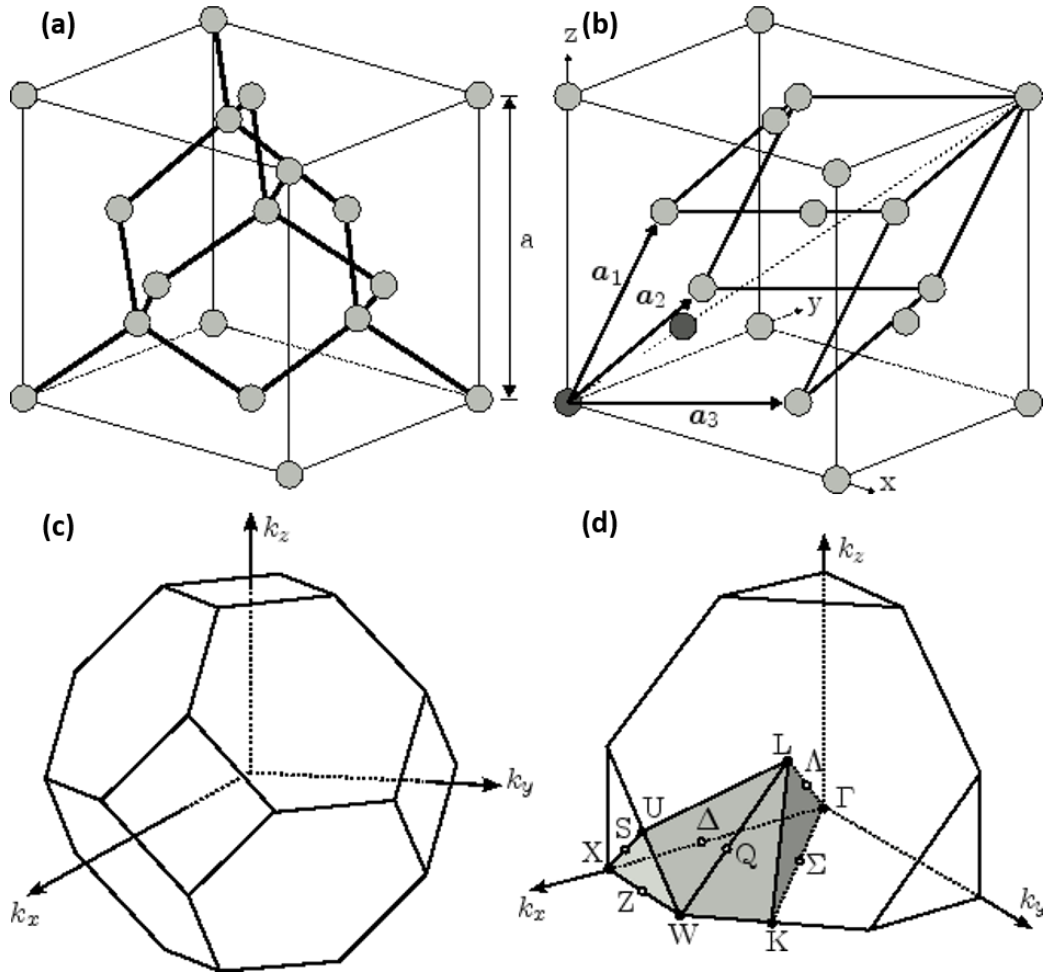


Figure 2.13. The crystal structure of diamond: (a) schematic of the unit cell, with the lattice constant (*a*) and the tetrahedral bond configuration displayed; (b) illustration of the primitive lattice vectors represented in ($a_1$, $a_2$, $a_3$); (c) the first Brillouin zone of the diamond structure; (d) high symmetry points illustrated in part of the first Brillouin zone.[87]

### 2.2.2 Electronic band structure

The electronic band structure of diamond, calculated using the nonlocal empirical pseudopotential method[88] and a lattice parameter of 3.56 Å, is shown in Figure 2.14. Diamond has a wide indirect bandgap of about 5.5 eV[88] and is intrinsically an excellent electrical insulator that is typically used as a dielectric. The valence band maximum is located at the Γ-point while the conduction band minimum is located near the L-point. Due to its very high electron and hole mobilities, 4500 and 3800 $cm^2V^{-1}s^{-1}$, respectively, and a high breakdown voltage (10 MV/cm), diamond has attracted wide interests in electronic applications. However, its doping remains a challenging problem. The p-type doping of diamond has been

realized with boron, although it is a rather deep acceptor (about 0.37 eV above the valence band maximum). While the n-type doping is recently reported through phosphorus or nitrogen but is still very challengeable and is the current focus of intense research.[89,90]

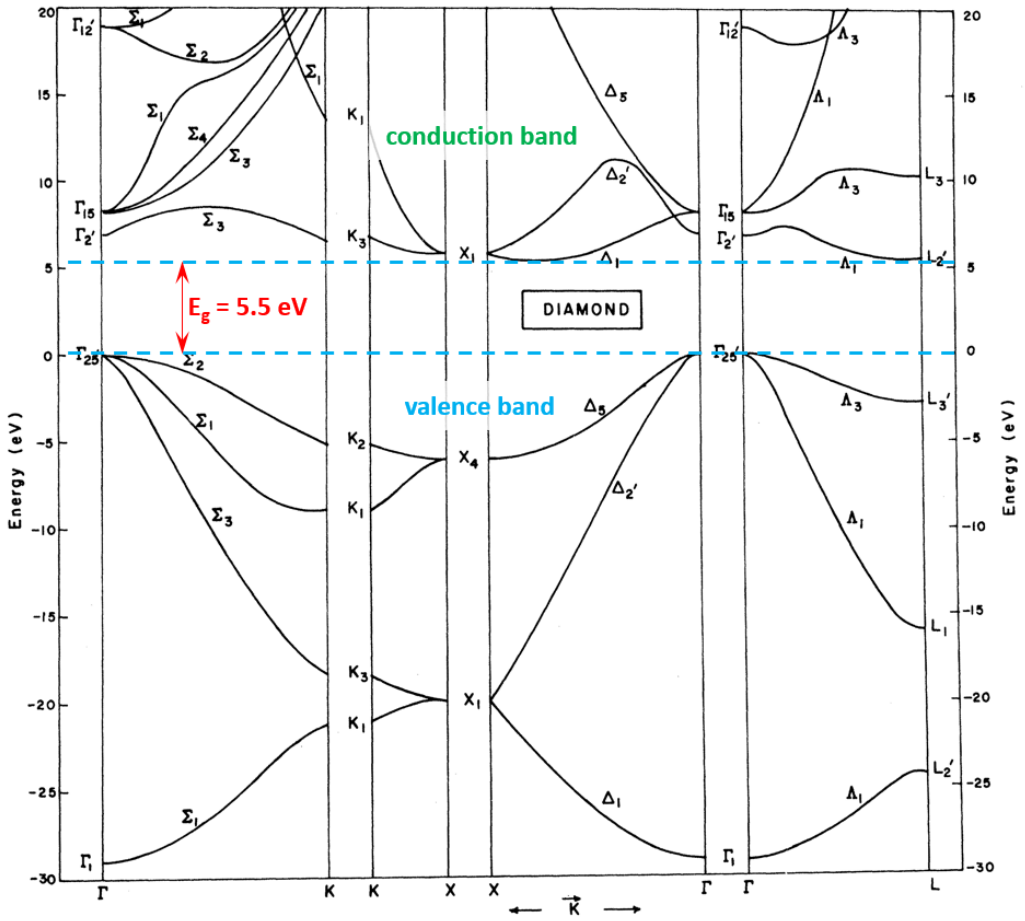


Figure 2.14. Electronic band structure along principal symmetry lines of diamond, calculated via the nonlocal empirical pseudo-potential method.[88] Adapted from Hemstreet *et al*.[88]

### 2.2.3 Phonon dispersion

The phonon dispersions of diamond calculated from a five-parameter adiabatic bond charge model (ABCM) proposed by Weber[91] is shown in Figure 2.15. There is a minor but interesting feature in this figure which is not obvious that the maximum energy of the optical phonon branch occurs along the Γ-X direction instead of at Γ-point as in Si and Ge. As the primitive cell of diamond structure has 2 atoms, there are 3 acoustic and 3 optical branch phonon modes. At the center of the Brillouin zone (Γ), the transverse modes are doubly degenerate, while all the optical modes at Γ–point exhibit the same frequency, bringing about a single triply degenerate optical phonon with a frequency of ~1332 $cm^{-1}$. The high thermal conductivity of diamond partly owns to its stiff $sp^3$ bonds that lead to high phonon cut-off

frequency (~41 THz) and high acoustic velocities (12-18 km/s). The high stiffness of the $sp^3$ bonds also results in the high Young's modulus (1220 GPa) in diamond.

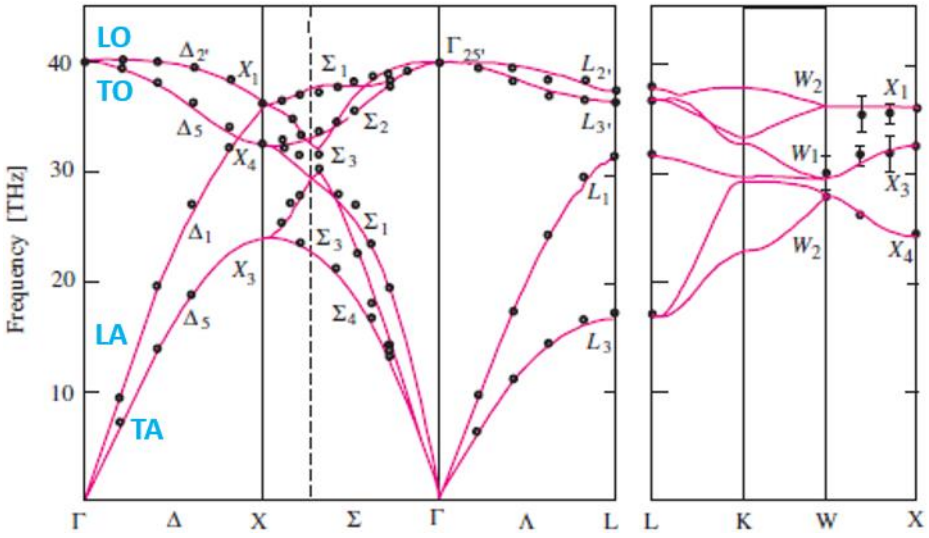


Figure 2.15. Phonon dispersion curves of diamond. The longitudinal (transverse) acoustic (LA/TA) and optical (LO/TO) branches are illustrated. The solid lines were calculated from a five-parameter adiabatic bond charge model (ABCM), the circles represent experimental data. Adapted from Weber *et al.*[91]

### 2.2.4 Thermal conductivity

High purity single-crystalline diamond (SCD) especially type-II diamond (see Table 2.3 for detailed classification) has the highest thermal conductivity ($\kappa_{Dia}$) of any natural bulk material, which is ~2200 W/mK at room temperature, and can even reach 10,000 W/mK at about 77 K. Recently, chemical vapor deposition (CVD) grown polycrystalline diamond (PCD), which is lower cost and easier to grow than SCD, can also reach a bulk thermal conductivity as high as ~2000 W/mK.[92,93] All the diamond related work investigated in this thesis are CVD-grown PCD films. However, affected strongly by the quality, grain structure and grain size (D), the measured room temperature thermal conductivity of CVD grown PCD films covers the range from ~1-10 W/mK[94-97] in ultra-nanocrystalline diamond (UNCD) film to ~550 W/mK in micro-crystalline diamond (MCD) film[98-104] (see Figure 2.16). This grain size dependence of thermal conductivity can be estimated from an empirical formula $\kappa_D = (1/3)Cv_D$, based on the assumption that phonon propagation inside the grain is the same as that in the bulk crystal.[99,100]

Table 2.3. Diamond types and characteristics.

| Diamond type | | Impurity type | Impurity | FTIR indicators | Most common colours |
|---|---|---|---|---|---|
| I | Ia | Nitrogen (aggregated); vacancy | ≤3000 ppm | Aggregated N (1282, 1175 $cm^{-1}$) | Colourless, brown, yellow, pink, orange, green, violet |
| | Ib | Nitrogen (isolated); | ≤500 ppm | Isolated N (1344, 1130 $cm^{-1}$) | Yellow, orange, brown |
| II | IIa | Nitrogen (isolated); | - | No detectable impurities | Colourless, brown, pink, green |
| | IIb | Nitrogen (isolated); | - | No detectable impurities | Blue, gray |
| | | Boron (isolated) | ≤1 ppm | Boron (2803, 2458 $cm^{-1}$) | |

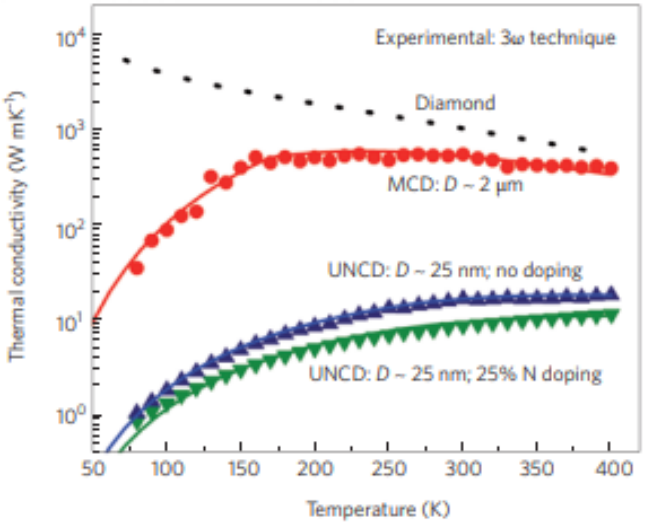


Figure 2.16. Comparison of diamond thermal conductivity for different grain sizes and their temperature dependence. Adapted from Shamsa *et al.* [104]

The thermal conductivity behavior can normally be well understood by phonon scattering mechanisms for both SCD and PCD, although there are still lots of debates for PCD.[25,105] Due to the complex grain structures obtained from different PCD growth methods, which range from homogeneous nanocrystals to needle-like or columnar shape structure, the phonon transport is disturbed in different ways. For example, the ultralow $\kappa_{Dia}$ of homogeneous UNCD is typically due the strong confinement of phonon mean free path (MFP) in pure diamond by its grain size and the high density of grain boundaries (this can be

understood from phonon scattering, see detailed explanation in Section 2.1.4). While a higher out-of-plane thermal conductivity than in-plane thermal conductivity is normally presented in columnar PCD, which is different to the isotropic behavior in SCD. It can be illustrated that phonon scattering centers prefer to distribute themselves along the grain boundaries and the phonons are diffusively scattered in the grain-grain inter-region, therefore creating an anisotropic MFP of the phonons in the columnar shape grain and therein an anisotropic thermal conductivity within the PCD. Besides, the grain boundary itself comprises of several types of bonding, defects and disordered phases (such as $sp^2$- and $sp^3$-bonding, C-$H_x$, C-vacancy), and other impurities also tend to accumulate at grain boundaries, which results in a thin layer with ultralow thermal conductivity, this lowers the total thermal conductivity. Another key factor that needs to be taken into account is that the columnar grains evolve in size with increased thickness of the PCD film. This evolution has been shown experimentally and computationally[35,106-108] both the lateral size of the grains and their aspect ratios strongly change with the PCD film thickness. Therefore, a different grain boundary density at each depth of the PCD film must be considered, especially when measuring their in-plane $\kappa_{Dia}$.

Nevertheless, due to its extremely high thermal conductivity which is about 4-5 times higher than that of presently commercialized SiC substrate (330-490 W/mK), CVD diamond has demonstrated its potential as a highly efficient heat spreading material, especially for microelectronic applications and optic-electrical devices. Recently, combining GaN-based devices with high thermal conductivity CVD grown polycrystalline diamond, which can reach a bulk thermal conductivity as high as ~2000 W/mK[92,93], has been shown to greatly improves the device thermal management. For example, substituting a SiC substrate with diamond, to form GaN-on-diamond, has been shown to improve the heat transport in these devices, enabling a potential three-fold increase in output power density. [27,28,109] This can be achieved through the integration of CVD diamond with GaN devices, either by direct growth,[27,28,109] or wafer bonding.[110-113]

### 2.2.5 Growth of CVD diamond

The formation of SCD is only thermodynamically stable at a high-pressure and high-temperature (HPHT) environment, which means to crystallize carbon in the diamond phase, these conditions need to be fulfilled. Similar to the process of natural formation of diamond in Earth's mantle, in the HPHT growth method, carbon is dissolved into molten metal (e.g., Fe, Co, Ni) at a temperature of over 2000 K and then pressed under several GPa by hydraulic-pressures, where diamond can crystallize from the melt.[31] A single-crystal diamond with a size of up to millimeters can be grown using the HPHT method, however, this growth method is not suitable for the fabrication of the large scale wafers that are typically required in today's semiconductor CMOS processing for applications such as electronics. It was discovered in the

1950s[114] that diamond can also form from gaseous precursors at much lower temperatures and pressures, this has become the foundation of the CVD diamond growth presently used.

Growth of CVD diamond has been well investigated in the past four decades. A series of CVD grown PCD films with grain size ranging from ultra-nanocrystalline to microcrystalline is presently available. Besides appropriate substrate and seeds, the CVD process conditions for diamond growth mainly include gaseous reactants (typically hydrogen and methane), temperature and pressure. Due to many practical reasons, two methods for the activation of gaseous and diamond growth are presently dominant in this field, namely hot filaments and plasmas (particularly microwave plasma) activated methods, initialized as HFCVD and MPCVD separately. A schematic of these two growth methods is shown in Figure 2.17. Successful growth processes need to consider seeding on non-diamond substrates, nucleation phenomena, and the hydrogen/hydrocarbon chemistry such as the methane/hydrogen ratio and the gas flow rate.

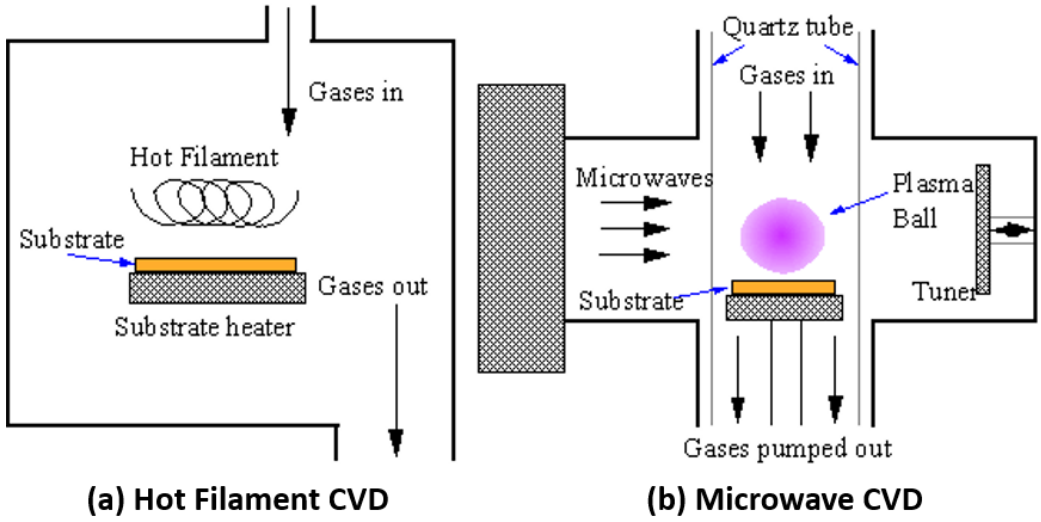


Figure 2.17. (a) Schematic of hot-filament (HFCVD) and (b) microwave-plasma CVD (MWCVD). (Adapted from http://www.chm.bris.ac.uk/pt/diamond/stuthesis/chapter1.htm)

The core process of CVD diamond synthesis is illustrated via a schematic principle of hot filament CVD in Figure 2.18. When a mixture of hydrogen gas and methane is introduced into the reactor, the gasses undergo an activation process, during which reactive hydrogen atoms and carbon-containing radicals such as $CH_3$, $CH_2$, CH et al., are created through a heated metal filament, or microwave plasma, etc. Then at a region close to the hot substrate called the diffusion layer, complex reactions happen among these reactive radicals, forming acetylene ($C_2H_2$) and other $C_xH_y$ compounds which can further react and bond with the surface carbon species on the substrate, provided a suitable surface chemistry is available. The substrate temperature is set relatively low compared to the gaseous phase so that the

adsorption rate can be higher than desorption rate which results in the deposition of carbon on the surface. Typically, both graphitic carbon and diamond form, but the growth of the latter is preferred under certain conditions. Notably, hydrogen atoms play a critical role in the growth which can etch back the deposited graphite at a higher rate than the diamond and therefore minimize the graphitic carbon in the growing film.

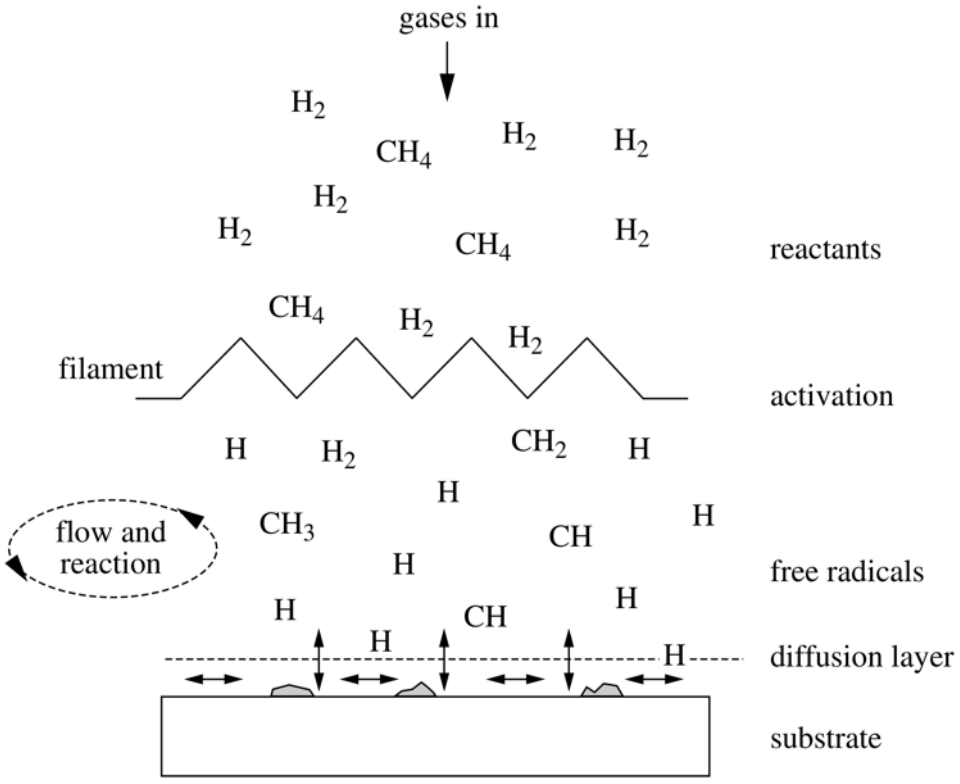


Figure 2.18. Schematics of the reactions of CVD diamond growth: in the case of a hot filament. Besides a heated filament, other activation sources such as microwave plasma, electric arc or combustion flame can also be used.[114]

For the fundamental understanding of CVD diamond growth, a 'standard model' was developed and summarized by Butler *et al*.,[115,116] containing the following key steps, as shown in Figure 2.18 and Figure 2.19. As the following detailed description which is mainly based on Butler *et al*.,[115,116] the diamond lattice is firstly stabilized and prevented from being rearranged into graphitic carbon through termination with hydrogen atoms (or other similar chemical species), and the environmental temperature is also too low to activate a spontaneous bulk rearrangement (i.e. it is below the Debye temperature of diamond). Secondly, the molecular hydrogen is dissociated by the gaseous activation process into atoms which react with the source methane and create a complex mixture of various hydrocarbon species involving the reactive carbon-containing radicals. The hydrogen atoms created during the gaseous activation process also react with the hydrogen atom from the surface CH bonds and generate hydrogen, thereby creating surface radical sites. Then these radical sites will

occasionally react with gas phase carbon-containing radicals and results in an adsorbed carbon species. However, most frequently, the radical sites are simply refilled through recombination with gaseous hydrogen atoms. This constant alternating of the surface-terminating species (hydrogen) further drives the surface chemistry to dehydrogenate the adsorbed carbon species and to incorporate carbon into the as-grown lattice. Finally, the atomic hydrogen, and other gaseous species (to a lesser extent), react with any *sp* or $sp^2$ carbon sites on the surface, converting them into $sp^3$ bonded carbon. Hydrogen also terminates as dangling bonds during the diamond growth, as in the last schematic shown in Figure 2.19.

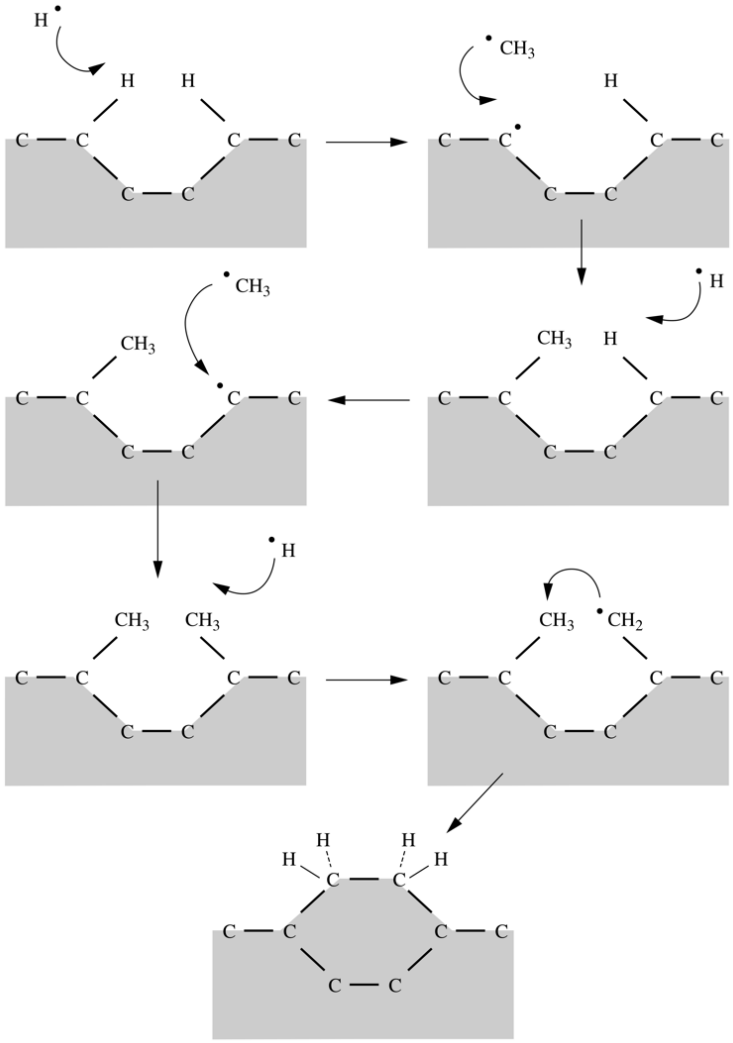

Figure 2.19. Schematics of the simplified reaction process occurring at the diamond surface: 'standard model', illustrating the adsorption of $CH_3$ radicals and desorption of H, as well as the function of atomic hydrogen.[114]

The growth carbon product is highly affected by the composition of gas mixture, as illustrated in the C-H-O composition phase diagram (Bachmann triangle diagram), shown in

Figure 2.20. Diamond can only form in a very narrow range of compositions. Especially, the composition region of the commonly used gas mixture precursor that is available for diamond growth is located on the C-H axis close to the H corner of the diagram, usually containing a range of 0.1-3% methane diluted in the hydrogen gas. The typical conditions for CVD diamond growth are 1.5-4 kPa and 600-1000 $^{o}$C. The growth rates can be up to 150 μm/h with a high purity using microwave plasma as an activation source,[31,114,117] but only about 0.1-1 μm/h by using HFCVD due to its lower ionization rates and ion energy although it is significantly cheaper. Notably, HFCVD can enable diamond grown on large substrates (4”-8”), while MWCVD limits the size to much smaller substrates. HFCVD also provides a less harsh environment (typically atomic hydrogen) from etching the substrates due to its lower ion energies. However, the metal filaments can cause contamination on the diamond, and become aged due to their interaction with the gas mixtures. Growth conditions may also change by updating the filaments, while MWCVD can provide better reproducibility of growth.

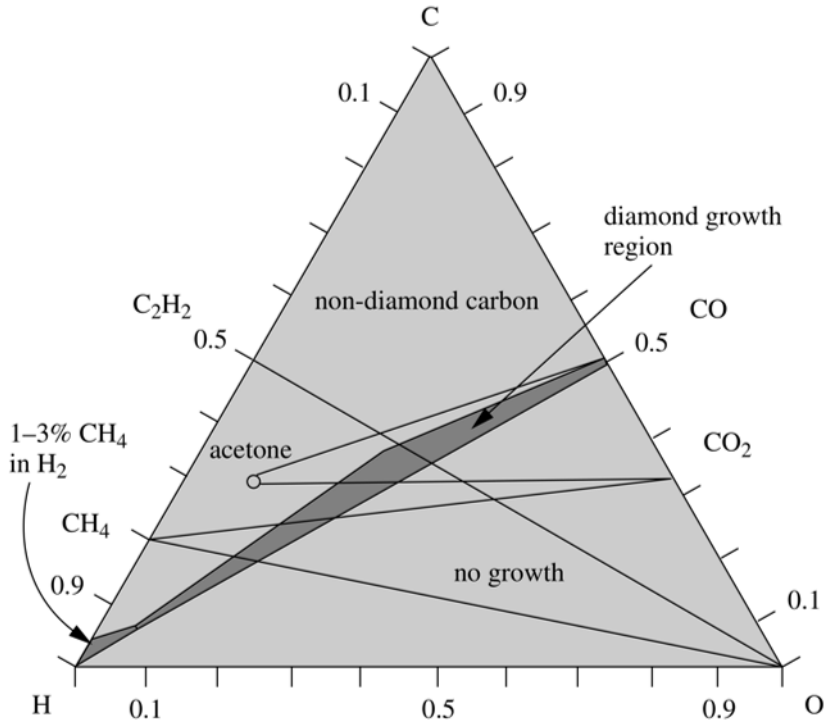


Figure 2.20. The Bachmann triangle diagram of C-H-O compositions, with the shaded region indicating the range suitable for CVD diamond growth. The commonly used compositions of gas mixtures are located near the H corner, consisting of a few % of methane diluted in $H_2$.[114]

During the CVD diamond growth, seeding and nucleation is a critical step, without which the continuous growth and high quality of diamond films is impossible. The purpose of seeding is to create bonding and nucleation sites for the reactive carbon-containing radicals to initialize the diamond growth. This can be realized by embedding diamond nano- or micro-

crystals into the substrate surface through appropriate methods, such as ultrasonic bathing a suspension of diamond nanocrystals, spin-coating the diamond nanocrystals onto the surface, or by abrasive treatment of the surface using diamond powder. Nucleation sites can also be formed by seeding a carbide layer on the surface via a chemical treatment, or biasing the carbon-containing ions, this technique is termed as bias-enhanced nucleation (BEN) and can be performed inside a modified reactor using the generated ions in the CVD process. With the help of a seeding technique, polycrystalline diamond can be grown on a wide range of commonly used substrates, such as Si, SiC, sapphire, and GaN, etc., without much consideration about the thermal expansion coefficient mismatch. However, large stress can be induced when growing thicker films that can lead to the cracking of the diamond. Presently, several hundred micrometers thick diamond have been achieved on Si and SiC. Notably, it is very difficult to form carbides with GaN and the GaN surface is easily etched by the harsh reactive environment, therefore a thin barrier layer e.g. SiN, AlN, AlGaN etc., can be used to protect the GaN epilayer from etching and alleviate the thermal stress due to the large thermal expansion coefficient mismatch between diamond and GaN.

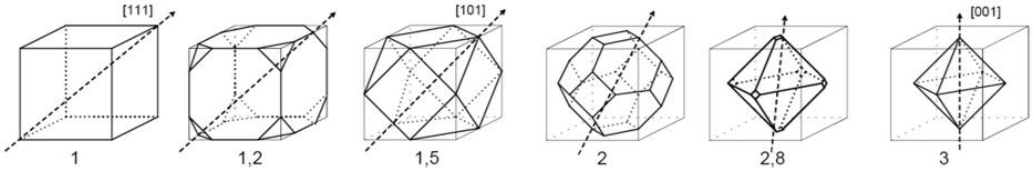


Figure 2.21. The grain shape evolution of a diamond crystallite at different values of the α-parameter that are individually grown under different conditions.[31,118]

At the initial stage of nucleation, the nuclei grains grow randomly in all three dimensions until they coalesce and form a dense and continuous film. In the following growth stage, the grains grow freely in the vertical direction but compete in the lateral, leading to the average grain size increasing with the film thickness. However, different grain morphology can form under different compositions of gas mixtures and growth temperatures. The evolution of morphology with thickness is found to be determined by the growth rates of different crystallite facets, which can be predicted through the ratio of the growth rates ($v$) of (100) and (111) facets (termed as $\alpha$-parameter):

$$\alpha = \sqrt{3}\frac{v_{(100)}}{v_{(111)}}. \tag{2.11}$$

Figure 2.21 illustrated that the shape of the crystallite grain can be defined by the $\alpha$-parameter, which is further found to be dependent on the gas mixture and growth temperature, as indicated in Figure 2.22 with different grain morphology micrographs illustrating this relationship. At high methane concentrations and low growth temperature, ultra-nanocrystalline diamond with crystallite sizes of only few nanometers forms due to the

inhibition of crystallite growth by the enhanced re-nucleation. While at low methane concentrations, texture-like crystallite structure of diamond is usually formed. Besides the composition of gas mixture and growth temperature, reactor pressure also significantly affects the grain structure of CVD diamond. By controlling these growth conditions, the average grain size, the grain orientation and the surface roughness can be fine-tuned to fulfill the requirements of different applications. It should be noted that growth conditions also affect the lattice quality of the grains, in the form of different concentrations of vacancies, twins, stacking faults, dislocations and extended defects. These factors determine the quality of grain boundaries where non-diamond carbon phases tend to accumulate. Consequently, the optically transparent or opaque of CVD diamond depends significantly on the growth conditions.

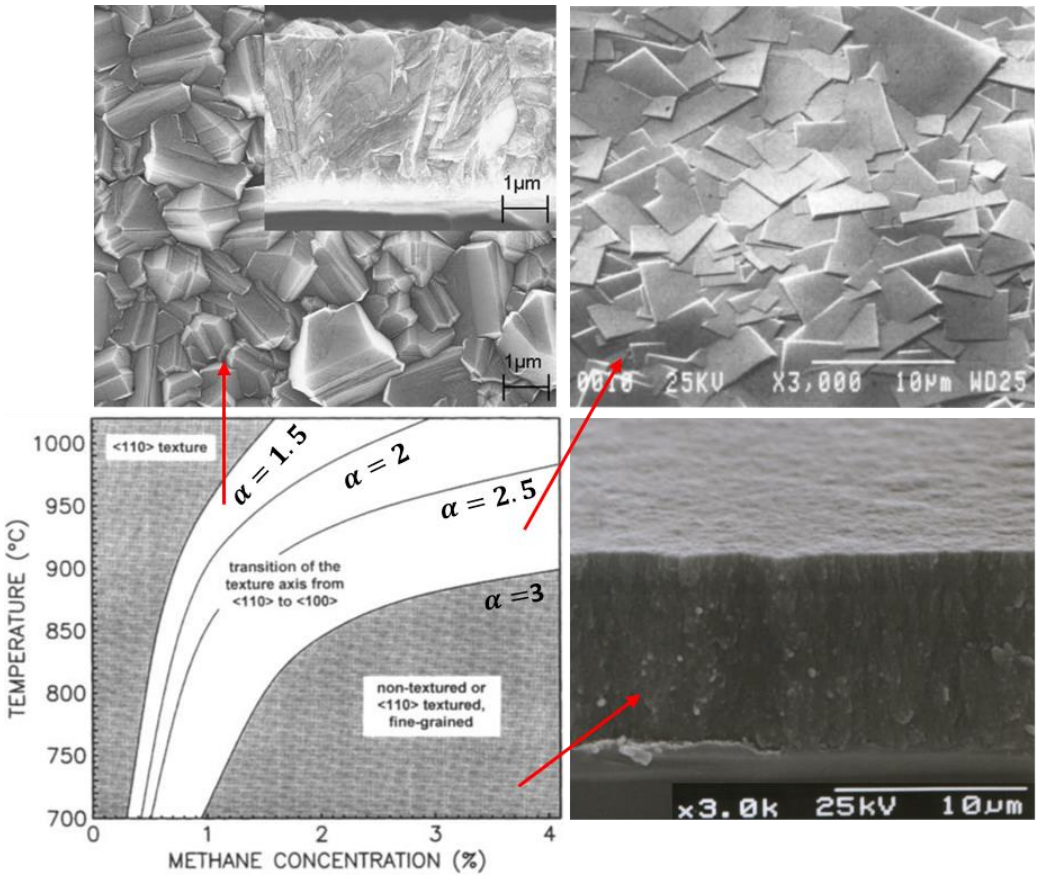


Figure 2.22. The temperature-methane-$\alpha$ parameter diagram, as shown in the bottom left of the figure, illustrates the dependence of temperature and gas mixture composition on the $\alpha$-parameter. The SEM images of typical grain morphologies of diamond grown at different growth condition regimes (methane concentration of 1% and 2% from top left to right respectively) using MWCVD and HFCVD technique are also shown.[118-120]

### 2.2.6 Thermal boundary resistance

To make full use of the excellent thermal performance of diamond, improving the thermal transport at interfaces is also critically important as a significant effective thermal boundary resistance ($TBR_{eff}$) still exists between the GaN epilayer and the substrate, as shown in Figure 2.23. For example, a lumped thermal resistance $TBR_{eff}$ between the GaN layer and the diamond substrate, including contributions from a dielectric barrier layer and the high grain boundary density of diamond near to the interface, can present a significant heat transfer barrier if not minimized carefully, which would limit the diamond thermal benefit for GaN-based devices.

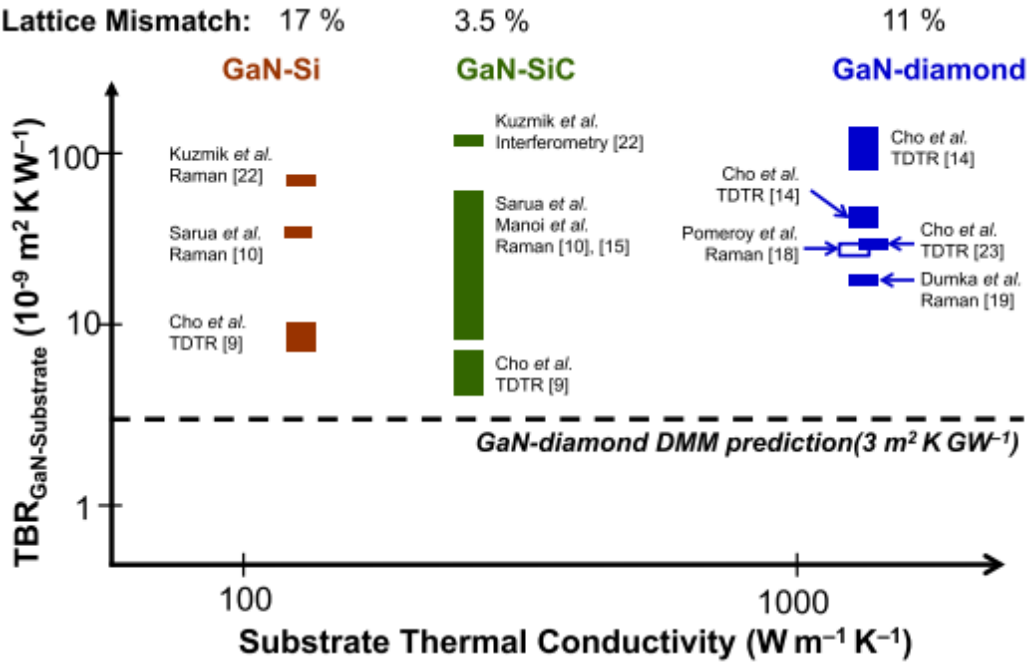


Figure 2.23. Comparison of TBR between GaN and substrate as a function of the substrate thermal conductivity for Si, SiC and diamond substrate, respectively. The TBR variations mainly result from the interfacial structure variations of samples fabricated under different conditions. A lattice mismatch between GaN and three investigated substrates is indicated. The corresponding measurement methods and the DMM model predicted TBR at GaN/diamond interface is also shown. Adapted from Won *et al.*[121]

For better understanding of the interfacial thermal transport, much work has been performed in the TBR mechanism, although there are often disagreements between predicted and experimental data[122,123]. In the case of purely specular phonon scattering, the acoustic mismatch model (AMM)[124] succeeds in predicting the TBR only at low temperatures ($T$<30 K) and ideal interfaces[125] by calculating the interfacial phonon transmissivity from the ratio of either side material's acoustic impedances. The AMM model can be written as:

$$\frac{1}{\mathrm{TBR}^{\mathrm{AMM}}} = \frac{1}{2}\sum_j \Gamma_{1,j} \int_0^{\omega_{c,1,j}} \hbar\omega_j v_{1,j} D_{1,j}(\omega_j) \frac{\partial n(\omega_j,T)}{\partial T} d\omega_j, \tag{2.12}$$

where $\hbar$ is the reduced Planck's constant, $\omega$ is the phonon frequency, $j$ represents the phonon polarization, $\omega_{c,1,j}$ is the Debye cutoff phonon frequency of material 1 (which normally is the one of lower Debye temperature), $v_{1,j}$ is the acoustic velocity of material 1 at the $j^{\mathrm{th}}$ polarization mode, and $D_{1,j}(\omega_j)$ is the phonon density of states. When assuming a Debye density of states, $D_{1,j}(\omega_j)$ can be calculated by $D_{1,j}(\omega_j) = {\omega_j}^2/2\pi^2 v_{1,j}^3$. $\Gamma_{1,j}$ is an integral and represents a complicated function of the densities and of the acoustic velocities of the two medium, $n(\omega_j, T)$ is the Bose-Einstein distribution function, and can be described as:

$$\Gamma_{1,j} = \int_0^{\pi/2} \alpha_{1\to2}(\theta, j)\cos\theta\sin\theta d\theta; \tag{2.13}$$

$$n(\omega_j, T)d\omega_j = \frac{d\omega_j}{[\exp(\hbar\omega_j/k_{\mathrm{B}}T)-1]}, \tag{2.14}$$

where $\theta$ is the phonon incident angle, $k_{\mathrm{B}}$ is the Boltzmann constant, $\alpha_{1\to2}(\theta, j)$ is the energy transmission probability of the interface for phonons incident at an angle of $\theta_1$ in medium 1 and $\theta_2$ in medium 2, and can be expressed as:

$$\alpha_{1\to2}(\theta_1, \theta_2, j) = \frac{4\frac{Z_2}{Z_1}\frac{\cos\theta_2}{\cos\theta_1}}{(\frac{Z_2}{Z_1}+\frac{\cos\theta_2}{\cos\theta_1})^2} = \frac{4Z_2Z_1}{(Z_1+Z_2)^2}\Big|_{\theta_1=\theta_2}, \tag{2.15}$$

where $Z_i$ is an acoustic impedance and equal to the product of the mass density ($\rho_i$) and the acoustic velocity ($v_i$), and can be described as $Z_i = \rho_i v_i$. As the AMM model only considers ideal interfaces, Swartz *et al.*[126] then developed the diffuse mismatch model (DMM) for predicting the TBR based on assumptions of elastic, completely diffuse, and isotropic phonon scattering, which predicts relatively well the TBR across imperfect interfaces at somewhat higher temperatures[125,126]. The DMM model can be obtained as:

$$\frac{1}{\mathrm{TBR}^{\mathrm{DMM}}} = \frac{1}{4}\sum_j \int_0^{\omega_{c,1,j}} \hbar\omega_j v_{1,j} D_{1,j}(\omega_j) \frac{\partial n(\omega_j,T)}{\partial T} \beta_{1\to2}^{(2)}(\omega_j, T)d\omega_j; \tag{2.16}$$

$$\beta_{1\to2}^{(2)}(\omega_j, T) = \frac{\sum_j v_{2,j} D_{2,j}(\omega_j)}{\sum_j v_{1,j} D_{1,j}(\omega_j) + \sum_j v_{2,j} D_{2,j}(\omega_j)}, \tag{2.17}$$

where $\beta_{1\to2}^{(2)}(\omega_j, T)$ is the phonon transmission coefficient from side 1 of the interface to side 2. However, the DMM has been shown to often overestimate the TBR experimental data[127,128] at above 60 K. The phonon radiation limit (PRL) model, estimating the minimum TBR from elastic scattering, is then developed[129] as:

$$\frac{1}{\mathrm{TBR}^{\mathrm{PRL}}} = \frac{1}{4}\sum_j \int_0^{\omega_{c,1,j}} \hbar\omega_j v_{2,j} D_{2,j}(\omega_j) \frac{\partial n(\omega_j,T)}{\partial T} d\omega_j. \tag{2.18}$$

In which, $v_{2,j}$ represents the phonon velocity of material 2 at the $j^{th}$ polarization mode. But for heavily mismatched interfaces at higher temperatures (>120 K), the PRL model still overpredicts the TBR. Recently, computational efforts[127,130-132] provide additional findings in phonon transport. Molecular dynamics (MD) simulations under a series of temperatures were performed by Stevens *et al.*,[132] on both lightly and highly mismatched interfaces and a strong linear temperature dependence of the TBR was observed, suggesting that both elastic and inelastic scattering have occurred at the interfaces. By contrast, although depending on the temperature derivative function of the Bose-Einstein distribution, the DMM still only predicts a constant TBR at higher temperatures ($T>\Theta_D$) when elastic scattering is assumed. Evidence of inelastic scattering has also been verified experimentally at medium temperatures (80-300 K)[130] and high temperatures (300-500 K)[131], by observing a linear trend in the TBR on heavily mismatched interfaces, suggesting that inelastic scattering can play a significant role in the TBR.

## 2.3 Properties of layered materials and GaTe

### 2.3.1 Properties of layered materials

Monolayer or few-layers layered materials, where each layer is atomically thin and bonded by van der Waals (vdW) forces between interlayers, are usually termed as two-dimensional (2D) materials. Recently the preparations of layered materials through mechanical exfoliation or chemical synthesis have achieved great advances, attracting considerable interest and enabling renewed investigations into 2D materials beyond graphene.[133] Various optical and electrical properties have been demonstrated by these materials which can be fundamentally ascribed to their unique solid-state structures,[134-141] such as the high electron and hole mobility (2300 and 1000 $cm^2v^{-1}s^{-1}$, respectively) in few-layers black phosphorus (BP),[142] the excellent room temperature current on/off ratio ($10^8$) in monolayer molybdenum disulfide ($MoS_2$),[143] the ultrahigh photo-responsibility ($10^4$ A/W) in multilayer gallium telluride (GaTe)[144] and the very fast photocurrent response speed (1.5 ps) in graphene.[145] The 2D materials contain large family members with various properties (Figure 2.24), among which structural symmetry plays a more and more interesting role, examples range from those with high in-plane symmetry such as graphene to those with low in-plane symmetry for example BP, GaTe, molybdenum ditelluride ($MoTe_2$), tin selenide (SnSe) and rhenium disulfide ($ReS_2$).[137,138,146-148] In particular, some low structural symmetry 2D materials whose material properties differ along different in-plane crystal orientations have demonstrated significant in-plane anisotropy in their optical, electrical and thermal properties.[136,137,149-151] For example, multilayered BP has demonstrated anisotropic electron-photon and electron-phonon interactions, thermal conductivity and thermoelectric properties[142] along its armchair and zigzag orientations;[136,142,149,152] highly anisotropic optical

and electrical properties have been found in layered SnSe.[151] In addition, in-plane optical anisotropy has recently been revealed in multilayered GaTe.[137] Many methods and tools have been developed to characterize these different properties in the nanoscale, among which, spectroscopy techniques have now proved to be the most efficient tools used to investigate the optical behaviors of 2D materials especially in understanding the light-material interaction.[136,137,147,153-157] For example, micro-Raman spectroscopy recently provides a quick, *in-situ*, nondestructive and noninvasive method for characterizing the in-plane anisotropic crystal orientation of 2D materials in comparison to the classical transmission electron microscopy (TEM), due to their typical large Raman cross section which results in a strong signal.[136,137,141,147] Also, micro-Raman spectroscopy has shown advantages in investigating the in-plane anisotropic light-material interactions involved in 2D materials through combining multiple techniques such as using recently developed circular or angle-resolved polarization metrology,[136,137,141,147] varying the laser excitation wavelength and power, or using resonant Raman[158,159] scattering.

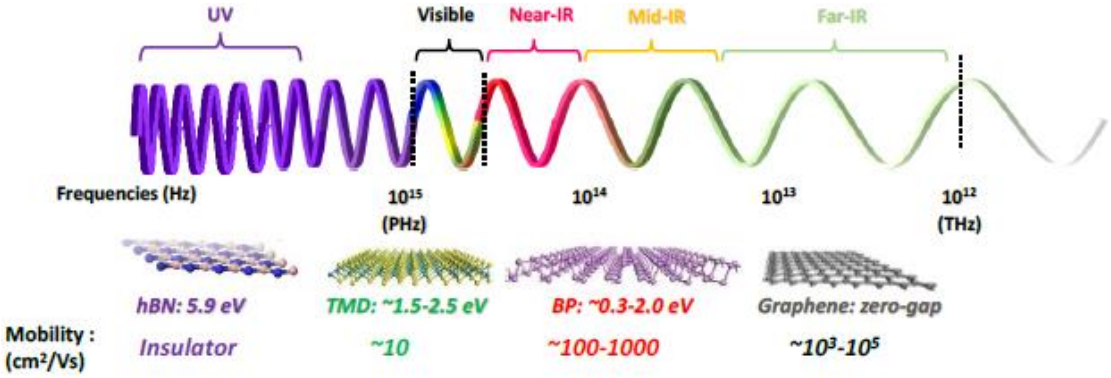


Figure 2.24. Schematic of various 2D materials with corresponding frequency ranges and mobility, bandgap, including graphene, black phosphors (BP), transitional metal dichalcogenide (TMDC) and hexagonal boron nitride (hBN). Adapted from Ling *et al*.[146]

The novel and distinguished properties of these ultrathin 2D materials that are significantly different from those of their bulk counterparts enable many interesting applications, ranging from examples such as sensor devices due to their large surface-to-volume ratio to photonic devices with stable excitons due to the reduced dimension.[135] Other examples include high switch ratio transistors ($MoS_2$),[143] anisotropic high performance thermoelectric devices (BP),[142,160] topological semimetals ($WTe_2$),[161] superconductors ($NbSe_2$)[162] and ferromagnets ($CrL_3$).[163] Besides, the versatile vdW heterostructures constructed on these 2D materials with their individual unique properties have also demonstrated many combined interesting properties, showing an unlimited potential for electronic, photonic and optoelectronic applications, such as optical modulators,[164] plasmonic devices,[165] light emitting diodes,[166] and photodetectors.[167-170] Many 2D materials are also

demonstrated as good candidates for fabricating nano- or flexible devices due to their outstanding flexibility and stretchability.

In practical applications of 2D semiconductors, great potential has also been shown for their electronic band structure and other solid-state physical properties being more easily manipulated by present technologies exploited in band structure engineering, making them appealing for various applications in such as controllable electronics,[171] optoelectronics,[172] spintronics[173] and valleytronics.[174-176] Approaches including chemical doping,[177-180] temperature,[181] strain[182-188] as well as intercalation[181], surface functionalization[189] and electrostatic carrier injection[190] have been undertaken for such band structure engineering. Compared to bulk materials, strain and stress are much more easily applied and controlled on 2D layered materials to modulate their band structure or even induce reversible phase transitions for promising nanoflexible and switchable devices. Hydrostatic pressure generated by a diamond anvil cell (DAC) is proven as a powerful tool to tune the lattice and electronic structure of semiconductors; many novel physics phenomena are also induced.[183,184,186] For example, multilayered $MoS_2$, $MoSe_2$, $WS_2$ and $WSe_2$ were reported to undergo a semiconducting to metallic electronic phase transition at high pressure, accompanied by an iso-structural phase transition in the form of a lattice distortion induced by tri-layer sliding, which can be ascribed to the increased interaction between the two adjacent layers of chalcogenide atoms overcoming the interlayer vdW force gap under high pressure; an intermediate state phase was normally generated between the semiconducting to metallic transition.[183,185,186,188] Meanwhile, Raman mode splitting into two peaks upon increased pressure in some 2D materials were noticed and found starting from the intermediate state, which was proposed due to the co-existence of a low-pressure semiconducting phase and a high-pressure iso-structural metallic phase,[186,188] however, the understanding of a detailed physical mechanism for peak splitting and its relationship with a phase transition still needs further exploration. Recently, a strain-induced direct-to-indirect bandgap transition was also discovered.[184,191] In contrast, few structural phase transitions of layered materials driven by hydrostatic pressure from DAC have been announced, except some reports about DAC pressured powder samples or a layer thickness dependent structural phase transition, or by thermal and chemical approaches;[192-197] an electrostatic doping driven structural phase transition in monolayer $MoTe_2$ has just been demonstrated.[198]

Furthermore, phase transitions from semiconductor state to metallic state are likely to be easily controlled in some 2D materials by strain (pressure) or temperature,[199-201] making them promising phase change materials (PCM). Raoux *et al*.[202] (in which the following introduction is mainly based on) illustrated that a PCM requires at least two phases with significantly different properties existed, and it also requires them to be able to be rapidly and repeatedly cycled between these phases; these unique properties make PCM promising candidates for use

as the memory material with renewed interests in phase change random access memory (PCRAM) devices.[203,204] Phase change devices can be used to store or retrieve information based on the difference in resistance resulting from a phase transition in the material, with the logical "1" or "0" characterized by the level of a current detected in the PCM layer during a read mode. Non-volatile memory devices are normally preferred in PCRAM devices, which are capable of storing data even with the power turned off. Besides, faster switch requires it is better to have only very little atomic motion induced during the fast crystallization process of the PCM,[205] rather than the phase segregation.[206] Another consideration for the future PCRAM devices are their dimension scaling to enable sizes much smaller (even atomic scale) than those of what can be built in devices today, under the increased system functionality from gigabytes to even more that requires higher device density in the same package size. Whatever, one aspect in scaling consideration for highly scaled PCRAM technology is how the properties of PCM can be affected by the thickness or even the properties of materials themselves when decreasing their dimensions. All these requirements make new nanoscale materials that with multiple phase transitions of significant difference under controlled temperature or pressure such as $VO_2$,[199-201] GaTe promising candidates for the future non-volatile microelectronic memory devices applications.

### 2.3.2 Properties of GaTe

GaTe as one of the important members in low symmetry layered materials with a direct bandgap of ~1.65 eV for thickness ranging from bulk to few layers, has obtained increased attention in recent years due to its extremely high photoresponsivity ($10^4$ A/W) and a fast response time (6 ms), showing advantageous application in photodetectors,[144,207,208] as well as other promising optoelectronic applications in solar cells, imaging arrays, radiation detectors[209], nonlinear optics[210] and thermoelectric devices.[211]

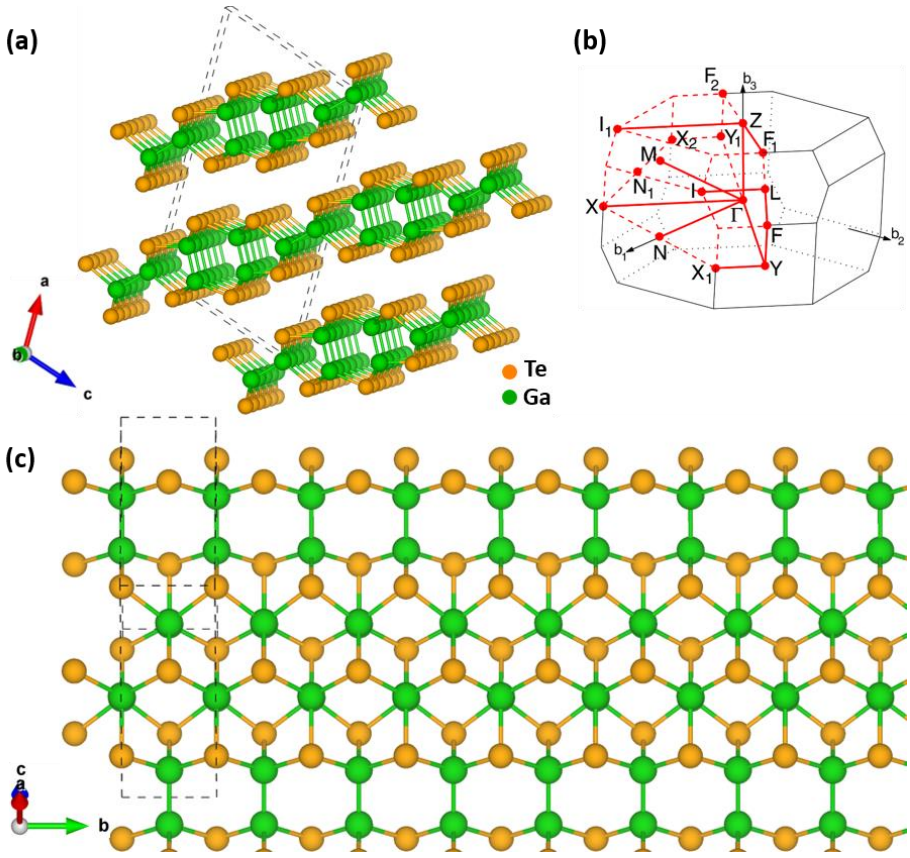


Figure 2.25. Schematic crystal structure of monoclinic GaTe: (a) normal view of unit cell indicating the bonds; (b) the first Brillouin zone and selected high-symmetry points for calculations (b1, b2, b3-axis corresponds to the a, b, c-axis in the reciprocal lattice structure, respectively); (c) top view, illustrating the armchair and zigzag in-plane atomic structures.

At ambient conditions, bulk GaTe crystallizes in a monoclinic lattice structure with space group of *C*2/*m* symmetry which comprises of a two-fold rotational axis $C_2$ (*b*-axis) and a mirror plane $\sigma_h$ (*a*-*c* plane), as shown in Figure 2.25(a) and (c); each monolayer GaTe unit consists of 6 Ga and 6 Te atoms in the primitive cell with the Ga atomic sub-layers sandwiched by 2 Te atomic sub-layers, demonstrating a high in-plane atomic configuration anisotropy in the *c*-(armchair) or *b*-(zigzag) direction, and the adjacent GaTe layers are stacked along the *a*-direction by vdW forces. In this structure, each Ga atom is surrounded by one Ga atom and three Te atoms, while each Te atom is bonded to three Ga atoms and interacts with other Te atoms of an adjacent monolayer by vdW force. Notably, there are two kinds of Ga-Ga bonds present: one third parallel to the in-plane direction, and two thirds perpendicular to the layers.[212] Figure 2.25(b) depicts the first Brillouin zone with selected high-symmetry points in the reciprocal lattice structure.

The in-plane anisotropic optical absorption, optical extinction, Raman scattering properties and related physics existed in multilayered GaTe flakes (~100 nm) have recently been investigated using angle-resolved polarized micro-Raman spectroscopy techniques combined with first-principles calculations, group theory, optical transition selection rules etc., with a weak anisotropic optical absorption and extinction in the visible spectral range but a strong crystalline orientation dependent anisotropic Raman intensity observed.[137] The Raman intensity anisotropies show an intricate dependence on flake thickness, excitation laser wavelength, phonon frequency and phonon mode symmetry, as shown in Figure 2.26. It was revealed that the major maximum of the Raman intensity was mostly aligned along armchair orientation under ≥ 633 nm wavelength laser excitation while along zigzag orientation under 532 nm wavelength laser excitation for all the Raman modes except the 161 $cm^{-1}$ mode, providing a convenient fingerprint character to determine the in-plane crystal orientations of GaTe flakes. However, how to tune these anisotropic properties into desirable applications and the related anisotropic interaction mechanism needs further intensive exploration.

| Laser / Peak ($cm^{-1}$) | 532 nm | | 633 nm | | 785 nm | |
|---|---|---|---|---|---|---|
| | Thin (58 nm) | Thick (136 nm) | Thin | Thick | Thin | Thick |
| **107** | 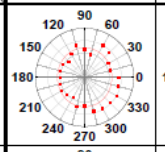 | 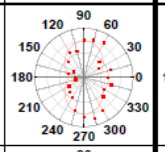 | 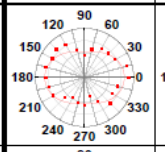 | 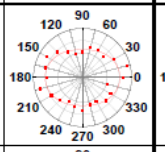 | 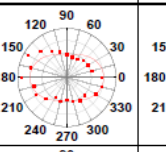 | 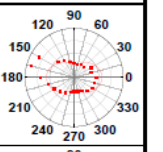 |
| **115** | 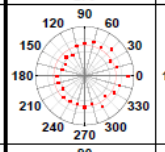 | 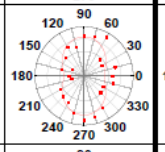 | 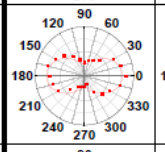 | 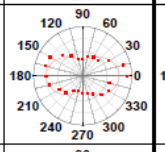 | 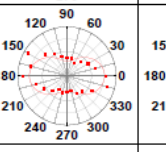 | 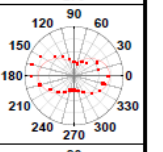 |
| **161** | 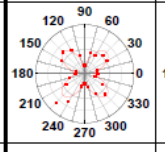 | 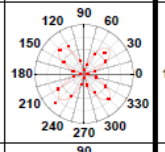 | 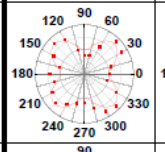 | 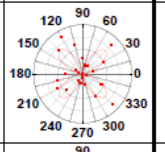 | weak | 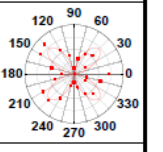 |
| **208** | weak | 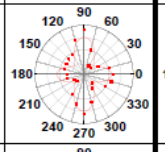 | 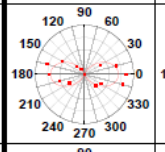 | 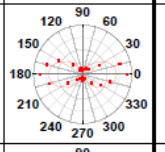 | weak | weak |
| **268** | 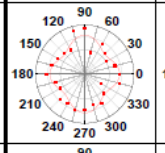 | 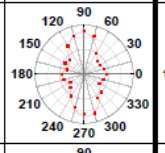 | 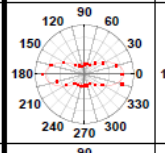 | 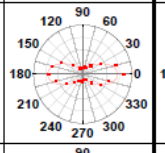 | 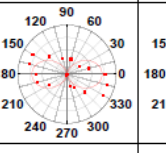 | 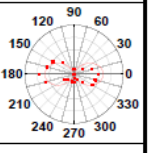 |
| **280** | 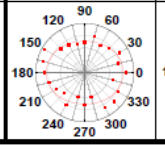 | 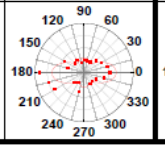 | 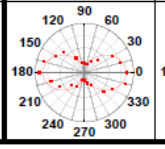 | 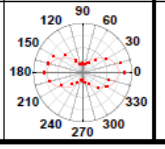 | weak | weak |

Figure 2.26. The anisotropy dependence of Raman intensity on flake thickness, laser wavelength and phonon frequency. Two flakes with typical thickness of 58 nm and 136 nm

and with the same crystal orientation were investigated. The Raman intensity polar plots with respect to different laser excitation wavelengths and the Raman mode frequencies were also labelled. $0^o$ ($90^o$) corresponds to armchair (zigzag) orientation of the GaTe crystal. (Adapted from Huang *et al.* [137])

### 2.3.3 Mechanical properties of layered materials

Among the many attractive and unusual properties of 2D layered materials, mechanical properties play an important role in performance, fabrication and integration of their potential applications, therefore the investigation of mechanical properties of 2D materials have been kept pushing forward both experimentally and theoretically. This section introduction is mainly based on a recent review by Deji *et al.*,[213] Since the exceptional high in-plane elastic properties of graphene with an intrinsic strength of 130 GPa and in-plane Young's modulus of 1 TPa being experimentally measured using AFM based nanoindentation,[214] more interest has been attracted onto the nanoscale mechanical properties and this method combined with DFT and MD simulations has been extended to measure the mechanical properties of other 2D materials such as $MoS_2$ and h-BN.[215-217] It was found that except elasticity, the mechanical properties of 2D materials seems very sensitive to the existence of vacancies and dislocations defects etc., resulting in surprisingly different strength, toughness and failure mechanism. For example, a nearly 2× higher Young's modulus was obtained by introducing a controlled defect density through irradiation,[218] while the strength of graphene can be significantly changed by the out-of-plane wrinkles-like deformation when under external shear loading[219] or by the intrinsic topological defects,[220] leading to a lower failure strength of only about 60 GPa in comparison to their ideal shear strength of about 97 GPa. However, the influence of defects on mechanical properties are expected to vary across different 2D materials due to their substantial difference in the stiffness and modulus, which deserves further study.

The coupling between the mechanical property and other properties (such as optical, electronic and thermal, etc.,) of 2D materials has also raised increasing interests in exploring novel applications. For example, although having many outstanding physical properties, graphene suffers a detrimental drawback of gaplessness in the band structure for potential application in electronics, but its large elastic deformability (~20%) implies potential changes can be induced in the lattice structure to have a bandgap opened in graphene, making the electrons flowing through the all-graphene electronic circuit controllable by strain engineering.[221] Alternatively, phase transitions can be induced under mechanical constraints as many 2D materials have several distinct crystal structures with different electrical properties shown for each phase, e.g., H (semiconducting) and T' (semi-metallic) phases in the Mo- and W-dichalcogenides (TMDCs).[222] Phase switching in TMDCs from a semiconducting to a semi-metallic phase, which is technologically important in applications

of PCM etc., electronic devices, was reported to can be driven by mechanical deformation[222] and electrostatic gating.[223] These new multi-physical coupling phenomenon make the establishment of a scalable theoretical framework in combination with condensed material physics for nanoscale mechanics of 2D materials urgently needed.

Moreover, the interactions of mechanical properties between 2D layered materials and different substrate materials cannot be ignored when integrating 2D materials into device applications, especially when they must be transferred from one to another substrate through selective wet etching or dry transfer utilizing a polymer stamp. Interfacial properties including adhesion and friction of 2D materials with substrates need to be measured and understood. In early stage, the measurements of adhesion between 2D materials were mainly performed through blister and laminated beam fracture experiments.[213] Via both classical and island blister tests, the adhesion energies of graphene membranes (1-5 layers) to silicon dioxide were measured to be vary from 0.1 to 0.45 $J/m^2$.[224-226] Recently, AFM-based nanoindentation experiments have been successfully developed for adhesion measurements,[227-229] ascribing to its high resolution in imaging surface morphology and accuracy in measuring displacements and interaction forces between 2D materials and substrates. A number of contact mechanics models which typically work by considering the interactions between an atomically flat surface and an ideal sphere tip,[230-232] as well as finite element modelling based numerical simulations, have been developed to convert the AFM measured adhesion force to adhesion energy, although the AFM tip shape is not spherical and is challenging for measurements. The atomic-scale friction and wear between the tip and surface atoms presently are mainly measured by AFM and MD simulations to provide insights into the evolution of the interaction forces both temporally and spatially.[233] The vdW interaction between 2D materials and the substrates are very challenging to measure and are mostly predicted by atomic-scale DFT[234,235] and MD[236] calculations, despite this, a strain-dependent sliding friction between graphene and the silicon dioxide substrate was recently observed with their vdW interactions extracted.[237] Meanwhile, the dry transfer pick-up technique that can be used to mechanically construct various layered materials into a heterostructure also needs to understand the relative strength of vdW interactions between various 2D materials and their possible effects,[238] which still needs lots of further study. Therefore, the mechanics of interfaces (especially adhesion and friction, vdW interaction) is essentially needed to be developed for the layered materials.

## 2.4 Theoretical background

### 2.4.1 Raman scattering theory

Light (electromagnetic radiation) incident on any media can be scattered elastically accompanied with inelastic scattering in the form of frequency shift with respect to the incident light. Raman scattering is light scattering on optical phonons (lattice vibration) and

plasmons (free carrier excitations), while Brillouin scattering can be used for describing the behaviors of acoustic phonons. In contrast to elastic (or Rayleigh) scattering, where the incident and scattered light have an equivalent frequency, Raman/Brillouin scattering detects the inelastic process where the frequency of scattered light is larger (or smaller) than that of the incident light. In this subsection, Raman scattering theory will be described and discussed, from a macroscopic and quantum mechanics viewpoint, including a description of optical selection rules.

#### 2.4.1.1 Macroscopic electromagnetic scattering theory

From a macroscopic interpretation of the classical electromagnetic theory, Raman scattering can be described on the basis of dipole radiation (polarizability). When excited by a laser light, the charge of ions at the lattice nuclei host as well as the surrounding electron clouds are distorted, which in turn can deviate the ions from their original equlibrillium positions. Therefore the induced electric dipole $\boldsymbol{P}$ (polarization) by the electromagnetic field ($\boldsymbol{E}$) can be expressed as:

$$\boldsymbol{P}(t) = \epsilon_0 \boldsymbol{\chi} \boldsymbol{E}(t) = \sum_j \chi_{ij} E_j(t), \tag{2.19}$$

where $\boldsymbol{\chi}$ is the second rank tensor used to describe volumetric susceptibility of the material and $\chi_{ij}$ is its normal anisotropic description. As the sinusoidal variation of the electromagnetic field $\boldsymbol{E(t)}$ with time and frequency can be described as:

$$\boldsymbol{E}(t) = \boldsymbol{E_0} \cos(\omega_{\mathrm{I}} t), \tag{2.20}$$

where $\boldsymbol{E_0}$ is the amplitude of the electromagnetic field and $\omega_{\mathrm{I}}$ is the incident laser frequency. By combining Equations 2.19 and 2.20, $\boldsymbol{P}$(t) can be re-written as:

$$\boldsymbol{P}(t) = \boldsymbol{\epsilon_0 \chi E_0} \cos(\omega_{\mathrm{I}} t). \tag{2.21}$$

Due to the lattice vibrations, for different normal modes *k, l…* nuclei will vibrate around their equilibrium positions with frequencies $\omega_k$, $\omega_l$, … and $\boldsymbol{P}$(t) will also vary with the atomic displacement. When the lattice vibrational and incident light frequencies are assumed to be small relative to the electromagnetic frequencies which determines $\boldsymbol{\chi}$, i.e. far from resonance conditions (termed as quasi-static or adiabatic approximation), the phonon can be treated as a static deformation of the medium and then $\boldsymbol{\chi}$ at each time depends on the normal mode coordinate and varies with the lattice vibration. Therefore, the tensor components can be expanded as a Taylor series with respect to the normal coordinates $Q_k$, $Q_l$, … of these nuclei vibrations with frequencies $\omega_k$, $\omega_l$, …:

$$\chi_{ij} = (\chi_{ij})_0 + \sum_k \left(\frac{\partial \chi_{ij}}{\partial Q_k}\right)_0 Q_k + \frac{1}{2} \sum_k \left(\frac{\partial^2 \chi_{ij}}{\partial Q_k \partial Q_l}\right)_0 Q_k Q_l + \cdots, \tag{2.22}$$

where $(\chi_{ij})_0$ is the electronic susceptibility of the medium under no fluctuations, and the summations are over all normal coordinates. By assuming the electrical harmonic approximation, those higher order terms beyond the first power of $Q$ in Equation 2.22 which are related to vibrations of two atoms or more, can be neglected. Therefore, only considering the first-order deviation, i.e. the $k_{\text{th}}$ normal mode of vibration, the susceptibility $\boldsymbol{\chi}$ can be given as:

$$\boldsymbol{\chi} = \boldsymbol{\chi_0} + \frac{\boldsymbol{\partial \chi}}{\boldsymbol{\partial Q_k}} \boldsymbol{Q_k}. \tag{2.23}$$

If the lattice vibration is approximated as a simple harmonic oscillator, the related atomic displacement $Q_k$ can be expressed as:

$$Q_k = Q_{k0} \cos(\omega_k t), \tag{2.24}$$

where $Q_{k0}$ is the atomic displacement amplitude, then the time dependence of $\boldsymbol{\chi}$ can be obtained:

$$\boldsymbol{\chi} = \boldsymbol{\chi_0} + \left(\frac{\boldsymbol{\partial \chi}}{\boldsymbol{\partial Q_k}}\right) Q_{k0} \cos(\omega_k t). \tag{2.25}$$

Combing the equations (2.21) and (2.25), the time dependent polarization is given as:

$$\boldsymbol{P}(t) = \boldsymbol{\epsilon_0 \chi_0 E_0} \cos(\omega_{\text{I}} t) + \left(\frac{\boldsymbol{\partial \chi}}{\boldsymbol{\partial Q_k}}\right) Q_{k0} \boldsymbol{\epsilon_0 E_0} \cos(\omega_{\text{I}} t) \cos(\omega_k t). \tag{2.26}$$

The second term in Equation 2.26 can be reformulated by using the following standard trigonometric identity:

$$\cos(\omega_{\text{I}} t) \cos(\omega_k t) = \frac{1}{2}[\cos(\omega_{\text{I}} t + \omega_k t) + \cos(\omega_{\text{I}} t - \omega_k t)]. \tag{2.27}$$

Then the induced electric dipole can be re-written as:

$$\boldsymbol{P}(t) = \boldsymbol{\epsilon_0 \chi_0 E_0} \cos(\omega_{\text{I}} t) + \boldsymbol{A}[\cos((\omega_{\text{I}} + \omega_k) t) + \cos((\omega_{\text{I}} - \omega_k) t)], \tag{2.28}$$

where

$$\boldsymbol{A} = \frac{1}{2}\left(\frac{\boldsymbol{\partial \chi}}{\boldsymbol{\partial Q_k}}\right) Q_{k0} \boldsymbol{\epsilon_0 E_0}. \tag{2.29}$$

The three components in Equation (2.28) reveal that the incident light can induce dipoles with three distinct vibration frequencies: $\omega_{\text{I}},\ \omega_{\text{I}} + \omega_k,\ \omega_{\text{I}} - \omega_k$, respectively. Therefore, the light induced polarization can result in the dipole radiation with three characteristic frequencies, corresponding to elastically scattered light at frequency $\omega_{\text{I}}$ (Rayleigh scattering), and inelastically scattered light with a Stokes ( $\omega_{\text{I}} - \omega_k$) and anti-Stokes ( $\omega_{\text{I}} + \omega_k$) frequency shift, respectively. The Stokes/anti-Stokes frequency shift relative to the incident light

frequency is equivalent to the phonon frequency and is termed as Raman shift. As a convention, the positive Raman shift is for Stokes scattering and the negative is for anti-Stokes scattering. The Raman shift is normally quantified in wavenumbers (1/λ), using the inverse centimeter $cm^{-1}$ unit (1 $cm^{-1}$ = 0.124 meV). If higher order susceptibility terms of the expansion given in Equation (2.22) are included, additional higher order scattering terms in Equation (2.28) will result, representing interacting scattering from multiple lattice vibrations with the same or different frequencies. Equation (2.28) also indicates that only when the associated derivative term $\frac{\partial \chi}{\partial Q_k}$ is non-zero, will the lattice vibration be Raman-active. This classical electromagnetic theory about Raman scattering has given a useful qualitative description of $\frac{\partial \chi}{\partial Q_k}$, illustrated through electric susceptibility (amplitude) modulation by normal mode lattice vibrations. However, in reality the light and lattice vibration are more elementally quantized as photons and phonons, respectively, which requires a more profound explanation from quantum mechanical theory to understand the Raman scattering process.

#### 2.4.1.2 Quantum mechanical theory for Raman scattering

In the quantum mechanical interpretation of Raman scattering, each elementary process of Raman scattering involves the annihilation of a photon with frequency $\omega_I$ from an incident light source, the generation of a scattered photon with frequency $\omega_S$ and the generation or annihilation of a phonon with frequency $\omega_{phon}$. This scattering is a complicated process, and cannot be simply described by an interaction Hamiltonian comprising only photons and phonons due their very weak interaction strength unless they have comparable energy. In general, the (anti-) Stokes Raman scattering has the following three processes, as the schematic in Figure 2.27:

(1) The semiconductor material is excited by an incident photon with frequency $\omega_I$ from an initial state $|i\rangle$ into an intermediate virtual state $|n\rangle$ accompanied by the generation of an electron-hole pair (or exciton). The photon energy $\omega_I$ is absorbed by an electron within the material via the electron-radiation Hamiltonian, $H_{eR}$.

(2) The electron-hole pair is excited and relaxed to another intermediate virtual state $|n'\rangle$, by absorbing or emitting, respectively, a phonon with frequency $\omega_{phon}$, via the electron-phonon interaction Hamiltonian, $H_{e\text{-}phon}$. In all materials this electron-phonon interaction can take place via a direct modulation of the periodic crystal potential, i.e. a deformation-potential interaction where the exciton is scattered by the atomic displacement associated phonon. In the case of crystals with ionic bonding, the associated LO polar phonons can interact with electrons via the Fröhlich interaction in which the exciton is scattered by their macroscopic electric field.

(3) The exciton recombines radiatively to the initial state by emitting a scattered photon with frequency( $\omega_{\mathrm{I}} - \omega_{\mathrm{phon}}$) or ( $\omega_{\mathrm{I}} + \omega_{\mathrm{phon}}$), representing Stokes and anti-Stokes Raman scattering, respectively.

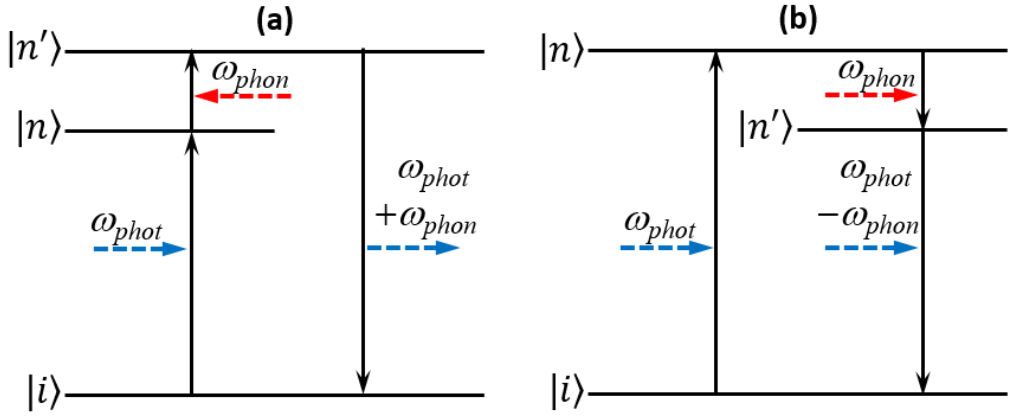


Figure 2.27. Schematic of the energy level diagram representing quantum mechanical (a) anti-Stokes and (b) Stokes Raman scattering processes.

### 2.4.1.3 Raman scattering cross section

For a Raman mode to be Raman-active, its Raman scattering cross-section ($\frac{d\sigma}{d\Omega}$) must be non-zero. This parameter can be derived from the energy of radiation ($W$) emitted per unit time with respect to the element solid angle ($d\Omega$) by the oscillating induced dipoles:

$$\frac{dW}{d\Omega} = \frac{\omega^4}{(4\pi)^2\epsilon_0 c^3}|\hat{e}_{\mathrm{S}} \cdot p|^2, \tag{2.30}$$

where $p$ is the total electric dipole moment, $\omega$ is the frequency of oscillation, $\epsilon_0$ is the permittivity of the vacuum medium, $c$ is the speed of light in vacuum, $\hat{e}_{\mathrm{S}}$ is an unit vector representing the polarization direction of the scattered light. Considering that the electromagnetic field of the incident light on the material ($E_{\mathrm{I}}$) is expressed as $\hat{e}_{\mathrm{I}}E_{\mathrm{I}}$ and the total dipole moment of the scattering volume of the material ($V$) is denoted as $p=PV$, Equation 2.30 can be combined with Equation 2.19 to give:

$$\frac{dW}{d\Omega} = \frac{\omega^4 V^2 \epsilon_0}{(4\pi)^2 c^3}|\hat{e}_{\mathrm{S}} \cdot \chi \cdot \hat{e}_{\mathrm{I}}|^2 E_{\mathrm{I}}^2. \tag{2.31}$$

The differential scattering cross section ($\frac{d\sigma}{d\Omega}$) is then obtained from $\frac{dW}{d\Omega}$ divided by the total energy of incident light per unit time ($W_{\mathrm{I}} = \epsilon_0 c E_{\mathrm{I}}^2$), and can be written as:

$$\frac{d\sigma}{d\Omega} = \frac{\omega^4 V^2}{(4\pi)^2 c^4} |\hat{e}_S \cdot \chi \cdot \hat{e}_I|^2. \quad (2.32)$$

Substituting $\chi$ with the second term in the Taylor series expansion of Equation 2.22 gives:

$$\frac{d\sigma}{d\Omega} = \frac{\omega^4 V^2}{(4\pi)^2 c^4} \left|\hat{e}_S \cdot \frac{\partial \chi}{\partial Q} Q \cdot \hat{e}_I\right|^2. \quad (2.33)$$

For Stokes and anti-Stokes scattering, the $\frac{\partial \chi}{\partial Q}$ term can be described as:

$$\frac{\partial \chi}{\partial Q} \propto \sum_i^{\text{unit-cell}} N^{-\frac{1}{2}} = \sum_i^{\text{unit-cell}} \left(\frac{V_c}{V}\right)^{\frac{1}{2}}, \quad (2.34)$$

where $V=NV_c$ is the volume, and $N$ is the number of atoms, $V_c$ is the unit cell volume of the material and therefore has the following relationship:

$$\frac{\partial \chi}{\partial Q} V^{\frac{1}{2}} \propto V_c^{\frac{1}{2}}. \quad (2.35)$$

Renormalizing the susceptibility to make it independent of volume, which is defined as:

$$\frac{\partial \chi}{\partial Q} V^{\frac{1}{2}} \propto \frac{\partial \chi'}{\partial Q}. \quad (2.36)$$

Therefore, the volume normalized phonon scattering cross section can be expressed as:

$$\frac{d\sigma}{d\Omega} = \frac{\omega^4 V^2}{(4\pi)^2 c^4} \left|\hat{e}_S \cdot \frac{\partial \chi'}{\partial Q} Q \cdot \hat{e}_I\right|^2. \quad (2.37)$$

#### 2.4.1.4 Raman scattering selection rules

The intensity of the scattered light ($I_S$) is proportional to $\frac{d\sigma}{d\Omega}$ and can be expressed as:

$$I_S \propto |\hat{e}_S \cdot \mathbb{R} \cdot \hat{e}_I|^2, \quad (2.38)$$

where $\mathbb{R}$ is defined as a second-rank tensor called the Raman tensor for convenience which is equivalent to $\frac{\partial \chi'}{\partial Q} Q$. The Raman tensor symmetry can be derived using the standard group theory method. For a phonon mode to be Raman-active, it indicated that the Raman tensor $\mathbb{R}$ must be non-zero. Taking the wurtzite GaN as an example, 8 normal phonon modes at the Brillouin zone center are predicted by the group theory (see explanation in Section 2.1.3). According to the further Raman tensor symmetry analysis, the $A_1$, $E_1$, and two $E_2$ optical phonon modes are Raman-active, while the $B_1$ optical phonon modes are Raman-inactive (and also infrared-inactive) and termed as a silent mode. The label of phonon modes are denoted according to irreducible representations of the corresponded crystallographic point group. The $\mathbb{R}$ for allowed scattering phonon modes (Raman-active) in the wurtzite GaN are:

$$\mathbb{R}_{A_1(z)} = \begin{pmatrix} a & 0 & 0 \\ 0 & a & 0 \\ 0 & 0 & b \end{pmatrix},$$

$$\mathbb{R}_{E_1(x)} = \begin{pmatrix} 0 & 0 & c \\ 0 & 0 & 0 \\ c & 0 & 0 \end{pmatrix}, \mathbb{R}_{E_1(y)} = \begin{pmatrix} 0 & 0 & 0 \\ 0 & 0 & c \\ 0 & c & 0 \end{pmatrix}, \tag{2.39}$$

$$\mathbb{R}_{E_2(z)} = \begin{pmatrix} 0 & d & 0 \\ d & 0 & 0 \\ 0 & 0 & 0 \end{pmatrix}, \mathbb{R}_{E_2(z)} = \begin{pmatrix} d & 0 & 0 \\ 0 & -d & 0 \\ 0 & 0 & 0 \end{pmatrix},$$

where *a*, *b*, *c*, *d* indicate the non-zero Raman tensor components, their concrete values are not normally given as absolute Raman efficiencies are usually not calculated; while *x*, *y* and *z* in parenthesis represent the electric dipole direction which is associated with the lattice vibration mode. As mentioned in Section 2.1.3, the $A_1$ and $E_1$ modes are polar and the $E_2$ mode is non-polar, which means that the polarization direction of an electric dipole is only associated with the $A_1$ and $E_1$ modes. Furthermore, the $A_1$ mode is along the direction parallel to the *c*-axis, and the $E_1$ and $E_2$ modes are within a plane that is perpendicular to the *c*-axis, which is apparent from their associated atomic displacements as shown in Figure 2.4. As the *z*-axis of the tensor is aligned with the *c*-axis of the crystal, the Raman tensors of $A_1$ and $E_1$ modes are described with polarization in the *z*, *x*, *y* directions, respectively. The *x* and *y* directions are not given in the Raman tensor of the $E_2$ modes as they are non-polar as indicated in Equation 2.39.

Besides the Raman tensor, the scattering geometry also affects the observation of Raman-active modes. In this scattering geometry, the direction and wavevector of the incident and scattered light can be expressed using the succinct Porto notation:

$$k_{\mathrm{I}}(\hat{e}_{\mathrm{I}}, \hat{e}_{\mathrm{S}})k_{\mathrm{S}} \tag{2.40}$$

where $k_{\mathrm{I}}, k_{\mathrm{S}}$ are the wavevectors, and $\hat{e}_{\mathrm{I}}, \hat{e}_{\mathrm{S}}$ are the polarization of the incident and scattered light, respectively. To simplify the Porto notation, typically, wavevectors and polarization are aligned with the principle crystallographic axis. For example, in wurtzite GaN crystals, the *z*-axis in Porto notation is conventionally equivalent to the *c*-axis, then $z(xy)\bar{z}$ denotes that the incident light onto the wurtzite crystal is along the *z* (*c*-axis) direction and is polarized in the *x* direction, while the scattered light is along the opposite of *z* direction (indicating back-scattering) and is polarized in the *y* direction. The configuration of the scattering geometry used in all the Raman characterization within this work is $z(x\ -)\bar{z}$, known as backscattering geometry. In this case, the dash indicates that the polarization of the scattered light is not analyzed. If $I_{\mathrm{S}}$ from a phonon mode is non-zero under a particular scattering geometry, this phonon mode will be observed in the Raman spectrum. Considering scattering in the $z(xx)\bar{z}$ configuration, the incident and scattered light are both described by $(\cos\theta, \sin\theta, 0)$,

then substituting the $E_2$ modes Raman tensors into Equation 2.38, the associated scattering intensity ($I_{E_2}$) can be written as:

$$I_{E_2} \propto \left|\hat{e}_{\mathrm{I}} \cdot \mathbb{R}_{E_2} \cdot \hat{e}_{\mathrm{S}}\right|^2 + \left|\hat{e}_{\mathrm{I}} \cdot \mathbb{R}_{E_2} \cdot \hat{e}_{\mathrm{S}}\right|^2;$$

$$I_{E_2} \propto \left|\begin{pmatrix}\cos\theta \\ \sin\theta \\ 0\end{pmatrix} \cdot \begin{pmatrix}0 & d & 0 \\ d & 0 & 0 \\ 0 & 0 & 0\end{pmatrix} \cdot \begin{pmatrix}\cos\theta \\ \sin\theta \\ 0\end{pmatrix}\right|^2 + \left|\begin{pmatrix}\cos\theta \\ \sin\theta \\ 0\end{pmatrix} \cdot \begin{pmatrix}d & 0 & 0 \\ 0 & -d & 0 \\ 0 & 0 & 0\end{pmatrix} \cdot \begin{pmatrix}\cos\theta \\ \sin\theta \\ 0\end{pmatrix}\right|^2;$$

$$I_{E_2} \propto |d(2\sin\theta\cos\theta)|^2 + |d(\cos^2\theta - \sin^2\theta)|^2;$$

$$I_{E_2} \propto |d(\sin^2 2\theta + \cos^2 2\theta)|^2;$$

$$I_{E_2} \propto d^2. \tag{2.41}$$

For the $A_1$ (LO) mode associated scattering intensity, $I_{A_1(\mathrm{LO})}$, can be expressed as:

$$I_{A_1(\mathrm{LO})} \propto \left|\hat{e}_{\mathrm{I}} \cdot \mathbb{R}_{A_1(\mathrm{LO})} \cdot \hat{e}_{\mathrm{S}}\right|^2;$$

$$I_{A_1(\mathrm{LO})} \propto \left|\begin{pmatrix}\cos\theta \\ \sin\theta \\ 0\end{pmatrix} \cdot \begin{pmatrix}a & 0 & 0 \\ 0 & a & 0 \\ 0 & 0 & b\end{pmatrix} \cdot \begin{pmatrix}\cos\theta \\ \sin\theta \\ 0\end{pmatrix}\right|^2;$$

$$I_{A_1(\mathrm{LO})} \propto |a(\sin^2\theta + \cos^2\theta)|^2;$$

$$I_{A_1(\mathrm{LO})} \propto a^2. \tag{2.42}$$

Therefore Raman scattering of the $E_2$ and $A_1$ (LO) modes is allowed and can be observed in the utilized backscattering geometry, and is invariant to the choice of the angle $\theta$ (represents rotation about the *c*-axis). Notably, the diagonal and off-diagonal components within the Raman tensor will determine whether the phonon mode can be observed in the parallel (*xx*, *yy*, *zz*) or crossed (*xy*, *xz*, *yz*) polarization configuration. For example, the $E_2$ modes have both diagonal and off-diagonal components in its Raman tensor, therefore can be observed in both parallel and crossed polarizations. While the $A_1$ (LO) mode has only diagonal components, therefore, can only be observed in the parallel polarizations for incident and scattered light. Based on the $I_S$, scattering geometry and the Raman tensor components of the phonon modes, analysis of all phonon modes gives the Raman selection rule. For wurtzite GaN under different scattering geometries, the corresponded observable Raman-active phonon modes at the Brillouin zone center are shown in Table 2.4.

Table 2.4. Selection rules for observable Raman-active phonon modes of wurtzite GaN under different scattering geometries, the *z*-direction means parallel to the *c*-axis of wurtzite crystal.[51]

| Scattering geometry | Allowed phonon modes |
|---|---|
| $z(xx)\bar{z}$ | $A_1$ (LO), $E_2$ |
| $z(xy)\bar{z}$ | $E_2$ |
| $x(yy)\bar{x}$ | $A_1$ (TO), $E_2$ |
| $x(zz)\bar{x}$ | $A_1$ (TO) |
| $x(yz)\bar{x}$ | $E_1$ (TO) |
| $x(yz)y$ | $E_1$ (TO), $E_1$ (LO) |
| $x(yy)z$ | $E_2$ |

For the silicon and diamond films investigated in this work, as these materials have a diamond-cubic crystal structure, there is only one optical phonon mode of $F_{2g}$ symmetry at the center of the first Brillouin zone predicted by group theory observable, which can be observed under the exploited backscattering geometry. "F" in the symmetry nomenclature indicates that the phonon mode can be along three axes in the *x*-, *y*-, and *z*-direction. The corresponding non-zero Raman tensors in these three directions therefore can be written as[239]:

$$\mathbb{R}_{(x)} = \begin{pmatrix} 0 & 0 & 0 \\ 0 & 0 & d \\ 0 & d & 0 \end{pmatrix}, \mathbb{R}_{(y)} = \begin{pmatrix} 0 & 0 & d \\ 0 & 0 & 0 \\ d & 0 & 0 \end{pmatrix}, \mathbb{R}_{(z)} = \begin{pmatrix} 0 & d & 0 \\ d & 0 & 0 \\ 0 & 0 & 0 \end{pmatrix}. \quad (2.43)$$

#### 2.4.1.5 Stress dependence of phonons

Stress applied on semiconductor materials can induce significant atomic displacement, this changes the interatomic spacing and alters the frequency of phonon modes. Stresses can be growth-induced, or caused by piezoelectric, external pressure, thermal or others. It is very important to quantify this stress as it can alter a material's electrical and optical properties. Raman spectroscopy is a very sensitive tool for measuring the stress. Strain ($\varepsilon_{ij}$) is related to stress ($\sigma_{kl}$) by a fourth rank compliance tensor ($S_{ijkl}$) through the following relationship:

$$\varepsilon_{ij} = \sum S_{ijkl}\sigma_{kl}. \quad (2.44)$$

The non-zero and independent components of the compliance tensor can be determined through symmetry analysis. In wurtzite GaN, the compliance tensor can be written in a compact 6 matrix form as:

$$\begin{pmatrix} \varepsilon_{xx} \\ \varepsilon_{yy} \\ \varepsilon_{zz} \\ 2\varepsilon_{zy} \\ 2\varepsilon_{zx} \\ 2\varepsilon_{xy} \end{pmatrix} = \begin{pmatrix} S_{11} & S_{12} & S_{13} & 0 & 0 & 0 \\ S_{12} & S_{11} & S_{13} & 0 & 0 & 0 \\ S_{13} & S_{13} & S_{33} & 0 & 0 & 0 \\ 0 & 0 & 0 & S_{44} & 0 & 0 \\ 0 & 0 & 0 & 0 & S_{44} & 0 \\ 0 & 0 & 0 & 0 & 0 & (S_{11} - S_{12})/2 \end{pmatrix} \begin{pmatrix} \sigma_{xx} \\ \sigma_{yy} \\ \sigma_{zz} \\ \sigma_{zy} \\ \sigma_{zx} \\ \sigma_{xy} \end{pmatrix}. \tag{2.45}$$

For bulk semiconductors and epitaxial layers, the biaxial and hydrostatic stresses are usually the only relevant stresses. These will be discussed in the following. For the wurtzite structure of GaN grown as an epilayer on a substrate, shear stress may only be induced in the GaN layer near the corners of the device contacts,[240] hence shear stress is normally neglected as it is approximately equal to zero in the non-corner area. The in-plane ($\varepsilon_{xx} = \varepsilon_{yy}$) and normal ($\varepsilon_{zz}$) components of the strain tensor are described as:

$$\varepsilon_{xx} = \varepsilon_{yy} = (a - a_0)/a_0, \tag{2.46}$$

$$\varepsilon_{zz} = (c - c_0)/c_0, \tag{2.47}$$

where $a$ and $c$ are the lattice parameters of wurtzites; $a_0$ and $c_0$ represents the relaxed state lattice parameters. Using Equation 2.45, strain can be correlated to the stress for the in-plane component,

$$\varepsilon_{xx} = \varepsilon_{yy} = (S_{11} + S_{12})\sigma_{xx} + S_{13}\sigma_{zz}, \tag{2.48}$$

and the normal component

$$\varepsilon_{zz} = 2S_{13}\sigma_{xx} + S_{33}\sigma_{zz}, \tag{2.49}$$

where $\sigma_{xx} = \sigma_{yy}$. In common conditions, strain is only considered as a perturbation on the lattice which can be explained using the linear deformation potential theory, therefore, the generated strain can be simply correlated to the phonon frequency shift for mode $i$ through the following linear coefficients:

$$\Delta\omega_i = a_i(\varepsilon_{xx} + \varepsilon_{yy}) + b_i\varepsilon_{zz} = 2a_i\varepsilon_{xx} + b_i\varepsilon_{zz}, \tag{2.50}$$

where $a_i$ and $b_i$ represent the phonon deformation potentials. The phonon frequency shift under the biaxial and hydrostatic stress is:

$$\Delta\omega_i = 2\tilde{a}_i\sigma_{xx} + \tilde{b}_i\sigma_{zz}, \tag{2.51}$$

where the coefficients are correlated to the phonon deformation potentials:

$$\tilde{a}_i = (S_{11} + S_{12})a_i + S_{13}b_i, \tag{2.52}$$

$$\tilde{b}_i = 2S_{13}a_i + S_{33}b_i. \tag{2.53}$$

In the biaxial conditions, the GaN epilayer is assumed to be mechanically clamped to the thick substrate that it is grown on. Therefore, combining Equations (2.51, 2.52, 2.53) and using $\sigma_{xx} = \sigma_{yy}, \sigma_{zz} = 0$ and $\sigma_{xx} = \sigma_{yy} = \sigma_{zz}$ for the case of biaxial and hydrostatic stress, respectively, the corresponding stress coefficients ($K_i = d\omega_i/d\sigma$) can be determined for biaxial stress,

$$K_i^B = 2(S_{11} + S_{12})a_i + S_{13}b_i, \tag{2.54}$$

and hydrostatic stress,

$$K_i^H = 2(S_{11} + S_{12} + S_{13})a_i + (2S_{13} + S_{33})b_i, \tag{2.55}$$

This hydrostatic linear pressure coefficient in combined with the bulk modulus $\boldsymbol{B_0}$ are normally correlated to the mode Grüneisen parameter ($\gamma_i$), which is used to describe the effect of the volume change on the phonon frequency change of a crystal lattice:

$$\gamma_i = -\frac{\partial(\ln \omega_i)}{\partial(\ln V)} = \frac{B_0}{\omega_0} K_i^H, \tag{2.56}$$

where $\omega_0$ is the zero-pressure frequency of the phonon and $V$ is the volume of the material. By measuring phonon frequencies in a material under biaxial and hydrostatic stress and solving Equations (2.54) and (2.55) simultaneously, the phonon deformation potentials can be determined experimentally or by first-principles calculations.

#### 2.4.1.6 Temperature dependence of phonons

Phonon frequencies of semiconductors normally display a negative dependence with temperature due to anharmonic effects. Increasing temperature causes the lattice of a material to expand which decreases the frequency of the lattice vibrations (phonons), resulting in a temperature dependent phonon frequency shift $\Delta\omega_{\mathrm{E}}(T)$ that can be determined from the mode Grüneisen parameter (see Eq. 2.56). Phonon damping through the anharmonic phonon-phonon interaction also introduces a temperature dependent frequency shift $\Delta\omega_d(T)$. In addition, there can be a temperature dependent frequency shift $\Delta\omega_{\mathrm{S}}(T)$ induced by thermal strain generated between an epilayer and substrate ($\Delta\omega_{\mathrm{S}}(T)$=0 for bulk material). Therefore the total temperature dependent phonon frequency shift from all of these contributions can be expressed as:

$$\omega(T) = \omega_0 - \Delta\omega_{\mathrm{E}}(T) - \Delta\omega_d(T) - \Delta\omega_{\mathrm{S}}(T), \tag{2.57}$$

where $\omega_0$ is the harmonic phonon frequency. The contribution of lattice thermal expansion on the phonon frequency shift is given as:

$$\Delta\omega_E(T) = \omega_0\gamma \int_0^T [\alpha_c(T) + 2\alpha_a(T)]\, dT, \tag{2.58}$$

where $\alpha_c$ and $\alpha_a$ are the linear thermal expansion coefficients along the parallel and perpendicular directions to the hexagonal *c*-axis, respectively. $\gamma$ is the mode Gruneisen parameter defined in Eq. 2.56. According to the cubic and quartic anharmonic terms of the phonon vibrational Hamiltonian, contribution to the phonon frequency shift from the phonon damping term ($\Delta\omega_d(T)$) is determined. In the case of only cubic terms:

$$\Delta\omega_d(T) = [1 + 2n(T, \omega_0/2)], \tag{2.59}$$

where $n(T, \omega)$ is the Bose-Einstein statistical factor. In high temperature conditions, i.e. when $k_B T \gg \hbar\omega_0$, this equation can be reduced to a linear expression, while at low temperature conditions it is normally accurate enough to consider only cubic terms. The thermal strain-induced phonon frequency shift can be determined from:

$$\Delta\omega_s(T) = \left[2\left(a - b\frac{C_{13}}{C_{13}}\right)\right]\varepsilon(T), \tag{2.60}$$

$$\varepsilon(T) = \frac{l_{\mathrm{S}}(T) - l_{\mathrm{E}}(T)}{l_{\mathrm{E}}(T)} = \left(1 + \varepsilon_{\mathrm{g}}\right)\frac{1 + \int_{T_{\mathrm{g}}}^{T} \alpha_{a,\mathrm{S}}(T)\, dT}{1 + \int_{T_{\mathrm{g}}}^{T} \alpha_{a,\mathrm{E}}(T)\, dT} - 1, \tag{2.61}$$

where *a* and *b* are phonon deformation potentials; $C_{13}$ and $C_{33}$ are elastic constants; $\varepsilon(T)$ is the induced thermal strain in the epilayer; while $\alpha_{a,\mathrm{S}}$ and $\alpha_{a,\mathrm{E}}$ represent the in-plane linear thermal expansion coefficients of the substrate and epilayer, respectively; $T_{\mathrm{g}}$ is the growth temperature and $T$ is the measurement temperature; $l_{\mathrm{S}}$ and $l_{\mathrm{E}}$ are the temperature-dependent lengths of the substrate and epilayer without attachment to each other, and $\varepsilon_{\mathrm{g}}$ is the residual strain at the growth temperature $T_{\mathrm{g}}$.

Often an empirically derived expression is used to describe the temperature dependence. For example, the temperature dependence ($T$) of the frequencies ($\omega$) of phonon modes in semiconductors such as GaN, diamond, Si and SiC can be accurately described by the following empirical expression, derived by Cui *et al.*:[241]

$$\omega(T) = \omega_0 - \frac{\mathrm{A}}{\mathrm{e}^{\mathrm{B}hc\omega_0/k_{\mathrm{B}}T} - 1} \tag{2.62}$$

where $h$ and $c$ are Planck's constant and the speed of light in vacuum, separately. While $\omega_0$ (phonon frequency at 0 K), A and B are fitting parameters, which will be different for different materials. At high temperature, the following reduced linear expression can be used:

$$\Delta\omega = \frac{-\mathrm{A}k_\mathrm{B}\Delta T}{\mathrm{B}hc\omega_0}, \tag{2.63}$$

where $\Delta\omega$ and $\Delta T$ corresponds to the change in phonon frequency and the change in temperature, respectively.

### 2.4.2 Theoretical background of thermoreflectance

The reflectivity of a material surface is temperature dependent, this property has been previously used in techniques such as time-domain thermoreflectance (TDTR), developed by David Cahill,[242] for the investigation of thermophysical properties of thin films and interfaces. The surface reflectivity is given by:

$$R = \frac{(n_1-n_2)^2+(k_1-k_2)^2}{(n_1+n_2)^2+(k_1+k_2)^2}, \tag{2.64}$$

where $n_1$ and $k_1$ are the refractive index and extinction coefficient of the material, while $n_2$ and $k_2$ are the refractive index and extinction coefficient of the surrounding medium. The refractive index, $n_1$, changes with temperature, therefore, the reflectivity, $R$, of the material is also temperature-dependent. For the gold film, the change in its surface reflectivity with temperature is approximately linear to the variations in its surface temperature within the range of 300-800 K,[243] which is normally expressed as:

$$\frac{\Delta R}{R} = \left(\frac{1}{R}\frac{\partial R}{\partial T}\right)\Delta T = C_\mathrm{TR}\Delta T, \tag{2.65}$$

where $C_\mathrm{TR}$ is the thermoreflectance coefficient. Notably, the $C_\mathrm{TR}$ is dependent on the type of metal and the wavelength of the probed reflected light. The principle for TDTR is that when the thin metal transducer layer (normally <100 nm) is irradiated by the high power, short laser pulses, it would absorb some energy of the pulse and become heated. The temperature of the metal transducer layer rapidly rises due to the photoexcitation of electrons by pulses. These electrons thermalize quickly (at the picosecond or femtosecond scale). Then the generated heat diffuses into the underlying layers gradually at different time scales which is governed by the thermal conductivity, heat capacity and density of the materials and by the thermal boundary resistance at the interfaces. The process of heat diffusion in materials and layers corresponds to the decay of surface temperature, which results in the temperature-dependent change of surface reflectivity. Hence the surface reflectivity can be directly probed to monitor the change in surface temperature. Conventionally, laser beams that were used to heat the

metal transducer and to probe its surface reflectivity change can be from the same or different laser sources.

Using the metal transducer as the heating source can shield the reflections from the underlying layers, but require additional metal film fabrication on the samples which should be removed for further device processing. When a material has a bandgap lower than that of the pump laser, for example $Al_{0.3}Ga_{0.7}N$/GaN thin film versus 355 nm pump laser, we can use the surface reflectivity of $Al_{0.3}Ga_{0.7}N$/GaN without a transducer to act as thermometer. Nevertheless, there are challenges that the multilayer structure can introduce interference in the reflectance from the surface and the underlying interfaces thus affect the detected surface reflectivity, especially when the wavelength of probing laser locates near the reflectance extrema of the interference spectrum. When the temperature increases in the $Al_{0.3}Ga_{0.7}N$/GaN thin film, the refractive index ($n_{tr}$) and optical thickness ($d_{tr}n_{tr}$, where $d_{tr}$ is the transducer thickness) also changes. Consequently the phase of light reflected from the interfaces also changes, resulting in a shift of the interference spectrum, as illustrated in Figure 2.28. Hence, a temperature increase can be equivalent to a shift in wavelength for the total reflectance. The position of the reflectance extreme and the interference spectrum depends on the refractive index and thickness of the layers in the structure. If the wavelength of probe laser is located at or near a local extreme, the reflectance has a non-linear dependence of the temperature, the reflectance spectra can even cross an extreme making the transients anomalous. Only when the probe laser wavelength lies far from the interference extreme is a linear temperature dependence of reflectance obtained. To rule out the interference effect on the transients, the interference spectrum of the actual layer materials and thicknesses at room temperature and higher temperature should be calculated and checked before measuring. If the wavelength of the probe laser is close to a local extreme of the calculated interference spectrum, another reasonable wavelength should be considered. The interference phenomenon can be experimentally verified through varying the pump laser power (corresponding to change the temperature rise) to see whether there is a change induced in the normalized transient.

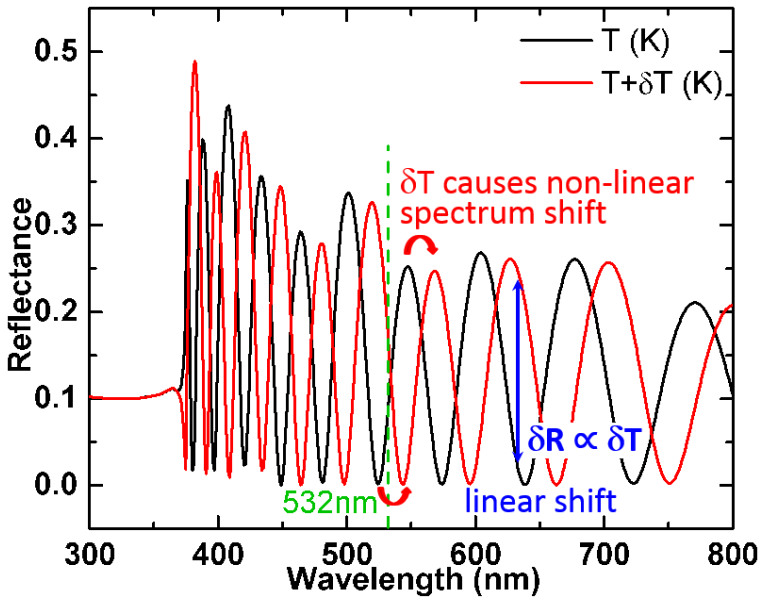


Figure 2.28. Calculated interference spectrum of reflectance based on Fresnel equations from the wavelength of 300 nm to 800 nm for a GaN (700 nm)-AlN (550 nm)-Si wafer investigated in this work and the reflectance spectrum shift induced by a temperature rise (δT~20 K). 532 nm is the wavelength of the probe laser commonly used in this work.

### 2.4.3 Synchrotron X-ray diffraction (XRD) scattering theory

X-ray crystallography technique is a typical method used to determine the atomic or molecular structure of a crystal. When a beam of X-rays that incidents onto the crystalline atoms is diffracted, the angles and intensities of diffracted beams can be elaborately measured to produce a 2-D picture of the diffracted pattern within the crystal, then the mean position of the atoms as well as their chemical bonds, disorder, and other information can be determined. Synchrotron XRD is a kind of XRD characterization but based on synchrotron radiation technique which nowadays can obtain highly coherent and less divergent X-ray beams with excellent brilliance, providing about 10 orders of magnitude brighter beams than the conventional laboratory sources as well as a wide range of photon energies. These brilliant X-ray light sources can enable X-ray diffraction measurements with monolayer sensitivity,[244] which is the most robust tool for investigating the structure, the change of lattice parameters and phase transitions of 2D materials with respect to pressure, as well as surfaces and heteroepitaxial interfaces.

A crystal is formed by repeatedly constructed periodic cell, or termed as unit cell, which is made from three unit vectors $a_1$, $a_2$, and $a_3$. Considering a unit cell that consists of $N$ atoms, the position of each unit cell ($r_{uc}$) and the $k^{th}$ atom ($r_k$) in the unit cell can be respectively written as:

$$r_{\mathrm{uc}} = k_1\mathrm{a}_1 + k_2\mathrm{a}_2 + k_3\mathrm{a}_3 \text{ } (k_1, k_2, k_3 \text{ are integers});\tag{2.66}$$

$$r_k = x_k\mathrm{a}_1 + y_k\mathrm{a}_2 + z_k\mathrm{a}_3 \text{ } (0 \le x_k, y_k, z_k \le 1).\tag{2.67}$$

Therefore the total scattering amplitude from a unit cell, $E_{\mathrm{uc}}$, can be expressed as a coherent sum of the scattering amplitudes from each in the unit cell:

$$E_{\mathrm{uc}} = E_0 \frac{r_e}{R} p\mathrm{e}^{iq\cdot(r+r_{\mathrm{uc}})}F(q),\tag{2.68}$$

$$F(q) = \sum_{k=1}^{N} f_k(q)\,\mathrm{e}^{iq\cdot r_k},\tag{2.69}$$

where $F(q)$ is defined as the structure factor of a unit cell for the momentum transfer vector $q$, while $f_k(q)$ is the atomic form factor, and $p$ is the polarization factor which varies between 0 and 1. In an actual 3D crystal, assuming there are $N_1$, $N_2$, $N_3$ unit cells stacked along the $\mathrm{a}_1$, $\mathrm{a}_2$, and $\mathrm{a}_3$ directions, respectively, then the scattering amplitude of this crystal can be expressed as:

$$E_{\mathrm{crystal}} = E_0 \frac{r_e}{R} p\mathrm{e}^{iq\cdot r}F(q)\sum_{k_1=1}^{N_1}\sum_{k_2=1}^{N_2}\sum_{k_3=1}^{N_3}\mathrm{e}^{iq\cdot(k_1\mathrm{a}_1+k_2\mathrm{a}_2+k_3\mathrm{a}_3)} \quad .\tag{2.70}$$

The term $\sum_{k_i=1}^{N_i} e^{iq\cdot(k_i\mathrm{a_i})}$ can be transformed in a geometric series as:

$$\sum_{k_i=1}^{N_i}\mathrm{e}^{iq\cdot(k_i\mathrm{a_i})} = \mathrm{e}^{iq\cdot\mathrm{a_i}(N_i+1)/2}\frac{\sin\left(N_i q\cdot(\mathrm{a_i}/2)\right)}{\sin\left(q\cdot(\mathrm{a_i}/2)\right)}.\tag{2.71}$$

Then the total scattering amplitude from the bulk crystal, $E_{\mathrm{crystal}}$, can be transformed as:

$$E_{\mathrm{crystal}} = E_0 \frac{r_e}{R} p\mathrm{e}^{iq\cdot r}F(q)\mathrm{e}^{i\varphi}\frac{\sin\left(N_1 q\cdot(\mathrm{a}_1/2)\right)}{\sin\left(q\cdot(\mathrm{a}_1/2)\right)}\frac{\sin\left(N_2 q\cdot(\mathrm{a}_2/2)\right)}{\sin\left(q\cdot(\mathrm{a}_2/2)\right)}\frac{\sin\left(N_3 q\cdot(\mathrm{a}_3/2)\right)}{\sin\left(q\cdot(\mathrm{a}_3/2)\right)},\tag{2.72}$$

$$\varphi = \frac{[(N_1+1)q\cdot\mathrm{a}_1+(N_2+1)q\cdot\mathrm{a}_2+(N_3+1)q\cdot\mathrm{a}_3]}{2},\tag{2.73}$$

where $\varphi$ is the phase factor, however, the scattering amplitude, E, cannot be directly measured. In experiments, what the photodetectors record are the scattering intensity, $I$, which equals to the squared magnitude of the scattering amplitude:

$$I = |E|^2 = EE^*.\tag{2.74}$$

The measurable scattering intensity from the crystal, $I_{\mathrm{crystal}}$, then can be expressed as:

$$I_{\mathrm{crystal}} = \left|E_{\mathrm{crystal}}\right|^2 = {E_0}^2\left(\frac{r_e}{R}\right)^2 p^2|F(q)|^2\frac{\sin^2\left(N_1 q\cdot(\mathrm{a}_1/2)\right)}{\sin^2\left(q\cdot(\mathrm{a}_1/2)\right)}\frac{\sin^2\left(N_2 q\cdot(\mathrm{a}_2/2)\right)}{\sin^2\left(q\cdot(\mathrm{a}_2/2)\right)}\frac{\sin^2\left(N_3 q\cdot(\mathrm{a}_3/2)\right)}{\sin^2\left(q\cdot(\mathrm{a}_3/2)\right)}.\tag{2.75}$$

For further simplification and easier understanding of the lattice scattering rules, Equation (2.75) can be transformed from the crystal lattice vectors $a_1$, $a_2$, and $a_3$ into the reciprocal lattice vectors $a_1^*$, $a_2^*$, and $a_3^*$, which are defined as the following:

$$\mathrm{a}_1^* = 2\pi\frac{\mathrm{a}_2\times\mathrm{a}_3}{\mathrm{a}_1\cdot(\mathrm{a}_2\times\mathrm{a}_3)},\ \mathrm{a}_2^* = 2\pi\frac{\mathrm{a}_3\times\mathrm{a}_1}{\mathrm{a}_1\cdot(\mathrm{a}_2\times\mathrm{a}_3)},\ \mathrm{a}_3^* = 2\pi\frac{\mathrm{a}_1\times\mathrm{a}_2}{\mathrm{a}_1\cdot(\mathrm{a}_2\times\mathrm{a}_3)}. \tag{2.76}$$

In which, the reciprocal lattice vectors have the following property of:

$$\mathrm{a}_i^*\cdot\mathrm{a}_\mathrm{j} = 2\pi l_{ij}\quad (\text{if } i=j, l_{ij}=1, \text{or } l_{ij}=0). \tag{2.77}$$

And the momentum transfer vector $q$ can be expressed using the reciprocal lattice vectors as the basis:

$$q = h\mathrm{a}_1^* + k\mathrm{a}_2^* + l\mathrm{a}_3^*. \tag{2.78}$$

Then combing Equation (2.77) and (2.78) with Equation (2.75), the scattering intensity from the crystal can be simplified as:

$$I_{\mathrm{crystal}} = {E_0}^2\left(\frac{r_e}{R}\right)^2 p^2|F(q)|^2\frac{\sin^2(N_1h\pi)}{\sin^2(h\pi)}\frac{\sin^2(N_2k\pi)}{\sin^2(k\pi)}\frac{\sin^2(N_3l\pi)}{\sin^2(l\pi)}. \tag{2.79}$$

When all the three squared sine functions in Equation (2.79) become zero simultaneously, the total product diverges and a very strong scattering intensity is expected to be observed. Conditions to meet these requirements are:

$$\sin(h\pi) = \sin(k\pi) = \sin(l\pi) = 0,\ (h, k, l \text{ are all integers}). \tag{2.80}$$

By combing Equation (2.78) and (2.80), strong diffraction intensities are expected when $q$ fulfills the following condition, which is known as *Laue Equation* for diffraction peaks:

$$q = H\mathrm{a}_1^* + K\mathrm{a}_2^* + L\mathrm{a}_3^*,\ (H, K, L \text{ are all integers}). \tag{2.81}$$

As seen from Equation (2.81), the diffraction conditions given in the *Laue Equation* is determined only by the lattice vectors, i.e. the shape of unit cell. Notably, as shown in Equation (2.79), another important factor, the structure factor $F(q)$, can also significantly affect the diffraction intensity. This structure factor comprises of information about the internal atomic structure of the unit cell. Therefore, different structure factor may result in those diffraction peaks satisfying the *Laue Equation* showing a significant different intensity from other peaks, and even displaying zero intensity (also termed as extinction) when the structure factor becomes zero at the corresponding momentum transfer vector $q$.

In typical X-ray diffraction experiments, *Fraunhofer approximation* is applied to obtain the diffraction pattern,[245] and the diffraction amplitude can be obtained by taking the Fourier transform[246] of the electron density function of the scattering crystal.

### 2.4.4 Density functional theory based first-principles calculations

Density functional theory (DFT) based first-principles calculation is employed to investigate the electronic, phonon, structure, etc., solid-state properties. The core physical theorem for DFT is the Schrödinger Equation, as presented in the following non-relativistic and time-independent form:

$$\widehat{H}\psi = E\psi, \tag{2.82}$$

where $\widehat{H}$ is the Hamiltonian operator, $\psi$ the wave function representing a stationary quantum state, $E$ the energy eigenvalue of the corresponded state. For a single atomic system consisting of electrons and nuclei, the Hamiltonian can be expressed as:

$$\widehat{H} = -\frac{\hbar^2}{2m_e}\sum_i \nabla_i^2 - \frac{\hbar^2}{2M_\alpha}\sum_\alpha \nabla_\alpha^2 + \sum_i\sum_\alpha \frac{Z_\alpha e^2}{|r_i - R_\alpha|} + \frac{1}{2}\sum_{i\neq j}\frac{e^2}{|r_i - r_j|} + \frac{1}{2}\sum_{\alpha\neq\beta}\frac{Z_\alpha Z_\beta e^2}{|R_\alpha - R_\beta|}, \tag{2.83}$$

where $\hbar$ is the reduced Planck's constant, $e$ is the charge of the electron, $Z_\alpha$ is the charges of the nuclei, while $r_i$ and $R_\alpha$ corresponds to the positions of the electrons and nuclei, $m_e$ and $M_\alpha$ represents the masses of the electrons and nuclei, respectively. The five terms in the Hamiltonian expression, from left to right, represent the kinetic energy of the electrons, the kinetic energy of the nuclei, the electron-nuclei interactions, the electron-electron interactions and the nuclei-nuclei interactions.

*Born-Oppenheimer approximation* can be applied to simplify the Hamiltonian for most condensed material calculations, on the premise that the motions of electrons and nuclei can be decoupled. As the nuclear mass is much larger than the electron mass, the electron velocities essentially can be assumed to be infinite in compare to that of much heavier nuclei, i.e., the position of nuclei can be regarded as fixed in comparison, and the electrons can be viewed as responding immediately to changes in the positions of the nuclei. Under this approximation, the nuclear kinetic energy term then can be eliminated from the Hamiltonian, and nuclei-nuclei interactions term also becomes a constant which can be subtracted. Hence, the simplified Hamiltonian is expressed as:

$$\widehat{H} = -\frac{\hbar^2}{2m_e}\sum_i \nabla_i^2 + \sum_i\sum_\alpha \frac{Z_\alpha e^2}{|r_i - R_\alpha|} + \frac{1}{2}\sum_{i\neq j}\frac{e^2}{|r_i - r_j|} = \hat{T} + \hat{V}_{\text{ion}} + \hat{V}_{\text{int}}, \tag{2.84}$$

where $\hat{T}$ represents the kinetic energy of electrons, and $\widehat{V}_{ion}$ represents the potential of the electrons imposed from the nuclei, while $\widehat{V}_{int}$ represents the electron-electron repulsions. This

Hamiltonian is the basis for the Hartree-Fock method, in which the electron exchange is taken into account. However, the Hartree-Fock is a "mean field" approximation through mapping the complex many-body interactions onto a simplified one-electron condition, which is treated by operating the wave function as orbitals to represent the discrete energy states of the system and defining the potential of the system as an average response for all electrons in the system. Therefore, it cannot resolve all of the electron correlation energies, resulting in the calculated energies always too high. Various methods have been developed to recover more of the existed correlation energy to achieve more accurate calculation.

The Hamiltonian for an electronic system, as stated in the Hohenberg-Kohn theorems,[247] can be determined exactly by a single function, i.e., the ground-state electron density. This ground-state density can be determined by minimizing the total energy of the associated density functional. These theorems have proved there is an exact solution to the many electron problem using a single function, however they do not provide an indication on how to construct the density functional and a means to find the ground-state density. Then a practical calculation method is developed in the form of Kohn-Sham equations in 1965,[247] and is written as:

$$\left(-\frac{\hbar^2}{2m_e}\nabla^2 + V_{\text{eff}}(\rho)\right)\Phi_i(\rho) = \epsilon_i\Phi_i(\rho), \tag{2.85}$$

where $V_{\text{eff}}(\rho)$ is the effective Kohn-Sham potential, while $\Phi_i(\rho)$ and $\epsilon_i$ are Kohn-Sham orbits and corresponding eigenvalue energies, respectively. The electron density, written in the form of Kohn-Sham orbitals, is then given by:

$$\rho(r) = \sum_{i=1}^{N}|\Phi_i(r)|^2, \tag{2.86}$$

where N is the number of occupied states. The effective Kohn-Sham potential is expressed in three terms as:

$$V_{\text{eff}}(\rho) = V_{\text{ion}}(\rho) + V_{\text{H}}(\rho) + V_{\text{ex}}(\rho), \tag{2.87}$$

where $V_{\text{ion}}(\rho)$ is the ionic potential representing electron-nuclei interactions, $V_{\text{H}}(\rho)$ is the Hartree potential accounting for electron-electron repulsions, and $V_{\text{ex}}(\rho)$ represents the exchange-correlation potential. The Hohenberg-Kohn theorems[247] and Kohn-Sham equations typically establishes the foundation for modern DFT theorems.

# Chapter 3.

## Experimental Methods and Characterization Techniques

In this chapter, the characterization techniques about micro-Raman spectroscopy, including the principles of its fundamental design and the spectrometer, as well as micro-Raman thermography and stress-metrology will be introduced. In addition, the principles for nanosecond time-domain thermoreflectance, another thermal characterization method used extensively in this work, will be discussed. Further, fundamental technical descriptions of high-pressure diamond anvil cells, Linkam temperature controlled stage, transfer methods of 2D flakes and the atomic force microscopy will also be given.

### 3.1 Micro-Raman spectroscopy

Micro-Raman spectroscopy is a very useful non-destructive experimental tool to measure material properties such as structure, stress, thermal and phonon properties. In this work, the steady-state module of the technique is used to probe the phonon modes within the GaN layers, GaTe layers, $SiO_2$/Si substrates, polycrystalline diamond layers, SiC substrates et al., for investigation of the stress and their thermal properties. This section covers many subjects from the fundamental design and key components of a Renishaw InVia Raman spectrometer to the operation of a Raman spectrometer and how the Raman spectrum is recorded and analyzed. Furthermore, the micro-Raman stress metrology and opto-thermography, angle-resolved polarized micro-Raman techniques are introduced.

#### 3.1.1 Micro-Raman spectroscopy characterization techniques

##### 3.1.1.1 Micro-Raman spectroscopy fundamental design

The Raman scattering signal in semiconductors is normally very weak, with a typical scattering efficiency in the range of $10^{-6}$-$10^{-7}$ compared to the Rayleigh scattered light. To measure this weak Raman scattering signal, three key experimental components are required in the spectrometer:

1) An intense, monochromatic, and collimated light source. As only ~1 in $10^6$-$10^8$

incident photons are inelastically scattered, to increase this ultra small Raman signal cross-section, an intense and collimated light source can be used to ensure that enough photons are incident on the semiconductor material to produce a Raman scattering signal which is large enough to be detected. The monochromaticity of the incident light is critical; the spectral bandwidth of the incident light should be much narrower than that of the phonon mode. Through the technique, light source was originally developed using emission lines such as mercury lamps and filtered sunlight, later on lasers were found to be an ideal light source containing all the above features and are now used in modern Raman spectrometers. Laser emission can also be polarized, therefore enabling phonon symmetry to be studied.

2) A highly sensitive photon detector. Due to the weak intensity in nature of the Raman signal, the detection of this Raman scattered light must have a high signal-to-noise ratio and a low dark current rate. Single or multi-channel detectors such as a photomultiplier tubes (PMT) or a charge-coupled device arrays (CCD), respectively, have been used to measure the Raman scattered light intensity. The PMT is highly sensitive, but has the disadvantage that its use requires a spectrometer scanning across the targeted measurement range and a sequential recording of the Raman scattering intensity which is time consuming. CCDs have very low noise and the ability to measure a spectrum over a wide spectral window within a single measurement which can significantly reduce the measurement time, and therefore are now the most widely used detectors in Raman scattering experiments.

3) An efficient filter to remove Rayleigh scattered light and a spectrometer for dispersing the Raman scattered light. As mentioned previously, the Rayleigh scattered light is much stronger than that of Raman scattering. Therefore it is vital to prevent the former from reaching the detector as its strong signal intensity would be easier to saturate or damage the detection system. This Rayleigh scattered light can be rejected by using a Rayleigh filter, e.g. notch or edge filter (holographic or graded dielectric type), which can reflect light with a frequency of or close to that of the incident light and transmit the Raman scattered light. For the notch filter, both the Stokes and anti-Stokes Raman scattered light can be transmitted whereas only one or the other can be transmitted by the edge filter. Alternatively, two or three aligned monochromators can also be used to reject the Rayleigh scattered light. Gratings with different line densities are mainly used to disperse the Raman scattered light depending on the spectral range investigated.

In this study, a range of lasers in the Raman measurements were used, including: a Laser Physics 488 nm (2.54 eV) argon ion laser and a Laser Quantum Torus 532 nm (2.33 eV)

continuous wave frequency-doubled Nd: YAG (neodymium-doped yttrium aluminium garnet) laser, with an full output power of 20 mW and 380 mW, respectively. Notably, these lasers' energies are below the bandgap of GaN, AlGaN, diamond and SiC, being transparent to those studied materials, with negligible absorption. Therefore the Raman signal can originate from the whole thickness of an investigated layer, or from the confocal volume of the bulk materials using the focusing system. Use of sub-bandgap lasers minimizes the generation of laser-induced electron-hole pairs, which would affect the performance of device operation. However, these lasers are above the bandgap of the Si substrate, and the absorption depth is ~0.4 μm into the Si substrate for a 488 nm laser.[248] If the power of the laser incident onto the material or device was sufficiently high, significant laser induced heating of the Si substrate would occur. Therefore, Raman shift with respect to laser power should be tested until convergence is achieved to avoid the laser heating for the sub-laser-energy materials.

Microscopy was used to focus the exciting laser light onto the surface of the sample and collect the backscattered light. This allows micron scale scattering volumes to be probed, and is highly efficient for the investigation of thin-film semiconductor layers. To achieve the expected resolution, the microscope objective lens is chosen depending on the required working distance, magnification and numerical aperture (NA). The lens NA determines the light collecting ability and theoretical lateral and depth resolution, which is defined as:

$$\mathrm{NA} = n\sin(\theta), \tag{3.1}$$

where $n$ is the refractive index of the focusing medium (air here) in which the lens is placed and $\theta$ is the half-angle of the angular aperture cone of the scattered light that can enter the lens from the sample. The larger the lens NA, the larger the half-angle, and the higher the light collecting ability due to the increased range of angles over those collected back-scattered light. In this thesis, various objective lenses with magnification of 50× or 100× and with different NA of 0.6~0.9 were typically used in Raman spectrum measurements. Very large NA (e.g. NA=0.9) can also allow some in-plane polarized scattered photons to be collected, for detection of some in-plane polarized Raman modes.

The ability of the lens to distinguish the two points on an illuminated sample is termed as spatial resolution. The theoretical lateral resolution of the lens can be expressed as the following:[249]

$$r_{\mathrm{lateral}} = \frac{0.51\lambda}{\mathrm{NA}}, \tag{3.2}$$

where $\lambda$ is the wavelength of the incident laser beam. While the depth resolution of the lens is defined as:[249]

$$r_{\text{depth}} = \frac{0.88\lambda}{n - \sqrt{n^2 - \text{NA}^2}}, \tag{3.3}$$

where *n* is the refractive index of the measured material through which the laser is focused. It is apparent from equation (3.2) and (3.3) that the larger the NA, the higher the lateral and depth resolution of the lens can be achieved.

Furthermore, a Prior XYZ-motorized stage was used to move the sample position under the objective lens with a resolution of 0.1 μm. The sample movement can be controlled by the computer in the *x*, *y*, and *z*-directions, and an automatic mapping routine can be set up in the Wire 2.0 software.

### 3.1.1.2 Renishaw InVia Raman spectrometer

In this work, a Renishaw InVia Raman spectrometer was used to perform the Raman spectroscopy measurements. A schematic of the Raman system is shown in Figure 3.1, with the key optical components (discussed later) labelled. In the following, the basic principles and operation procedures of the Renishaw Invia spectrometer using different continuous wave (CW) laser excitations are described.

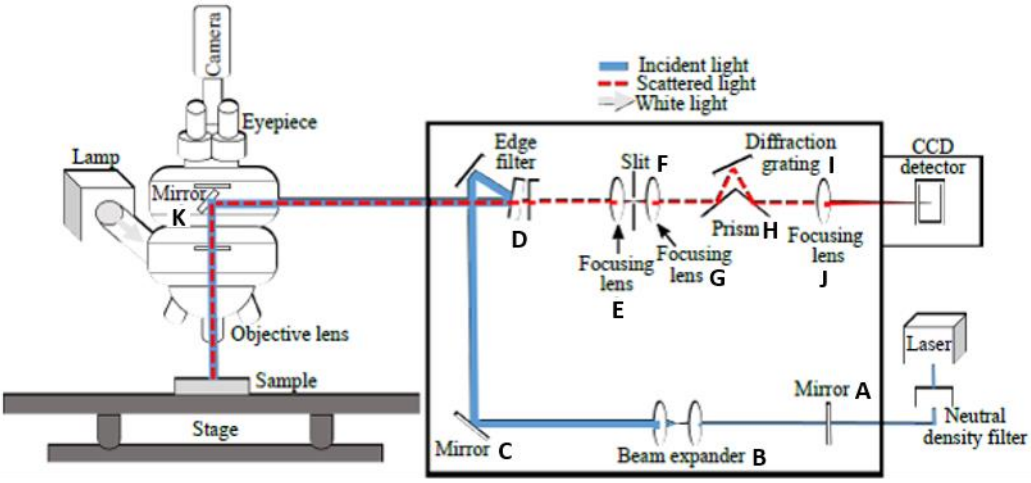


Figure 3.1. Schematic of the micro-Raman system showing the main components of the Renishaw InVia micro-Raman spectrometer. (Adapted from Power *et al.*[250])

As shown in Figure 3.1, the emitted laser light passes through a variable neutral density filter which is used to attenuate the laser power to the desired level before entering the spectrometer. Next, the laser light is directed by the first adjustable beam steering mirror (A) through a beam expander. The beam expander (B) consists of two aligned lenses with their focal points coinciding, so that the beam remains collimated and its diameter can be expanded to fill the aperture of the microscope objective lens. This generates the highest spatial

resolution available for the smallest possible spot size focused on the sample surface under study. After passing through the beam expander, the collimated and expanded beam is directed by the second adjustable beam steering mirror (C) to the Rayleigh filter (D); a cylindrical lens can be added to produce a line-focus beam rather than a point-focus beam and reduce the laser power density at the sample.

The laser light reflected by the Rayleigh filter needs to be reflected again by a mirror within the microscope (Leica DMLM here) focused by an objective lens onto the sample under study. After being excited by the laser, both back-scattered Rayleigh and Raman scattered light from the sample are collected by the objective lens and reflected back to the Rayleigh filter. The Rayleigh scattered light is blocked by the filter while the Raman scattered light transmits through until it reaches the spectrometer. Before entering the dispersing part of the spectrometer, an adjustable slit (F) and a pair of lenses (E and G) are used to block some of the divergent light which originates from outside of the objective lens focus point, in order to enhance the spectral resolution that can be realized through the following process: the Rayleigh filter transmitted light is focused by a pre-slit lens, E, and directed onto the adjustable slit (F) opening, then this light is collimated by a post-slit lens, G, and directed to a prism. Notably, reducing the slit width and decreasing the number of summed pixels of CCD (these two parts co-work as a virtual pinhole) enable us to measure only the volume within the objective lens focal point (i.e. confocal configuration). The slit width is typically set to 50 μm for standard measurements and 10 μm for confocal measurements. The prism (H) is installed with two-side mirrored surfaces which can reflect the light onto the diffraction grating (I) and then to the CCD. Several diffraction gratings with different line densities can be chosen according to the dispersion required in the spectral range investigated: 1200 lines/mm for near-IR, 3600 lines/mm for near-UV and 1800 lines/mm or 2400 lines/mm for the visible range. All gratings are motorized, mounted and controlled by the PC. Also, spectrum can be acquired by fixing (static mode) or constantly rotating (extended mode) the grating angle; the later mode is used to measure a larger spectral range. Finally, the dispersed light is reflected towards another lens (J) by the second mirrored surface of the prism and focused onto the CCD detector.

The CCD detector is a 576×384 pixel array camera, in which each pixel corresponds to a metal-oxide semiconductor (MOS) capacitor on the surface of a silicon wafer. To improve its signal-to-noise ratio, it was thermoelectrically cooled to -70 $^{o}$C using a Peltier element. During exposure, the CCD shutter opens, the scattered light incidents on the MOS capacitors (pixels) of the CCD array and an electric charge proportional to the incident light intensity accumulates on each pixel. After the completion of the exposure, the shutter closes and the accumulated electric charge is transferred along the lateral array across the CCD from pixel to pixel. When the charge is transferred to the pixel at the edge of the CCD array it is amplified

and digitalized to an intensity value. The position of each pixel within the lateral array is corresponding to frequency and can be converted into the actual frequency of the accumulated light, i.e. a Raman spectrum, considering the grating dispersion, as shown in Figure 3.2. Perpendicular to this frequency dispersion axis, a predefined number of pixels along the vertical array are summed together (binned) to produce the intensity of the resulting spectrum (Figure 3.2). The number of summed pixels is selectable, which is analogous to adjusting the width of another slit perpendicular to the aforementioned slit. The standard and confocal bin sizes are 10 pixels and 1 pixel, respectively. An in-plane spatial resolution of ~0.5-0.7 μm was achieved in this work. The depth resolution, besides considerations in Equation 3.3, also depends on the bandgap of the material compared to the excitation wavelength of the laser used, and the thickness of the measured sample.

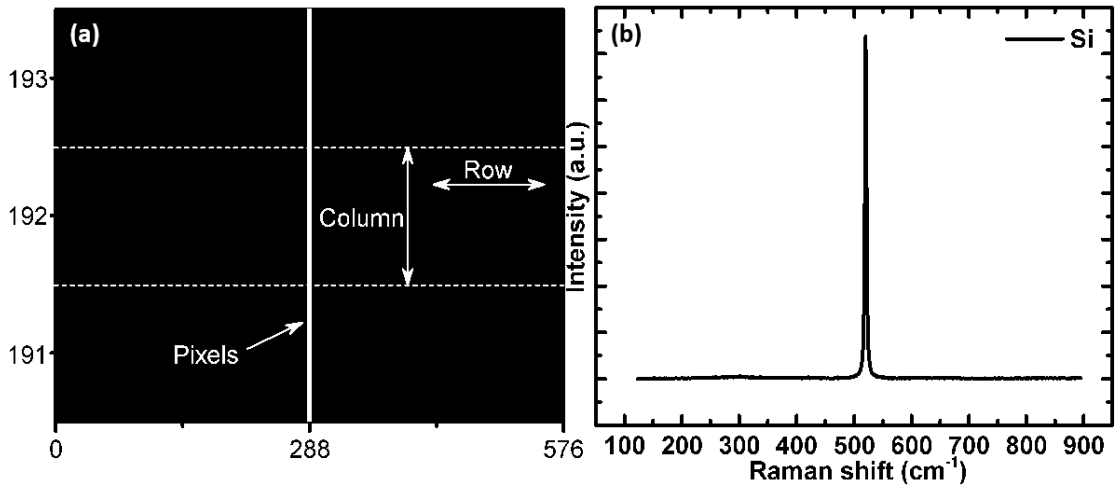


Figure 3.2. (a) Pixel calibrated CCD image and (b) Raman spectrum of a Si sample.

The spectrometer needs to be kept at a constant temperature (i.e. air-conditioning) to avoid any thermally-induced spectral shifts, and be enclosed in a dark cabinet to prevent ambient light interfering. In addition, the whole system must be isolated from the environmental vibrations, which can be achieved by being mounted on an optical bench (such as Ocean Optics) equipped with pneumatic vibration-isolated legs to maximize the precision of spatial resolution especially during mapping measurements.

### 3.1.1.3 Measurements, analysis and considerations of Raman spectrums

The operation procedure of the Raman system is as follows:

(1) Before a Raman measurement, the first step is to turn on the laser and warm it up for about half an hour, which is normally aimed for ensuring a stable laser beam is generated.

(2) Next, the system needs careful calibration in terms of beam alignment and phonon frequency calibration. The former is performed by adjusting the optical components along the

beam path to get the beam spot size on the sample as small as possible, and the signal intensity collected by the CCD maximized. The latter can be realized by measuring the spectrum of a Si reference sample (Figure 3.2(b)), and through adjusting the position of the diffraction grating motor until the frequency of the Si $F_{2g}$ Raman peak is fixed at 520.3 $cm^{-1}$. A second calibration using the Si reference sample is also performed after the measurement to check for the spectral stability during the measurements which can also be considered as the measurement error of Raman shift.

(3) Once the calibration of the Raman system is finished, the sample under study is mounted and fixed on the microscope stage for measurement. A heating or a vacuum chuck, Linkam heating/cooling stage, or other specialized stages sometimes are used for measurements. Another consideration during sample-mounting is an appropriate lens working distance for the available lens-to-sample height. In terms of the sample requirements for Raman measurements, apart from having the sample under study clean from surface contamination, no other special sample preparation is required to perform micro-Raman measurements.

(4) A various type of the measurements can be selected in the Wire 2.0 software, such as single-point, line mapping, area mapping and depth mapping. The spectrum acquisition method can be chosen between static and extended mode, as well as normal and confocal mode. In this work, single-point and various mapping methods were performed in both static or extended mode, and normal or confocal mode. The percentage of the laser power exposed onto the sample can be chosen from 100% to 0.0001%. The exposure time of the scattered light incident onto the CCD, as well as the number of exposure times the CCD detector undergoes (accumulation number) can be also set. Notably, the data collected from each accumulation is summed to produce a final spectrum by the software. This accumulation number setting is very useful especially when analyzing the Raman spectrum with extremely high and low intensity peaks as it can allow a high enough signal to be recorded for those peaks with low intensity while avoiding saturation for the peaks with high intensity during the measurements. Saturation is normally characterized as a flat-topped shape of a peak due to the inability of the initially charged pixels relating to this peak on the CCD array to accept more photons from the scattered light. In the case of saturation, extraction of the center frequency of this peak will be unavailable.

(5) After finishing all measurements, turn off the laser, including the laser shutter, Wire 2.0 software and microscopy in sequence, and recover the microscope stage to its initial status.

Figure 3.3 shows a typical Raman spectrum of an AlGaN/GaN-on-Si device and a GaN-on-SiC device, respectively, both measured in this work. The Raman shift is expressed in

wavenumber ($cm^{-1}$) on the *x*-axis represents the related phonon frequency obtained from the Stokes shift of the scattered light frequency in relative to that of the incident laser. Every peak in the spectrum is a Raman-active phonon mode that can be characterized at the first Brillouin zone center of the corresponding materials within the device layers. The common Raman shifts (phonon frequency) of the Si, GaN, SiC and diamond are shown in Table 3.1. When analyzing diamond samples, it should be noted that fluorescence can be superimposed on the Raman spectrum that can cover up the main character peaks. To enhance the signal-to-noise ratio of diamond $F_{2g}$ peaks, a higher energy laser such as a 488 nm or a 325 nm tends to produce better Raman spectrum than the 532 nm laser.

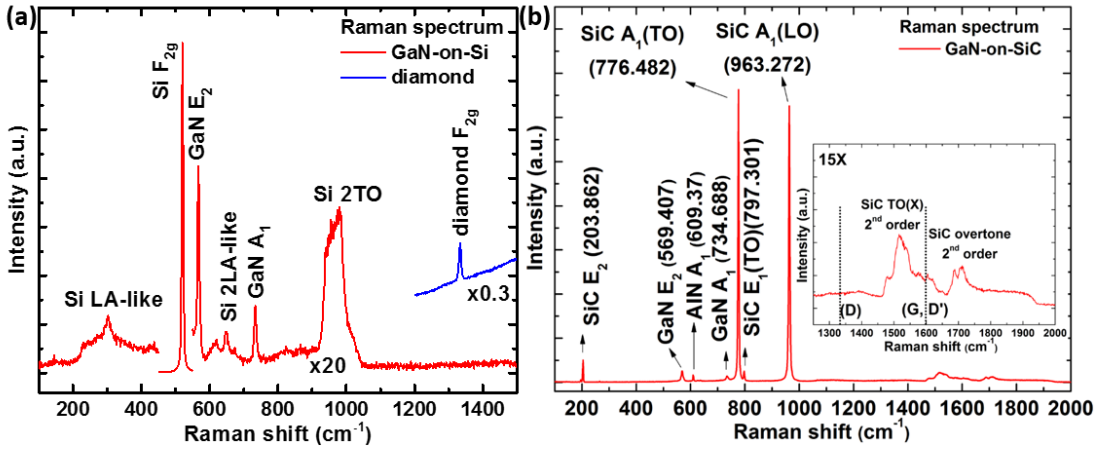


Figure 3.3. Typical Raman spectrum of (a) the AlGaN/GaN-on-Si sample and diamond, and (b) the GaN-on-SiC sample, the inset shows a zoom in figure of the 1250-2000 $cm^{-1}$ region.

Table 3.1. Commonly measured Raman shifts of the first Brillouin zone center phonons of GaN, Si, diamond, SiC at room temperature.

| Phonon mode | Frequency ($cm^{-1}$) |
|---|---|
| GaN $A_1$ (LO) | 734[50] |
| GaN $E_2^{high}$ | 568[50] |
| Si ($F_{2g}$) | 520[251] |
| Diamond ($F_{2g}$) | 1332[252] |
| SiC $A_1$ (LO) | 963[253] |
| SiC $E_1$ (TO) | 797[253] |
| SiC $A_1$ (TO) | 776[253] |
| SiC $E_2$ | 204[253] |

The peak position (i.e., the center frequency of the peaks) of the spectrum is analyzed and determined by a mixed ratio of Gaussian-Lorentzian line shape fitting, performed using the Wire 2.0 software. Based on the principle of pseudo-Voigt profile, different Gaussian: Lorentzian ratios setting from 10:90-100:0 were automatically determined and adjusted in the fitting, enabling the positions of the GaN $A_1$ (LO), Si and diamond $F_{2g}$ peaks varying in a range less than the minimum resolvable peak shift by curve fitting of about 0.1 $cm^{-1}$. Therefore, it is possible to use any of the above Gaussian: Lorentzian ratio for curve fitting these Raman peaks. Note that when there is a need to accurately analyse the full width at half maximum (FWHM) of the peak to determine the phonon width, it is important to use Voigt profile for accurate fitting; when only the quality or homogeneity of the materials is needed to evaluate, the above pseudo-Voigt profile fitting is enough. A template curve fitting routine can be saved and loaded for each peak, which is useful when analyzing the same peaks across all spectrum measured within the same sample. This method can ensure that the curve fitting is the same or consistent for different measurements.

### 3.1.2 Micro-Raman stress metrology

Micro-Raman stress metrology is one typical function of Raman spectroscopy which makes use of the stress dependence of the Raman mode frequency to evaluate the magnitude of stress within a material. Stress can have significant impact on a material's or a device's performance, for example, piezoelectric stress in the GaN layer of AlGaN/GaN devices is induced by the electric field under bias. When large enough this can form defects and result in detrimental effects. Cracks or delamination can even form within a material or at the interfaces when under the large stresses introduced by nanoindentation when investigating a material's mechanical properties. Therefore, it is important to know the magnitude of induced stresses for evaluation of their effects. As discussed in Section 2.4.1.4, phonon frequencies are sensitive to the change of the interatomic potential and lattice parameters, therein can be used to monitor the stress change and can be measured using micro-Raman spectroscopy.

The stress was first measured by acquiring the frequency of phonon modes of an unstressed reference sample ($\omega_r$), e.g., an unbiased device sample or a reference sample with relative perfect quality and a stressed sample ($\omega_s$) which was biased at high voltage or indented or pressured from their corresponding Raman spectrum. Secondly, the Raman shift in the frequency of phonon modes due to the applied high voltage or indentation load ($\omega_s$ - $\omega_r$) was calculated, which is equivalent to $\Delta\omega$ in Equation 2.51. Using these equations, the corresponding stress ($\sigma$) can be determined from different phonon mode shifts. The stress distribution of the interested region can also be calculated from the mapping of phonon mode shifts.

### 3.1.3 Micro-Raman thermography

Micro-Raman thermography is another typical function of Raman spectroscopy which uses the temperature dependence in the frequency shift of the Raman modes to extract the temperature. As discussed in Section 2.1.6, a large local temperature rise occurs in AlGaN/GaN devices under high power operation which can lead to significant degradation in device performance and reliability or even failure. It is therefore very important to reliably and accurately measure this temperature rise for understanding the mechanism of thermal degradation on these devices, as well as obtaining accurate thermal parameters such as thermal conductivity of the materials and thermal resistance at interfaces. The lattice expansion caused by increased temperature can be detected from the frequency shifts of phonon modes, as expressed in Equation 2.62 in Section 2.4.1.5, making micro-Raman thermography a particularly useful tool for probing local temperature rise. This technique is non-invasive and can provide a high spatial resolution, enabling characterization of the submicron hotspots localized near the gate foot at the drain side of the devices; but it also requires fabrication of appropriate heaters to heat the sample. As different temperature ranges were investigated for different samples in the Raman measurements, it is very important to calibrate the frequency shift of the phonon modes as a function of the temperature in order to accurately probe the temperature rise in devices. This was achieved by using an accurate temperature-controlled stage; a Linkam THMSG600 was used in this work, and this will be introduced in Figure 3.8.

Despite providing sub-micron spatial resolution and being noninvasive, there are limitations to the micro-Raman thermography techniques: 1) they are unable to measure the peak temperature generated near the AlGaN/GaN interface because the GaN layer is transparent to the visible laser wavelength, resulting in only an average temperature through the whole GaN layer being measured. Therefore, device simulation is normally used to help estimate the peak temperature value according to the measured average temperature; 2) the measurement time is normally long, especially when the probed phonon mode has a low Raman peak intensity.

When using an above bandgap laser for a known material, part of the laser energy will be absorbed by the material and heat the sample. By varying the laser power irradiated on the sample, different magnitudes of heating i.e. temperature rise can be introduced and measured from the frequency shifts of the phonon modes in the Raman spectra. Thermal properties such as the thermal conductivity of the materials therein can be extracted. This laser self-heated thermography technique is called micro-Raman opto-thermography, which is very convenient in measuring the thermal properties of 2D materials. However, the laser absorption in

measured materials must be known, this can be calculated from the reflectivity and transmissivity which is relatively easier to measure.

### 3.1.4 Angle-resolved polarized micro-Raman spectrum

In some materials, there exists some phonon modes that induce a non-zero component element in the susceptibility tensor along a certain crystal orientation while a zero susceptibility in the perpendicular orientation. Hence, under a backscattering configuration, when these materials are probed with the polarization of incident laser perpendicular to the orientation of the phonon modes, those phonon modes will not be observed. Alternatively, when the sample is rotated in the lateral direction where the angle $\theta$ between the laser polarization and phonon mode orientation is less than 90°, we start to probe the phonon band, whose Raman intensity can change linearly with $\cos^2\theta$. This technique is very useful in studying materials with low crystal symmetry, in which many phonon bands exist with a susceptibility change along one axis of the unit cell. Therefore the crystal orientations can be determined from the polar plot of the Raman intensity change of certain phonon modes with respect to the angle.[136,137,254,255]

Angle-resolved polarized Raman spectrum is performed under different rotation angles by fixing samples onto an angle-resolved polarizer and collecting under the backscattering configuration ($z(xx)\bar{z}$), i.e., the polarization of the scattered Raman light is parallel to that of the incident light. Then the Raman intensity of certain phonon modes can be plotted against the angle and investigated.

## 3.2 Nanosecond time-domain thermoreflectance

### 3.2.1 Nanosecond TDTR techniques

To assess the thermal conductivity of diamond and the thermal boundary resistance at interfaces of the GaN-on-diamond multilayer structures quickly and efficiently, the nanosecond TDTR technique combined with analytical modelling was exploited. As mentioned in Section 3.1.3, the micro-Raman thermography technique combined with device thermal simulation can also be used to extract the above thermal parameters, but processed devices are required. The nanosecond TDTR technique is non-destructive, although for some materials with a bandgap lower than the photon energy of pump laser, a metal transducer thin layer must be deposited, it can normally be easily etched away without destroying the underlying material. TDTR is also contactless and fast with the option of wafer mapping, there is no need for device processing so it can provide quick and efficient feedback for thermal optimization of materials from the initial growth. In this section, the nanosecond TDTR system, the measurement procedure and data analysis using Monte-Carlo analytical heat transport model are described.

#### 3.2.1.1 Nanosecond TDTR system

The nanosecond TDTR system utilized is demonstrated in Figure 3.4. As a pump-probe technique in the TDTR measurements, a pump beam from a dual-output Q-switched frequency-tripled Nd: YAG laser (Photon Industries DC100H-532NL) was used to heat the surface of the sample with an 8 ns pulse duration and 355 nm wavelength; a probe beam from a frequency-doubled Nd: YAG continuous wave (CW) laser (Laser Quantum Torus) was used to probe the surface reflectivity change of the sample with a 532 nm wavelength. The pump laser was operated at a repetition rate of 30 kHz, and the generated ultraviolet (UV) beam with a third harmonic wavelength of 355 nm was produced by optical sum-frequency generation of the infrared beam with a fundamental wavelength of 1064 nm and the green beam with a second harmonic wavelength of 532 nm through a Lithium Triborate (LBO) non-linear crystal. The surface reflectivity change at the probing laser wavelength for the investigated sample structures in this work is proportional to the transient temperature rise. The 8 ns pulse width is significantly larger than the picosecond pulse width that is used in conventional TDTR, however, sensitivity calculations (see examples in Chapter 4 and 5) of the investigated structures in this work indicated that the TBR of the GaN/diamond interface (the thermal conductivity of diamond) affects temperature transients at the 100 ns (50 ns) scale after the heating pulse stops, hence this width pump pulse is short enough to investigate the TBR of the GaN/diamond interface (diamond thermal conductivity).

As shown in the Figure 3.4, after passing through the nonlinear (LBO) crystal, the UV beam together with the IR and green beam were collimated by lens 1 and directed to a dielectric mirror where the UV beam was reflected while most IR and green beam were transmitted and absorbed by a subsequent beam dump. To exclude the effects from residual IR and green beam on the recorded transients, a prism was used to disperse all the three reflected beams to separate the generated UV beam from the residual beams. With the help of mirrors, the separated UV beam was directed into an adjustable Keplerian beam expander (consisting of two quartz biconvex lens with a focal length of 30 mm in order to produce a tunable beam size of about 50-80 μm for the exiting UV beam) to increase its diameter, a similar function as that performed in the micro-Raman spectroscopy system. This expanded UV beam was then mostly reflected off a low-pass dichromic mirror where a green beam from the CW laser is transmitted. The dichromic mirror was placed in both beams paths at an angle of 45º. The collimated probe green beam needs to pass through a 50/50 beam splitter before joining the dichromic mirror so that the reflected beam can be more easily separated and collected by a photodetector. It should be noted that at the point of the dichromic mirror, the pump UV beam must be optically aligned to be accurately co-axial with the probe green beam. Both beams were directed into and reflected off a mirror within the Leica DMLM microscope, followed by being projected onto the sample via a 15× quartz objective lens with

an NA of 0.3. The sample was mounted on the prior XYZ-motorized microscope stage and adjusted until both the pump beam and probe beam were focused on the surface. The pump and probe beam diameters at the sample were ~70 μm and ~2 μm, respectively. The reflected probe beam by the sample surface was then directed out the microscope along the incident beam path until being reflected off the beam splitter and directed into a fast-response, amplified silicon photodiode (Thorlabs PDA100A) through a long-pass filter. The collected signal was finally output to and recorded by a digital oscilloscope (InfiniiVision DSO-X3034A, Agilent Technologies), which is triggered from the Sync output of the pump laser. A long-pass filter was used to block most of the reflected pump UV beam to avoid being detected by the photodiode and minimize its effect on the probe signal. The energy of the pump pulses can be adjusted to result in only few 10 K temperature rise at the area of the beam diameter, which can avoid overheating or burning the sample but is sufficient enough to induce a significant change in the reflectance to allow it being directly detected within the sensitivity of silicon photodiode and the resolution (10 bit) of oscilloscope. To reduce the noise of the detected transient signal, the oscilloscope was set to enable capturing $2^{16}$ consecutive traces and recording their average simultaneously (average mode with the highest setting), followed by saving of the transient data for further evaluation.

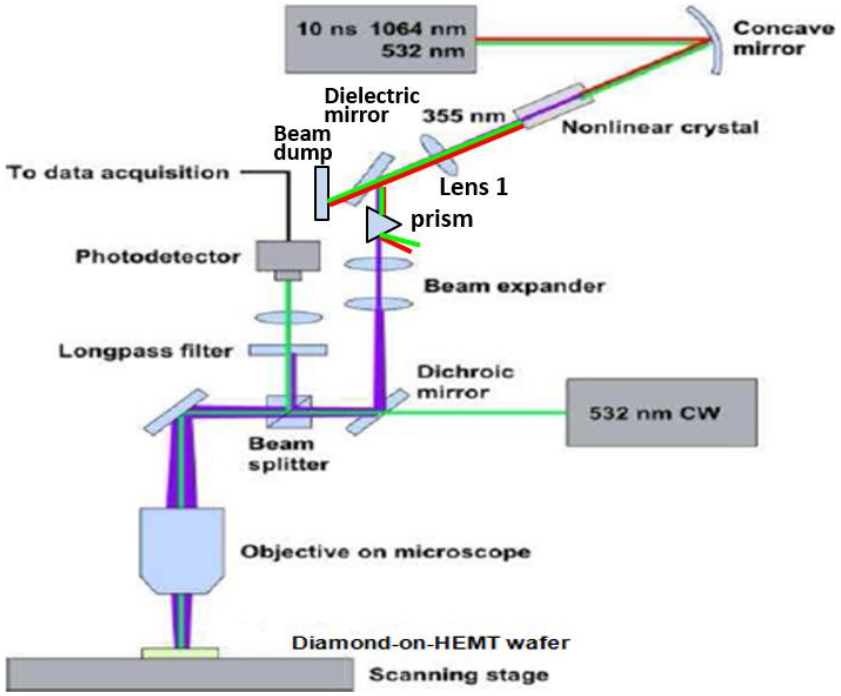


Figure 3.4. A schematic of the nanosecond TDTR system.

During heating the sample surface using the pump pulse, cross-plane direction heat diffusion is preferred as the investigated polycrystalline diamond mainly presents a cross-

plane columnar structure which can result in anisotropic heat transport. To achieve a uniform vertical heat flow from the sample surface with a negligible lateral heat spreading in the layers, it is desirable to obtain a large diameter of the UV spot through adjusting the beam expander. To adjust and measure the spot size of UV beam, it was very helpful to make the UV spot visible under the microscope. Therefore a polished GaAs wafer was used to emit IR photoluminescence under the irradiation of the UV laser which can be observed by the CCD camera, as indicated in Figure 3.5. Further methods to determine spot size was to use the knife-edge method. In this method, a gold-coated glass slide that needs to be primarily adjusted to the same focus plane of the sample surface is stepwise offset into the beam which can be precisely achieved through the motorized Prior stage, and recording the reflected UV intensity via the photodiode and oscilloscope simultaneously; then by plotting the curve of intensity with respect to the gold-coated glass slide moving distance, the UV beam spot size can be determined from the FWHM of the plotted curve.

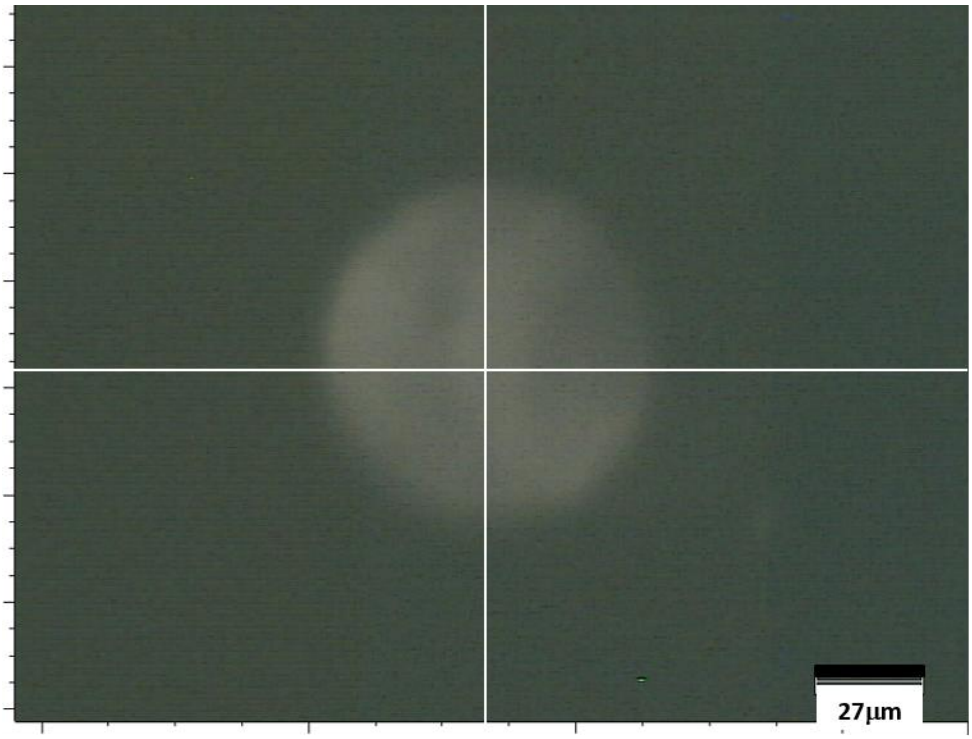


Figure 3.5. Optical image of the IR photoluminescence of the UV beam spot on a GaAs wafer.

### 3.2.1.2 Sample and measurements

As in the investigated sample structures, i.e., diamond-on-GaN HEMTs, the UV beam is transparent to the diamond, a 100 nm-thick Au film metal transducer layer was used to form an efficient heating source due to its strong ability in absorbing the energy from the UV pump laser pulse (Figure 3.6).[256] The thermoreflectance coefficient of gold is the largest at the wavelength of 532 nm[257] and its surface reflectivity shows a highly linear response with temperature over the investigated temperature range (25-225 $^{o}$C). Due to the poor bonding ability of gold with diamond, a 30 nm-thick Ti or Cr adhesion layer was deposited onto the diamond prior to the gold deposition. The metal films were deposited using the same procedure by thermal evaporation for all the samples and the nominal metal film thickness was further confirmed using AFM, which was about 131.5 nm in average, as shown in the profile in Figure 3.7. This thickness parameter was vital in the following analytical model analysis.

After alignments and warming up of lasers, the thermoreflectance transients ($\Delta R/R$, in form of an AC signal) of samples from the contribution of both pump laser and probe laser were first detected and then recorded by the photodiode and oscilloscope. As is evident in Figure 3.6(a), the recorded AC signal had presented a negative response in all of the transients; this is because the thermoreflectance coefficient of gold is negative at the wavelength (532 nm) of exploited probe laser. Next, the probe laser beam is switched off so that all the contribution from the pump laser signal on the transients was measured. This pump laser signal demonstrated a positive sharp peak (Figure 3.6(b)) with its maximum at the same time point as that of the above negative peak of AC signal. Finally the pump laser signal was subtracted from the above negative AC signal in Figure 3.6(a), giving the actual probe laser signal from the sample (see Figure 3.6(c)). Note that the baselines of both signals should be normalized to zero before the subtraction. The resulting signal was normally multiplied by -1 to make it positive so that it can be normalized to peak value to produce the $\Delta R/R$ transients in either linear or logarithmic scale for analysis and comparison.

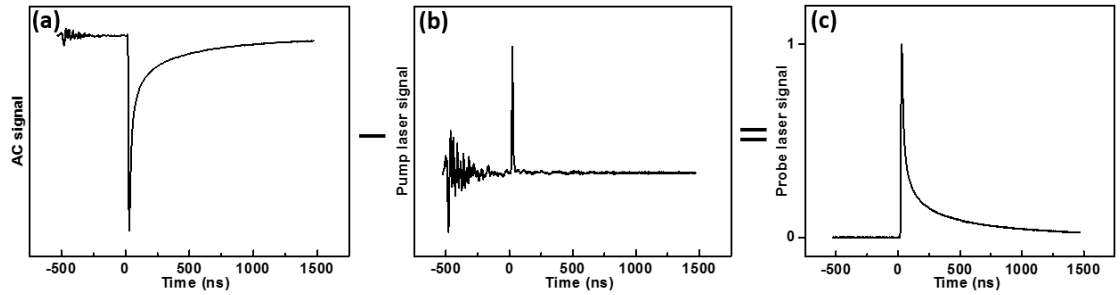


Figure 3.6. (a) The total AC signal from the reflected laser light detected by photodiode; (b) the pump laser signal after switching off the probe laser; (c) the normalized (ΔR/R) probe laser signal in linear scale.

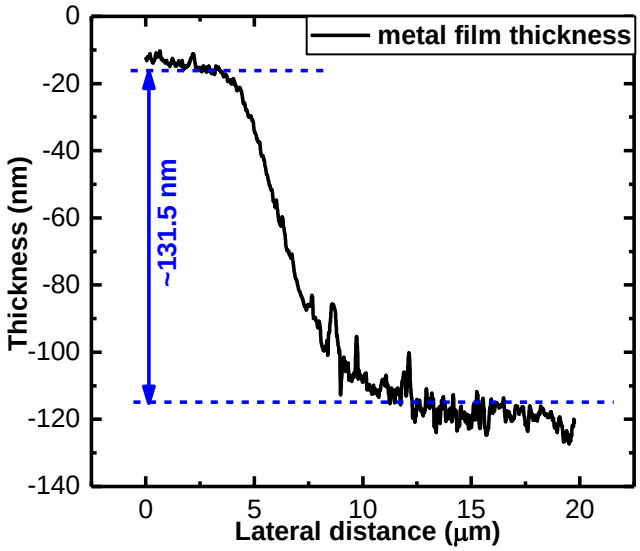


Figure 3.7. Metal film thickness which was used as the thermal transducer.

### 3.2.2 Heat transport model for thermoreflectance transients

#### 3.2.2.1 Analytical transmission-line axis-symmetric thermal transport model

To understand how reflectivity changes as function of time after heating up a metal layer on top of a material, an analytical transmission-line axis-symmetric thermal transport model has been developed by Hui and Tan[258,259] by solving the transient heat transport equation in the multilayer stack. The transmission-line model for thermoreflectance transient is based on analogies between Fourier's law for thermal conduction and Ohm's law for electrical conduction, and is detailed introduced in the following on basis of the methods described by Chen and Hui *et al.*,[258,259] in which the temperature excursion $\bar{\varepsilon}(z,s)$ (i.e. the Laplace transform of the temperature excursion $\varepsilon(z,t)$ in time domain in z direction) is equivalent to the voltage $V(z)$, and the heat flux $-\kappa\partial\bar{\varepsilon}(z,s)/\partial z$ to the current $I(z)$, with $\kappa$ the thermal conductivity, $t$ the time and $s$ the frequency, yielding

$$\frac{dV(z)}{dz} = -\frac{1}{\kappa} I(z), \tag{3.4a}$$

$$\frac{dI(z)}{dz} = -\rho C s V(z), \tag{3.4b}$$

where $\rho$ is the density and $C$ is the specific heat. Then the equivalent transmission-lines describing the heat diffusion in the $z$ direction (i.e. the voltage and current along the transmission-line) can be expressed as

$$V(z) = V^{+}(0)[\exp(-\gamma z) + \Gamma(0)\exp(\gamma z)], \tag{3.5a}$$

$$I(z) = \frac{V^{+}(0)}{Z_{\mathrm{c}}}[\exp(-\gamma z) - \Gamma(0)\exp(\gamma z)], \tag{3.5b}$$

where $z_{\mathrm{c}}$ is the characteristic impedance given as $1/\kappa\gamma$, with $\gamma$ defined as $\sqrt{s/\alpha}$ and $\alpha = \kappa/\rho C$ the thermal diffusivity. $\Gamma(0)$, the ratio of the reflection coefficient at $z$=0, is defined as

$$\Gamma(0) = \frac{V^{-}(0)}{V^{+}(0)} = \frac{Z_{\mathrm{L}} - Z_{\mathrm{c}}}{Z_{\mathrm{L}} + Z_{\mathrm{c}}}, \tag{3.6}$$

where $z_{\mathrm{L}}$ is the load impedance, corresponding to the thermal impedance of the rear face of the film. Therefore the input impedance at $z$=-$d$ can be given as

$$Z_{\mathrm{in}}(-d) = Z_{\mathrm{c}} \frac{Z_{\mathrm{L}} + Z_{\mathrm{c}}\tanh(\gamma d)}{Z_{\mathrm{c}} + Z_{\mathrm{L}}\tanh(\gamma d)}, \tag{3.7}$$

Basing on the above description, the surface temperature of a film or the voltage at $z$=-$d$, $V$(-$d$), can be illustrated as

$$V(-d) = Q(s) Z_{\mathrm{in}}(-d), \tag{3.8}$$

where $Q(s)$ is the current source, corresponding to the shape of a heat pulse which incidents at the film's front surface. The thermal characheristics of a film ($\kappa$, $\alpha$) of a thickness $d$ can be represented by its analogue transmission line characteristics ($\gamma$,$Z_{\mathrm{c}}$).

Once the heat excitation is given, the thermal parameters of each layer can be determined from the above formula. The inputs of this model are the thermal conductivity, thickness, density and volumetric heat capacity of each layer/material including consideration of the interfacial thermal resistances, as well as the geometrical and temporal characteristics of both pump and probe lasers.

### 3.2.2.2 Monte-Carlo analytical heat transport model

On the basis of the above analytical transmission-line axis-symmetric thermal transport model in Section 3.2.2.1, a Monte-Carlo analytical heat transport model, described in the following and developed by Dr. Julian Anaya in Mathematical Software, was exploited to analyze the thermoreflectance transients and to extract the thermal parameters. This model provides an analytical closed form for the temperature rise on the surface of a multilayer material exposed to a surface heat load. A detailed explanation of this method and its nuances were illustrated in the above Section 3.2.2.1. Following that derivation, the temperature rise on the surface can be evaluated from:

$$\Delta T(r,t) = L^{-1}\left(\int_0^{\infty}\left(Q(q_0,w_0,t_0,\beta,s)\times Z\left(\left(\kappa^i,d^i,\rho^i,c_p^i\right)_{i=1}^{i=n},\beta,s\right)\times J_0(r,\beta)\times\beta d\beta\right)\right), \tag{3.9}$$

where $L^{-1}$is the inverse Laplace transform and the integral term corresponding to the inverse Hankel transform. $J_0(r,\beta)$ is the first kind Bessel function, $Q(q_0,w_0,t_0,\beta,s)$ describes the Laplace/Hankel transformed heat source with $q_0$ the laser peak energy, $w_0$ and $t_0$ the spatial and temporal FWHM of the laser pump source which has a mathematical form given as:

$$Q(q_0,w_0,t_0,\beta,s) = \frac{0.44\times q_0 w_0^2\times e^{-\left(w_0^2/8\right)\beta^2}\left(e^{s(st_0^2-8t_{ini})/8}\times Erfc\left(\frac{(st_0-4t_{ini}/t_0)}{2\sqrt{2}}\right)\right)}{4t_0}. \tag{3.10}$$

Finally $Z\left(\left(\kappa^i,d^i,\rho^i,c_p^i\right)_{i=1}^{i=n},\beta,s\right)$in equation (3.9) stands for the Laplace/Hankel transformed thermal impedance of the stack of materials where $\left(\kappa^i,d^i,\rho^i,c_p^i\right)$ are the thermal conductivity, thickness, density and specific heat respectively for each of the $i^{\text{th}}$ layers composing the materials stack. Following the derivation in Section 3.2.2.1, the mathematical form for this impedance is therefore calculated recursively as:

$$Z\left(\left(\kappa^i,d^i,\rho^i,c_p^i\right)_{i=1}^{i=n},\beta,s\right) = \hat{Z}\left(\kappa^n,\rho^n,c_p^n\right)\times\frac{\left(Z\left(\left(\kappa^i,d^i,\rho^i,c_p^i\right)_{i=1}^{i=n-1},\beta,s\right)+\hat{Z}\left(\kappa^n,\rho^n,c_p^n\right)\times\gamma\left(\kappa^n,d^n,\rho^n,c_p^n\right)\right)}{\hat{Z}\left(\kappa^n,\rho^n,c_p^n\right)+\gamma\left(\kappa^n,d^n,\rho^n,c_p^n\right)\times Z\left(\left(\kappa^i,d^i,\rho^i,c_p^i\right)_{i=1}^{i=n-1},\beta,s\right)}, \tag{3.11}$$

where the values for $\hat{Z}\left(\kappa^n,\rho^n,c_p^n\right)$ and $\gamma\left(\kappa^n,d^n,\rho^n,c_p^n\right)$ are determined as:

$$\hat{Z}\left(\kappa^n,\rho^n,c_p^n\right) = \begin{cases}0, & n=1\\ \left(\sqrt{\kappa^n\rho^n c_p^n s+\beta^2}\right)^{-1}, & n>1\end{cases}; \tag{3.12a}$$

$$\gamma\left(\kappa^n,d^n,\rho^n,c_p^n\right) = \mathrm{Tanh}\left(d^n\sqrt{\rho^n c_p^n s/\kappa^n+\beta^2}\right). \tag{3.12b}$$

Under these conditions the integration of the equation (3.9) was solved numerically using the built-in Gauss-Berntsen-Espelid-Rule implemented in Mathematica, while the inverse Laplace transform is solved numerically using the Gaver-Stehfest method[260] with N=18. The model was validated against the solutions obtained by finite elements method in ANSYS for the same problem, yielding identical results in both cases. Finally, given the nonlinear nature of the problem, the thermal parameters and their uncertainty were determined via a nonlinear fitting routine implemented in Mathematica based on the built-in Nelder-Mead algorithm with a Monte-Carlo algorithm populating the initial values for each iteration of the method.[37] The uncertainties were then extracted from the standard deviation for each parameter through achieving the best fit to the experimental data, similar to the method described in reference.[37] Considering this, a 99% confidence level was set in the Monte-Carlo model to obtain the best fitting range for each parameter. Also, due to the diamond surface roughness, a conservative gold layer thickness variation is considered; in this work, the range of gold layer thickness is measured from the sample cross-section imaged by TEM and determined to be within ~80-120 nm. To account for this range, fitting was performed with the transducer thickness fixed at the maximum and minimum values to estimate the uncertainty introduced to the remaining fitting parameters

With the layers and parameters increased in the test structure, the process of decoupling the parameters normally becomes more and more complicated and difficult. As heat diffusion through each layer influences the recorded reflectivity change (surface temperature) over a range of different time scales, we can employ sensitivity analysis to see how to decouple the different contributions to the reflectivity transients. By considering a small change, for example, of $\pm 10\%$ in each layer thermal conductivity or $TBR_{eff}$ or other parameters, and calculating the difference between each modified transients and original transients with respect to time, as examples detailed shown in Chapter 4 and 5, the sensitivity curve for each parameter can be plotted and compared. This model has been proved to be able to deal with complex multilayer samples accurately.[29,37]

### 3.3 Linkam THMSG 600 temperature controlled stage

To perform the temperature-dependent measurements, a Linkam THMSG 600 temperature controlled stage is used and shown in Figure 3.8. This THMSG 600 stage can regulate the sample temperatures between -196 $^{o}$C and 600 $^{o}$C. To enable *in-situ* Raman measurements, a quartz window allowing optical transmittance to the sample within the stage is exploited. An air-tight lid can be unscrewed to set up the sample onto the chamber. For samples <6 mm in diameter, they are placed on a small quartz disc and are together attached to a manipulator arm. The quartz disc holding the samples are then fixed onto a silver block, and a silver cap with a small hole in the top is then placed over the sample to ensure a uniform

temperature distribution in the enclosed volume. An electrical heating element and a thermocouple are fixed to the silver block; they are connected to the external control unit for regulating the temperature automatically, which can control the temperature increments of the block as low as 0.1 $^{o}$C. When the chamber is heated above 300 $^{o}$C for more than 10 minutes, the stage mantle must be cooled by circulating water through an external reservoir using a pump (see Figure 3.8).

Low temperature measurements (below room temperature) are performed by connecting a 2 liters liquid nitrogen dewar to the stage via a thermal insulated pipe (see Figure 3.8). A $N_2$ pump draws the liquid nitrogen from the dewar through the silver block, which is cooled by the latent heat of vaporisation. Moisture within the chamber will freeze on the sample surface when it is cooled and interference with Raman measurements. To avoid this, it is very important to use $N_2$ to purge the chamber repeatedly through two valves before cooling. The $N_2$ pump is connected within the control unit for automated temperature regulation. Gas annealing can be performed by controlling the gas atmosphere (such as $N_2$, Ar) within the chamber using the above purge process, with the gas flowing through the chamber in a controlled rate during the heating, dwelling and cooling. It should be noted that thermal expansion will alter the sample position when it is measured over a large temperature range. This can be compensated by using a manipulator arm to adjust the sample laterally and the stage vertically. It is efficient to use some local characters of the samples for performing in-situ measurements.

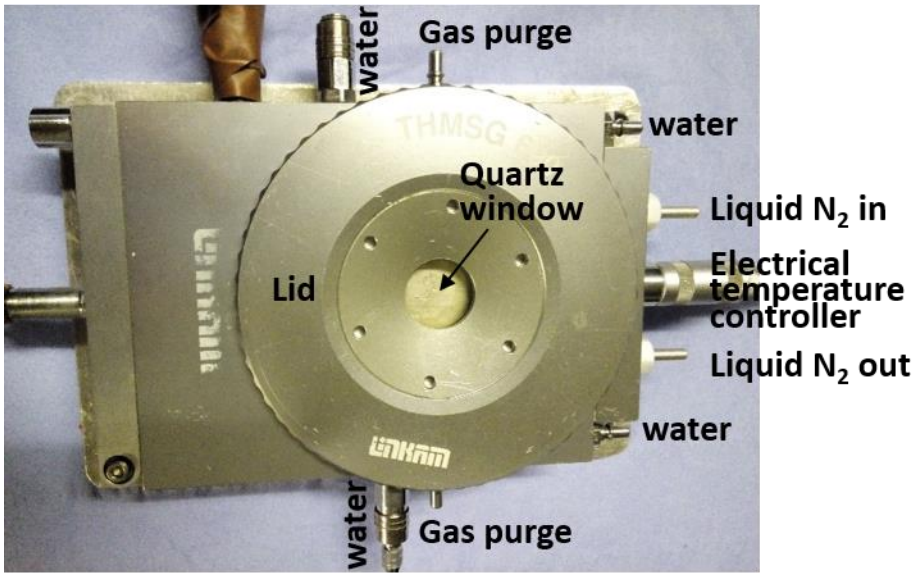


Figure 3.8. A photograph of the Linkam THMSG600 stage with cooling/heating components.

## 3.4 High-pressure diamond anvil cell techniques

Besides unique optoelectric properties, GaTe also shows potential for phase-change memory devices as some thickness- or pressure-dependent structural changes have been revealed in multi-to-fewlayers or bulk-powders, respectively. To investigate the pressure-dependent structural properties of GaTe flakes for potential strain-modulation applications, a Princeton-type symmetric diamond anvil cell (DAC) containing type-II low fluorescence diamonds with 300 μm diameter culets was used to generate pressures. As shown in the schematic cross section in Figure 3.9. A stainless steel gasket was pre-indented to a thickness of 50 μm, and then drilled centrally using a UV laser to give a 100 μm diameter sample chamber into which was loaded a sample. A new steel gasket needs to be prepared in the same way before every experiment. To avoid touching the gasket and both diamond anvils, the sample dimension needs to be less than 50 μm wide and 20 μm high, respectively. A hypodermic needle with a very sharp tip was used to place the sample on the bottom diamond anvil culet and within the center of the gasket hole. Some small ruby spheres were placed alongside the sample and used to gauge the pressure during each measurement. The remaining volume of the sample chamber was then filled with methanol:ethanol (4:1) solvent solution that acted as the pressure medium. Then the cell was closed by placing back the upper diamond anvil. Cell pressure can be increased or decreased gradually during the experiments by loading or unloading additional force to the diamond anvils. Attention must be paid that cell pressure can only be increased until asymmetric gasket deformation occurs. Cell pressure must be decreased at this point, or catastrophic gasket failure such as damage to the cell or the diamond anvils may be resulted in. It also should be noted that the anvils must be correctly aligned prior to any force loading, because incorrect alignment will cause non-uniform gasket deformation and increase the possibilities of gasket failure.

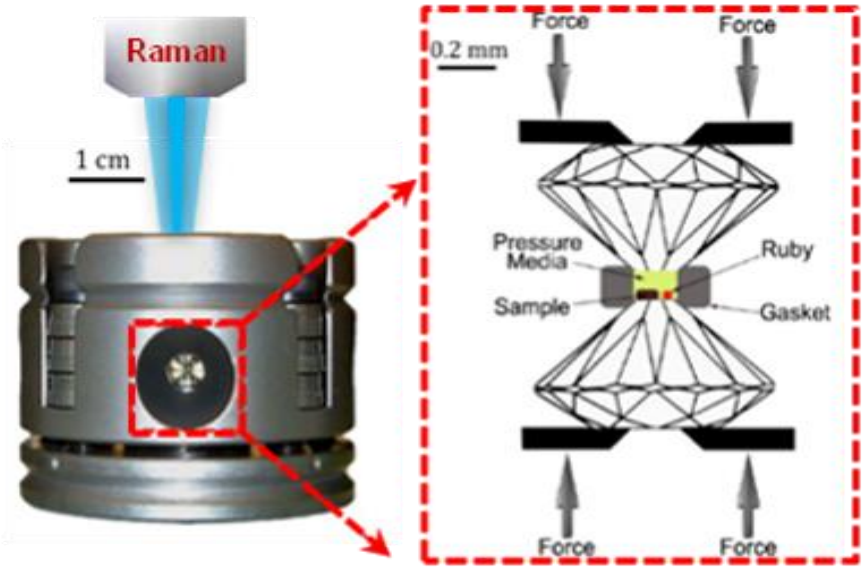


Figure 3.9. A photo and a schematic cross-section of the diamond anvil cell.

Pressures and their uncertainties were determined from the wavelength of the fluorescence peak of ruby spheres placed close to the sample flakes in the sample chamber of the DAC before and after each Raman measurement. A long working distance objective normally needs to be equipped to focus the incident and scattered light through the upper diamond anvil onto the surface of the sample during the Raman scattering experiment, therefore, to achieve high quality Raman signal, it is very important to choose appropriate diamond anvils with low fluorescence in the investigated spectral range. Besides, there is also an attenuation of the Raman scattered light due to reflection at the surfaces of diamond anvils. Both diamond luminescence and light attenuation will make high-pressure Raman experiments particularly challenging for materials with low Raman scattering cross-section.

### 3.5 Fabrication and transfer of ultrathin flakes of two-dimensional layered materials

2D layered materials are mainly fabricated from two approaches: exfoliation from bulk crystals, or using chemical/physical vapor deposition techniques. The former method can produce high crystallinity and high quality samples, although the samples dimension are normally limited and not practical for large scale production. Instead, vapor deposition technique can yield large area samples but is usually accompanied with relative low crystal quality.

There are two major methods to exfoliate bulk crystals: mechanical and chemical exfoliation. Mechanical cleavage presently is the most common method to isolate monolayers from bulk crystals, which was firstly discovered by Geim *et al*. in graphene.[261] To obtain few-layers and monolayer 2D flakes, there are two types of mechanical exfoliation methods: one is by attaching adhesive tape to a piece of crystal and cleaving the target 2D flakes by re-folding the adhesive tapes repeatedly (as schematic in Figure 3.10(a)). The weak van der Waals interaction between layers can be easier broken by exfoliation, therefore thinning the materials. The tape containing the flakes is then directly pressed firmly onto a target substrate and peeled off slowly, leaving some colorful thin flakes on the substrate. However, lots of residue glue is also left onto the substrate simultaneously, making it difficult to clean and locate the sample. The other way is to use PDMS film as a mediator which can reduce the residual glue greatly, then the PDMS film with flakes are firmly attached to a pre-treated substrate and peeled off from the substrate slowly, leaving flakes adhered on the substrate (as illustrated in Figure 3.10(b)).[262] Although less glue residual formed, this method has a disadvantage of low yield. The common substrates for 2D layered materials are the silicon wafer with a layer of 300 nm thermally oxidized $SiO_2$ on top, and are normally cleaned by the following standard procedure: rinsed in acetone, isopropanol (IPA) and deionized water (DI) for 5 minutes sequentially. Compared to the low yield of mechanical cleavage, chemical

exfoliation (or other methods such as liquid exfoliation) can enhance the production of 2D flakes.

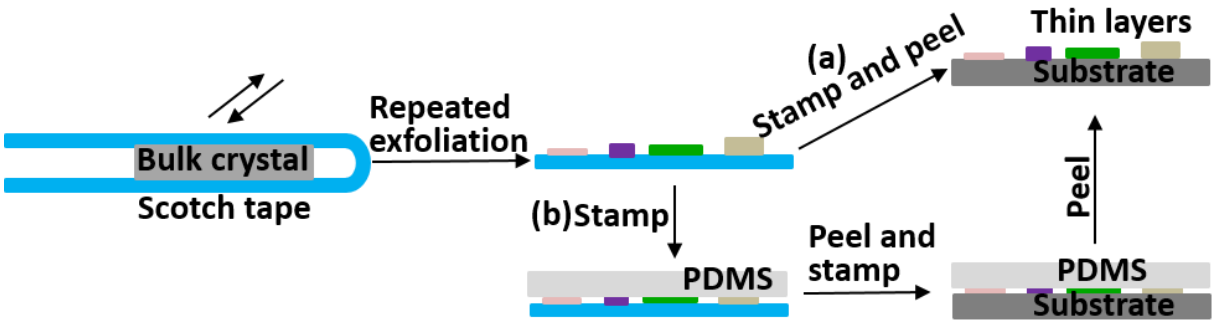


Figure 3.10. Exfoliation methods of 2D layered materials: (a) direct stamp and peel from the Scotch tape onto a substrate; (b) stamp onto a PDMS mediator firstly and then attach to and peel off a substrate.

For devices or vertical heterostructure fabrication, multilayer or monolayer flakes are often needed to be transferred onto a different substrate. Wet-etching transfer and dry transfer are the present two common techniques. Generally, the former method is by dissolving the growth substrate without harming the flakes using wet-etching techniques. As shown in Figure 3.11, the detailed process is as following: ~2 μm polymethyl methacrylate (PMMA) is firstly deposited onto the 2D materials by spin-coating, which acts as a carrier layer and prevents the 2D flakes from significant damage during the rest of the transfer process. After all being rinsed in an appropriate solvent until the substrate is completely etched, the PMMA carrier and 2D flakes stack, which finally remain and float on the surface of the solution, are carefully lifted out of the etch solution and rinsed into the DI water. Then the stack sample is transferred into a bath of IPA to flush any remaining DI water away the surface of the material. In the following, the 2D flakes together with PMMA are attached onto the new substrate and lifted out of the solvent, followed by a thorough $N_2$ blow-drying until the residual solvent is evaporated as much as possible. The whole sample is then placed onto a cold hot-plate and heated up to 220 $^{o}$C at a rate of 20 $^{o}$C/min, baking for 5 min to evaporate any remaining solvent as well as to soften the PMMA carrier and strengthen the contact of flakes with the attached substrate. Finally, after being cooled, the whole sample is immersed into acetone to dissolve the PMMA carrier until only the 2D flakes left on the new substrate.

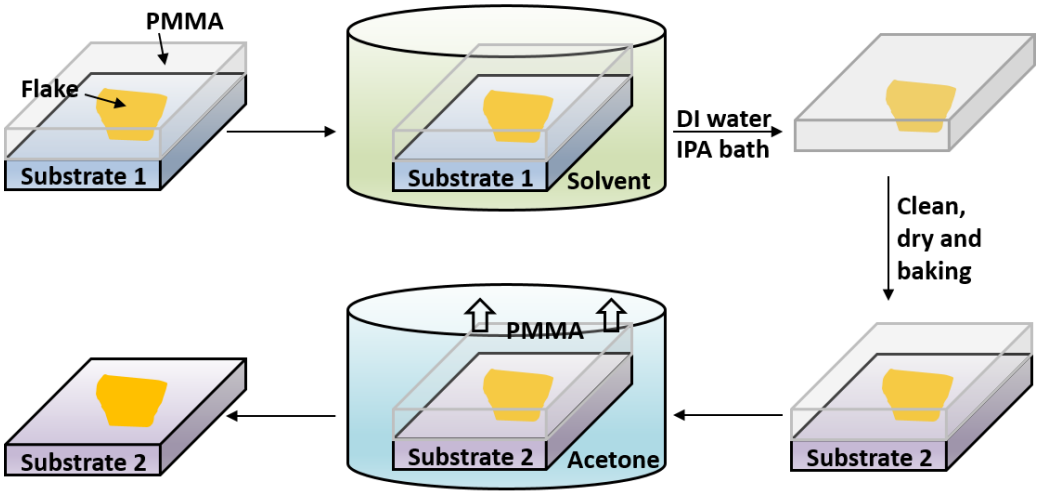


Figure 3.11. Schematic of wet-etching transfer process.

The dry transfer technique, or termed as mechanical layer assembly technique, hot pick-up technique, is a recently developed but the presently most effective method for transfer and layer assembly of various 2D flakes in terms of cleanliness, ease and reproducibility. This method makes use of the stronger vdW force interaction between 2D layered materials than that between the substrate and 2D flakes, getting the flakes prefer to stick to each other rather than the substrate during the contact and lift up process, therefore can transfer or produce heterostructures with clean interfaces, precisely aligned and undamaged 2D flakes. The concrete steps of this technique are detailed explained in the following, as depicted in Figure 3.12[263]:

(1) Fabricating a transparent polymer stamp block which serves as a substrate for the flakes and a handle carrier during the transfer process. This stamp consists of a thin poly dimethyl siloxane (PDMS) film firmly attached onto a microscope glass slide, followed by a thin (~1 μm) layer of poly-propylene carbonate (PPC) placed on top which can well adhere to the PDMS. The first layer 2D flake can be either exfoliated cleanly using a PDMS sheet to directly attach onto the top of the PPC, or picked up from a substrate.

(2) The glass slide and polymer stamp block are then together positioned in *x*, *y* and *z* directions, and adjusted using a micromanipulator with the stamp facing down. The micromanipulator is fixed on a motor-controlled chuck stage, while the target structure on the substrate or target flake supported by the substrate is fixed on a heating module which is amounted on the same motorized chuck stage. Notably, the heating module can be heated up or cooled down by a temperature-controlled heater.

(3) With the help of different lens (with a magnitude of 5×, 20×, 50×) and camera, the target flake (structure) and polymer stamp block are then accurately aligned on top of each other and brought into contact under a microscopy. For method of picking up flakes using PDMS/PPC polymer block from the substrate, firstly, the heating module is heated up to 35 $^{o}$C and cooled back to room temperature after some minutes dwelling, then the polymer block is slowly lifted up from the substrate. Normally, the flake prefers to be adhered to the stamp and be picked up after several repeats. The following flakes can be aligned or assembled to the previous flake and picked up using the same process. However, to enhance the time efficiency, it is more preferable to exfoliate the first flake directly onto the PDMS/PPC polymer block.

(4) Once the desired heterostructure is assembled or the desired flake is aligned with the target substrate structure, the stamp is then attached onto the final substrate by heating the module stage to 90 $^{o}$C. At this temperature, the PPC softens and prefers to adhere to the substrate together with the flakes, which allows the PDMS and glass slide being separated during the lifted up process. The PPC film can finally be removed by rinsing the transferred samples into acetone and IPA, leaving the target flakes on the substrate.

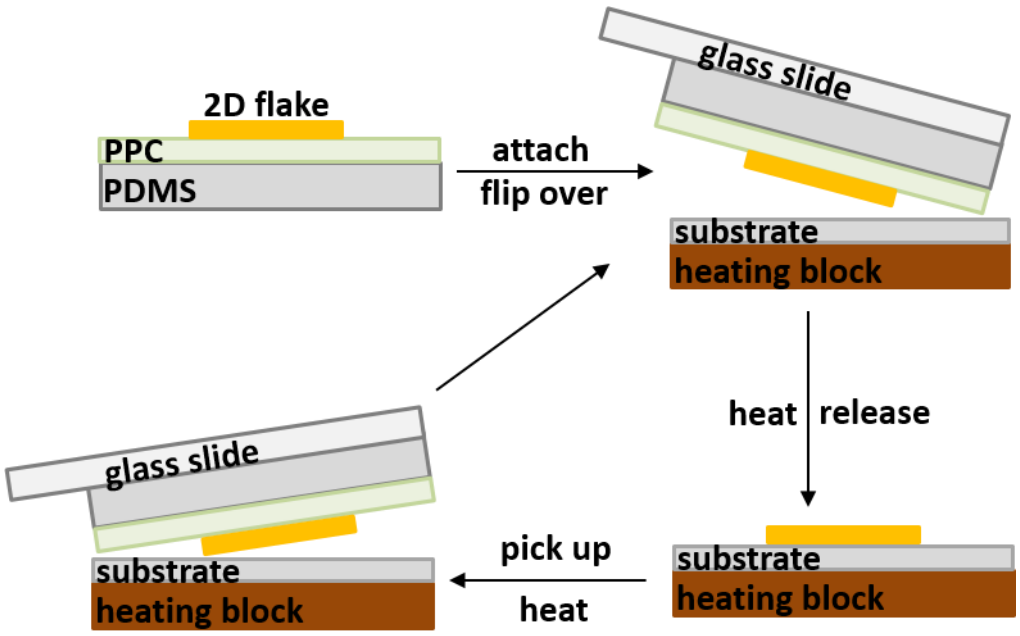


Figure 3.12. Schematic of dry transfer process.

## 3.6 Atomic force microscopy

### 3.6.1 Principles of atomic force microscopy

Atomic force microscopy (AFM), developed by Binnig, Quate and Gerber in 1986, aims to obtain the surface structure or morphology of samples by measuring the mapping of certain force through a sharp tip moving on top of the samples, either in ways of grating-scan or line-scan, this technique can even achieve an atomic scale resolution. AFM is evolved from the scanning tunneling microscopy (STM) but the main difference lies in that the sharp tip of AFM is fixed on one end of the cantilever which has an ultra-small elastic coefficient. The backside of cantilever at the tip side is fabricated into an optical mirror which can efficiently reflect the detected laser beam for the further collection by a photon sensitive photodetector. The principle of AFM is to probe the force between the sharp tip and the sample surface. The elaborated measurement of force is to accurately digitalize the deflection of cantilever, which is described by the *Hooke's Law* as following:

$$\Delta z = \frac{\Delta F}{c}, \tag{3.13}$$

where $c$ is the elastic coefficient of cantilever, and the deflection of cantilever, $\Delta z$, is determined by the change of force, $\Delta F$. Based on Equation (3.13), the smaller the $c$, the higher the sensitivity in force. Notably, the resonant frequency of the cantilever is:

$$\omega_0 = \sqrt{c/m}. \tag{3.14}$$

To minimize the environment disturbance, higher resonant frequency is expected, thus smaller mass and larger elastic coefficient are required for the cantilever. This conflicts with the requirement of sensitivity in force. Furthermore, the sensitivity in force measurement is also limited by the thermal excitation of cantilever, whose displacement can be expressed as:

$$(\Delta z)_{rms} = \sqrt{kT/c}. \tag{3.15}$$

In which, $(\Delta z)_{rms}$ is the tip side amplitude of cantilever due to thermal excitation. When the gradient in force is equivalent to the elastic coefficient of cantilever, the position of the tip will become instable and result in contact bounce. Therefore, to enable the tip approaching enough to the sample surface without contact bounce, there is a limit in minimum $c$: it should be able to match the atomic coupling strength within the solids. The typical $c$ for commercial cantilever made from Si, $SiO_2$, $Si_3N_4$ is within the range of $10^{-2}$ N/m $\leq c \leq 10^2$ N/m, and its typical resonant frequency is 10 kHz $\leq \omega_0 \leq$ 500 kHz, while the tip radius is normally around 10 nm.

The deflection level of cantilever under the function of force can be detected from the relative displacement of the laser beam reflected from the backside of cantilever. This reflected laser beam can be detected by position sensitive photodetectors (PSPD) which are located at the four quadrants as shown in Figure 3.13. Then the deflection of cantilever can be derived from the total photocurrent obtained from each quadrant. If the reflected laser beam moves vertically, the difference of photocurrent in vertical direction can be written as:

$$\Delta I_V = (\Delta I_A + \Delta I_B) - (\Delta I_C + \Delta I_D), \tag{3.16}$$

where $\Delta I_A, \Delta I_B, \Delta I_C, \Delta I_D$is the detected photocurrent in the A, B, C, D quadrant, respectively. The relative deflection of laser beam, $\Delta y$, which is calculated from $\Delta I_V$, can be correlated to the vertical displacement of tip:

$$\Delta y = \frac{d}{l}\Delta z, \tag{3.17}$$

where $l$ is the length of the cantilever, $d$ is the reflected optical path from cantilever to the photodetector. The generated photocurrent is corresponded to the energy density of laser ($J$) irradiated on the photodiode, and has the following relationship:

$$\Delta I_V \propto \Delta y d J, \tag{3.18}$$

$$J \propto 1/d^2. \tag{3.19}$$

Combing Equations (3.18) and (3.19), it shows that $\Delta I_V$ is independent on $d$, this is valid especially when the deflection is negligible in compare to the beam diameter. While for larger deflection, nonlinear behavior is shown between $\Delta I_V$ and $\Delta y$. Also, this independent relationship on $d$ can make the detector structure designed to be more compacted. It should be noted that the twisting of cantilever can also introduce fluctuation on tip, which results in the laser spot moving horizontally on the detector, thus the corresponding photocurrent difference in horizontal direction can be expressed as:

$$\Delta I_H = (\Delta I_B + \Delta I_D) - (\Delta I_A + \Delta I_C). \tag{3.20}$$

However, this horizontal force from the tip is normally unexpected as it will affect the imaging quality by introducing complex behaviors on the tip.

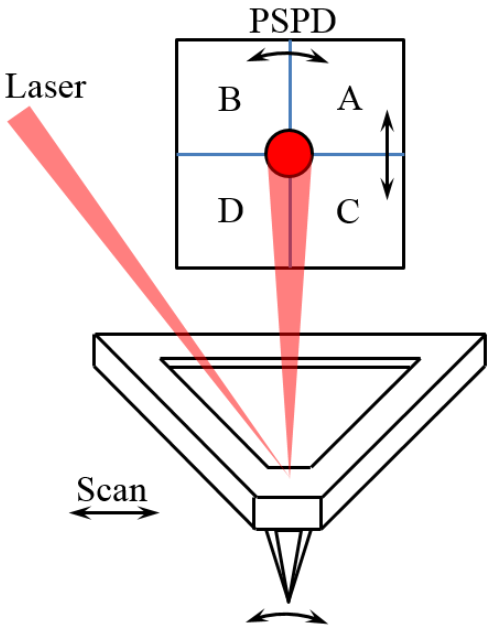


Figure 3.13. Schematic of laser beam deflection for simultaneous detection of forces along horizontal and vertical directions. PSPD is the abbreviation of position sensitive photodetectors.

### 3.6.2 Atomic force microscopy techniques

As a kind of scanning probe microscopy (SPM), AFM has a nanometer scale resolution. The high spatial resolution of AFM enables to visualize the nanoscale structures. In the study of 2D layered materials, AFM is mainly used for imaging the surface topography, measuring the thickness profile, and investigating the mechanical properties. The basic principle of AFM is to probe the force between the sharp tip of a cantilever and the sample surface. When the tip is tapping into the proximity of the surface of a sample, a force (mechanical contact, van der Waals, electrostatic, magnetic, chemical bonding, etc.) between the tip and the sample deflects the cantilever and its movement will be recorded by the detector (see the schematic in Figure 3.14). Piezoelectric elements are normally used to facilitate tiny but accurate movements upon electrical control which enable precise scanning. The cantilever is normally made of silicon nitride or silicon with its tip radius of curvature can be on the scale of only several nanometres. For imaging purpose, AFM is usually operated under three modes: contact mode (also known as static mode, while the other two modes are dynamic), tapping mode and non-contact mode. In the contact mode, the tip is in contact with and dragged across the sample surface, then the surface contours can be measured through the deflection of the cantilever or feedback signal. However, due to a strong lateral force applied onto the surface, the contact mode can cause surface damage or removal of loosely attached objects on the surface, or even the tip being snapped into the surface. To overcome this major problem,

the tapping mode (which is also called intermittent/dynamic contact mode, or AC mode) can be operated at where the probe tip is kept as close as possible to the sample surface until it can detect the short-range forces. In the tapping mode, the cantilever is slightly lifted up from the sample surface and driven to be able to oscillate vertically (i.e. up and down), at or near its resonant frequency with a constant amplitude and frequency. This oscillation is normally achieved through a small piezoelectric element in the cantilever holder, and its amplitude usually varies from several nm to 200 nm. When the tip is brought close to the sample surface, the interaction of forces between the tip and surface changes the amplitude of the cantilever's oscillation. This change in the amplitude of oscillation is then used as a parameter to adjust the height of cantilever above the sample to maintain it as constant during the tip being scanned over the near surface of the sample. Therefore an AFM image from a tapping mode is produced through the force detection and imaging of the intermittent contacts with minimized damage introduced during scanning, enabling the tapping mode a reliable method for comparison of surface topography before and after the sample treatment. The phase of the cantilever's oscillation relative to the driving signal can also be recorded simultaneously under the tapping mode operation, which reflects the energy dissipation of cantilever in each oscillation cycle. This can create a contrast between the regions with different stiffness or adhesion properties. In non-contact mode, the tip does not contact the surface of samples, instead, oscillating at either the resonant frequency (frequency modulation) of the cantilever or just above (amplitude modulation), with a typical amplitude of a few nanometers down to a few picometers. The resonant frequency of cantilever is mainly decreased by long-range forces, and is recorded through combined feedback loop system which can adjust the average tip-to-sample distance to enable a constant oscillation amplitude or frequency being maintained. A topographic image of the sample surface then can be constructed through the tip-to-sample distance which is measured at each scanning data point. Non-contact mode has an advantage of free from tip or sample degradation, even after numerous scans.

The thickness profile and concrete value of a sample can be extracted from the topography image when a substrate or a contrast is also scanned during measurements. Besides imaging, the AFM system is also capable of many other characterizations, such as conductive AFM (cAFM) for electrical properties, and Kelvin probe force microscopy (KPFM) for surface potential and work function measurements, photoconductive AFM, frictional force mapping, etc.

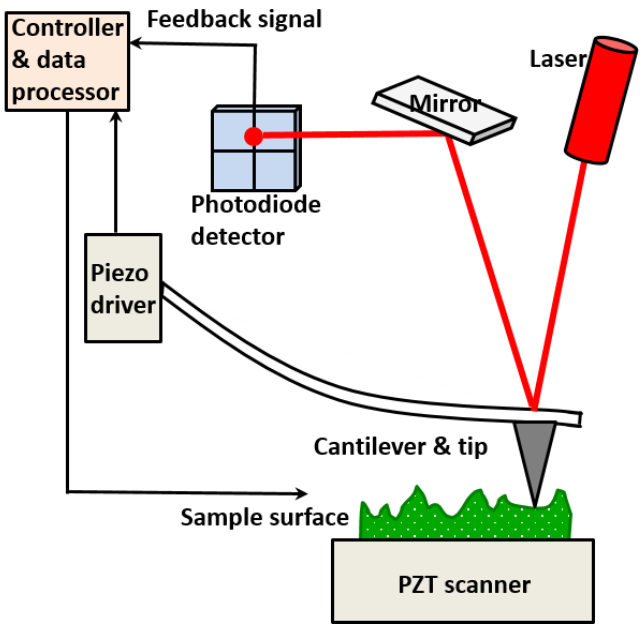


Figure 3.14. Schematic of working principle of the atomic force microscope.

# Chapter 4.

## Thermal Optimization of Barrier Layer at Diamond/GaN Interfaces for Enhanced GaN-on-Diamond Device Cooling

GaN-on-diamond device cooling can be enhanced by reducing the effective thermal boundary resistance ($TBR_{eff}$) at the GaN/diamond interface. In this chapter, the thermal properties of this interface and of the polycrystalline diamond grown onto GaN using SiN and AlN barrier layers, as well as without any barrier layer under different growth conditions are investigated and systematically compared. $TBR_{eff}$ values are correlated with transmission electron microscopy analysis, showing that a lowest reported $TBR_{eff}$ (~6.5 $m^2K/GW$) is obtained by using ultrathin SiN barrier layers with a smooth interface formed, while direct growth of diamond onto GaN results in one to two orders of magnitude higher $TBR_{eff}$ due to the formation of a rough interface. AlN barrier layers can produce a $TBR_{eff}$ as low as SiN barrier layers in some cases; however its $TBR_{eff}$ is rather dependent on the diamond growth conditions. We also observe a decreasing diamond thermal resistance with increasing growth temperature. This chapter has significant content reproduced from my published work as a first author (published in ACS Applied Materials & Interfaces 9(39), 34416-34422),[29] with permission from ACS ©2017. Some additions have been made. Reproduced figures have been indicated.

### 4.1 Introduction

A barrier layer is often used to protect the GaN epilayer from the harsh diamond growth environment and uniformly deposit the diamond seeds, however, it also introduces a significant $TBR_{eff}$ that acts as a heat transfer barrier. The $TBR_{eff}$ between diamond and GaN ($TBR_{eff, Dia/GaN}$) can be reduced by minimizing the thickness of the dielectric barrier layer and phonon mismatch, without lowering the quality of the subsequent diamond growth.[27,28,112] The theoretical minimum $TBR_{eff}$ (predicted by DMM model which was detailed introduced in Section 2.2.6) may be achievable without any barrier layer at the GaN/diamond interface,

however direct seeding of diamond onto GaN without degrading the GaN is very challenging. The current GaN-on-diamond uses SiN as the barrier layer material but it is amorphous and has a very low thermal conductivity[28]. Other materials which may also work such as $Al_{0.5}Ga_{0.5}N$/AlN,[112] AlN,[264] graphene,[265] have once been explored as barrier layer but the thermal properties have not been seriously or experimentally studied; also an unambiguous conclusion has not been made as to which results in the lowest thermal resistance for GaN-on-diamond. In this work, we study the $TBR_{eff}$ at the GaN/diamond interface and the thermal conductivity of diamond by growing polycrystalline diamond onto GaN using various barrier layers under different growth temperatures and recipes. Nanosecond time-domain thermoreflectance (TDTR) is used to characterize the thermal properties of these samples, which is correlated with TEM cross-sectional microstructural analysis, providing insight into how the thermal resistance of GaN-on-diamond devices may be minimized and a guideline for choosing the barrier material for GaN-on-diamond wafer manufacturers.

## 4.2 Experimental Details

### 4.2.1 Sample fabrication and polycrystalline diamond growth method

A 500 nm-thick GaN layer grown on a SiC substrate was used as the starting material. To study how the barrier layer influences the thermal properties of GaN-on-diamond, a well-controlled 5 nm-thick barrier layer of amorphous SiN or AlN was then grown onto the GaN, followed by the seeding and growth of a ~1 μm-thick polycrystalline diamond layer using microwave plasma CVD. The diamond was also directly seeded and deposited onto the GaN without any barrier layer. Here the diamond is grown on the N-polar GaN surface,[81,266] whereas most GaN-on-diamond integration uses the Ga-polar surface,[27,28,267] although for the samples with barrier layer this should not make any difference. The diamond seeding was completed with a nucleation layer created using a process that pretreats the surface before the diamond deposition. The initial microwave plasma-assisted CVD diamond growth conditions create a uniform, high nucleation density diamond layer with minimal voids between the barrier layer and initial diamond growth. Different methane concentrations in the feed gas from 0.1% to 1% of the total gas flow, which included hydrogen and argon, were controlled. A one color optical pyrometer set with an emissivity of 0.6 was used to monitor the substrate temperature. The microwave input power was adjusted in range of 2000-2500 W to reach the desired temperature. (The detailed growth method of diamond are introduced in Section 2.2.5) All the samples are provided by Qorvo Company. Figure 4.1 shows the surface morphology of the diamond films (selected from controlled samples grown under similar conditions) imaged by Scanning Electron Microscopy (SEM, taken by Dr. Xin Gu *et al.*, at Qorvo Company). All samples present columnar-like grain morphology with similar grain size, indicating negligible effect on diamond growth from the exploited different barrier layers. In

further, cross-sectional TEM analysis of the GaN-on-diamond interface region was performed (by Dr. Gu *et al.*, at Qorvo Company) to evaluate the influence of different barrier layers on the interfacial microstructure.

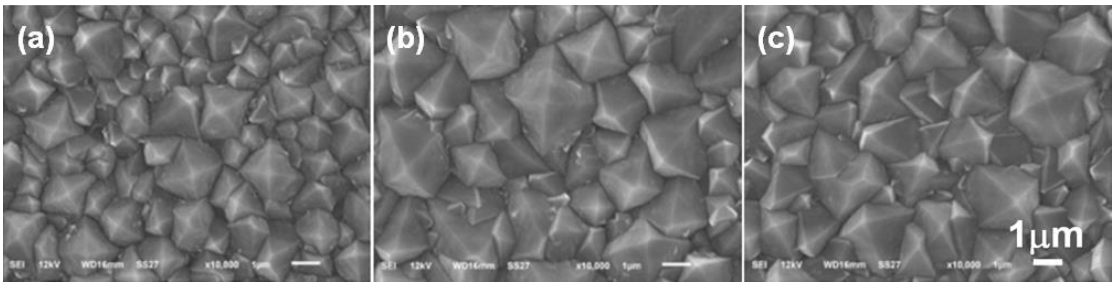


Figure 4.1. SEM micrographs on the diamond film surfaces for samples with (a) SiN, (b) AlN, (c) no barrier layer grown between GaN and diamond. Growth conditions: 1% $CH_4/(H_2–Ar)$ for gas recipe, 750-780 °C for growth temperature. The extracted diamond thermal conductivities were 130±50, 160±90 and 375±190 W/mK, respectively. Experiments were performed by Dr. Gu *et al.*, at Qorvo.

### 4.2.2 Time-domain thermoreflectance characterization and Monte-Carlo analytical heat transport model simulation

To assess the thermal properties of the resulting material, a 20 nm-thick Ti adhesion layer was deposited onto the diamond, followed by a 100 nm-thick Au film transducer layer, which was used for the nanosecond TDTR measurements. The pump-probe TDTR measurements used a heating pump beam with an 8 ns pulse duration, 355 nm wavelength (frequency-tripled Nd: YAG laser); the probe beam was continuous wave (CW) with a 532 nm wavelength (frequency-doubled Nd: YAG laser). The pump and probe beam diameter at the sample surface were ~70 μm and ~2 μm, respectively. The probe beam was used to measure the reflectivity change of the gold transducer induced by the pump beam, which is proportional to the transient temperature rise. The sample structure and the thermoreflectance measurement scheme are illustrated in Figure 4.2. More details of the technique and the experimental setup[28,242,267] is given in Section 2.4.2 and Section 3.2, and details of the analytical Monte-Carlo heat transport model that used to extract each layer thermal parameters were introduced in Section 3.2.2.

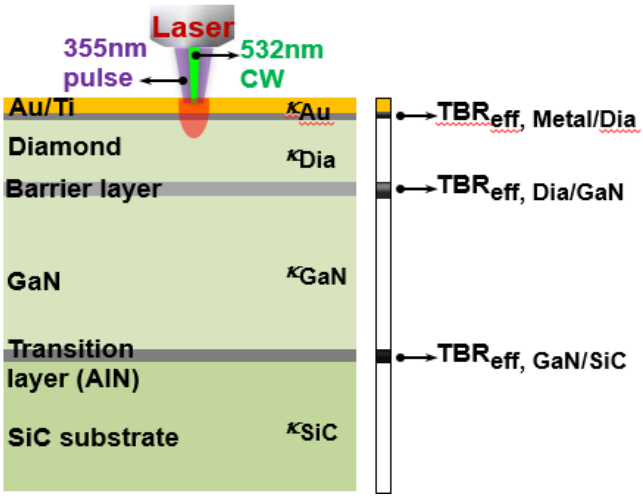


Figure 4.2. Sample structure and thermoreflectance measurement scheme. ©2017 ACS

## 4.3 Results and Discussion

### 4.3.1 Time-domain thermoreflectance characterization and sensitivity analysis

Figure 4.3 shows normalized thermoreflectance transients of three selected samples deposited under identical diamond growth conditions but with different barrier layers, measured at room temperature. These transients illustrate that there are significant differences in the thermal properties of each structure. Heat diffusion through each layer influences the recorded reflectivity change (surface temperature) over a range of different time scales.

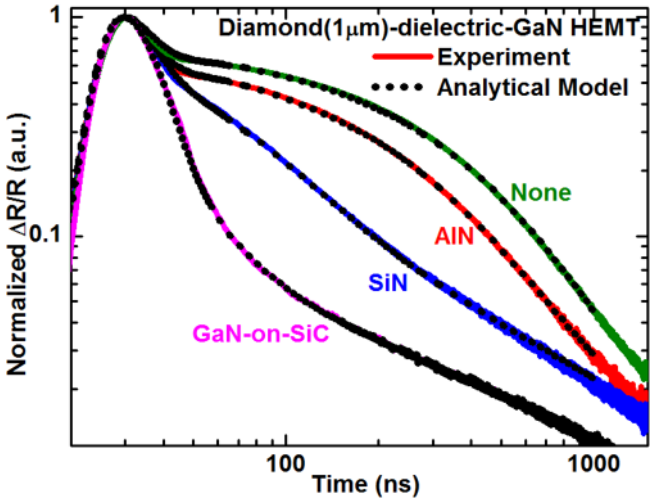


Figure 4.3. Normalized thermoreflectance signal as a function of time of GaN-on-diamond samples for different barrier layers of SiN, AlN and no barrier layer between diamond and GaN, as well as of Au-GaN-on-SiC sample on logarithmic scale; lines represent experimental value and dots represent an analytical model fitted to the experimental values. ©2017 ACS

When considering a small change, for example, of ±10% in each layer thermal conductivity or $TBR_{eff}$ of a typical sample shown in Figure 4.4(a) and (b), one can see how to decouple the different contributions to the reflectivity transients. For simplicity, the Ti layer was lumped into a single thermal boundary resistance between the gold transducer and diamond ($TBR_{eff,\ Metal/Dia}$), while the barrier layer was lumped into $TBR_{eff,Dia/GaN}$; the $TBR_{eff}$ between GaN and SiC ($TBR_{eff,\ GaN/SiC}$) was also considered. As apparent in Figure 4.4(b), the measurements are most sensitive to $TBR_{eff,Metal/Dia}$ in 0-200 ns time window, and $TBR_{eff,Dia/GaN}$ in 20-200 ns after the heating pulse; $TBR_{eff,GaN/SiC}$ mostly impacts the response in the 70-200 ns time window, while the thermal conductivity of diamond $\kappa_{Dia}$ mainly for 0-20 ns (as is compared more obviously in Figure 4.4(a)), and the SiC substrate $\kappa_{SiC}$ for >200 ns. We note the GaN/SiC interface impacts the thermal behavior >70 ns after the laser pulse; a reference thermoreflectance spectrum of the GaN-on-SiC starting material (without diamond deposition) using the same transducer as aforementioned was also measured, shown in Figure 4.3. This is needed as each GaN-on-SiC structure can have differences in $TBR_{eff}$ due to microstructural differences as discussed in Ref..[26]

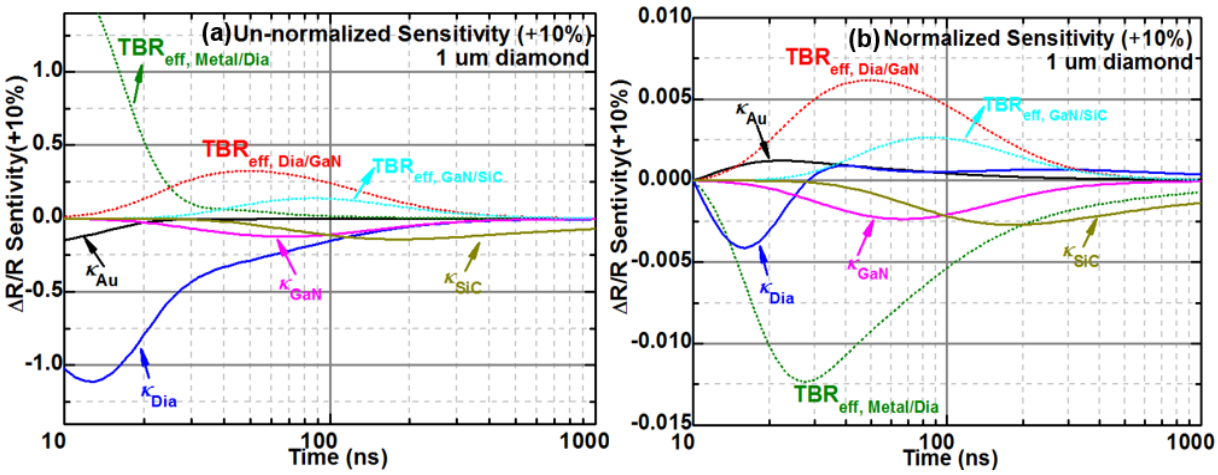


Figure 4.4. (a) Un-normalized and (b) normalized sensitivity curves for the GaN-SiN-diamond samples, with the sensitivity of ΔR/R corresponding to ±10% change in each input parameter in the model (the laser heating pulse stop at 10 ns). ©2017 ACS

### 4.3.2 Thermal parameter extraction and summarization

The thermoreflectance data were then fitted using the analytical Monte-Carlo heat transport model to extract the thermal parameters of each layer, and the values extracted for the GaN-on-SiC starting material are given in Table 4.1. These parameters are consistent with what has been reported in the literature for similar structures (see Table 4.2) and were used as fixed input parameters when fitting the thermal transients obtained on the GaN-on-diamond structures. We note the GaN thermal conductivity measured here is lower than we have previously reported for thicker GaN layers;[268] this is consistent with recently reported values

with similar GaN thickness (~500 nm)[269-271] and is attributed to a reduction of the phonon mean free path (or the strong confinement of phonon mean free path by the ultrathin thickness). Other fixed inputs into the thermal model of GaN-on-diamond structures are summarized in Table 4.2. The remaining parameters, i.e. $TBR_{eff,Dia/GaN}$, $\kappa_{Dia}$ and $TBR_{eff,Metal/Dia}$ are treated as variables adjusted to best fit the experimental data (Figure 4.3) using the previously described methodology.

Table 4.1. Extracted thermal parameters of GaN-on-SiC using the typical AlN nucleation layer. ©2017 ACS

| **Fitting results** | **Thermal conductivity (W/mK)** | | **$TBR_{eff}$ ($m^2K/GW$)** | |
|---|---|---|---|---|
| **Parameters** | **GaN** | **SiC** | **Metal/GaN** | **GaN/SiC** |
| **Value** | 129±33 | 460±52 | 14±6 | 3.5±1.5 |

Table 4.2. Fixed input parameters for different materials in the GaN-on-Diamond samples. ©2017 ACS

| **Layer** | **Au** | **Diamond** | **GaN** | **SiC** |
|---|---|---|---|---|
| **Thickness (nm)** | 120 | 1000 | 500 | 500000 |
| **Thermal conductivity ($W\ m^{-1}\ K^{-1}$)** | 200[a] | Fitted | 130[b] | 460[c] |
| **Specific heat ($J\ Kg^{-1}\ K^{-1}$)** | 129[d] | 500[e] | 430[f] | 690[g] |
| **Density ($Kg\ m^{-3}$)** | 19800 | 3510 | 6150 | 2320 |

(a is consistent with literature values from reference[99], while b,[57,269-271] c,[272] d,[273] e[274,275], f,[52] g[276])

### 4.3.3 Effect of barrier layer material on the $TBR_{eff,Dia/GaN}$ and its variation

Figure 4.5(a) shows the extracted $TBR_{eff,Dia/GaN}$ for different barrier layers under various diamond growth temperatures. The SiN barrier layer resulted in the lowest $TBR_{eff,Dia/GaN}$ for all the growth temperatures investigated. In contrast, direct growth of diamond onto GaN without a barrier layer resulted in one to two orders of magnitude higher $TBR_{eff,Dia/GaN}$ than using a SiN barrier layer (see Figure 4.5(b)). For the AlN barrier layer, $TBR_{eff,Dia/GaN}$ can be as low as some values for the SiN barrier layer, although it varied over one order of magnitude over the studied growth parameters. Furthermore, we found larger $TBR_{eff,Dia/GaN}$ variations

across the wafers for AlN barrier layers (up to two orders of magnitude; Figure 4.5(c)). Variations of a similar magnitude were observed across the wafer for without barrier layer samples. GaN-on-diamond with SiN barrier layers did not exhibit any large $TBR_{eff,Dia/GaN}$ variation across the wafer. As displayed in Figure 4.5(d), these $TBR_{eff,Dia/GaN}$ variations can also be directly reflected from their measured thermoreflectance transients. As summarized in Figure 4.5(b) (statistical results for all samples grown under different parameters for different barrier layers), an average state-of-the-art lower $TBR_{eff,Dia/GaN}$ value of ~6.5 $m^2K/GW$ is achieved by using the 5 nm ultrathin SiN barrier layer; this is close to the calculated lower limit of 5.5 $m^2K/GW$, which includes contribution of the diffuse mismatch model (DMM) theory predicted boundary thermal resistance and SiN layer thermal conductivity.[28,270,277,278] For comparison, the lowest achievable $TBR_{eff,Dia/GaN}$ is ~3 $m^2K/GW$, considering the mismatch of phonon parameters only between GaN and diamond.[121] According to Sun *et al.*[28], this low $TBR_{eff,Dia/GaN}$ value will enable ~45% reduction in device peak temperature with respect to GaN-on-SiC.

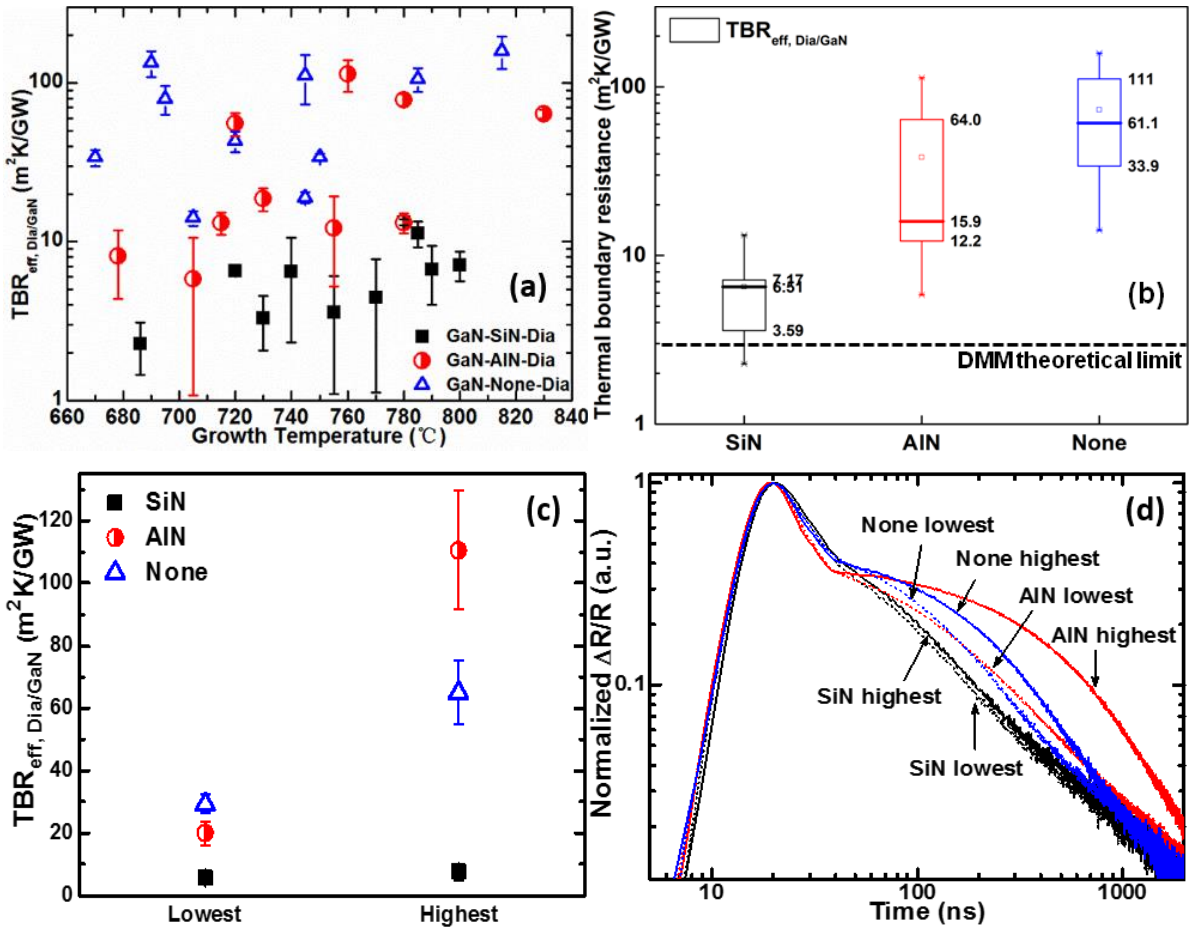


Figure 4.5. (a) $TBR_{eff,\ Dia/GaN}$ for different barrier layers between diamond and GaN under various diamond growth temperatures. Different error bars sizes are due to variation in the

signal/noise of the recorded TTR traces. (b) Average $TBR_{eff,\ Dia/GaN}$ (for all growth parameters) with its variation for different barrier layers. The maximum value, minimum value, median value, and mean are indicated in the box chart. Errors were extracted using a statistic method with the lower limit (upper limit) determined by the 25th (75th) percentiles of the corresponding average values of each whole set samples for different barrier layers. The dotted line is the DMM theory predicted value. (c) $TBR_{eff,\ Dia/GaN}$ variation and (d) thermoreflectance transients variation across 2×2000 $\mu m^2$ area for samples with SiN, AlN and no barrier layer, for growth conditions of 1% $CH_4/(H_2–Ar)$ gas recipe, 755 °C for SiN, 730 °C for AlN, 720 °C for no barrier layer. Figures (a), (b) and (c) ©2017 ACS

### 4.3.4 Effect of polycrystalline diamond growth temperature and growth recipe on the $TBR_{eff,Dia/GaN}$

Figure 4.6 displays the dependence of $TBR_{eff,Dia/GaN}$ as a function of growth temperature for different diamond growth recipes. As shown in Figure 4.6(a) and consistent with the earlier results, using the SiN barrier layer, $TBR_{eff,Dia/GaN}$ is lower and not that dependent on the diamond growth temperature, but no clear trend as a function of growth recipe could be identified. The extracted average $TBR_{eff}$ value is consistent with the reported thermal conductivity of SiN thin films of ~1 W/mK (dashed line in Figure 4.6(a)),[270,277,278] considering its 5 nm thickness. In Figure 4.6(b) and Figure 4.6(c), $TBR_{eff,Dia/GaN}$ for samples using the AlN barrier layers and grown without barrier layer are displayed, all showing relatively higher $TBR_{eff}$ values and larger $TBR_{eff}$ variation than using the SiN barrier layer; no clear correlation with the diamond growth temperatures and recipes could again be observed. We note AlN has a similar thermal conductivity as SiN for ultrathin films, for amorphous material.[279,280]

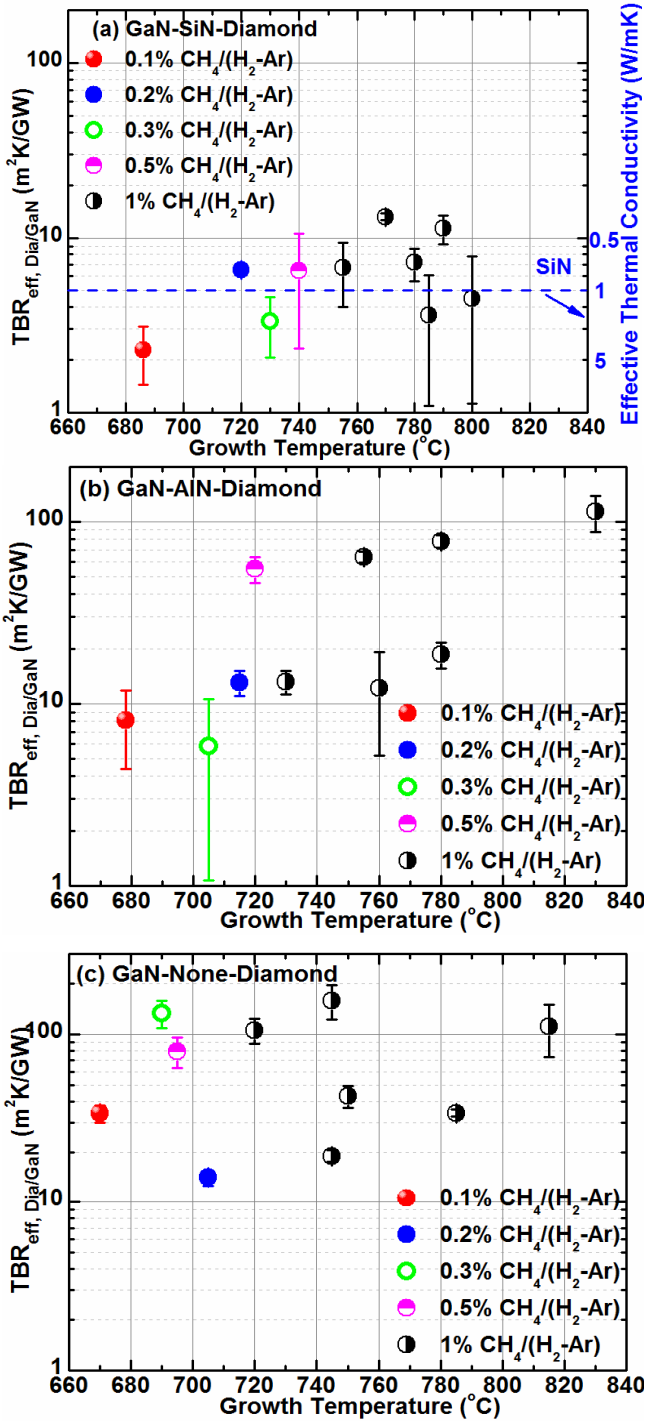


Figure 4.6. Effective thermal boundary resistance between diamond and GaN ($TBR_{eff,Dia/GaN}$) of (a) GaN-SiN-diamond samples as a function of growth temperature for different growth recipes on a logarithmic scale, (b) for GaN-AlN-diamond samples, (c) for GaN-on-diamond samples without barrier layer. ©2017 ACS

### 4.3.5 Effect of interfacial microstructure on the $TBR_{eff,Dia/GaN}$

Cross-sectional TEM micrographs of the GaN/diamond interfacial region, shown in Figure 4.7, were used to investigate the microstructural reasons for the differences in $TBR_{eff,Dia/GaN}$ values observed for each barrier layer. For the GaN-SiN-diamond samples, smooth diamond/SiN and SiN/GaN interfaces are apparent (see Figure 4.7(a) and (d)). This is consistent with a low value for the $TBR_{eff,Dia/GaN}$, i.e. good interfacial thermal transport due to low phonon scattering rates.[132,281] In the TEM micrograph an estimated thickness of the diamond nucleation layer of ~10 nm is apparent. The nucleation layer in general includes a higher density of different orientation nano-crystalline diamond grains, grain boundaries, impurities and defects, thus enhancing the phonon scattering resulting in a higher local thermal resistance. Sun *et al.*[28] illustrated that a lower $TBR_{eff,Dia/GaN}$ can be achieved by having a thinner nucleation layer.

For AlN barrier layers, a rougher interface with a step-shape microstructure is formed, as illustrated in Figure 4.7(b). While in certain parts marked as region A smooth diamond/AlN and AlN/GaN interfaces exist, in other parts marked as region B rougher interfaces are apparent. Consequently, in region B, ~60 nm of GaN has been etched away due lack of protection from the harsh diamond growth environment during the diamond growth. The thickness of the diamond nucleation layer in region A is similar to that of the samples made with SiN barrier layers, however, in region B, it is much thicker (~50 nm). It is possible for the regions without AlN layer, some of the nucleation sites are lost during the initial stage of the diamond CVD process growth initialization, reducing the nucleation density, causing a thicker nucleation region. Both the rougher interface and the thicker diamond nucleation layer in region B are responsible for the higher $TBR_{eff}$ than for those samples grown with SiN barrier layer. The large variations in $TBR_{eff}$ across the wafer for those samples (as displayed in Figure 4.5(c)) may also be related to these microstructural interfacial variations (see Figure 4.7(e)). Therefore, optimization of the AlN layer to form a continuous barrier layer may provide an alternative to using SiN barrier layers for GaN-on-diamond samples. We note that the TTR measurement is an average over the probe laser spot area (~2 μm in diameter), which may account for the variability in values measured for the samples with non-uniform AlN barrier layers.

The TEM micrograph of diamond directly seeded onto GaN in Figure 4.7(c) and (f) shows a rough interface formed between GaN and diamond, and there is almost no obvious diamond nucleation layer at the interface. This explains the significantly higher $TBR_{eff,Dia/GaN}$ observed for this case. A seeding density of greater than $10^{10}$ $cm^{-2}$ was used with diamond nanocrystals of 5 nm in size which may not form a continuous layer that fully protects the GaN surface from the plasma. This is in contrast to the SiN and AlN barrier layer protecting

the GaN from the plasma. Future improvement in seeding and nucleation may enable smoother interfaces to be achieved.[282]

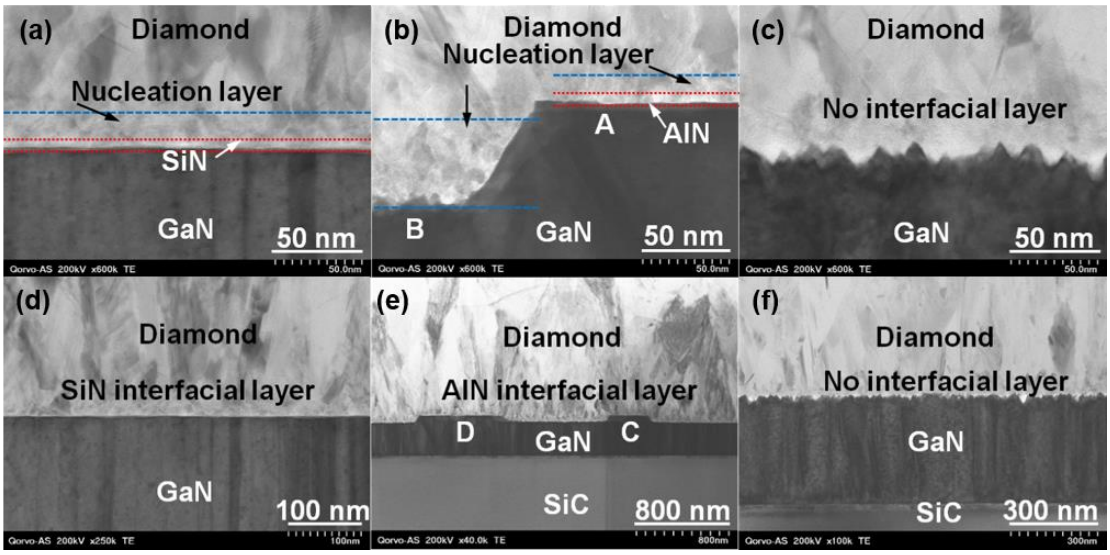


Figure 4.7. Transmission electron microscopy micrographs of cross-sections of GaN-on-diamond interfaces grown with different barrier layer of (a, d) SiN, (b, e) AlN (different areas A and B are marked) and (c, f) no barrier layer, displaying in different magnification. Growth conditions: 1% $CH_4$/ ($H_2$–Ar) gas recipe, 755 °C for SiN, 730 °C for AlN, 720 °C for no barrier layer. Experiments were performed by Dr. Gu *et al.*, at Qorvo. Figures (a), (b) and (c) ©2017 ACS

### 4.3.6 Effect of polycrystalline diamond growth temperature on the thermal conductivity of diamond

Apart from $TBR_{eff}$ at the interfaces, the diamond thermal conductivity of the initial diamond growth (beyond the very initial nucleation layer which is included here in $TBR_{eff}$) also influences the thermal transport in GaN-on-diamond.[25,102,283] As demonstrated in Figure 4.8, the thermal conductivity of the first micrometer of diamond is consistent with what has been reported by other researchers for columnar polycrystalline diamond films of similar thicknesses (~180-500 W/mK).[19,101,284,285] It should be noted that the measured $\kappa_{Dia}$ value represents a depth average in the cross-plane direction (through the layer). It is significantly lower than thermal conductivity of single-crystalline diamond due to phonon scattering at grain boundaries and point defects.[25] Above 750 °C, we find the diamond thermal conductivity to increase with growth temperature for the same growth recipe, regardless of the barrier layer material, while within 650-750 °C, the diamond thermal conductivity appears

almost independent of growth temperature for the temperature range studied. The lower temperature growth was also tried, however very poor thermal conductivity was obtained presently; this technology could be further improved and may be more advantageous for the GaN quality but was not a focus in this work. We note the measurement uncertainty increases when $\kappa_{Dia}$>300 W/mK because the transient is mainly affected by $\kappa_{Dia}$ in the 0-20 ns range where the measurement sensitivity is lower (see Figure 4.4(a). The thermal conductivity measured for the 750 °C sample is consistent with the trend seen by Anaya *et al.* who have reported that growth conditions can be used to tune the thermal conductivity of the initial diamond layer, showing that decreasing $CH_4/H_2$ gas ratio can increase diamond thermal conductivity.[19,25,286] Moreover, based on Sun *et al.*,[28] considering the same device structure as GaN-on-SiC and the present available average $TBR_{eff,Dia/GaN}$ value of ~20 $m^2K/GW$, diamond substrate with a thermal conductivity over ~500 W/mK would be commercially beneficial for GaN-on-diamond devices.

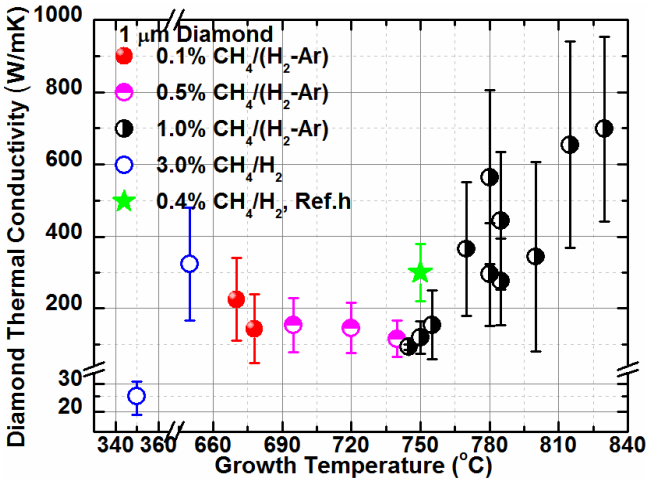


Figure 4.8. Effective thermal conductivity of the first micrometre of diamond as a function of growth temperature, for different growth recipes and different barrier layer materials. Data of Ref.h is taken from the work by Anaya *et al.*.[19] ©2017 ACS

## 4.4 Conclusions

Polycrystalline diamond films grown on GaN using SiN and AlN dielectric material as barrier layers as well as without barrier layer were studied and systematically compared for the first time to gain insight into their thermal properties via transient thermoreflectance complemented by TEM microstructural analysis. Results show that SiN barrier layers result in the lowest $TBR_{eff,\ Dia/GaN}$ for all of the growth temperatures studied. A state-of-the-art low value of ~6.5 $m^2K/GW$ was achieved by using a 5 nm ultrathin SiN barrier layer, forming smooth interfaces, making it a good candidate for the seeding and growth of diamond onto GaN. In contrast, direct seeding and growth of diamond onto GaN without barrier layer resulted in one to two orders of magnitude higher $TBR_{eff}$ than SiN due to rougher interfaces

formed. AlN might be an alternative to SiN as barrier material to achieve low $TBR_{eff}$ but it introduced a variation in interfacial roughness and therefore a larger $TBR_{eff}$ variation, which needs to be further optimized. The effective thermal conductivity of the first micrometer diamond increased with higher growth temperature.

# Chapter 5.

## Thermal Characterization of Polycrystalline Diamond Thin Film Heat Spreaders Grown on GaN HEMTs

In this chapter, polycrystalline diamond (PCD) grown onto high-k dielectric $Si_3N_4$ passivated AlGaN/GaN-on-Si HEMT structures (diamond-on-GaN HEMTs) was investigated, with diamond film thicknesses ranging from 155 to 1000 nm. Nanosecond TDTR characterization were combined with device thermal simulations to systematically investigate the heat spreading benefit of the diamond layer. The thermal properties of these samples were characterized over the temperature range from 25 to 225 °C. This information was then used in a finite-element model of a multi-finger AlGaN/GaN-on-Si HEMT device to evaluate the heat spreading benefit of integrating PCD in close proximity to the channel. This chapter has significant content reproduced from my published work as a first author (published in Applied Physics Letters 111(3), 041901),[37] with permission from AIP ©2017. Some additions have been made. Reproduced figures have been indicated.

### 5.1 Introduction

The high operating power density of AlGaN/GaN HEMTs, combined with localized near-junction self-heating, can cause a large temperature rise which must be minimized to avoid premature degradation.[10,15,287] Heat transport in the near-junction region of GaN HEMTs is particularly important and is influenced by the thermal conductivities of GaN, strain relief layer and substrate layers as well as the effective thermal boundary resistance ($TBR_{eff}$) between the epilayers and substrate and between the epilayers.[26,288] The heat extraction benefit of integrating high thermal conductivity diamond with GaN-based devices has recently been demonstrated, resulting in improved thermal management.[24] Bulk PCD grown by CVD not only can reach thermal conductivities almost as high as those of single-crystal diamond,[92] but has the advantage of larger wafer-size availability which is suitable for commercial semiconductor manufacturing. To maximize the benefit of diamond heat spreaders integrated with AlGaN/GaN HEMTs, PCD should be placed as close as possible to the Joule heating location, which is the 2DEG channel at the AlGaN/GaN interface, close to

gate foot on the drain side. PCD heat spreaders can be integrated in different areas of an AlGaN/GaN HEMT, including: a) Replacing the Si or SiC substrate by direct growth,[109] or wafer bonding;[110] b) growing PCD directly on top of the passivated HEMT channel.[289,290] For the first strategy, both the electrical[109,291] and thermal device characterization[27,28,267,292] have been studied extensively, with a potential three-fold increase in output power density reported.[27,28] For the second strategy, improved electrical performance and 20% lower device temperature have been shown for PCD-capped and gate-after-PCD HEMT devices.[34,293,294] However, the thermal resistance of PCD-on-HEMT structures has not been measured directly in previous work.[34,293,294]

## 5.2 Experimental details

### 5.2.1 Growth and fabrication of diamond-on-GaN HEMT samples

The AlGaN/GaN heterostructure studied here was grown by metal-organic chemical vapor deposition (MOCVD) on a Si(111) substrate, consisting of 20 nm-thick AlGaN on a 600 nm-thick GaN buffer layer and a strain-relief-layer (Figure 5.2(a)). The Si(111) substrate is widely used in the GaN-based electronics as it can provide compatible hexagonal atomic configuration to achieve good quality c-plane GaN growth by reducing the lattice mismatch herein the stress between GaN and Si, although Si(100) substrate is preferred in the Si-CMOS electronics. The AlGaN/GaN heterostructure was passivated using a 50 nm-thick layer of amorphous stoichiometric $Si_3N_4$, grown in-situ using MOCVD. After cleaning and a low-power (20 W) $O_2$-plasma treatment of the $Si_3N_4$ surface to ensure a uniform seeding of diamond nanoparticles (the growth method of PCD are detailed introduced in Section 2.2.5),[295] the seeded-passivated heterostructure substrate was then loaded onto a microwave-CVD reactor for the PCD growth at 650 °C, 20 Torr and a $CH_4/H_2$ gas flows of 485/15 sccm.[296] PCD layers were grown on a number of samples under the same step-by-step conditions to yield a thickness ranging from 155 to 1000 nm, followed by surface oxidation in $H_2SO_4$-$KNO_3$ solution to remove graphitic phases.

### 5.2.2 Thermal characterization and temperature-dependent measurement

A 30 nm-thick Cr adhesion layer and a 100 nm-thick Au film were then deposited onto the diamond as a transducer for the nanosecond TDTR measurements. The concrete procedure and setup details for nanosecond TDTR measurements are the same as previously detailed introduced in Section 3.2, which will not be described again here. The temperature dependent analysis of these samples was carried out by mounting these samples into a Linkam TS600 microscope chamber (the introduction and operation methods see details in Section 3.3) and heating the substrates from 25 to 225 °C, in a step of 50 °C. Notably, thermal conducting paste was used to help to improve the thermal transport from the heating stage to the Si

substrate of these samples, and water cooling system was applied to keep the heating at a more stable phase. During the measurements at each temperature, it was set to dwell at least 5 minutes until a stable temperature was achieved before performing the Raman measurements.

### 5.2.3 3D finite element thermal simulation

To investigate the impact of PCD heat spreaders on the actual thermal characteristics of devices, a 3D finite-element steady-state thermal model of a 16×125 μm-wide, 50 μm gate-pitch AlGaN/GaN-on-Si HEMT was constructed in ANSYS based on a layer structure described in section 5.2.1 (and shown in Figure 5.2(a)).[35] The power density was set at a typical value of 5 W/mm, dissipated in a 0.5 μm-long, 100 nm-thick volume at the drain edge of the gate foot where most Joule heating occurs.[297] Considering the reliability and the calculation efficiency, a mesh-independent solution (convergence of $<10^{-4}$) has been achieved before further thermal results being resolved, using an optimized mesh (~1.5 MDOFs, Solid90 elements) which can accurately capture the different features and scales of the simulation geometry. The schematic results of a 3D finite-element thermal mapping and the meshing details of the device profile are shown in Figure 5.1.

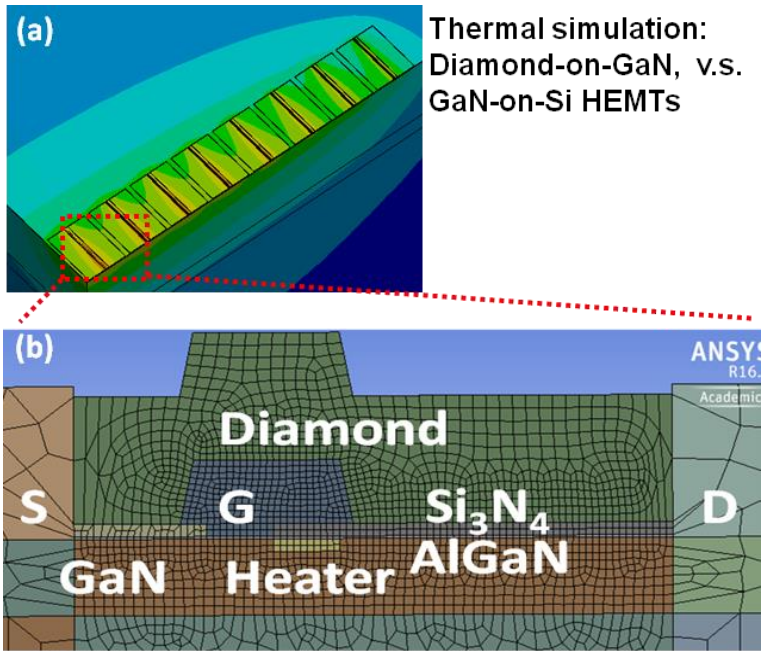


Figure 5.1. (a) 3D finite-element model of a 16 finger×125 μm-wide, 50 μm gate-pitch AlGaN/GaN-on-Si HEMT device, with diamond heat spreader on top of the $Si_3N_4$ passivation layer. (b) Meshing details of the device profile. (Not to scale.)

## 5.3 Characterization of diamond-on-GaN HEMT sample structure

Figure 5.2(a) shows the cross-sectional Transmission Electron Microscopy (TEM) image of the heterostructure after completion of the processing, recorded by Svetlana Korneychuk *et al*., at University of Antwerp. Sharp interfaces and no damage underlying device heterostructure are observed, even after the diamond growth. Figure 5.2(a) also illustrates the columnar outgrowth of diamond into micrograins. Figure 5.2(b) displays the different elements mapping taken by EDX on the same cross-section region as that measured in Figure 5.2(a), indicating the composition distribution of each layer, which was performed by Korneychuk *et al*., at University of Antwerp. This composition mapping also provides rough thickness information between different layers, and confirms the expected materials structure for here studied HEMT device.

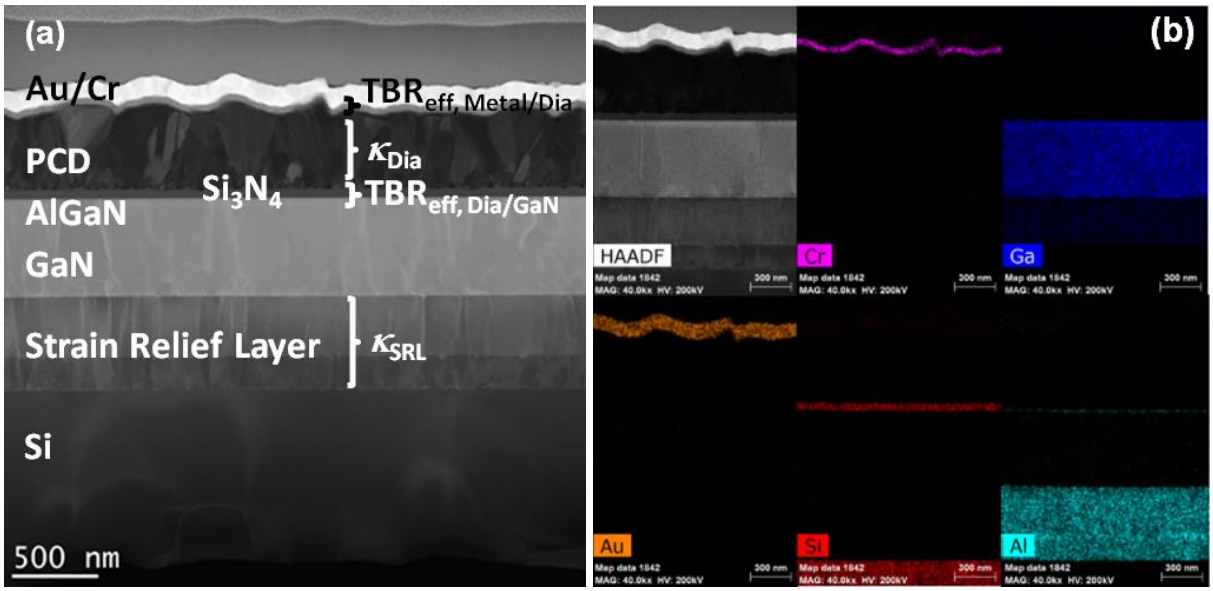


Figure 5.2. (a) TEM cross-section of the measured structure. ©2017 AIP. (b) EDS composition mapping on the same TEM cross-section of the measured structure, The scale bar is 500 nm for all. Experiments were performed by Korneychuk *et al*., at University of Antwerp.

Figure 5.3(a) shows the surface morphology (columnar-like grain) of the PCD films imaged by Scanning Electron Microscopy (SEM), which was performed by Rajesh Ramaneti *et al*., at University of Hasselt. The in-plane grain size on the top surface was determined using the three-circle procedure[298], as a sample shown in Figure 5.3(b), and with the results displayed in Figure 5.3(c). The observed in-plane grain size demonstrates an approximately linear correlation with the diamond film thickness.

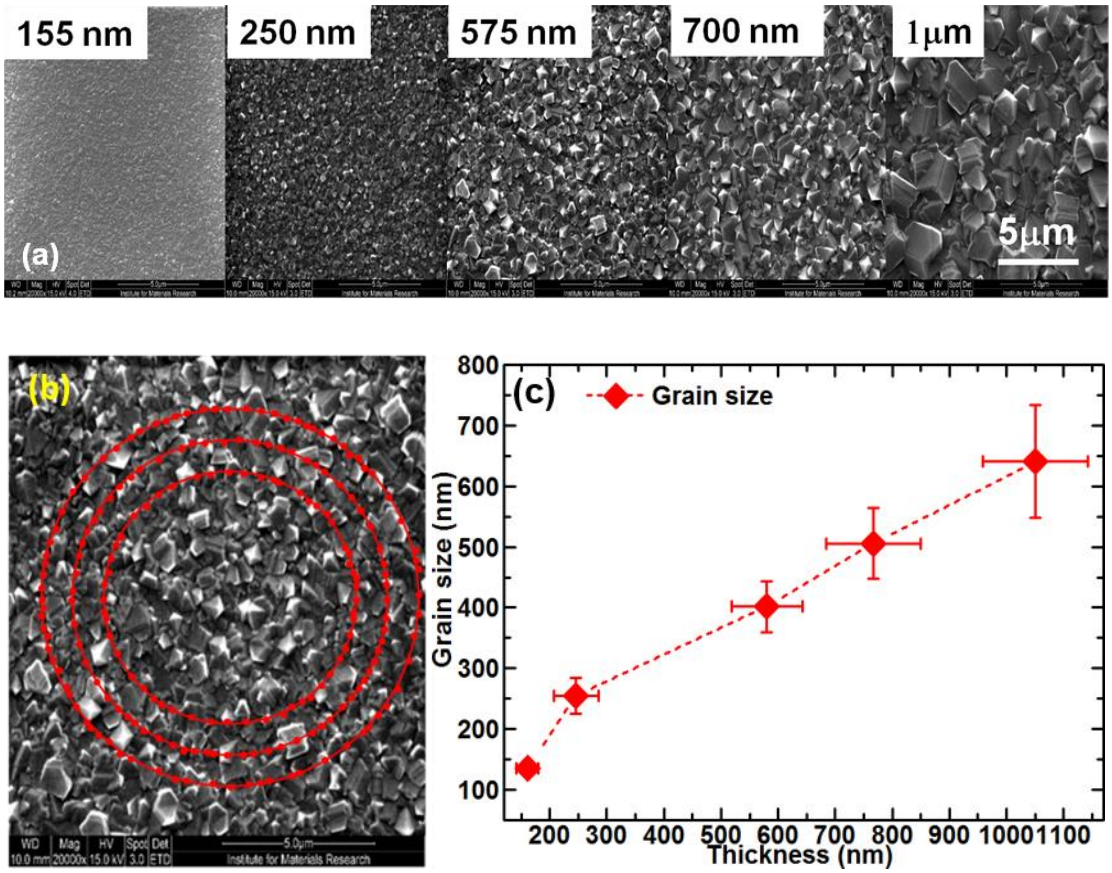


Figure 5.3. (a) SEM micrographs on the diamond film surfaces with film thickness labelled, performed by Ramaneti *et al*., at University of Hasselt, ©2017 AIP. (b) The in-plane grain size determined using the three-circle procedure. (c) In-plane grain size at diamond surface as a function of PCD film thickness, ©2017 AIP

## 5.4 Thermal properties of diamond-on-GaN HEMTs

### 5.4.1 Thermal characterization, sensitivity analysis and thermal parameters extraction

Figure 5.4(a) shows the normalized thermoreflectance transients of diamond-on-GaN HEMT structures, measured at 25 °C for a range of PCD film thicknesses (155-1000 nm). The thermoreflectance data was analyzed by previously introduced Monte-Carlo analytical heat transport model (see details in section 3.2.2). A reference nanosecond TDTR measurement was made first on each GaN-on-Si wafer prior to diamond growth, using an identical transducer; an example plot is shown in Figure 5.4(a). The individual layer parameters obtained for the GaN-on-Si HEMT structure are consistent with values reported in Refs.,[57,272] as shown in Table 5.1 and the reported TBR in Figure 2.24. Measured strain-relief-layer thermal conductivities ($\kappa_{SRL}$) were found to be sample-dependent and within the 4.3-9 W/mK range, consistent with results extracted from previous reports, as given in Table 5.1.[279,299,300]

Table 5.1 also shows the resulting parameters which were fixed in the subsequent simulations. The remaining parameters, i.e., the $TBR_{eff}$ between the metal transducer and diamond ($TBR_{eff,\ Metal/Dia}$), the thermal conductivity of diamond ($\kappa_{Dia}$), and the $TBR_{eff}$ between diamond and GaN ($TBR_{eff,\ Dia/GaN}$) are treated as variables and adjusted to fit the experimental data. It should be noted that the measured $\kappa_{Dia}$ value represents a depth average in the cross-plane direction (through the layer). For simplification, the thin Cr layer was lumped into a single thermal boundary resistance between Au and diamond, $TBR_{eff,\ Metal/Dia}$. Similarly, the thin AlGaN barrier layer and $Si_3N_4$ layer were lumped into $TBR_{eff,\ Dia/GaN}$. These variables and their uncertainties are fitted and determined using Monte-Carlo algorithm and Nelder-Mead algorithm built in Mathematica software; the procedure and details are introduced in section 3.2.2. Figure 5.4(a) shows an example of the analytical model curves well fitted to the experimental data.

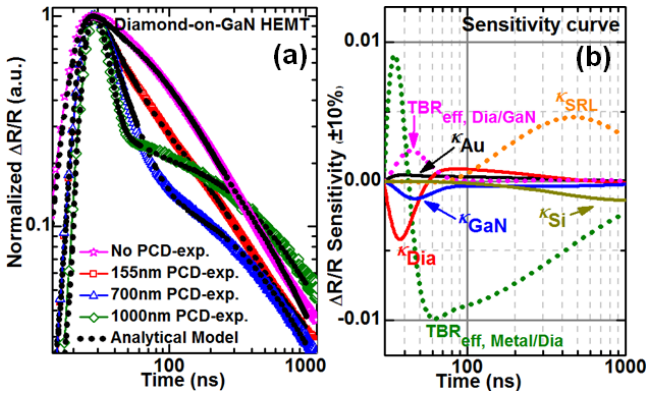


Figure 5.4. (a) Normalized thermoreflectance transients of GaN-on-Si reference sample and of diamond-on-GaN HEMT samples for diamond thickness of 155 nm, 700 nm and 1000 nm, on a logarithmic scale; lines represent experimental values and dots represent analytical model fitted. (b) Sensitivity analysis, with the sensitivity of ΔR/R corresponding to ±10% change in each input parameter in the model. ©2017 AIP

Figure 5.4(b) illustrates the sensitivity plot for each parameter in the heat diffusion model. Some parameters have distinct time constants, whereas others overlap, e.g., $TBR_{eff,\ Dia/GaN}$ mostly impacts the measured response in the 10-40 ns time window, while the diamond thermal conductivity ($\kappa_{Dia}$) mainly affects the 0-40 ns range. Considering this, a 99% confidence level was set in the Monte-Carlo model to obtain the best fitting range for each parameter. Compared to the sensitivity analysis of similar parameters described in Section 4.3.1, the difference in the sensitivity time window for some parameters such as $TBR_{eff,\ Metal/Dia}$, $TBR_{eff,\ Dia/GaN}$ and $\kappa_{GaN}$ mainly originate from the material and thickness change of each layer in the cross-sectional structure of various device. This highlights the importance of indispensable sensitivity analysis for each device structure. The conservative gold layer

thickness variation due to the diamond surface roughness is ~80-120 nm, as measured by TEM. To account for this range, fitting was performed with the transducer thickness fixed at the maximum and minimum values to estimate the uncertainty introduced to the remaining fitting parameters.

Table 5.1. Fixed input parameters for analytical model simulation.

| Layer | Au | Diamond | GaN | Si | AlN | $Al_{0.5}Ga_{0.5}N$ |
|---|---|---|---|---|---|---|
| **Thickness (nm)** | 100 | 155-1000 | 600 | 500000 | 250 | 300 |
| **Thermal conductivity ($W\ m^{-1}\ K^{-1}$)** | 200[a] | fitted | 124[b] | 148[c] | 1.4-5.4[d] | 20[e] |
| **Specific heat ($J\ Kg^{-1}\ K^{-1}$)** | 129[f] | 500[g] | 430[h] | 665. 2[i] | 1082[j] | 756 |
| **Density ($Kg\ m^{-3}$)** | 19800 | 3510 | 6150 | 2320 | 3300 | 4725 |

(a is consistent with Refs.31and 34[99], while b,[57] c,[272] d,[272] e,[272] f,[273] g[274,275], h,[52] i[301], j[52])

### 5.4.2 Thermal conductivity of polycrystalline diamond and its temperature dependence

Figure 5.5(a) summarizes the above analysis, showing that $\kappa_{Dia}$ increases almost linearly with PCD thickness. To fundamentally understand this PCD thermal conductivity behavior, the evolution of the in-plane grain size with films thickness needs to be considered. As the in-plane grain size clearly correlates with the diamond film thickness (see Figure 5.3), this increases $\kappa_{Dia}$ for thicker layers due to the increased phonon mean-free-path.[25,302] We note the $\kappa_{Dia}$ (from $55\pm15$ to $320\pm150$ W/mK) is one-to-two orders of magnitude lower than that of single-crystal diamond, consistent with the thickness-dependency concluded in literature.[35] An incremental layer-by-layer (considering that the grain size varies with depth through the diamond layer) Callaway-like KC-model[25] was fitted to the diamond thermal conductivities determined here. A good agreement is observed between the measurement and model in the diamond thickness range of 0-800 nm, using an intra-grain thermal conductivity ($k_{lattice}$) of 1250 W/mK[25,303] and a grain boundary thermal conductance ($G$) of 0.3 GW/m$^2$K. The modeled and measured values diverge above a diamond thickness of 800 nm, suggesting that either $k_{lattice}$ or $G$ is not constant through the diamond film. The PCD grain size in thin layers is much shorter than the phonon mean-free-path in single-crystal diamond, which essentially limits heat transport. Grain boundaries are prone to accumulate defects, including disordered-bonding structures, which lower the $G$ value.

Figure 5.5(b) shows $\kappa_{Dia}$ as a function of temperature. All samples exhibit a negligible temperature dependence of the thermal conductivity of the diamond. This is very different from bulk PCD and bulk Si where it is seen to decrease with temperature,[92,272] but similar to the characteristics of the disordered material.[304] Such disordered-like negligible temperature dependence is mainly due to the dominant phonon-grain boundary scattering still stronger than the increased phonon-phonon scattering in the investigated higher temperature range. The amorphous-like $SiN_x$ also behaves with a non-decreased temperature dependence which is beneficial for devices working at higher temperature; however its thermal conductivity is much lower than that of even 155 nm PCD thin film.

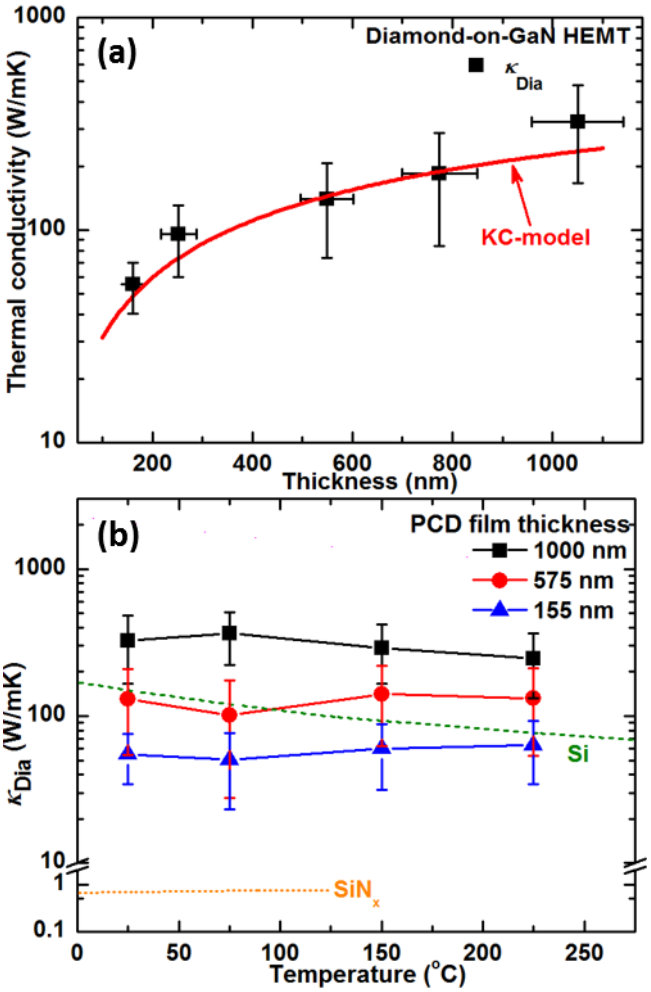


Figure 5.5. (a) Thermal conductivity of PCD, the line is a predicted KC-model.[25], ©2017 AIP. (b) Thermal conductivity of different thickness PCD films from 25 to 225 °C measured by transient thermoreflectance. Data of Si is taken from Glassbrenner *et al.*,[272] and data of $SiN_x$ is taken from Lee *et al.*[305] Solid lines are a guide to the eye.

### 5.4.3 Thermal boundary resistance at diamond/GaN interfaces and its temperature dependence

We also note that $TBR_{eff,\ Dia/GaN}$ is higher than that in recent reports,[27,28,112,267,306] as shown in Table 5.2, mainly attributed to the thicker $Si_3N_4$ in our structure (which is very commonly used for passivation and also as a protective layer during the initial diamond growth), and is not identical in all samples although the growth parameters were nominally identical (see Figure 5.6(a)); this variation may be related to the slightly inhomogeneous initial seeding conditions or different initial microstructual disorders.[284,307] Figure 5.6(b) shows the $TBR_{eff,\ Dia/GaN}$ as a function of temperature. No obvious temperature dependence can be concluded for all studied samples although they seem to have presented a weak decreasing trend with temperature if not considering the relatively large error.

Table 5.2. Reported $TBR_{eff,\ Dia/GaN}$ in recent references. (All diamond means PCD except specially denoted; TTR represents transient thermoreflectance, TIM represents Transient interferometric method, TDTR represents time-domain thermoreflectance).

| Structure | Transition layer thickness (nm) | $TBR_{eff,\ Dia/GaN}$ ($m^2K/GW$) | Method | Reference |
|---|---|---|---|---|
| GaN-on-diamond | $SiN_x$, 25 and 50 | 27±3 and 36 | Raman | Pomeroy, *et al.*[27] |
| GaN-on-diamond | $SiN_x$, 50 and 90 | 17 and 41 | TTR | Pomeroy, *et al.*[267] |
| GaN-on-diamond | $SiN_x$, 28-100 | 12-50 | TTR | Sun, *et al.*[28] |
| GaN-on-diamond (single crystal) | no | <10 | TIM | Kuzmik, *et al.*[306] |
| GaN-on-diamond | $Al_{0.5}Ga_{0.5}N$/AlN, 1200 | 108 ± 27 | TDTR | Cho, *et al.*[112] |
| GaN-on-diamond | $Al_{0.5}Ga_{0.5}N$ /adhesion, 142/3~42 | 36 ± 12 | TDTR | Cho, *et al.*[112] |
| GaN-on-diamond | $Al_{0.5}Ga_{0.5}N$ /adhesion, 269/38~55 | 47 ± 15 | TDTR | Cho, *et al.*[112] |

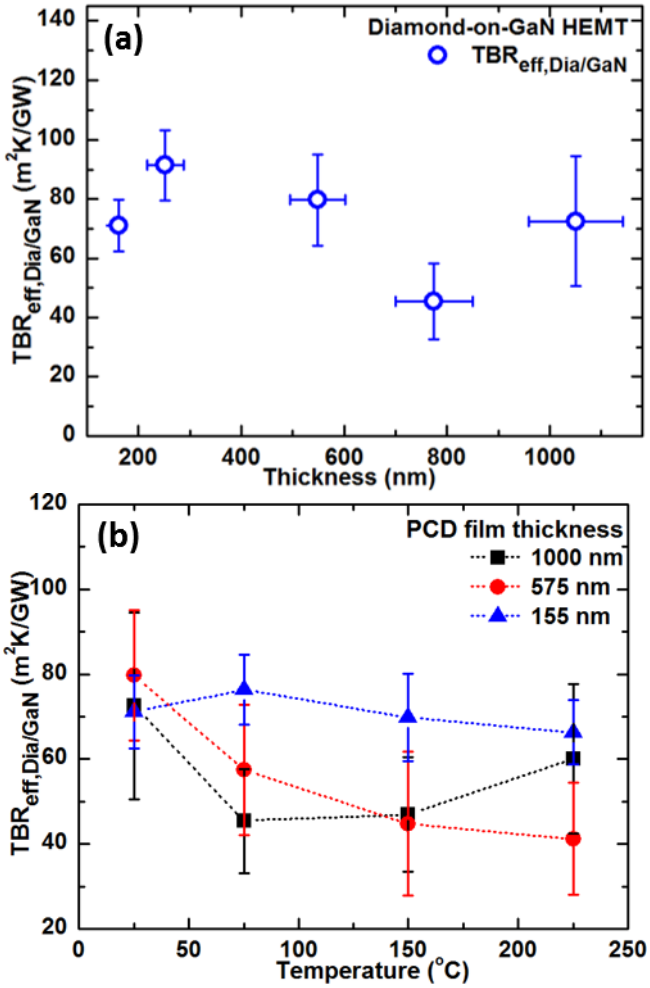


Figure 5.6. (a) TBR between PCD and GaN as a function of PCD film thickness, ©2017 AIP. (b) TBR between PCD and GaN for different PCD film thickness from 25 to 225 °C measured by transient thermoreflectance. Dot lines are a guide to the eye.

## 5.5 Effect of interfacial microstructure and intra-grain disorder on the thermal properties of polycrystalline diamond

To further investigate the reasons for difference in $TBR_{eff,\ Dia/GaN}$ and low $\kappa_{Dia}$, cross-sectional TEM micrographs of the sample has been imaged which was taken by Korneychuk *et al.*, at University of Antwerp, as shown in Figure 5.7. Very sharp and smooth interface between AlGaN and $SiN_x$ layer (see Figure 5.7(a)) indicates the initial homogeneous MOCVD growth and smooth surface of $SiN_x$ before the deposition of PCD. However, as displayed in Figure 5.7(b), very rough $SiN_x$/diamond interface including some intermediate state such as silicon carbide phase is formed during the deposition of diamond. This rough interface probably results from the damage of initial diamond seeding and harsh diamond growth environment, and is one of the reasons accounting for the variation in $TBR_{eff,\ Dia/GaN}$.

Figure 5.7(c) shows a high-resolution TEM image in the vicinity of a diamond grain boundary, where numerous disordered intragrain structures such as twins and stacking faults are observed, which will greatly increase the phonon scattering (by modifying the phonon-impurity scattering term) within the diamond grains. Thus, the diamond crystallinity (the ordering of the $sp^3$ phase within the diamond grain), amorphicity, and defects[308] can also introduce significant phonon scattering (as detailed introduced in Section 2.1.4), lowering $\kappa_{lattice}$ and $\kappa_{Dia}$, which agrees well with the aforementioned KC-model predicted trend. The quantitative effects of these defects on the phonon scattering and $\kappa_{lattice}$ still need further intensive statistical study.

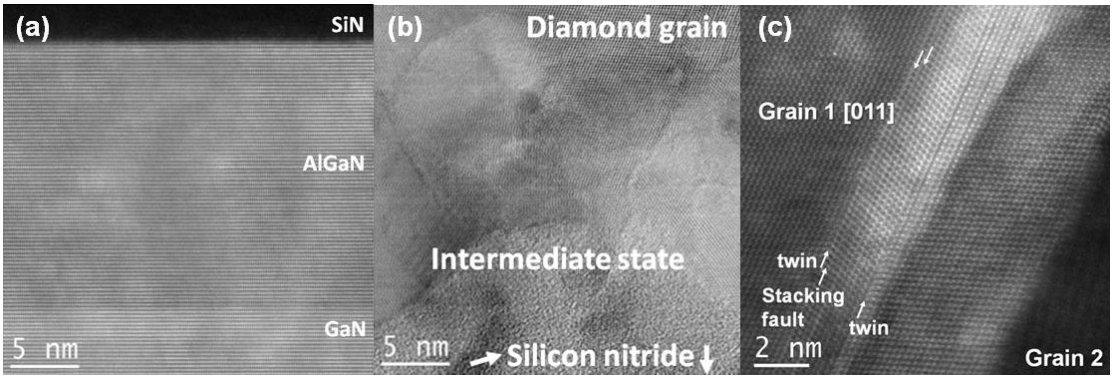


Figure 5.7. High resolution ADF-STEM (annular dark-field scanning transmission electron microscopy) image of (a) the SiN/AlGaN interface, (b) the diamond/SiN interface, (c) the diamond intragrain structure. Experiments were performed by Korneychuk *et al.*, at University of Antwerp. ©2017 AIP.

## 5.6 Diamond-on-GaN HEMT device thermal properties using 3D finite element thermal simulation

3D finite-element steady-state thermal models were constructed in ANSYS to investigate the impact of PCD heat spreaders on the actual thermal characteristics of here studied GaN-on-Si HEMT devices, using the experimentally determined $\kappa_{Dia}$ and $TBR_{eff}$ values; other parameters of materials are taken from Table 5.1. The concrete procedure and simulation details are described in section 5.2.3. The simulated temperature profile through an AlGaN/GaN HEMT device structure with and without different thickness of PCD film heat spreaders grown on top are shown in Figure 5.8. According to the plotted three conditions, i.e., with 155 nm or 1000 nm diamond film or without a diamond film deposited on top of the GaN HEMT channel, the largest temperature drop occurs across the strain relieve layer (550 nm thick and with a low thermal conductivity of ~4.3-9 W/mK) between the GaN layer and Si

substrate, but this temperature drop can be reduced to half when a 1000 nm PCD film is grown on top of the device source-drain opening; this illustrates the very need of heat extraction through the topside of the device structure as studied in this work (this strain relieve layer in fact is needed to grow GaN onto Si).

Given that the cross-plane thermal conductivity is always higher than the in-plane thermal conductivity for this columnar PCD,[19] the experimental value can be thus used to determine an upper limit of the expected thermal benefit of PCD. By adding a PCD heat spreader on top of the device source-drain opening, Figure 5.8 shows that a 12% maximum reduction in peak channel temperature could be achieved using a 1000 nm PCD film. We note that if the $TBR_{eff}$ at the diamond/GaN interface is not included, then there is a further 10% temperature reduction.

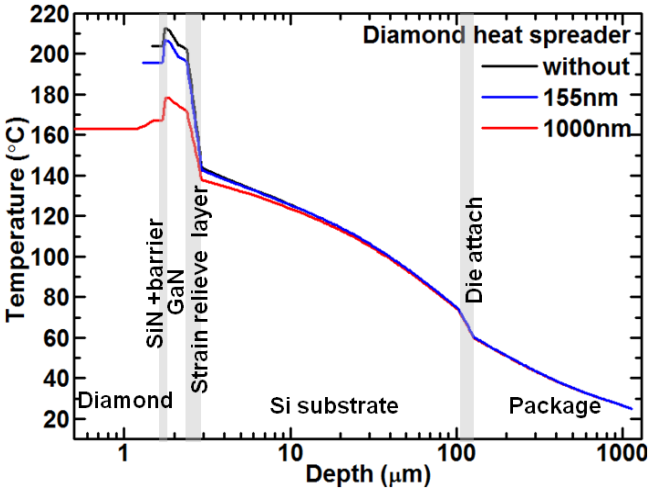


Figure 5.8. The simulated temperature profile through an AlGaN/GaN HEMT device structure w/wo different thickness of PCD film heat spreaders grown on top of the device source-drain opening.

As the thermal conductivity varies through the diamond films in the cross-plane direction, we have also investigated the effect of this on the device thermal properties by simulating the 1000 nm PCD film using from one to five layers, corresponding to the thermal conductivity data of each layer extracted from Figure 5.5(a). Figure 5.9(a) illustrates the schematic of 1-layer, 2-layers and 5-layers models for gradient in thermal conductivity consideration of 1000 nm thick PCD film. Figure 5.9(b) shows there is little difference in peak channel temperature by considering the gradient in thermal conductivity, illustrating the validity and simplicity of using the average $\kappa_{Dia}$ to simulate steady-state thermal performance of devices. However, the anisotropy in each layer of the gradient in thermal conductivity model has not been considered here, due to the unavailability of experimental values presently for the in-plane thermal conductivity of each layer. This anisotropic consideration for multi-

layers' gradient in thermal conductivity model may result in larger difference in peak channel temperature in comparison to only one-layer average $\kappa_{Dia}$ considered.

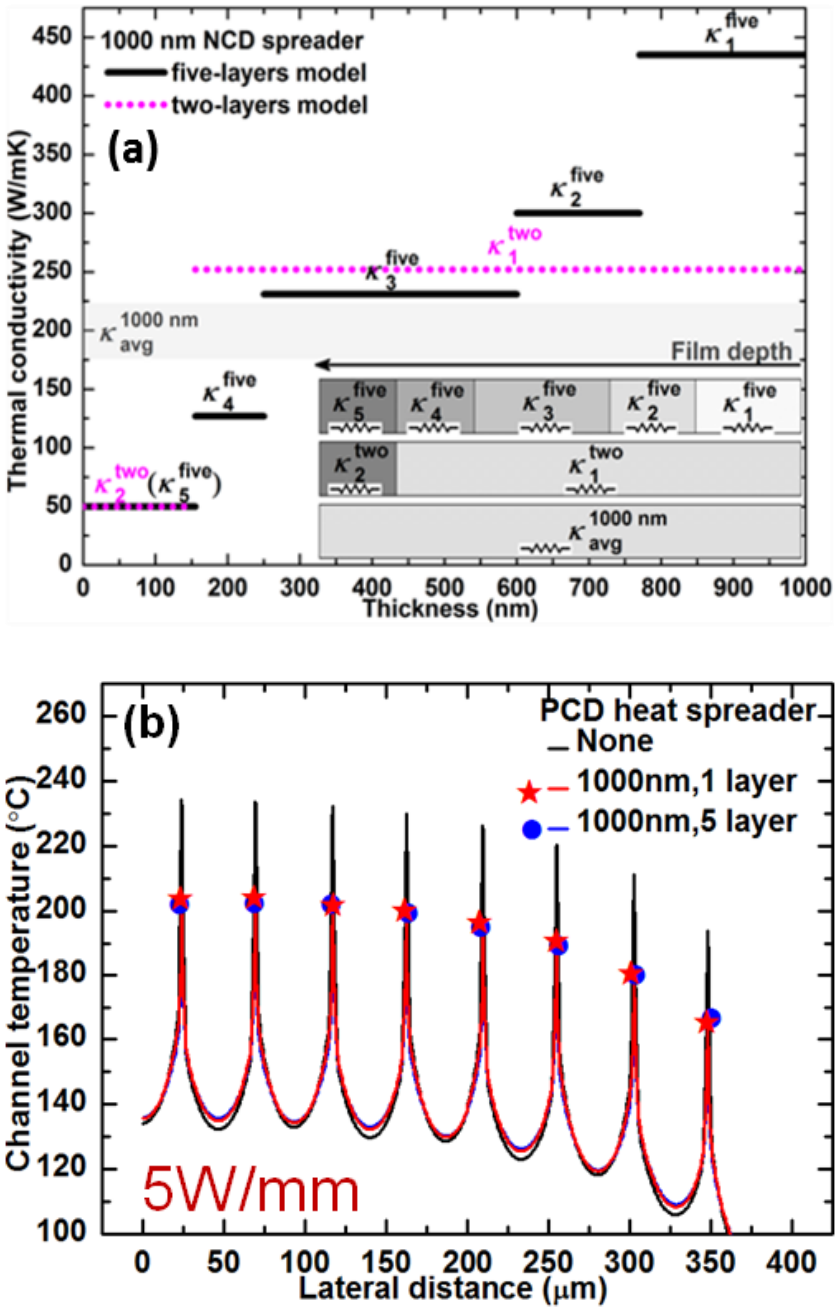


Figure 5.9. (a) The schematic of 1-layer, 2-layers and 5-layers models for gradient in thermal conductivity consideration of 1000 nm thick PCD film. Inset: schematic of thermal resistance according to Matthiessen rule. (b) Peak channel temperature distribution in lateral direction with and without 1000 nm PCD film layer, ©2017 AIP.

The device peak temperature as a function of PCD film thickness, when only covering the source-drain opening, is illustrated in Figure 5.10. Little further thermal benefit is

predicted when using PCD films thicker than 2 μm, with only a maximum 15% reduction, using either the measured cross-plane $\kappa_{Dia}$, or using the 0.4-0.6 anisotropic thermal conductivity ratio from literature.[35] These results highlight the importance of the crystalline quality of the very first micrometer of diamond in heat spreading layers. However, if PCD could be grown on both source-drain opening and metal contacts (Figure 5.10 inset), a 1.5× better thermal benefit would be achieved for thicker films by increasing the area of the heat spreader.

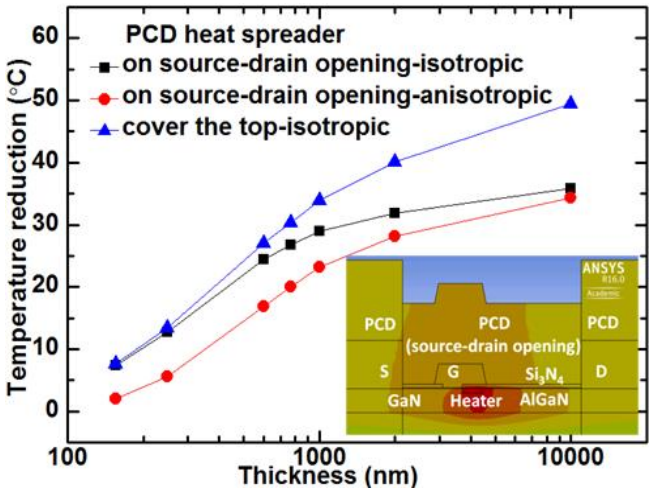


Figure 5.10. Device peak temperature as a function of PCD film thickness; the lines represent a guide to the eye. Inset: schematic of PCD grown on source-drain opening and metal contacts. ©2017 AIP

## 5.7 Conclusions

PCD heat spreader structures were grown on passivated AlGaN/GaN HEMT structures and studied, with diamond film thicknesses varying from 155 to 1000 nm. The results show that $\kappa_{Dia}$ has a strong film thickness dependence, which can be attributed to the in-plane grain size evolution with film thickness, with the measured values of 320±150 W/mK for 1 μm-thick PCD, which is nearly one order of magnitude lower than the bulk PCD value of ~2200 W/mK. The PCD layers do not show a sizable temperature dependence of $\kappa_{Dia}$ in the measured range from 25 to 225 °C. Transistor thermal modeling shows that growing the PCD film heat spreader in the source-drain opening only reduces the peak temperature by a maximum of 15%. There is limited thermal benefit when the PCD film thickness is increased beyond ~2 μm, unless both source-drain opening and metal contacts are overgrown by PCD to increase the area of the heat spreader.

# Chapter 6.

## Pressure-dependent Structure and Optical Properties of GaTe Multilayers

### 6.1 Introduction

The next generation higher compacted electronics for future communications or computing (with much higher data rates) require sub-10-nm or even atomic dimension scaling to extend Moore's law which is very difficult based on present channel materials and devices, incorporation of a new 2D materials channel with distinguished properties then has emerged as a highly attractive solution to address this challenge. Gallium telluride (GaTe) is a 2D layered material that recently raised considerable interests due to its unique optoelectronic properties (with a very high photoresponsivity of $10^4$ A/W) and significant in-plane anisotropic properties in multilayers, but is still under extensive exploration of its fundamental properties for potential applications, such as new generation transformative high performance optoelectronic and phase-switch memory devices. Although flakes of more than several monolayers (~1.7 nm for each layer) do not exhibit the exact 2D properties, GaTe multilayers whose thickness below few hundreds of nm have already presented significant difference in properties compared to that of its bulk materials. Also, in contrast to graphene, GaTe has an actual bandgap which enable proper bandgap engineering to manipulate its anisotropic properties for the design of more 2D materials based functional devices.

As a low symmetry layered material with significant in-plane anisotropy, although the in-plane anisotropic optical properties and related physics existing in GaTe multilayers have just been observed and investigated,[137] how potential of all its anisotropic properties can be tuned for specific applications for example strain-modulation devices and the related mechanisms are still under exploration. In this section, we have investigated exfoliated single-crystal GaTe multilayers with thickness of ~153 nm by employing pressure-dependent *in-situ* micro-Raman spectroscopy, synchrotron XRD characterisation, and first-principles theoretical calculations to study the structural, vibrational, optical and electronic properties at pressures up to 46 GPa. Among them, pressure-dependent *in-situ* micro-Raman and transmission measurements were carried out at the University of Bristol with the help of Dr. Oliver Lord and Dr. James Pomeroy, while pressure-dependent synchrotron XRD measurements were performed by Dr. Oliver Lord at Diamond Light Source (UK) and the data were analysed with

the help of Dr. Oliver Lord. TEM and ambient condition XRD experiments were performed and analysed by Qinghua Zhao at Northwestern Polytechnical University (China). First-principles theoretical calculations were mainly designed and analysed by the author, while were performed by Tao Fan at Northwestern Polytechnical University (China) who also helped to analyse the results.

A reversible iso-structural phase transition was revealed from the strong anisotropic peak splitting of Raman modes starting at ~6.5 GPa, followed by a structural phase transition into a metallic cubic phase at ~15 GPa which coexisted with the iso-structural phase over a wide pressure region (intermediate state). First-principles calculations attributed these phase transitions to changes in telluride-telluride interactions between adjacent GaTe layers with the gradual closure of the van de Waals gap coupled with a symmetry change at high pressures. Our combined experimental and theoretical results provide insights into other low symmetry layered materials besides transition metal dichalcogenides (TMDCs) with potential applications for phase-change devices and strain-modulated optoelectronics, as well as shedding light on new physics for understanding strain-dependent anisotropic light-material interaction and manipulating the anisotropic coupling of structural, electronic, thermal, mechanical and optical properties of low symmetry 2D materials.

## 6.2 Experimental details

### 6.2.1 Sample preparation and characterization

The single-crystal bulk GaTe ingot was grown by the modified vertical Bridgeman method, and the accelerated crucible rotation technique[309] was exploited to improve the mass and heat transport and smooth the solid-liquid interface during crystal growth. A 1:1 stoichiometric mixture of high purity powders of gallium (99.99%, Alfa Aesar) and tellurium (99.99%, Alfa Aesar) were mixed in a rocking synthesizing furnace and sealed in an evacuated quartz ampoule ($<10^{-4}$ torr vacuum). Single-crystal GaTe wafers with dimensions of ~15×15×2 $mm^3$ were cut from the GaTe ingot. GaTe flakes were mechanically exfoliated from a single-crystal bulk GaTe wafer onto 300 nm $SiO_2$/Si or PDMS substrates.

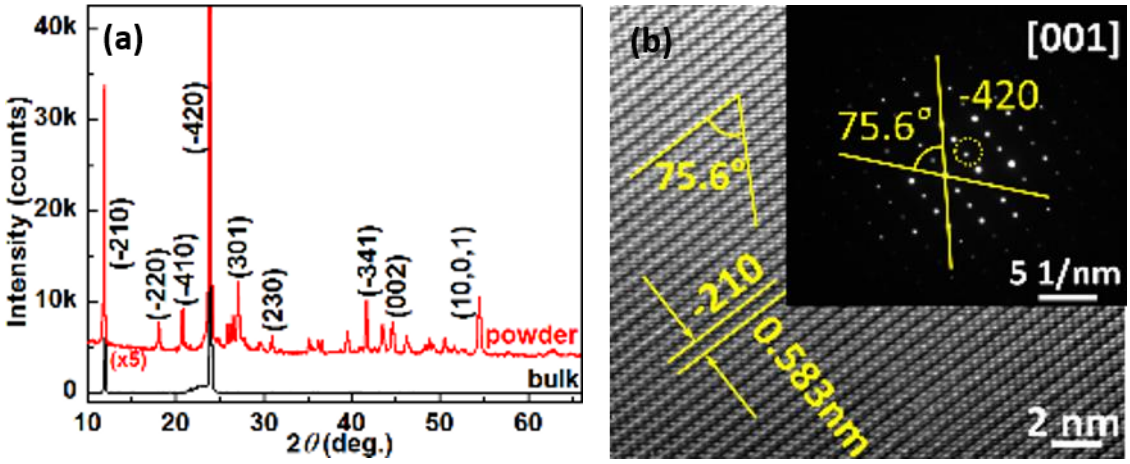


Figure 6.1. (a) Room temperature XRD spectrum for powder and bulk GaTe using Cu X-ray radiation ($K_\alpha$=1.5418 Å); (b) high-resolution transmission electron microscopy (HR-TEM) and selected area electron diffraction (SAED, see the inset) for multi-layered GaTe flakes. Experiments were performed by Qinghua Zhao *et al.*, at Northwestern Polytechnical University (China).

The thicknesses of the GaTe flakes were measured by AFM. The crystal structure was characterized by room temperature XRD with Cu X-ray radiation ($K_\alpha$=1.5418 Å) for both bulk and powder samples (see Figure 6.1(a)), showing a (-2*l*, *l*, 0) preferred orientation and very narrow diffraction peaks indicating the high quality of the as-grown single crystal. To rule out the effects of possible lattice defects, a further critical characterization through high-resolution transmission electron microscopy (HR-TEM) and selected area electron diffraction (SAED) was performed. Sharp diffraction patterns and a lattice morphology with $\gamma^*$=75.56° in reciprocal space and an interlayer separation of 0.583 nm were observed, confirming the monoclinic structure and the high quality of the measured GaTe flakes, as shown in Figure 6.1(b). The lattice parameters of monoclinic GaTe obtained here are a=17.37964 Å, b=10.46465 Å, c=4.07548 Å, and $\gamma$=104.222°, respectively, similar to values reported in the literature.[192]

### 6.2.2 High-pressure Raman measurements

Pressure was generated using a Princeton-type symmetric DAC with a stainless steel gasket. Details about this type of DAC and the fabrication method of the gasket as well as the sample chamber are introduced in Section 3.4. A freshly exfoliated single-crystal GaTe flake (dimensions of ~100×70×0.1 μm$^3$) was loaded into the 100 μm diameter sample chamber of the DAC. To transfer the flakes onto the culet of the diamond anvil, they were firstly exfoliated onto a solvent-cleaned glass slide using Scotch tape, rinsed in acetone immediately and then carefully picked up using a sharp needle under an optical microscope (equipped with a long working distance objective) and transferred onto the diamond culet. The remaining

volume of the sample chamber was then filled with methanol: ethanol (4:1) solvent solution that acted as the pressure medium.

Pressures and their uncertainties were determined from the wavelength of the fluorescence peak of ruby spheres placed close to the sample flakes in the sample chamber of the DAC before and after each Raman measurement. Both Raman and fluorescence measurements were performed using a commercial Renishaw InVia system with a probe laser wavelength of 488 nm or 532 nm (see detailed introduction in Section 3.1). A 2400 *l*/mm grating was used to disperse the scattered light onto a CCD resulting in a spectral resolution of 0.5 $cm^{-1}$. The Raman system was first calibrated using the characteristic 520.3 $cm^{-1}$ peak of undoped single-crystal silicon with an uncertainty of 0.05 $cm^{-1}$. The spot size of the focused laser beam was about 1 μm. The incident laser power was 5% and the exposure time was 150s.

### 6.2.3 High-pressure synchrotron XRD experiments

High pressure synchrotron based XRD experiments were performed at beamline I15 of the Diamond Light Source, Rutherford Appleton Laboratory, UK. Pressures were generated using a Le-Toullec type membrane driven symmetric DAC with a culet diameter of 300 μm. A Rhenium gasket was pre-indented to a thickness of 45 μm and drilled centrally using spark erosion to give a 150 μm diameter sample chamber. Three items were then loaded into the sample chamber: a thin foil made from fine powder produced by grinding as-grown single crystals of GaTe under ethanol in an agate mortar, a loose pile of Cu powder and a single ruby sphere. The last two items acted as pressure calibrants. The remainder of the sample chamber was filled with supercritical fluid Neon that acted as the pressure-transmitting medium. Pressure was increased incrementally by increasing the gas pressure on the cell membrane using a digital pressure controller. The cell was left to equilibrate for 5 minutes after each compression before being analyzed. A focused monochromatic X-ray beam with a wavelength of 0.4246 Å was used for the X-ray diffraction experiments. Diffracted X-rays were collected by a MAR CCD (see the 2D diffraction image of a powder GaTe sample at ambient pressure displayed in Figure 6.2). Diffraction patterns were integrated into 1-D spectra and fitted using the GSAS-II software package and the Le Bail refinement method.[310]

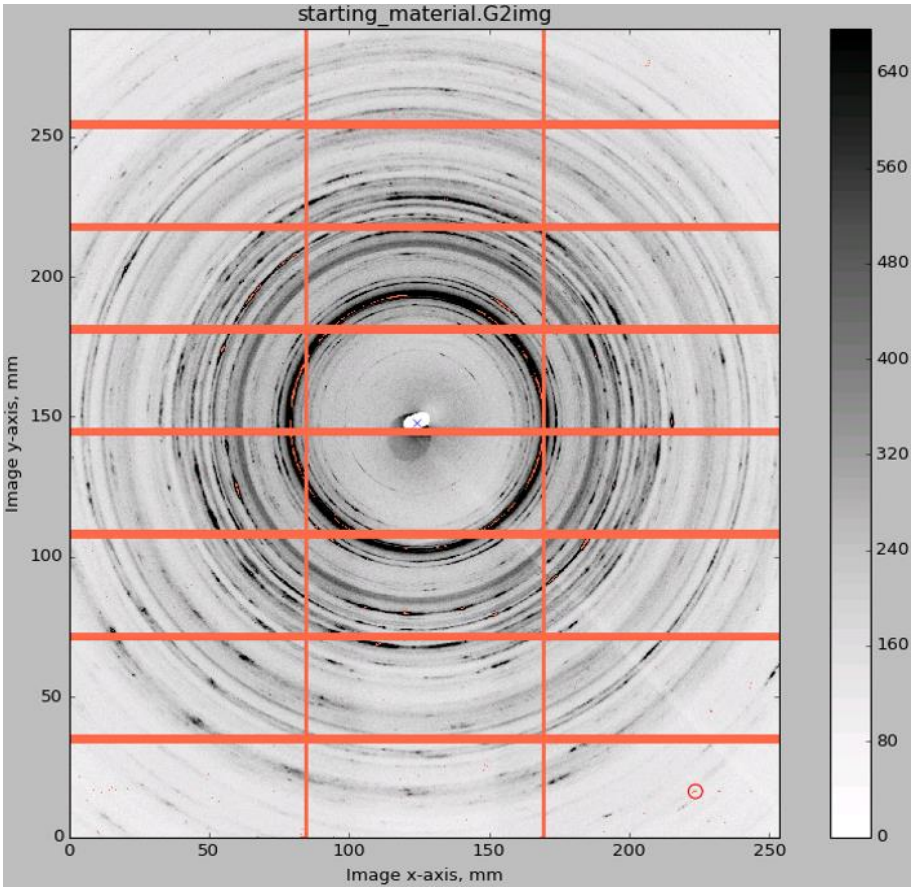


Figure 6.2. A 2D XRD image of powdered GaTe at ambient pressure collected by a MAR CCD.

### 6.2.4 First-principles theoretical calculations

Theoretical calculations were carried out mainly by Tao Fan and Prof. Qingfeng Zeng at Northwestern Polytechnical University using density functional theory (DFT) as implemented in the Vienna *ab initio* Simulation Package (VASP) and Universal Structure Predictor: Evolutionary Xtallography (USPEX). According to the USPEX manual and its website description, to identify stable structures under different pressures for fixed composition GaTe, a state-of-the-art evolutionary algorithm (EA) method implemented in the USPEX code was employed for structure prediction,[311-313] while VASP[314,315] was used to relax the predicted structures and determine their formation energy. Evolutionary predictions were performed at 0 GPa and 15 GPa with up to 30 atoms allowed in the primitive cell. The first generation of GaTe structures were produced using the random symmetric algorithm,[316] and all subsequent generations of GaTe structures were produced in the following manner: 20% were generated randomly, and the rest by variation operators including heredity (20%), lattice mutation (20%), soft mutation (20%) and transmutation (20%). In every generation, candidate structures based on the above variation operators were considered, generated and calculated for at least 30 generations until the convergence was achieved.

In order to obtain phonon dispersion curves, the second-order interatomic force constants (IFCs) need to be calculated. For each structure, a 2×2×2 supercell was built and the density functional perturbation theory (DFPT)[317] was applied to calculated IFCs, as implemented in VASP. Then the dynamical matrix was constructed based on the harmonic IFCs and phonon frequencies were obtained by diagonalizing the dynamical matrix using Phonopy package.[318]

Band structures and density of states (DOS) were calculated using the VASP package. A Perdew-Burke-Ernzerhof exchange-correlation energy functional was treated using the generalized gradient approximation (GGA-PBE).[319] The energy cutoff for the plane-wave basis was set to 600 eV and the Brillouin zone was sampled using Γ-centred uniform Monkhorst-Pack (MP) meshes[320] with a resolution of $2\pi \times 0.02$ Å$^{-1}$ in all calculations. The calculation would not be stopped until the total energy difference between consecutive cycles was less than $10^{-8}$ eV and the maximum Hellmann-Feynman force was less than $10^{-3}$ eV/Å.

## 6.3 Effects of pressure on structure

### 6.3.1 Angle-resolved polarized Raman spectrum of GaTe multilayer flakes

To get insights into the in-plane anisotropic properties as well as the mechanism of the high-pressure phase transition and structural symmetry change that was not investigated or solved in an early XRD study to 20 GPa,[193] we carried out *in-situ* micro-Raman measurements combined with angle-resolved polarized Raman at room temperature from ambient pressure up to ~33 GPa. This method presently is known to be the most sensitive and effective technique in detecting subtle structural transitions and investigating the optical properties, especially light-material interactions within 2D materials. Before measuring the pressure dependence of the Raman spectrum, angle-resolved polar plots of Raman intensity for various phonon modes were generated, as shown in Figure 6.3(a-d), to distinguish different crystal orientations (i.e. armchair or zigzag in-plane crystal orientations) for the following investigation of the detailed in-plane light-material interactions at higher pressures. Similar to Huang *et al*.'s results[137], an anisotropic four-fold symmetry (i.e., four maximums along either 0° or 90° as seen in Figure 6.3(c), where 0° represents armchair orientation and 90° represents zigzag orientation) was apparent for the 161 cm$^{-1}$ Raman mode using a 488 nm laser excitation as well as a major maximum along 0° crystal orientation with a secondary maximum at 90° for the 268 cm$^{-1}$ mode. In contrast to previous work, the 176 cm$^{-1}$ mode which was not distinguishable in Huang *et al*.'s work[137] became apparent with a similar anisotropic symmetry as that of the 268 cm$^{-1}$ mode, while the 281 cm$^{-1}$ mode shows an anisotropic four-fold symmetry similar to that of the 161 cm$^{-1}$ mode when using the shorter 488 nm wavelength laser excitation. Such different polarization shapes of Raman modes can be understood through optical transition selection rules described by Huang *et al*.[137]; the detailed mechanism of the optical transition selection rules for different Raman modes are introduced in Section 2.4.1.4. Therefore the highly anisotropic polar symmetry correlation of these Raman modes with their related crystal structure have provided an interesting and reliable fingerprint method to identify the crystal orientation of the GaTe flakes for the further investigation of pressure-dependent light-material interactions along different in-plane crystal

orientations. Details about our angle-resolved polarized Raman measurements can be found in Section 3.1.4.

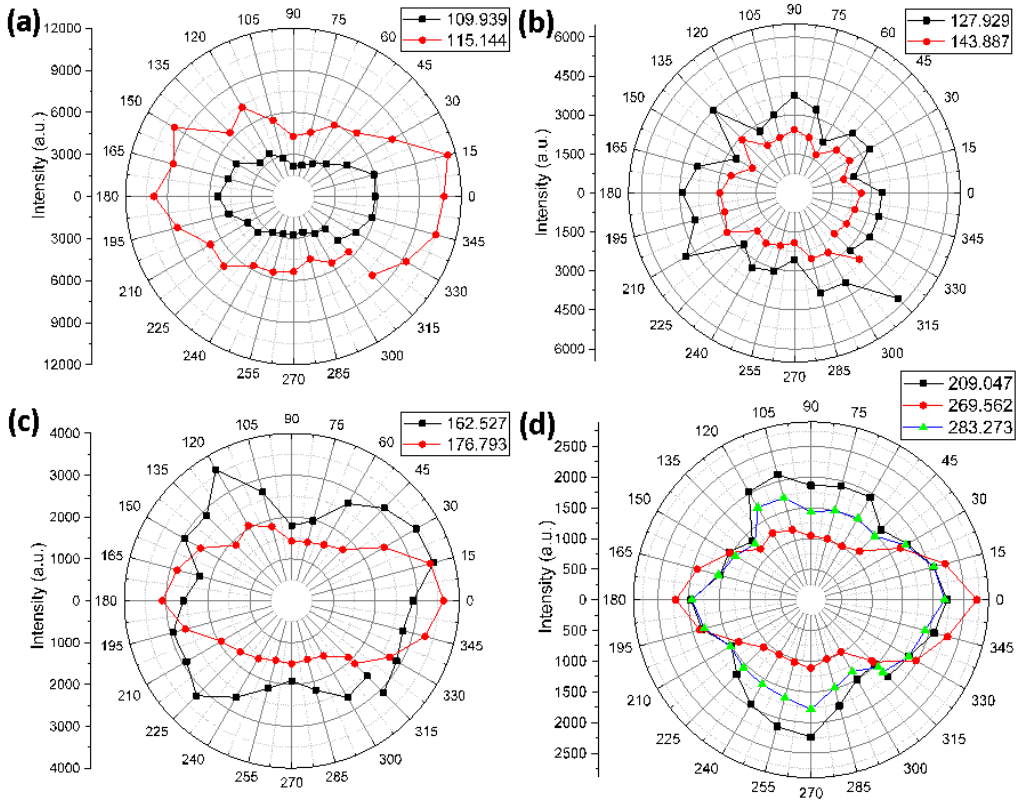


Figure 6.3. Polarized polar plots of different Raman modes in monoclinic GaTe as a function of angles between the laser polarization and in-plane crystal orientation with different anisotropic symmetry displayed: (a) 109 and 115 $cm^{-1}$ modes; (b) 127 and 143 $cm^{-1}$ modes; (c) 162 and 176 $cm^{-1}$ modes; (d) 209, 268 and 283 $cm^{-1}$ modes.

### 6.3.2 High-pressure Raman scattering of GaTe multilayer flakes

#### 6.3.2.1 Raman spectrum under compression and decompression conditions

A continuous range of pressures on both compression and decompression were produced using the DAC; a detailed schematic is illustrated in Figure 3.9 in Section 3.4. In combination with the micro-Raman system, *in-situ* pressure dependent polarized Raman measurements were conducted to minimize or exclude other unknown effects on our results. In Figure 6.4(a) and (b), the optical images of measured GaTe flakes under different polarization orientations were evident with the help of a 50× long working distance objective lens, at pressures of 2.51±0.02 GPa and 19.88±0.02 GPa separately; the mark on the flakes indicated where the laser position is located and fixed. The GaTe flake thickness measured using atomic force microscopy (AFM, Bruker) was ~153 nm, as indicated in the inset of Figure 6.4(a). Selected Raman spectroscopy during compression and decompression are demonstrated in Figure 6.5.

A total of three compression and two decompression cycles with very fine pressure steps and with Raman measurements at each step along both 0° (armchair) and 90° (zigzag) crystal orientations were performed, as shown in Figure 6.6(a) and (b), during which two strong Raman peak splitting occurred in the frequency range of 60-450 $cm^{-1}$ starting at ~6.5 GPa and ending at ~15 GPa. These peak splitting transitions were robustly reversible and even anisotropic, and much stronger and complicated than previously reported peak splitting in other layered materials such as $MoS_2$, $WSe_2$.[186,188] As discussed by Wang *et al*.,[188] Raman peak splitting can be due to pressure induced isostructural phase transitions or coexistence of both low- and high-pressure phases. When the flakes were further pressured to over 15 GPa, almost no Raman peaks were visible. This vanishing behaviour of Raman peaks could be accounted for by two possibilities: (1) there is a structural transition where no Raman mode is allowed by the structural symmetry; or (2) a transition into a metallic state happens where the Raman signal becomes extremely weak due to the limited penetration depth of the exciting laser. However, either mechanism needs to be verified by other characterization methods such as synchrotron XRD, theoretical calculations or electrical measurements; in this work, a structural transition into a high symmetry cubic phase with a metallic state was found at ~15 GPa, a point that will be further verified and explained later. In contrast to the reversible phase transition at ~6.5 GPa, the structure change at ~15 GPa seemed to be irreversible which is apparent from the broaden Raman bands shown in Figure 6.5 when the samples were decompressed from ~33 GPa to ambient pressure and re-compressed to ~3 GPa. A permanent structure change probably had formed at pressures over 15 GPa and the broadening of the Raman peaks indicated the formation of an amorphous or disordered phase after decompression from high pressure.

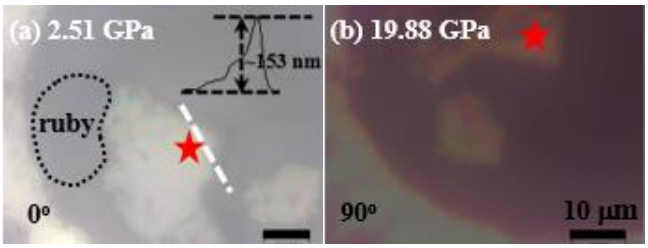


Figure 6.4. Measured multi-layered GaTe flakes in the DAC at pressure of (a) 2.51±0.02 GPa and (b) 19.88±0.02 GPa.

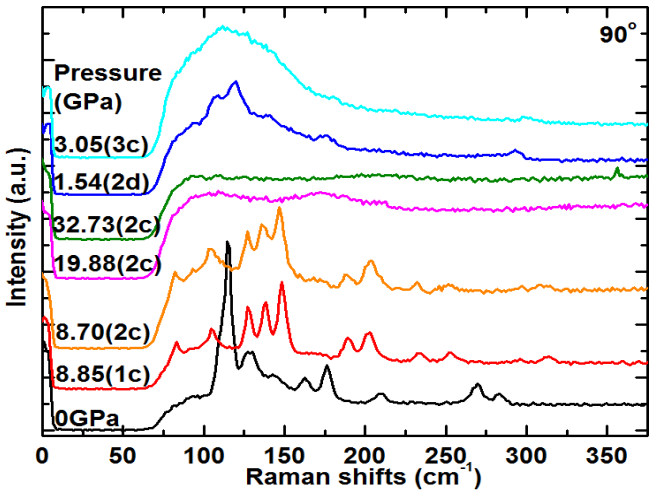


Figure 6.5. The evolution of Raman spectra of GaTe flakes with respect to pressure along 90$^{o}$ (zigzag) crystal orientations ('c' represents compression, while 'd' represents decompression and the numbers 1-3 represent the cycle; error in pressure is 0.02 GPa).

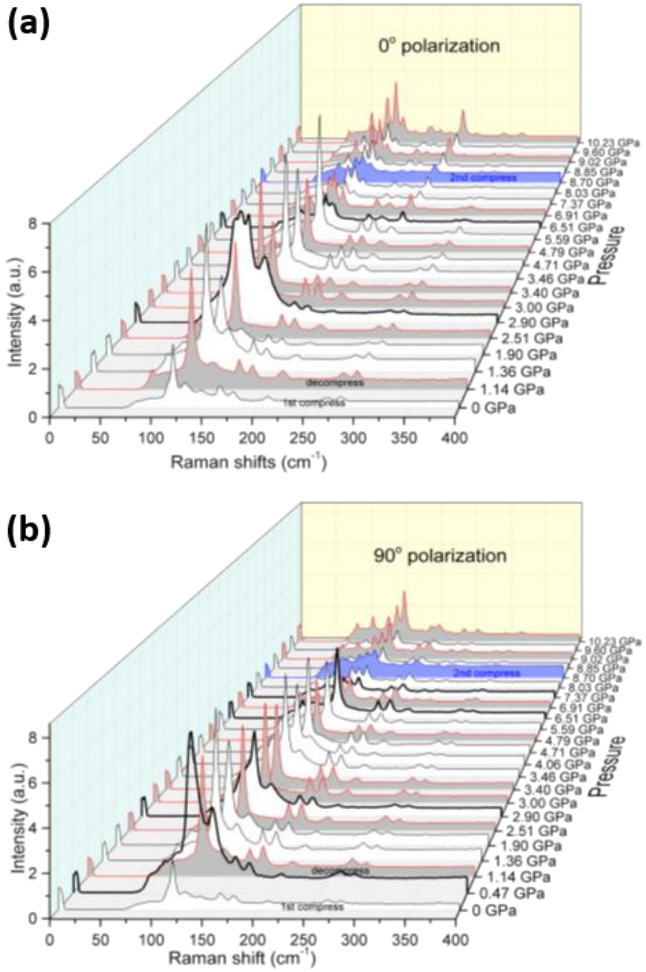


Figure 6.6. From compression to decompression and re-compression, the evolution of Raman spectra of GaTe flakes with respect to pressure along (a) 0$^{o}$ (armchair) and (b) 90$^{o}$ (zigzag) crystal orientations, respectively. Error in pressure is 0.02 GPa.

### 6.3.2.2 Pressure dependence of Raman modes and peak splitting analysis

To elucidate the possible phase transitions and understand the light-material interactions under pressure, comprehensive pressure dependent polarized Raman spectra were measured and analysed. Representative polarized Raman spectra along armchair and zigzag orientations of GaTe flakes as a function of pressure are displayed in Figure 6.8(a). The 532 nm excitation laser results are similar to Huang *et al*.'s work,[137] with the armchair (zigzag) orientation along the 0° (90°) axis in the polar plots of Figure 6.3(a-d), corresponding to the *c*(*b*)-axis of the crystal orientation shown in Figure 2.25(a) and (c) in Section 2.3.2; Raman spectra for other polarization angles under 532 nm laser excitation are shown in Figure 6.7. As illustrated previously,[137] GaTe has 36 phonon modes in total, among which 18 are Raman-active including 12 $A_g$ modes and 6 $B_g$ modes. In accordance with the theoretical and experimental work by Huang *et al*.,[137] nine Raman modes can be directly observed in our experimental spectrum when excited by a 488 nm laser: 109, 115, 127, 143, 162, 176, 209, 268, and 283 $cm^{-1}$. Among them, five Raman modes (109, 115, 209, 268, 283 $cm^{-1}$) are $A_g$ modes, two (162, 176 $cm^{-1}$) are $B_g$ modes, while the remaining two (127, 143 $cm^{-1}$) probably are double-resonant or oxidation-related modes but seem to be sensitive to the degradation level.[137,321,322] The main difference lies in the weaker 127, 143 $cm^{-1}$ modes and stronger 176 $cm^{-1}$ mode compared to Huang *et al*.,[137] this is probably due to the minimisation of degradation of fresh GaTe flakes when they were transferred from air to the pressure transmission medium liquid-sealed environment immediately.[321,322] Therefore, this angle-resolved micro-Raman method can be reliably used to determine the crystal orientation of GaTe flakes based on the above Raman spectral fingerprints with much more convenience than the TEM method. On pressure increase, peak intensity showed different evolution for different modes, but all experienced a sudden change either in values or in pressure dependence at ~6.5 GPa for both orientations (see detailed discussion in Section 6.3.2.3). When the samples were compressed above ~6.5 GPa, strong peak splitting appeared on 115 and 209 $cm^{-1}$ modes simultaneously. These peak splittings are anisotropic, as a typical polarized Raman spectrum at 8.85±0.02 GPa demonstrated in Figure 6.8(b). From ~6.5 GPa, the 115 $cm^{-1}$ mode started to split into three peaks for both armchair and zigzag orientations, but the intensity ratio of these three peaks was different along different orientations. At the same time, the 209 $cm^{-1}$ mode also appeared to split into three peaks along the 0° orientation, having a high intensity middle peak surrounded by two weaker but obvious shoulder peaks located at both sides with almost equivalent frequency distance to the middle peak; while along the 90° orientation, this mode had only split into two peaks with comparable weaker intensity and frequency difference as that of the 268 and 283 $cm^{-1}$ modes. In addition, another low frequency Raman mode which was originally below our ~70 $cm^{-1}$ detection limit became observable from 6.5 GPa besides the 77 $cm^{-1}$ one at ambient pressure, however, this low frequency mode not only shows intensity change but also peak position shift with respect to polarization angle. Notably, along

the 0° orientation, the intensity for both the 77 $cm^{-1}$ and the middle peak of the split 209 $cm^{-1}$ mode was enhanced with increasing pressure such that it was even higher than the minimum of the three split 115 $cm^{-1}$ modes (Figure 6.8(b)). These peak splitting phenomena for GaTe flakes under pressure were reproducible in other samples and reversible from compression to decompression within the investigated range of 6.5-11 GPa. Both the splitting of peaks and change of peak intensity probably indicate a pressure-induced iso-structural phase transition as discussed for $MoS_2$, $WSe_2$.[186,188]

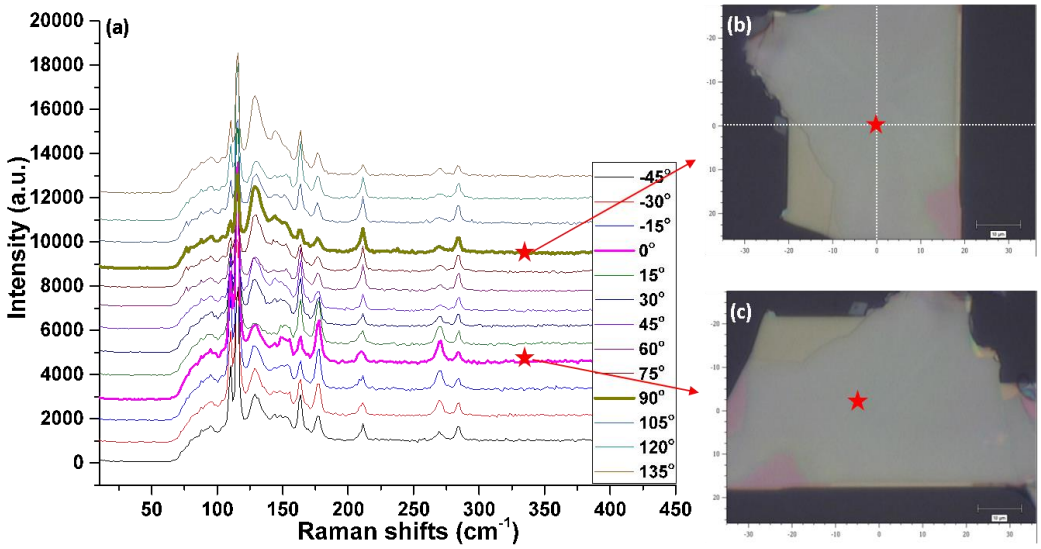


Figure 6.7. (a) Raman spectra as a function of polarization angle, as well as the optical images and measured laser position for corresponding (b) zigzag and (c) armchair in-plane crystal orientations of the GaTe flakes under 532 nm laser excitation. All scale bars represent 10 μm.

To further understand the anisotropic behaviour under pressure and the possible iso-structural phase transition, the pressure dependence of the Raman shifts of the 115 and 209 $cm^{-1}$ modes are shown in Figure 6.8(c-f). As known, the symmetry of the monoclinic GaTe lattice can be described by the $C_{2h}^3$ space group, where $A_g$ modes are out-of-plane lattice vibrations, while $B_g$ modes are in-plane lattice vibrations. Here, both split peaks can be ascribed to $A_g$ modes. Upon compression and decompression within the pressure range of 0-6.5 GPa, both modes show almost linear dependence on pressure for all orientations, but the slope is obviously different along 0° and 90° orientations for the 115 $cm^{-1}$ mode at 2.93±0.39 and 3.41±0.09 $cm^{-1}$ $GPa^{-1}$, respectively. After ~6.5 GPa, although the peak has split, the slope of this mode (assigned to the middle peak due to its smallest frequency gap with the peak position before peak splitting) for the above two orientations decreased to 2.72±0.2 and 2.74±0.12 $cm^{-1}$ $GPa^{-1}$, respectively, showing negligible difference. There is also no obvious distinction shown in the slope of the split lower frequency mode for different orientations, though it has only half of the compressibility of the middle peak, ~1.38±0.14 $cm^{-1}$ $GPa^{-1}$; however, the slope of the higher frequency mode of the split peak displays significant anisotropy, with slopes of 3.27±0.53 at 0° and 2.54±0.1 $cm^{-1}$ $GPa^{-1}$ at 90°. These differences in the slope have illustrated the anisotropic compressibility which is greater along the *b*-axis (90°) than the *c*-axis (0°) at lower pressure, but seems to have changed its preferred compressibility orientation after ~6.5 GPa, indicating an in-plane lattice distortion or

relaxation governed by layer sliding or a strengthening of the repulsive force between the Te atoms of the adjacent two monolayers upon compression. It is noted that the intensity of the split peaks also evolve anisotropically but in general increase gradually with pressure, implying the persistent enhancement of in-plane atomic interactions. In terms of the 209 $cm^{-1}$ mode, its slope of pressure dependence has negligible difference between $0^o$ and $90^o$ orientations, before and after ~6.5 GPa. However, this mode splits into three peaks along the $0^o$ orientation with a dominant middle peak accompanied by two weak shoulder peaks, while it only splits into two similar intensity peaks along the $90^o$ orientation from ~6.5 GPa. In addition, firstly, the split lower frequency shoulder peak along the $0^o$ orientation is much harder to compress, resulting in a slope value of 0.65±0.16 $cm^{-1}$ $GPa^{-1}$ compared to 3.56±0.25 $cm^{-1}$ $GPa^{-1}$ for the higher frequency shoulder peak; secondly, the slope of the split higher frequency peak is similar along $0^o$ and $90^o$ orientations and thirdly, the intensity of the split middle peak along the $0^o$ orientation increases much faster. All these anisotropic behaviours reveal that the structural symmetry and atomic interactions have changed at ~6.5 GPa. Besides the obvious 115 and 209 $cm^{-1}$ modes, other Raman modes without peak splitting behaviour including the 162, 176, 268 and 283 $cm^{-1}$ modes also demonstrate sudden changes either in peak position or in the slope of pressure dependence, again confirming a phase transition exists at ~6.5 GPa (as detailed shown in Figure 6.9).

The pressure dependence of the spacing Raman shifts between the 162 and 176 $cm^{-1}$ Raman bands ($B_g$ modes) and the 268 and 283 $cm^{-1}$ Raman bands ($A_g$ modes), shows a distinct change at the iso-structural transition pressure of 6.5 GPa, as displayed in Figure 6.8(g) and (h). Before ~6.5 GPa, there is almost no difference in either the value of the spacing Raman shifts or the slope of its pressure dependences for both $A_g$ and $B_g$ modes, including consideration of both $0^o$ and $90^o$ orientations; although Figure 6.9 shows that the slope of pressure dependence are slightly higher along the $0^o$ orientation than the $90^o$ orientation for all of the four Raman modes. However, after this critical pressure, a one third drop in spacing Raman shifts occurs suddenly for the pair of $A_g$ modes, with the drop along the $90^o$ orientation being the larger of the two, followed by a rapid increase with increasing pressure. Figure 6.9(c) and (d) illustrates that this drop mainly originates from the compressibility change of the 283 $cm^{-1}$ mode, for which the slope of pressure dependence changes oppositely along the two different orientations, with it being higher along the zigzag ($90^o$) orientation. For the pair of $B_g$ modes, although no sudden drop in the spacing Raman shifts occurs at the transition, a change from an increasing to a decreasing trend in the slope of pressure dependence is obvious. Also, along the $0^o$ orientation, the spacing Raman shifts saturates gradually, whereas along the $90^o$ orientation, it keeps decreasing faster with pressure mainly due to the quick hardening of the 176 $cm^{-1}$ mode than that along the $0^o$ orientation. As $B_g$ modes reflect in-plane vibrations, their anisotropic compressibility after ~6.5 GPa tells us that the lattice reconstruction (or lattice distortion) is mainly along the $0^o$ (i.e., armchair) orientation. At the same time, the strong hardening of the 268 $cm^{-1}$ mode (in-plane Ga-Ga vibration) and the strong softening of the 283 $cm^{-1}$ mode (out-of-plane Ga-Ga vibration) indicates that the distortion of out-of-plane Ga-Ga bonding plays a prominent role in the lattice reconstruction process.

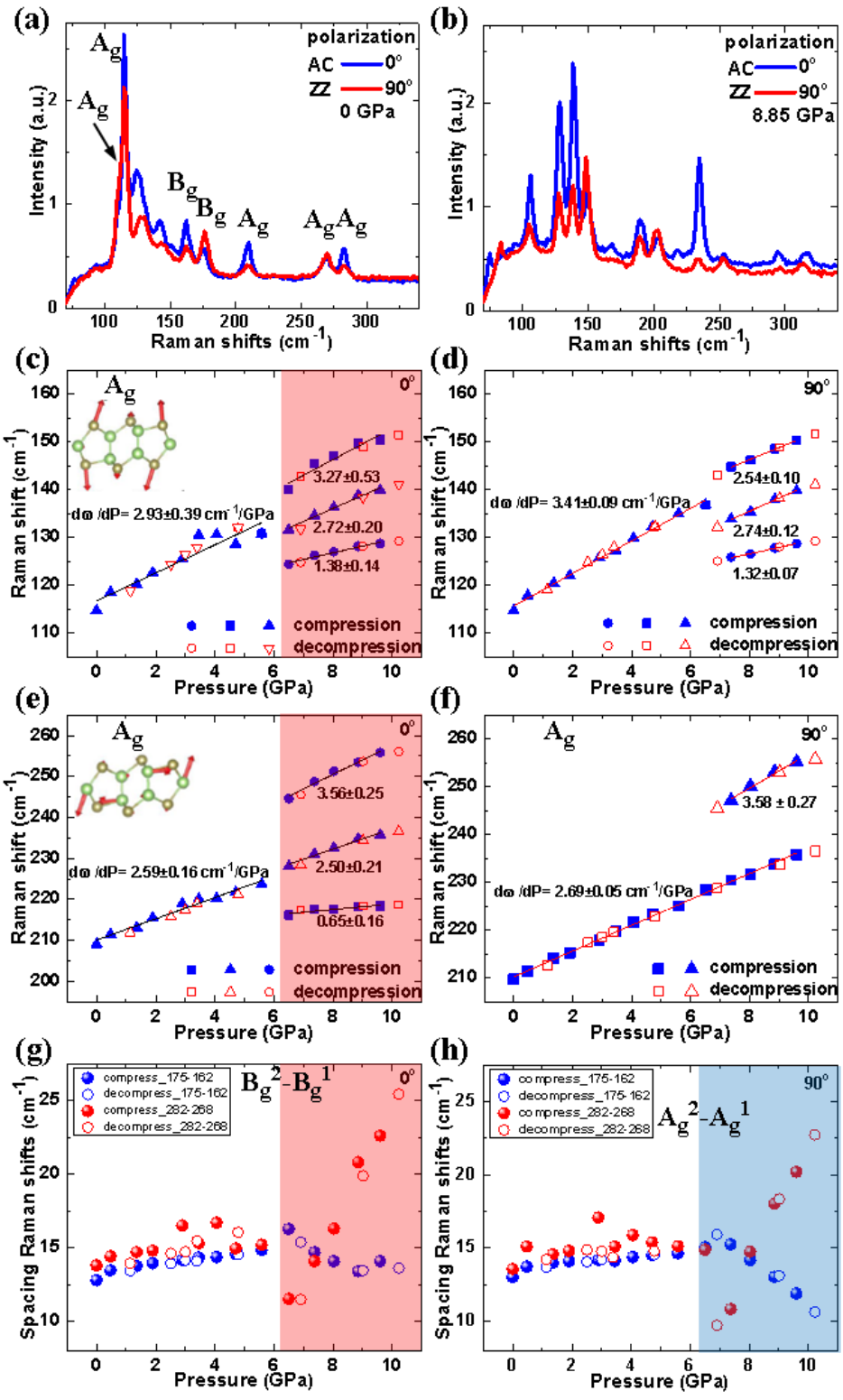


Figure 6.8. Micro-Raman characterization of multi-layered GaTe flakes under pressure. (a) Raman spectrum of GaTe multilayer flakes at ambient pressure, and at (b) 8.85GPa; polarization angle of 0° and 90° is along armchair and zigzag in-plane crystal orientation of the flakes. (c) and (d) Pressure dependence of the 115 $cm^{-1}$ mode, (e) and (f) the 209 $cm^{-1}$ mode, along the 0° and 90° orientations respectively. (g) and (h) The difference in Raman frequencies (spacing Raman shifts) between a pair of $A_g$ modes and a pair of $B_g$ modes along both 0° and 90° orientations.

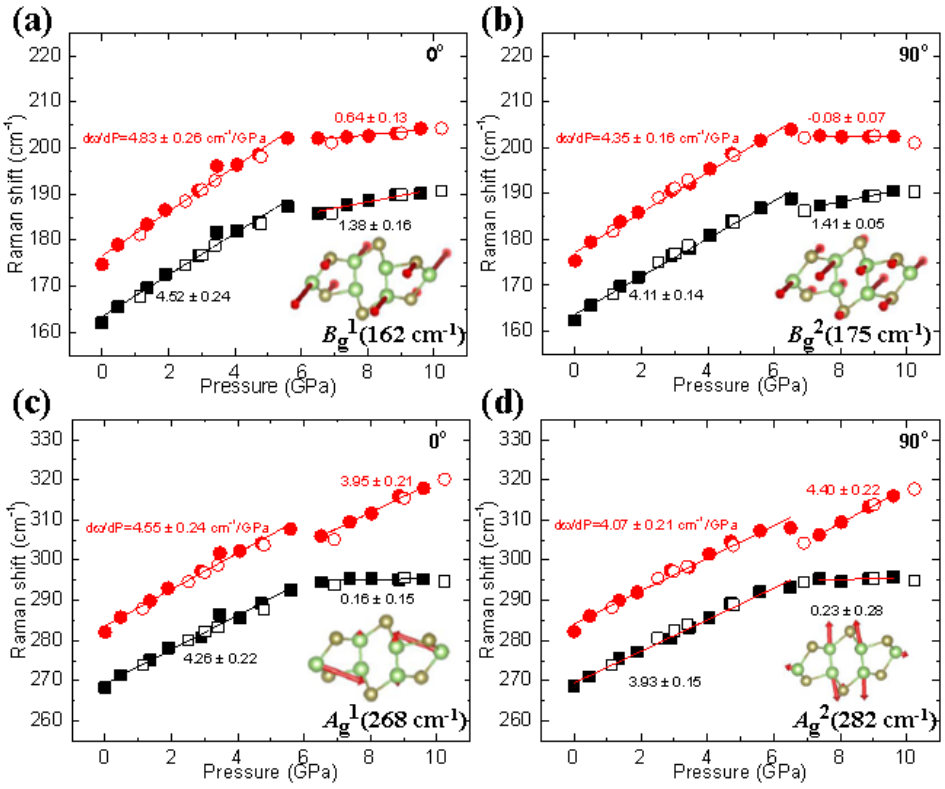


Figure 6.9. Raman peak frequencies between (a and b) a pair of $B_g$ modes (162 and 176 $cm^{-1}$ mode), and (c and d) a pair of $A_g$ modes (268 and 283 $cm^{-1}$ mode), as a function of pressure along 0° and 90° in-plane crystal orientations of the GaTe multilayers respectively.

### 6.3.2.3 Pressure dependence of Raman peak intensity and analysis

As mentioned above, the peak intensity of Raman modes also experiences sudden changes at about 6.5 GPa. For the 115 $cm^{-1}$ mode, as shown in Figure 6.10, the intensity at 0° orientation increases from ambient pressure to 6.5 GPa, while at 90° orientation the mode experiences a maximum at around 3 GPa and then decreases with pressure. After a significant drop at 6.5 GPa, the intensity along both orientations gradually increases again. Also, the split peaks present very different behaviours: the middle peak intensity is the highest at the 0° orientation and keeps increasing with pressure, while the relative intensity of the two split peaks with respect to the middle peak decrease gradually with pressure until they saturate; for the 90° orientation, the middle peak intensity is ranked 2$^{nd}$ and close to the minimum one, and the relative intensity of the split lowest frequency one with respect to the middle peak decreases but the split highest frequency one increases with pressures above 6.5 GPa. In Section 2.4.1.4 concerning Raman selection rules, the Raman peak intensity mainly depends on the constant values in the Raman tensor $\mathbb{R}$, which are structure symmetry related parameters. Therefore the intensity changes here reflect changes in the lattice and symmetry, but need more analysis.

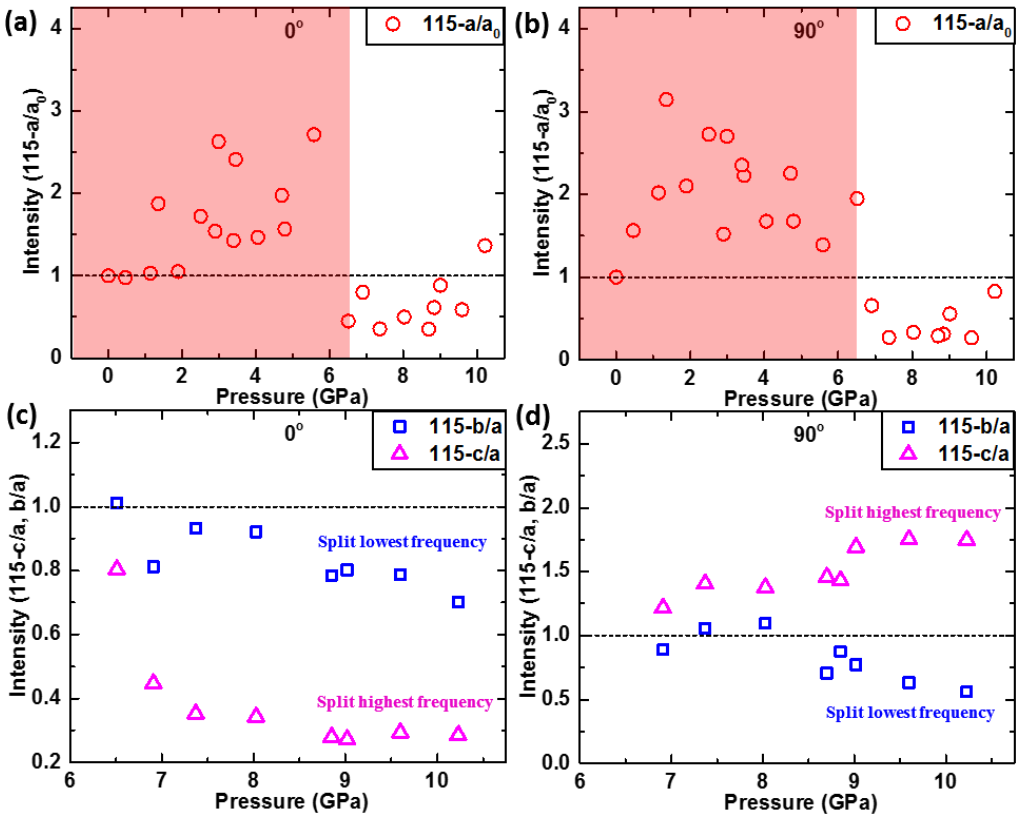


Figure 6.10. Raman peak intensity evolution of (a) and (b) domain peaks (115 $cm^{-1}$ mode), (c) and (d) split peaks, as a function of pressure along 0° and 90° orientations of the GaTe multilayers respectively. In this figure, 'a' represents the middle frequency phonon mode and 'b' represents the lower frequency phonon mode, while 'c' represent the higher frequency phonon mode.

For the other split mode at 209 $cm^{-1}$, the intensity change behaves very different for 0° and 90° orientations (see Figure 6.11): from ambient pressure to 6.5 GPa, the peak intensity almost doesn't change along the 0° orientation but increases along the 90° orientation; after 6.5 GPa, the split middle peak intensity seems keep increasing robustly along the 0° orientation, while a sudden drop followed by an increased trend is present along the 90° orientation. The relative intensity of the split two shoulder peaks with respect to the middle peak at 0° orientation also increase with increasing pressure. The intensity ratios of the split higher frequency peaks with respect to the original one show no significant trend after 6.5 GPa along the 90° orientation.

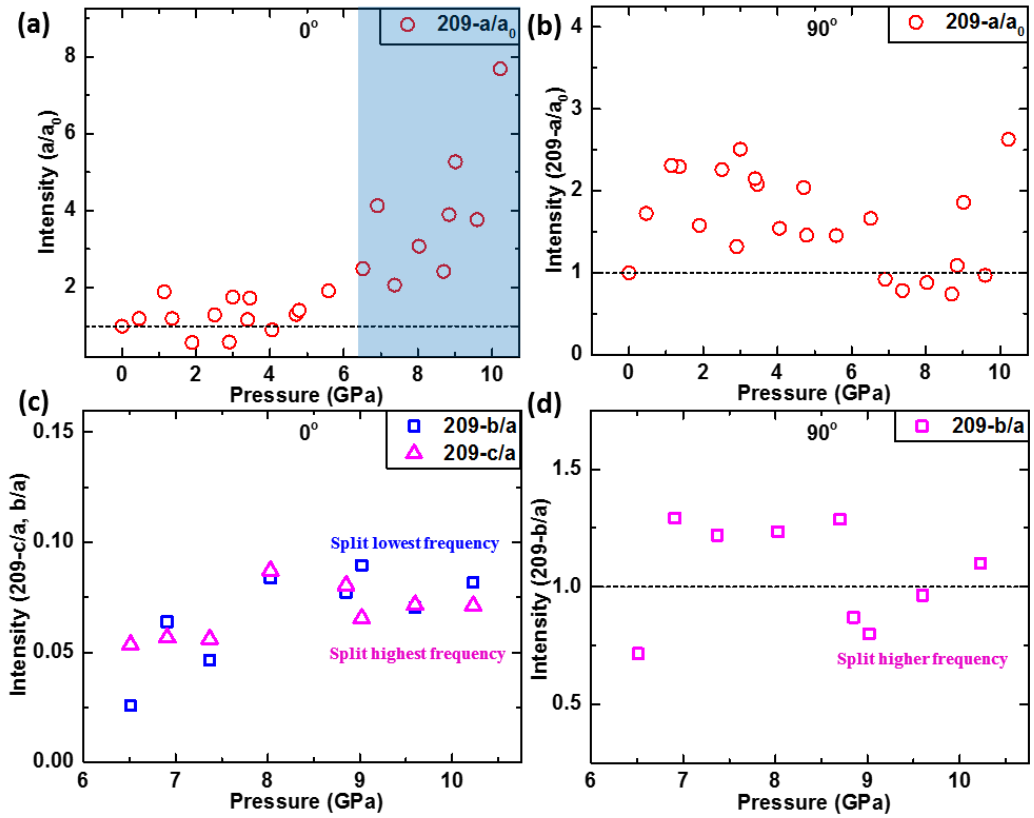


Figure 6.11. Raman peak intensity evolution of (a) and (b) domain peaks (209 $cm^{-1}$ mode), (c) and (d) split peaks, as a function of pressure along 0° and 90° orientations of the GaTe multilayers respectively. In this figure, along 0° orientation, 'a' represents the middle frequency phonon mode and 'b' represents the lower frequency phonon mode, while 'c' represent the higher frequency phonon mode; along 90° orientation, 'a' represents the lower frequency phonon mode while 'b' represents the higher frequency phonon mode.

Figure 6.12 demonstrated that the pairs of $B_g$ and $A_g$ modes present very different behaviours: for 0° orientation, both the intensity ratio of peaks 162/175 and 268/282 decrease gradually from ambient pressure to 6.5 GPa, and experience a sudden increase at 6.5 GPa followed by an increased slope until they saturate at about 9 GPa; for the 90° orientation, both the intensity ratio of peaks 162/175 and 268/282 drops suddenly at 6.5 GPa and then remains almost unchanged for both 0° and 90° orientations after 6.5 GPa, notably, the intensity ratio of peaks 162/175 saturates at ~1 before 6.5 GPa, while peaks 268/282 show a maximum of ~2 at ~2 GPa. Therefore, all the intensity changes of Raman modes present interesting phenomena, and agree well with the peak position change at 6.5 GPa, but the detailed mechanism still need further theoretical analysis.

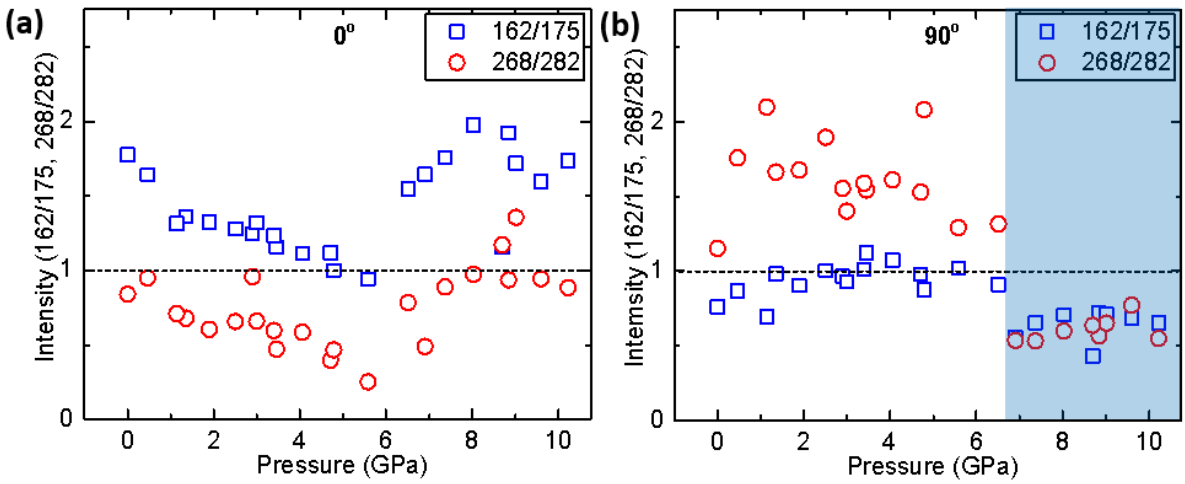


Figure 6.12. Raman peak intensity evolution of (a) 162/175 $cm^{-1}$ modes, (b) 268/282 $cm^{-1}$ modes, as a function of pressure along 0° and 90° orientations of the GaTe multilayers respectively.

### 6.3.3 High-pressure synchrotron XRD measurements

In order to verify the crystal structure types of those two possible phase transitions at ~6.5 GPa and ~15 GPa revealed from changes in the micro-Raman spectra, and to understand such phase transition mechanism from the knowledge of lattice dynamics, we carried out *in-situ* synchrotron XRD measurements by extending the pressure up to 46 GPa at room temperature under quasi-hydrostatic pressure using a symmetric DAC. Selected experimental diffraction patterns are displayed in Figure 6.13(a). All the Bragg peaks shift to larger diffraction angles, indicating the shrinkage of the GaTe lattice under pressure. At ambient pressure (i.e. 0 GPa), the XRD pattern is well fitted by the *C2/m* phase (see the bottom diffraction indices of Figure 6.13(a)) using Rietveld refinement with GSAS-II software.[310] The extracted lattice parameters from synchrotron XRD at ambient pressure are: a=17.43528 Å, b=10.47525 Å, c=4.0759 Å, and $\gamma$=104.692°, respectively, consistent with the results obtained from HRTEM. During refinement, diffraction from the rhenium gasket[323] and neon pressure transmitting media[324] were firstly considered and excluded in the following analysis: Re started to influence the diffraction pattern from ~3.6 GPa, while Ne appears after it freezes at ~5.3 GPa. Upon compression to 15.9±0.07 GPa, besides changes in the peak shape and intensity (broadening and lowering with pressure, respectively), there are several new characteristic peaks in the XRD patterns: at angles of about 7.77°, 8.91°, 15.57° and 20.07°, illustrating a first-order phase transition. On compression to 46.7±0.17 GPa, these new peaks become dominant, while residual peaks at 8.2° and 14.9° characteristic of the *C2/m* phase disappear gradually by about 23.5±0.1 GPa, implying the low-pressure phase co-exists with the high-pressure phase over a wide pressure range. This new high pressure phase can be well

reproduced by the common NaCl-type structure with the space group of *Fm-3m*; this is in agreement with the structure previously reported by Schwarz *et al*[193] who claimed a similar phase transition started at ~10 GPa in bulk GaTe powders. There seems no evident changes in the pattern at 6.9±0.05 GPa where strong peak splitting appeared in the micro-Raman spectra. After adding the *Fm-3m* phase into consideration either alone or co-existing with the monoclinic structure, the 6.9 GPa pattern can only be better fitted by considering *C2/m* phase. The broaden diffraction peaks at high pressure can be attributed to a high degree of lattice disorder resulted in the GaTe crystals.

Assuming that the *C2/m* phase of GaTe co-exists with the high pressure phase from 6 to 26 GPa where distinguishable changes can be found in the spectra, we performed refinement fittings of these XRD patterns using both *C2/m* phase and *Fm-3m* phase, and calculated the normalized lattice parameters $a/a_0$, $b/b_0$ and $c/c_0$ as well as the volume $V$ as a function of pressure, and the results are displayed in Figure 6.13(b-e). For comparison, previous experimental structural data and their fitted curves[193] as well as our first-principles predicted results are also included. It is apparent that, below 6.5 GPa (marked as $P_{T1}$), all data agrees well with those of Schwarz *et al*.[193] However, above $P_{T1}$, some deviations start to appear: lattice parameter $a$ enters a plateau firstly until ~11 GPa and then decreases slowly, reaching saturation at ~15 GPa (marked as $P_{T2}$); while $b$ and $c$ have an abnormal increase at $P_{T1}$ but continue to decrease again; accordingly, volume $V$ of *C2/m* phase seems to experience a small drop at $P_{T1}$ implying a structural transition but maybe also due to the imperfect quality of the data; the volume $V$ of the *Fm-3m* phase also seems no change in the region of 6-14 GPa but then decreases continually with the same trend as Schwarz *et al*[193] observed. To further check whether there is a structural or iso-structural phase transition at $P_{T1}$, we plotted the axis angle ($\gamma$) and axis ratio ($a/c$) as a function of pressure. As illustrated in Figure 6.13(f), $\gamma$ shows a linear decrease of ~2.5° in the range of 0-15 GPa and then decreases nonlinearly until saturating at about 101.5° near $P_{T2}$. This implies that the monoclinic structure still dominates after $P_{T1}$. It is apparent in Figure 6.13(g) that $a/c$ turns into an increasing trend at $P_{T1}$ from a linear decreasing trend. This reveals that the in-plane compressibility has prevailed over the out-of-plane compressibility when the GaTe was hydrostatically pressured above $P_{T1}$. This agrees with the strong softening trend of the 268 $cm^{-1}$ mode shown in Figure 6.8(h) and XRD results also confirm that the in-plane bonding has a drastic change after ~6.5 GPa.

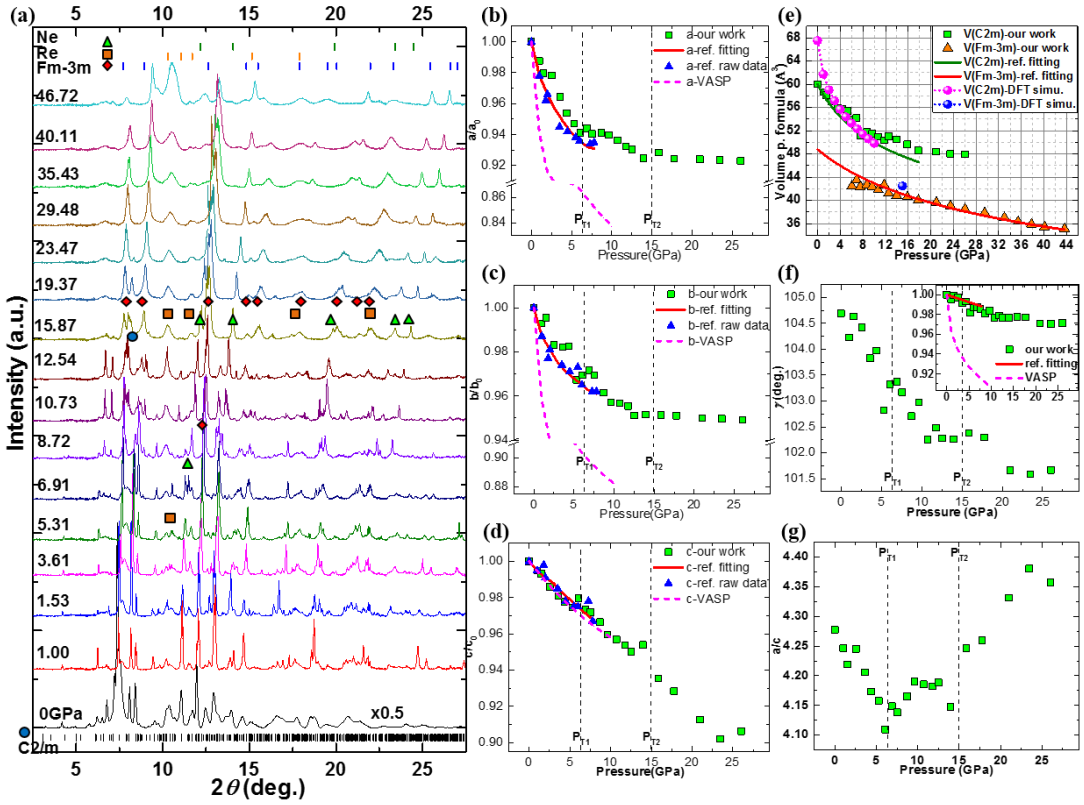


Figure 6.13. Structural lattice parameters in multi-layered GaTe. (a) Synchrotron XRD diffraction spectra of GaTe bulk powders as a function of pressure from ambient conditions up to 46.7 GPa (λ=0.4246 Å). Pressure dependence of the normalized lattice parameters (b) $a/a_0$, (c) $b/b_0$, (d) $c/c_0$, (e) volume per unit cell, (f) angle γ, and (g) axis ratio a/c. The experimental data and fitting curve from Schwarz et al. and theoretical calculated data are plotted for comparison.

### 6.3.4 USPEX prediction

Theoretical calculations using crystal structure prediction under pressure were carried out using DFT based USPEX (see the detailed introduction in Section 6.2.4).[311-313] Based on the pressure dependent micro-Raman and synchrotron XRD results, to identify the stable structures of the transformed phase at 15 GPa for fixed composition GaTe, the enthalpy of formation for every predicted structure with respect to the variable composition ratio of Te/(Ga+Te) in a wide range of structure candidates at 15 GPa were calculated. It is apparent from Figure 6.14(a) that *Fm-3m* phase has the lowest enthalpy of formation and is the most stable structure at 15 GPa, confirming the structure extracted from synchrotron XRD. This prediction also confirms the existence of a first-order phase transformation from monoclinic phase (*C2/m*) at ambient pressure into cubic phase (*Fm-3m*) at about 15 GPa within the multi-layered GaTe. We are also performing the structure search at 9 GPa using USPEX to check the structure change, as the above micro-Raman and synchrotron results indicate. According to the present progress, only the *C2/m* phase has the lowest enthalpy of formation at 9 GPa,

but the lattice parameters have changed. The detailed understanding of the physical mechanism for such two phase transitions induced by applied pressures are still underway.

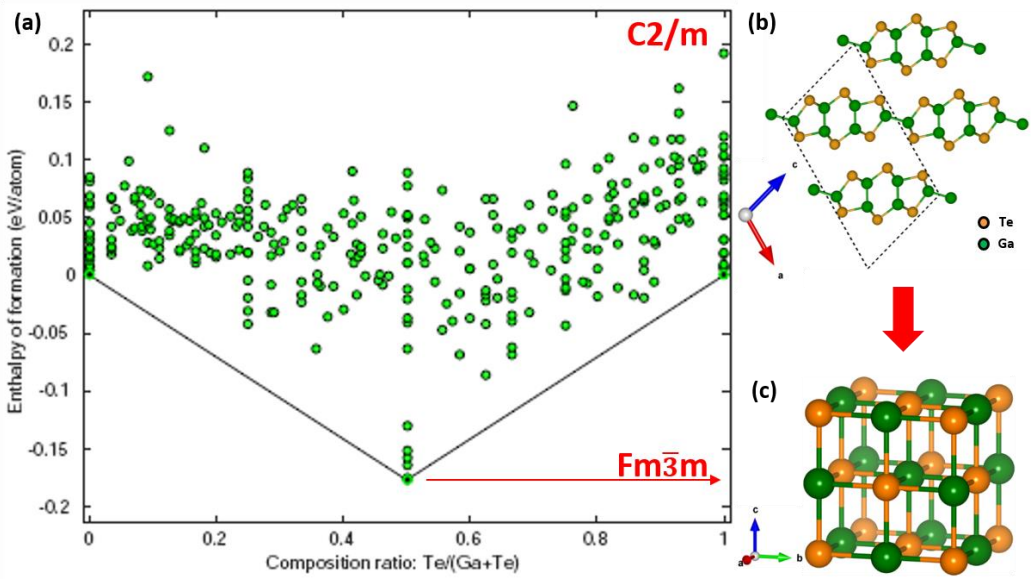


Figure 6.14. DFT-based USPEX predictions for the crystal structure change at 15 GPa of GaTe. (a) USPEX predicted enthalpy of formation with respect to the composition ratio of Te/(Ga+Te) for a wide range of structure candidates at 15 GPa; (b) schematic of monoclinic structure (C2/m) of GaTe at ambient pressure; (c) schematic of cubic structure (Fm-3m) of GaTe at 15 GPa. DFT calculations were mainly designed by the author, while performed by Tao Fan at Northwestern Polytechnical University who also helped to analyse the results.

## 6.4 Effects of pressure on electronic band structure

The electronic band structure of monoclinic GaTe under pressure from 0-9 GPa using the synchrotron XRD extracted lattice parameters were calculated. Figure 6.15(a) shows a direct bandgap of about 1.2 eV (DFT normally predicts slightly smaller bandgap than the actual value) located at the Z-point at ambient pressure, and the valence band maximum (VBM) and the conduction band minimum (CBM) along the first Brillouin zone are almost flat, which looks like a 'Mexican hat' structure along the *X-Γ-Z-I* line, consistent with previous works.[137,325,326] On pressure increase, the bandgap decreases at the initial stage, where the CBM decreases rapidly while the VBM increases slowly, and the VBM at the Γ-point drops dramatically. When the pressure is further increased to 6 GPa, significant changes happen on the global VBM which shifts from the Z-point to the Z-Γ line, resulting in an electronic transition from a direct to an indirect bandgap. An interesting phenomenon appears as the pressure further increases to 9 GPa, where the minimum indirect bandgap transition path jumps from the Z-(Z-Γ) direction to the Y-(X-Y) direction.

The density of states (DOS) was also calculated to help understand the contribution from different orbitals to the changes in bonding, as well as the changes in the states of both

conduction and valence bands. No significant changes happen in the total DOS shape from 0 GPa to 9 GPa, except some slight changes at the edge of the valence band. As shown in Figure 6.15(e), the main contribution to the valence band edge is from Te atoms. Therefore the changes in the valence bands can be correlated to the enhanced interaction between adjacent Te atomic layers which overcome their interlayer van de Waals force gradually with increasing pressure.

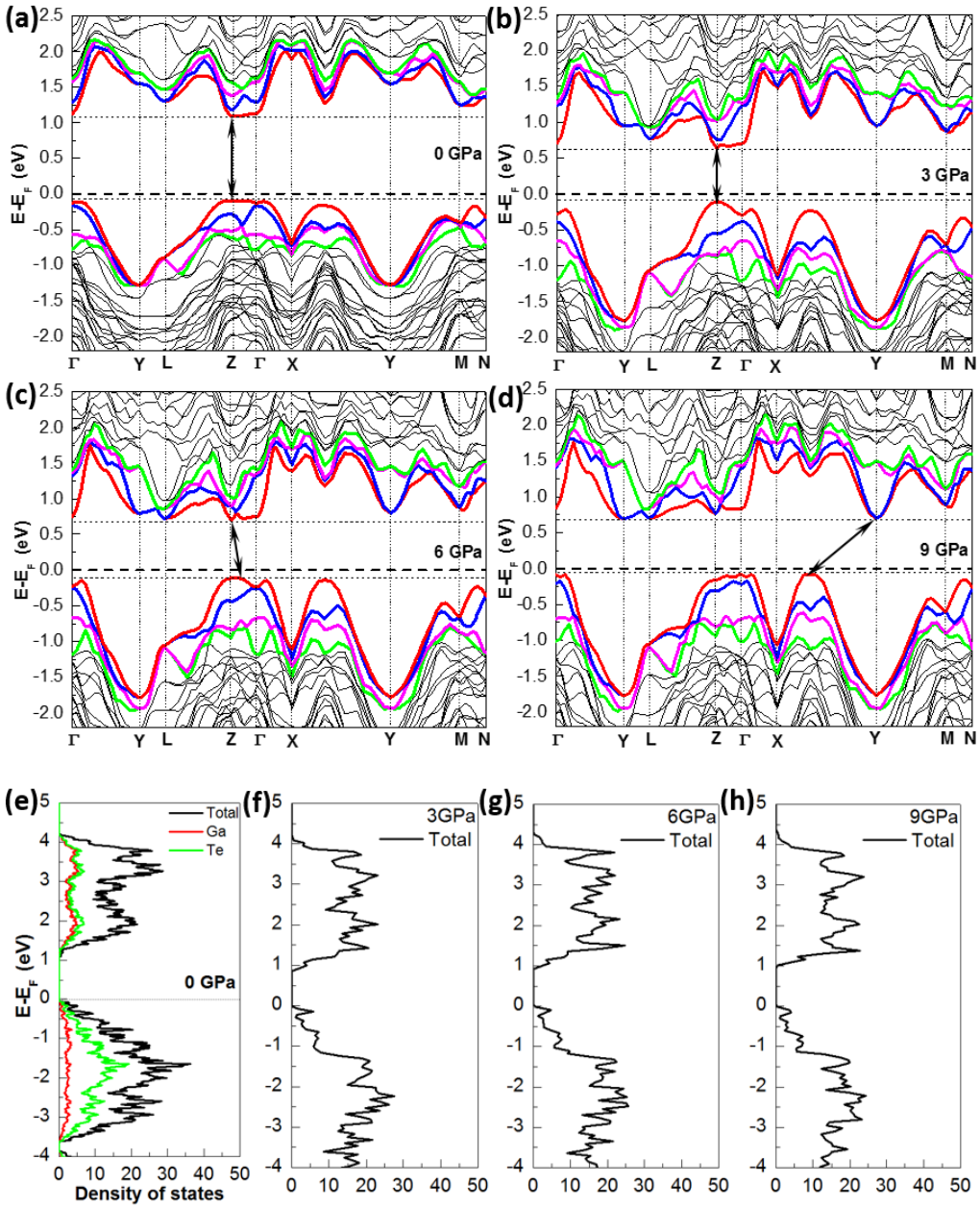


Figure 6.15. First-principles calculations for the relationship of electronic energy bands and density of states versus pressure in monoclinic GaTe. (a-d) electronic energy bands, and (e-h) density of states at 0 GPa, 3 GPa, 6 GPa and 9 GPa, respectively. DFT calculations were mainly designed by the author, while performed by Tao Fan at Northwestern Polytechnical University who also helped to analyse the results.

By plotting the direct bandgap at Z-point, Γ-point, the indirect bandgap at Z-Γ direction and the overall minimum indirect bandgap, an interesting trend is presented in Figure 6.16. Initially, all these bandgaps decrease rapidly with the increasing pressure, but all change to a slow increase trend after 3 GPa. It should be noted that at 6 GPa the bandgap changes from a direct to an indirect one, which increases with pressure at first but then changes to a decrease trend again after 7 GPa. Both the pressure-dependent bandgaps at Γ-Γ and Z-Γ direction behave a similar trend, and start to decrease at a samller pressure of 5 GPa. While the bandgap at Z-Z direction keeps increasing to an even higher value than that of Γ-Γ direction at 9 GPa. Looking at Figure 6.15(b-d), the crossover from direct to indirect between 3 GPa and 6 GPa is mainly due to the change of VBM along the Z-Γ line; notably, the VBM between X-Y line also keeps increasing with pressure. While the minimum indirect path transition from 6 GPa to 9 GPa is not only due to changes of VBM along the Z-Γ line and X-Y line, but also because of the faster decreasing of CBM at the Y-valley and the increasing of CBM along the Z-Γ valley. However, to understand the changes of VBM and CBM with pressure which in fact originate from the changes of bonding characters, futher accurate calculations of the sub-orbital distributions are needed.

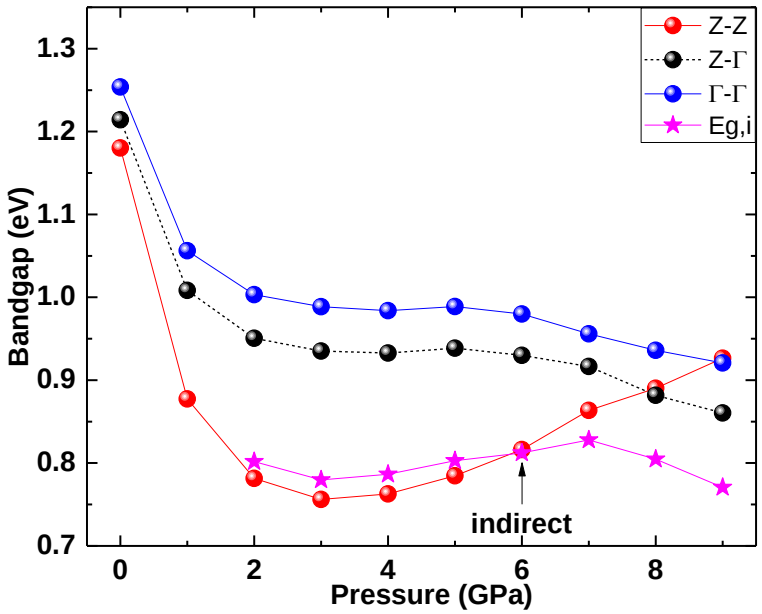


Figure 6.16. Calculated relationship of bandgap versus pressure in monoclinic GaTe. Red, blue and black dots represents the Z-Z, Γ- Γ, and Z- Γ transitions, respectively; star represents the indirect bandgap.

The electronic band structure of transformed cubic GaTe at 15 GPa was also calculated, as displayed in Figure 6.17. The metallic nature of cubic GaTe is evident as the Fermi level crosses through both the valence and conduction bands. The corresponding DOS also confirmed no bandgap near the Fermi level. The detailed physical mechanism of such structure transformation is under intensive analysis.

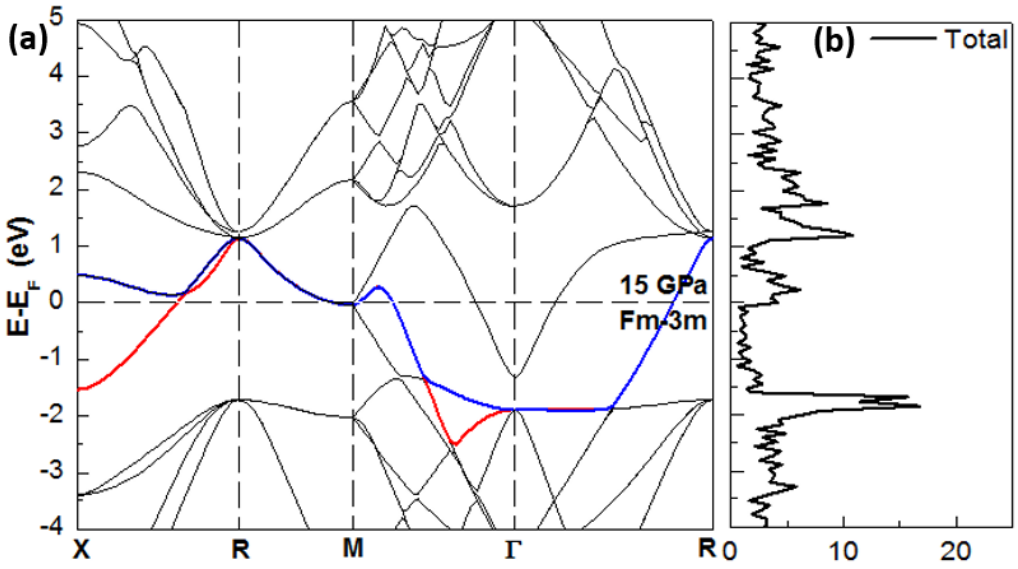


Figure 6.17. First-principles calculated electronic energy bands and density of states in cubic phase GaTe. (a) Electronic energy bands; (b) density of states. DFT calculations were mainly designed by the author, while performed by Tao Fan at Northwestern Polytechnical University who also helped to analyse the results.

## 6.5 Effects of pressure on phonon dispersion

The full phonon dispersion of monoclinic GaTe under ambient pressures and cubic phase GaTe at 15 GPa were calculated. Figure 6.18 shows no imaginary frequency in both phonon dispersion spectra, indicating the stability of the two structures formed at the above two pressures. Three acoustic branches were apparent in both structures, while fewer optical branches are shown in the cubic phase due to there being fewer atoms in its unit cell. As shown in Figure 6.18(a), the monoclinic phase at the Brillouin zone centre (Γ) has significant differences in the acoustic phonon branches and acoustic velocities between the Γ-Y (zigzag) and Γ-Z (armchair) directions; this illustrates that significant anisotropy exists in thermal conductivity along different in-plane crystal orientations. In contrast, the acoustic phonon branches in Figure 6.18(b) imply a much higher thermal conductivity for the cubic phase.

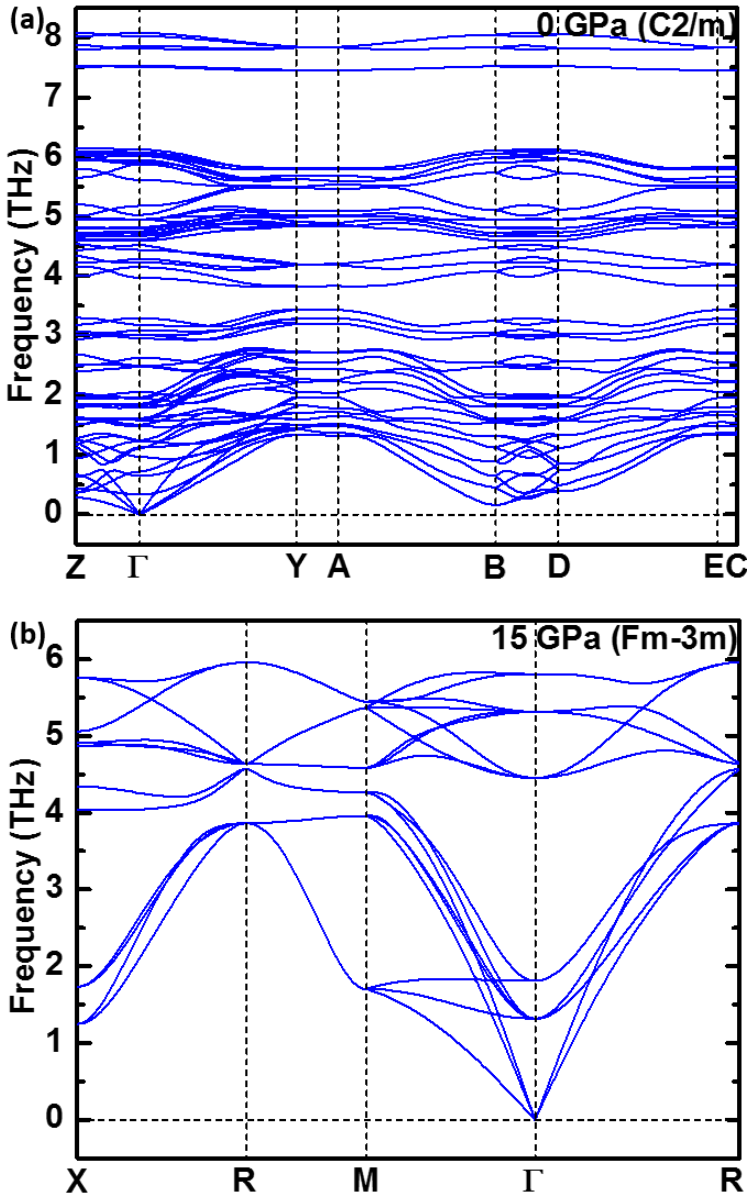


Figure 6.18. Phonon dispersion (phonon frequency versus momentum q) calculated by DFPT in VASP for GaTe at (a) 0 GPa (Y corresponds to in-plane zigzag orientation, while Z corresponds to in-plane armchair orientation), and (b) 15 GPa along high symmetry points. DFT calculations were mainly designed by the author, while performed by Tao Fan at Northwestern Polytechnical University who also helped to analyse the results.

## 6.6 Conclusions

In Summary, we have systematically explored the pressure-dependent anisotropic properties of multi-layered GaTe using combined experimental techniques with first-principles calculations. We have demonstrated a strong anisotropic and reversible peak splitting of Raman modes starting at ~6.5 GPa, originating from a lattice distortion induced iso-structural phase transition which is mainly due to the enhanced interaction between Te atoms in adjacent monolayers over their van de Waals gap, inducing changes in the in-plane

bonding. A subsequent structural phase transition into a cubic phase at ~15 GPa accompanied by an electronic transition from semiconducting to metallic has also been observed. The transformed iso-structural monoclinic phase was also found to co-exist with the cubic phase across a broad pressure range due to the inhomogeneous strain introduced by the mixed phase formed during compression. These pressure-tuned properties of multi-layered GaTe flakes provide new insights for further investigation and the manipulation of strain-dependent anisotropic light-material interactions. Our findings also reveal new opportunities for low symmetry materials in phase-switch devices and strain-modulated optoelectronics.

# Chapter 7.

## Thermal and Mechanical Properties of GaTe Multilayers

In this chapter, the thermal properties in particular the in-plane anisotropic thermal conductivities of free-standing GaTe multilayers (~150 nm-thick) were studied. Then, considering the application in 2D flexible devices, the mechanical properties of multilayered GaTe including $SiO_2$/Si substrates supported and suspended flakes were analyzed.

### 7.1 Introduction

2D materials have attracted tremendous interests ascribing to their extraordinary optical, electronic and mechanical properties compared to their bulk counterparts. Although electronic and optical properties of 2D materials have been extensively investigated, gaining insight into their thermal and mechanical properties, in particular for the recently emerging low in-plane symmetry layered materials, such as 2D BP,[142,149,152] GaTe, etc., is just starting or still lacking. Due to the puckered nature of their in-plane lattice structure, intriguing anisotropic properties have been shown on these low in-plane symmetry 2D materials, for example, multilayered BP has demonstrated anisotropic electron-photon and electron-phonon interactions, thermal conductivity and thermoelectric properties[142] along its armchair and zigzag orientations,[136,142,149,152] enabling potential applications in novel electronic and optoelectronic devices[134,142,327,328]. However, no experimental demonstration about such in-plane anisotropy of thermal conductivity and mechanical properties are reported in here studied GaTe multilayers and 2D samples yet, mainly due to the technical challenges in sample preparation and measurements. As thermal management is important in all electronic, optoelectronic and photonic devices, including 2D based nanoscale devices, it is extremely necessary to understand the thermal transport in 2D materials, especially the intriguing anisotropic in-plane thermal properties due to its potential applications in nano-thermal diode/rectifier. Besides, thermoelectric conversion requires materials with low lattice thermal conductivity[329-332] which is a typical character of some low-symmetry layered materials, this

is another reason to study these materials.[142,152] Since an ultrahigh intrinsic Young's modulus and strength were predicted and characterized using AFM based nano-indentation in graphene,[214] much attention was also paid on the mechanical properties of other 2D materials, with future applications in curved window surfaces, rollable screens and so on. Flexible devices also require knowledge about fracture, deformation ability, and potential phase transition of these 2D materials. Also, notable electrical-mechanical coupling is likely to cause a change in the electronic structure of 2D materials during straining process[333] for flexible device application, which requires knowledge of their individual mechanical abilities.

## 7.2 Experimental details

### 7.2.1 Fabrication of materials and structures for thermal and mechanical characterization

To characterize the in-plane anisotropic thermal and mechanical properties of layered GaTe, suspended GaTe monolayer-to-multilayer flakes are needed. A series of membrane structures consisting of two mutually perpendicular rectangular slits to form "T-shape" structures were patterned and fabricated on $SiO_2$/Si substrates, and are shown in Figure 7.1. The rectangular geometry of these slits was designed to be 3-6 μm in width, 20-40 μm in length, and 3-6 μm in separation between the two perpendicular slits. These slits were fabricated on 300-nm-thick $SiO_2$ films which was formed by thermal evaporating on the surface of Si substrates. Then the $SiO_2$/Si substrates were cleaned using acetone and IPA for 5 minutes ultrasonic separately, and dried using nitrogen gas. After spin-coating a thin layer of positive photoresist (S1805) and pre-baking the photoresist immediately under conditions of 115 $^oC$ for 60 s, an UV lithography with an exposure for 30-60 s was used, followed by rinsing the samples in the MF319 developer for 90 s and DI water to remove the exposure parts and developer residue, respectively. Notably, after drying using nitrogen gas, it is necessary to test the quality especially the edge resolution of developing under the microscopy. Also, a post-baking at 90 $^oC$ for about 60 s was needed to strengthen the adhesion between the remaining photoresist and substrate surface.

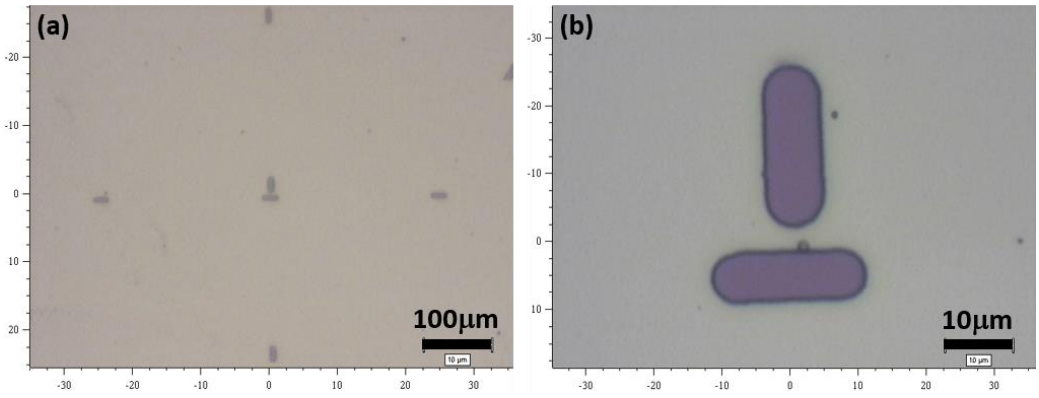


Figure 7.1. "T-shape" membrane structures patterned and fabricated on $SiO_2$/Si substrates: (a) 5× objective; (b) 50× objective.

The patterned exposure parts of $SiO_2$ films were then etched using reaction ion etching (RIE) using $SiF_6$ reactant for about 30 minutes. This dry etching would remove the patterned $SiO_2$ and stop at the Si surface. These etched samples were rinsed in the acetone and DI water to remove all the remaining photoresist. It should be noted that the above $SiO_2$/Si substrates normally needed to be further treated in the oxygen plasma for about 10 minutes to enhance their surface activity to minimize the surface roughness and provide stronger vdW interactions between the flakes and the substrate. A cross section schematic of the resulting structure is shown in Figure 7.2.

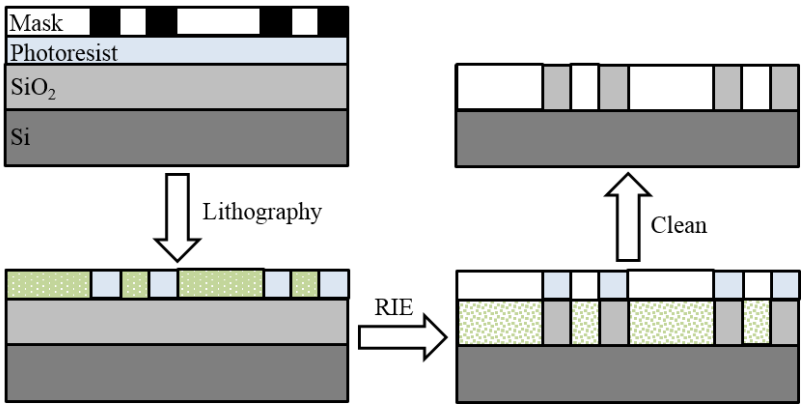


Figure 7.2. A schematic process of the 'T-slits' membrane structure fabrication and a cross section schematic of the RIE etched structure along the 'T-slits' axis.

The GaTe multilayer flakes were then fabricated by exfoliating from the bulk crystals using Scotch tape. The initial GaTe flakes were ~100-400 nm thick and needed to be further thinned to obtain few-layers or even monolayer flakes through repeated exfoliation of the flakes between adhesive tapes. Then the tape was attached to a piece of PDMS substrate where the GaTe flakes were directly exfoliate onto after peeling off the tape; this exfoliation

method would result in negligible glue residue on the GaTe. Flakes on the PDMS were then characterized using polarized micro-Raman spectroscopy. Raman spectra from the PDMS substrate and the tape were also collected for investigation of their influence. For the characterization of in-plane anisotropic properties, the zigzag and armchair crystal orientations of GaTe flakes were firstly determined through angle-resolved polarized micro-Raman spectroscopy, the same as that detailed described in Section 3.1.4. The hot pick-up dry transfer technique was then exploited to directional transfer the target GaTe flakes with determined in-plane crystal orientation aligned onto the parallel or vertical slit orientation of the "T-slits" membrane structure on the $SiO_2$/Si substrates; this dry transfer technique was detailed introduced in Section 3.5.

### 7.2.2 Nanoindentation experiments

To investigate and understand the mechanical properties of the above GaTe multilayer flakes, nanoindentation tests (Hysitron TI 980 Nanoindenter) were performed on the supported and suspended GaTe flakes which were obtained by transferring them onto the smooth area of the plasma treated $SiO_2$/Si substrates and the aforementioned "T-slits" patterned membrane areas of the $SiO_2$/Si substrates, respectively. A Berkovich indenter with a $65.3^o$ tip angle was used to generate a series of indents with different indent depth on the sample under the displacement control mode. To explore the morphology evolution and visualize the crack details of indents that were induced by different forces, high-resolution field-emission SEM (Quanta200 FEG, FEI) images were taken. Detailed sample thickness, indentation depths and the topography of indents were obtained through AFM using the tapping mode. Residual stress and its distribution after indentation were characterized through measuring the Raman shifts of typical Raman modes. A reference Raman spectrum of GaTe flakes was measured in prior at the indent area before performing the indentation which was later used for the evaluation of residue stress. According to the results in Chapter 6, 210 $cm^{-1}$ peaks were used to determine the residue stress as they shift with 2.59 $cm^{-1}$/GPa and had a relative higher peak intensity for better peak decoupling.

## 7.3 Thermal properties of GaTe multilayer flakes

### 7.3.1 Absorption, reflectivity and transmissivity of GaTe multilayer flakes

Considering the easier degradation of GaTe multilayer flakes in the ambient condition after exfoliation, which was thought as being mainly affected by the oxygen,[321,322] micro-Raman experiments were then all conducted in the inertia nitrogen atmosphere at room temperature via a Linkam THMSG 600 stage to investigate the thermal conductivity of GaTe flakes. The GaTe flake along different in-plane crystal orientations is shown in Figure 7.3. In contrast with the methods developed by Luo *et al.*,[149] where the following description in

Section 7.3 about the in-plane thermal conductivity extraction of GaTe flakes are mainly based on, to best achieve a one-dimensional heat transfer, apart from the special designed 'T-slits' membrane structures, a semi-cylindral lens enabling to produce a laser focal line aligned with the slits were used, instead of a circular spot, as a schematic illustrated in Figure 7.3(a, b) and an experimental image demonstrated in the inset of Figure 7.3(b). The Gaussian width $w_0$ and length $l_0$ of the measured laser focal line are determined to be 1 and 25 μm, respectively, using ImageJ software (see Figure 7.3(c)). Notably, the laser focal line needs to be aligned to the centreline of the slit during the measurements, this creates a centralized one-dimensional heat flow in the suspended GaTe film (about 150 nm thick) and results in the dominant heat flow generated along the width direction of the slit, hence isolating the thermal conductivity along the armchair and zigzag orientations.

The GaTe flake is heated up by the absorbed laser power ($P_A$); Raman spectrum were collected as a function of laser power and converted into the temperature rise generated at the laser focal line as a function of laser power. The absorbed laser power in the GaTe film can be determined through the following equation: $P_A = AP = (1\text{-}R\text{-}T)P$, where $P$ represents the incident laser power, $R$ means the reflectivity, $T$ is the transmissivity and $A$ stands for the absorptivity. By transferring the same color (of the same thickness, confirmed by AFM) GaTe flakes onto a center-emptied copper grids (20×20 $\mu m^2$ for each grid) which was fixed on an extra trench (a series of 2×10 $mm^2$ rectangular holes in dimension fabricated by pattern-etching an aluminum thin plate), the reflectivity of the GaTe films was determined by comparing the measured back-reflected laser intensity from suspended GaTe flakes with the reflected intensity from an aluminum-coated mirror which was used as a reference. The transmissivity of the multilayered GaTe flake was measured under the slits, and was obtained by dividing the transmitted laser intensity from the GaTe flake-covered slits by that measured at the neighbour empty slits. It should be noted that $R$, $T$ and $A$ in nature are all anisotropic quantities considering the crystal structure of the GaTe, as shown in Figure 7.3(d). The measurements were performed at different incident laser power; slight differences in the reflectance and absorption were found, therefore averaged values for absorptivity and reflectivity from different incident laser powers were used for both armchair and zigzag orientations. The absorptivity along armchair and zigzag orientations are about (66.1 ± 8) % and (82.9 ± 5.9)%, while the reflectivity are about (23.2 ± 5.6) % and (9.4 ± 1.6)% respectively.

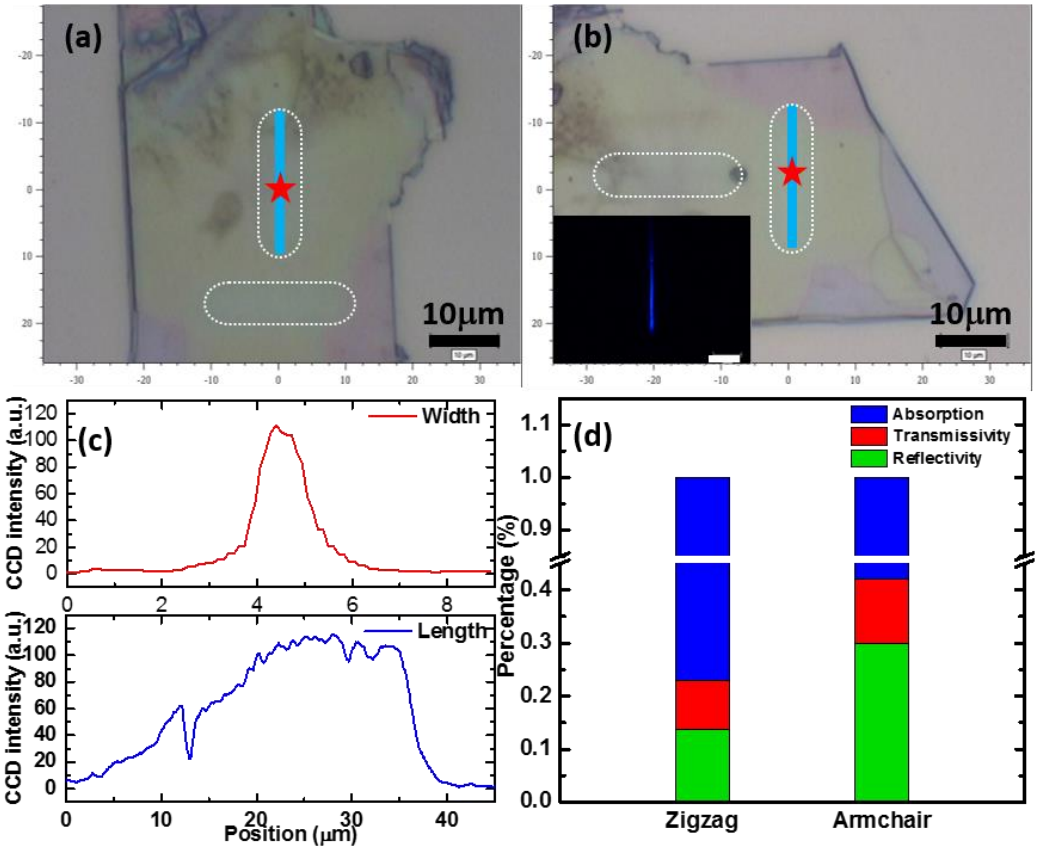


Figure 7.3. Measured GaTe flakes along in-plane crystal orientation of (a) 90$^{o}$ (zigzag), (b) 0$^{o}$ (armchair). Inset: measured laser focal line. All the scale bar represents 10 μm. The dash outline is the geometry of the underneath slits. The blue solid line within the dash outline represents the schematic of the laser focal line, and the star marks represent where the center of the laser focal line is positioned. (c) The experimentally measured width and length of the laser focal line, where the Gaussian FWHM width $w_0$ and length $l_0$ are determined to be 1 and 25 μm, respectively. (d) The absorption, transmissivity and reflectivity of the ~150 nm-thick suspended GaTe flake with respect to zigzag and armchair in-plane crystal orientations under the laser power (11.6 ± 0.03 μW ~ 137.7 ± 1.3 μW) incident.

### 7.3.2 Calibration of temperature dependence

The Raman optical thermometer of each GaTe flake, i.e. the temperature dependence of target Raman modes, was calibrated using the InVia Raman spectrometer and Linkam heating stage which was filled with nitrogen atmosphere. During the calibration process, the power of the incident laser was chosen to be <160 μW to minimize the laser heating effects, this was determined through a preliminary power dependent measurements until the shifts of all Raman modes achieve convergence by showing negligible difference. Considering the anisotropy of the material, the calibrations along both in-plane armchair and zigzag crystal orientations under the polarized laser were performed separately. Figure 7.4(a) shows

representative Raman spectrum collected at different temperatures from the ~150 nm-thick suspended GaTe flake under the excitation of polarized laser along armchair orientation, in which we can find that the Raman peaks, when on heating, shift towards relative lower frequency. Figure 7.4(b) shows an example of the 210 $cm^{-1}$ $A_g$ mode. For temperature rise less than 100 $^oC$, the frequency change of the Raman mode can be expressed as $\omega = \omega_0 + \chi\theta$ and the higher order terms can be neglected (see Section 2.4.1.6). In this equation, $\omega_0$ is the Raman frequency at room temperature, $\chi$ is the temperature coefficient, and $\theta$ is the temperature rise. For different in-plane crystal orientations of the ~150 nm-thick GaTe flake, the extracted temperature coefficients determined were $\chi_{armchair,\ 210}$= -0.0198±0.002 $cm^{-1}K^{-1}$ and $\chi_{zigzag,\ 210}$= -0.0204±0.003 $cm^{-1}K^{-1}$ respectively as shown in Figure 7.4. With the laser polarization aligned along the zigzag orientation there is a larger absolute temperature coefficients. This is probably caused by the anisotropic in-plane thermal expansion of the material during the heating process.

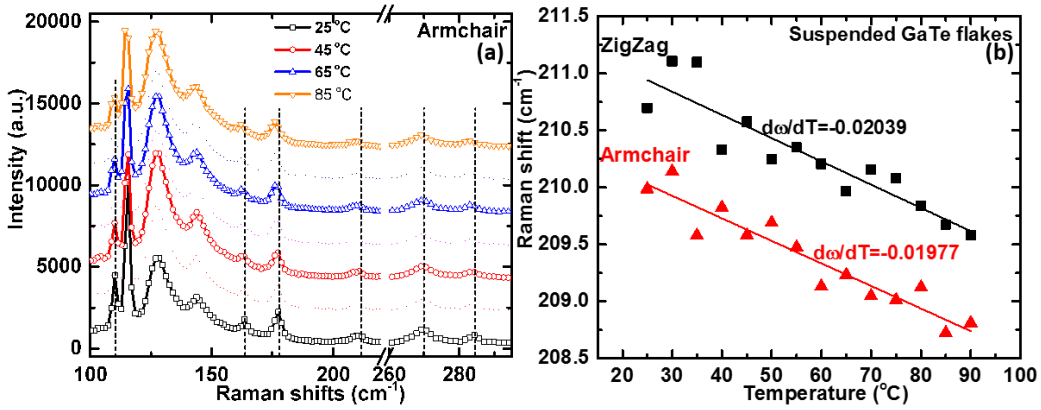


Figure 7.4. (a) Four sample Raman spectrum taken at 25, 45, 65 and 85 $^oC$ with the laser polarization aligned along the armchair orientation; (b) measured Raman shift of the 210 $cm^{-1}$ mode as functions of temperatures for both the laser polarization aligned along the in-plane armchair and zigzag orientations for ~150 nm-thick GaTe flakes. The solid lines show a linear fit to the experimental results.

### 7.3.3 Thermal conductivity of GaTe and its in-plane anisotropic properties

Figure 7.5 shows the measured temperature rise from Raman shifts ($\theta_{Raman}$) induced by different absorbed laser powers for the ~150 nm thick suspended GaTe flake. This temperature rise and the experimentally measured slopes $d\theta_{Raman}/dP_A$ was used for the following extraction of thermal conductivity using analytical steady-state thermal models.

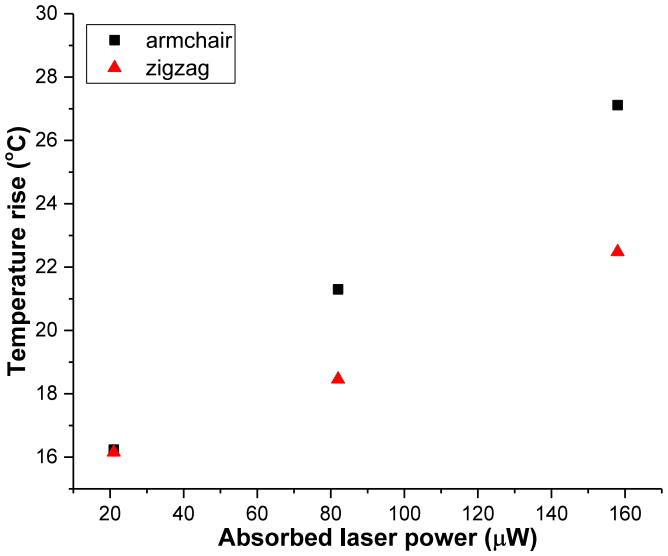


Figure 7.5. Laser power dependent temperature rise of the 150 nm-thick GaTe flake determined by the Raman spectra along armchair and zigzag in-plane crystal orientations for 210 $cm^{-1}$ modes.

A 3D anisotropic heat transport equation built by Luo *et al.*,[149] was used to extract the in-plane thermal conductivity of a GaTe flake, which is written as:[149]

$$\frac{\partial}{\partial x}\left(k_x \frac{\partial \theta}{\partial x}\right) + \frac{\partial}{\partial y}\left(k_y \frac{\partial \theta}{\partial y}\right) + \frac{\partial}{\partial z}\left(k_z \frac{\partial \theta}{\partial z}\right) + \dot{q} = 0. \tag{7.1}$$

This equation was then solved using the finite volume method[149], among which the heat source term ($\dot{q}$) of the laser focal line can be expressed as:[149]

$$\dot{q} = \frac{\alpha(1-R)P}{\pi w_0 l_0} e^{-(w^2/w_0^2 + l^2/l_0^2)} e^{-\alpha z}, \tag{7.2}$$

where $\alpha$ stands for the absorption coefficient, while $l$ and $w$ represents the corresponding coordinates along the length and width directions of the laser focal line, respectively. The Gaussian-weighted-average form[149] is then used to express the temperature rise within the laser focal line:

$$\theta_{Raman} = \frac{\int_0^t \int_0^\infty \int_0^\infty \theta e^{-(w^2/w_0^2 + l^2/l_0^2 + 2\alpha z)} dw dl dz}{\int_0^t \int_0^\infty \int_0^\infty e^{-(w^2/w_0^2 + l^2/l_0^2 + 2\alpha z)} dw dl dz}, \tag{7.3}$$

where $t$ represents the thickness of the GaTe film while the factor 2 is from the absorption of Raman scattered photons when they travel backwards to the surface within the film. By comparing the calculated slopes with the experimentally measured slopes, both the armchair and zigzag orientation in-plane thermal conductivity ($\kappa_{armchair}$ and $\kappa_{zigzag}$) of the suspended GaTe flakes can be extracted by iterative calculations between the two directions. For the above measured 150 nm thick suspended GaTe film, the in-plane anisotropic thermal conductivities were extracted as: $\kappa_{zigzag}$ = 5 ± 0.31 W/mK, while $\kappa_{armchair}$ = 3 ± 0.21 W/mK.

These anisotropic values are about one factor of three lower than those corresponding values of BP with similar thickness,[152] and may be much lower for thinner samples. The errors of $\kappa_{armchair}$ and $\kappa_{zigzag}$ are determined by standard error method and error propagation theory, i.e., $\sigma_k = [\sum(A_i\sigma_i)^2]^{1/2}$ where $\sigma_i$ is the error of a single parameter, and $A_i$ represents the linearized coefficient of this parameter has on the final result. All uncertainties of concern have been concluded for the measured flake here such as that of temperature coefficient $\chi$, temperature-power slope $d\theta/dP$, thickness $t$ and absorptivity $A$. This very low lattice thermal conductivity of GaTe multilayers and its anisotropy are thermally beneficial for the thermoelectric applications. In further, the thickness and temperature dependence of the lattice thermal conductivity and the anisotropy of GaTe multilayers are under further investigation, helping to understand the thermal transport at nano- or even atomic scale.

## 7.4 Mechanical properties of GaTe multilayer flakes

### 7.4.1 Mechanical properties of $SiO_2$/Si supported GaTe multilayer flakes

#### 7.4.1.1 Nanoindentation characterization

Figure 7.6 shows representative load-displacement (*P-h*) curves obtained from different indentation depth up to 300 nm, on a ~375 nm thick GaTe multilayer flake. Due to the existence of defects and preferred cleavage plane in single crystal layered GaTe materials, region-to-region variations in thickness may exist in the exfoliated flakes (has the same crystal plane for all exfoliated surfaces). This variation in thickness becomes more pronounced in the thicker flakes, but many relative larger flat surface regions can still be obtained. Considering such thickness variation of exfoliated flakes, the thickness for each indent was measured by AFM according to their relative height to the substrate and listed in Table 7.1. As apparent, the main difference in these *P-h* curves can be categorized into three types: (I) only pop-in (PI), relative smooth loading curve with multiple small pop-in events present (see Figure 7.6(a)); (II) PI + push-out (PO), in addition to the multiple PIs in the loading curve, a weak PO appears in the unloading curve (Figure 7.6(b)); (III) PI + load-drop (LD) + PO, as shown in Figure 7.6(c), significant load drops accompanied the large PI events e.g. at (185 nm, ~1550 μN) and (240 nm, ~2100 μN) and a push-out was observed during unloading at a similar load (~1300 μN) as shown in Figure 7.6(c). These multiple PIs, LDs and POs appeared in different types of *P-h* curves imply different mechanical failure events and strain accommodating mechanisms existed in multilayered GaTe materials.

A PO is often seen an indicator of phase transition while the PI is correlated with the dislocation nucleation and slip behavior.[334] To check the influence from the $SiO_2$/Si substrate under the above testing conditions, a series of repetitive indents with the same peak load, i.e., 500, 1000, 1500, 2000, 2500 and 3000 μN were undertaken on the same $SiO_2$/Si substrate,

and the *P*-*h* curves were shown in Figure 7.6(d). The *P*-*h* curves obtained from this $SiO_2$/Si substrate were free of PIs and POs presented.

Table 7.1. GaTe multilayer thickness measured by AFM for different indents.

| Indent number | Indent depth, *h* (nm) | Thickness (nm) |
|---|---|---|
| Indent 1 (supported) | 80 | 301.8 |
| Indent 41 (supported) | 200 | 321.7 |
| Indent 42 (supported) | 200 | 373.8 |
| Indent 43 (supported) | 200 | 233.3 |
| Indent 6 (supported) | 250 | 354.3 |
| Indent 5 (supported) | 300 | 372.1 |
| Indent 4 (suspended) | 350 | 779.7 |

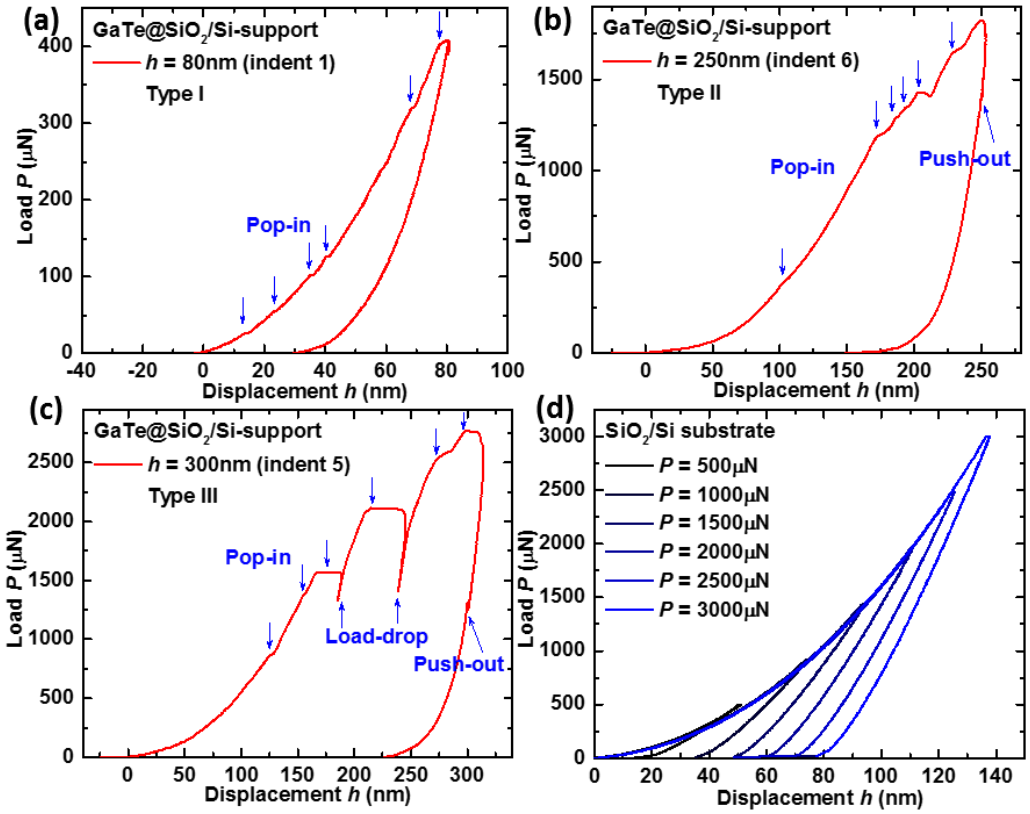


Figure 7.6. Load-displacement (*P*-*h*) curves of ~375 nm-thick GaTe multilayer under different indentation depths from (a) 80 nm and (b) 250 nm, to (c) 300 nm; (d) *P*-*h* curves of the indents on $SiO_2$/Si substrate under different loads. PIs and LDs (POs) are labelled in downward and upward arrows respectively in all *P*-*h* curves (the same in the following).

Comparing the three types of *P-h* curves for GaTe, as demonstrated in Figure 7.7, some PIs (LDs) were found appearing at the same depth (indicated by the vertical dash lines) or the same load, implying similar mechanical failure behaviors probably were involved in these different samples. Obviously, significant PIs in the 250 nm sample are induced at the same depth or load of where large PIs and LDs occurred in the 300 nm sample, i.e., ~170 nm, 185 nm, 210 nm, 240 nm in depth and ~1400 μN, 1550 μN in load, respectively. Also, in the 300 nm sample, the two large LDs are spaced at loading steps of ~550 μN, and the displacement of the two large PI stages at constant loads of ~1550 μN and 2100 μN are increased by ~20 nm and 30 nm, respectively, which implies interlayer sliding likely being generated within the GaTe multilayer flakes. The same slope of the two LDs as that of the initial region unloading curve, indicates the generation of fractures. Upon unloading, the residual displacement increases with the indentation depth, indicating plastic or unrecoverable deformation happened in the GaTe. By zooming into the low loading range of <500 μN, some small PIs were also found at similar loads or depths. A significant PI without LD happens around 400 μN on all curves. The initial PI normally occurs at ~25 nm and ~55 μN except the 250 nm depth sample where no obvious PI can be found at the depth of <100 nm. This illustrates the initial force to drive the interlayer sliding is ~55 μN in $SiO_2$/Si substrate supported GaTe multilayers. The different area under the loading curve at the same displacement depth (Figure 7.7(b)), reflecting different degree of energy dissipation during the interlayer sliding.

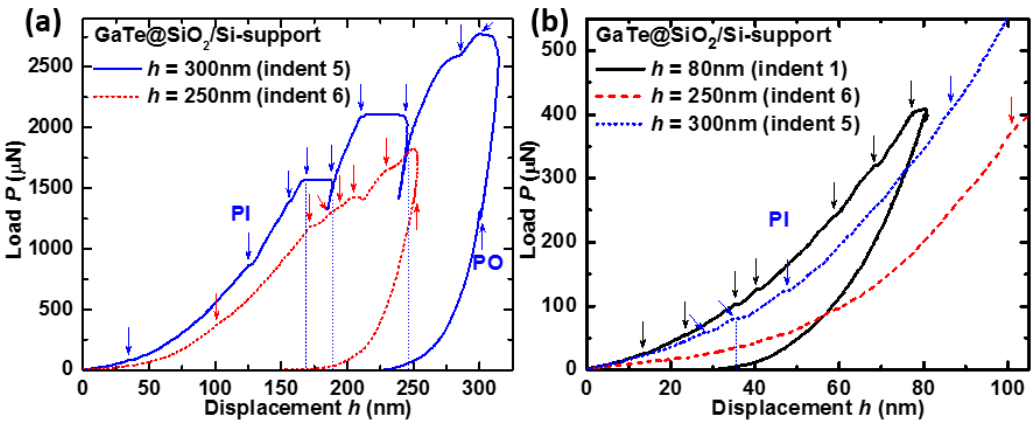


Figure 7.7. Comparison of *P-h* curves for: (a) *h*=300 nm vs. *h*=250 nm; (b) details of lower loading region (0-105 nm) and *h*=80 nm, where the vertical dash lines mean PI (LD) on the compared *P-h* curves appeared at the same indentation depth (the same in the following).

As the previous indents were undertaken and compared under varied depths, three additional indents at a fixed depth of 200 nm was performed in random locations on the same supported GaTe flake; the results are plotted in Figure 7.8. As expected, all the events demonstrated in Figure 7.6 were present in these three indents. In addition, the maximum load was consistent for indent 41 and indent 42 samples (see Figure 7.8(a), (b) and (d)) while it

decreased to about one third in Figure 7.8(c) which indicates that indent 43 sample is an exceptional case but it also shows an interesting larger PI stage in the final loading stage. It is found that at ~1500 μN and ~185 nm depth, a similar LD occurred in Figure 7.8(b) as that in Figure 7.6(c); besides, another LD at a lower load (115 nm, 600 μN) which was absent in Figure 7.6(c) became obvious in this sample; the similar slope of these two LDs to that of the corresponding region on the unloading curve again indicates similar fracture mechanism. Similar to the comparison in Figure 7.7, some PIs/LDs appear at the same depth or load for both samples (Figure 7.8(d) and (e)); and again, almost no obvious PI can be found at the depth of <100 nm for indent 41 sample which present a similar Type II *P-h* curve as that of indent 6 sample (see Figure 7.8(e) and Figure 7.7(b)). It is also found that the PO appears at a similar load of ~200 μN in both indent 41 and indent 43 samples while absent in indent 42 sample (Figure 7.8(d) and (f)); the PO in these lower indentation depth samples locate at a much lower load than those ~1300 μN of >200 nm depth samples (see Figure 7.7(a)). On the low loading depth, the area under the loading curve of indent 42 sample (Type III) is relative larger than that of indent 41 sample (Type II), indicating larger energy dissipation within the later sample. Also, upon unloading, the residual displacement of Type II curve is found a little larger than that of Type III curve, indicating larger plastic or unrecoverable deformation resulted in the former due to larger energy dissipation within the GaTe material. These comparison confirms different mechanical failure mechanisms exist in the supported GaTe multilayers.

No matter under different or the same indentation depth for those >100 nm, two types of *P-h* curves (Type II and III) are always observed (see Figure 7.7(a) and Figure 7.8(d)). Comparing the obtained Type III curves, see Figure 7.9(a) and (b), although under different indentation depth, many PIs and LDs are induced at the similar depth or load especially in depth region of 150-200 nm despite slight variations. The occurred depth and the slope of the obvious LD are the same for these two samples; the area under the two loading curves until ~200 nm are also very similar. For comparison of the Type II *P-h* curves (see Figure 7.9(c) and (d)), many PIs appear at similar load or depth especially in the >1000 μN region; but only one obvious PI can be clearly distinguished in the <1000 μN load region for these two samples. The samples compared in Figure 7.9(a) that demonstrates the most similarities are noted having almost the same thickness (see Table 7.1, only one layer difference), and regardless of different indentation depth, thicker samples tend to present Type III *P-h* curves (see Figure 7.7(a), Figure 7.8(d) and Figure 7.9); this illustrates that besides indentation depth, sample thickness may also affect the shape of the *P-h* curves. Considering each GaTe monolayer is only bonded with weak vdW force along the normal direction to the exfoliated planes and the existence of defects, it is likely that various interlayer sliding and fracture behaviors have been driven in different thickness samples so that different PIs, LDs and POs events are induced.

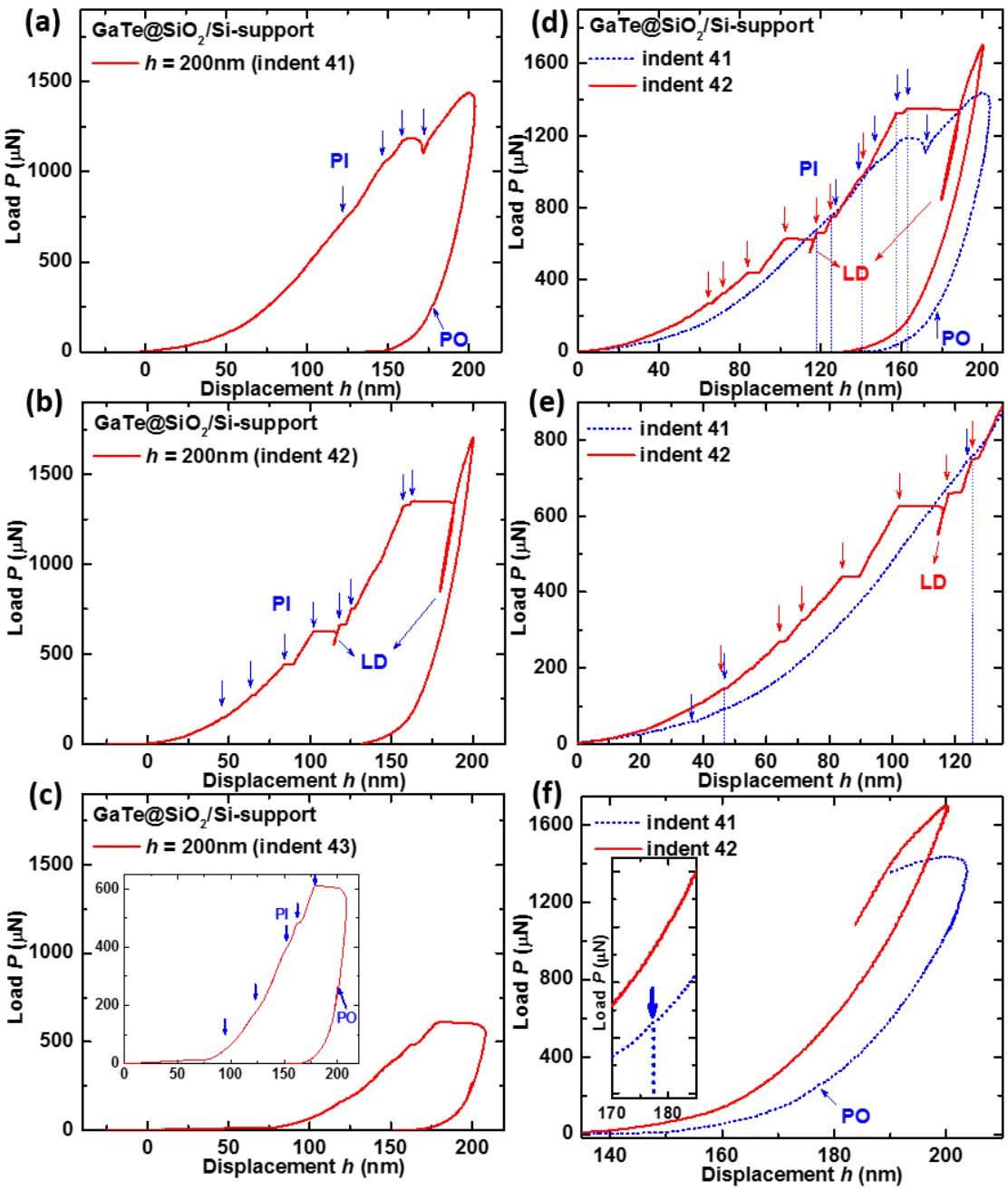


Figure 7.8. Different types of *P-h* curves under the same indentation depth of 200 nm by the displacement-controlled mode, for samples of: (a) indent 41 (type II), (b) indent 42 (type III) and (c) indent 43 (type II), with inset showing the details. (d) Comparison of *P-h* curves for conditions (a) and (b), with their lower loading (<135 nm) and unloading details shown in (e) and (f), respectively.

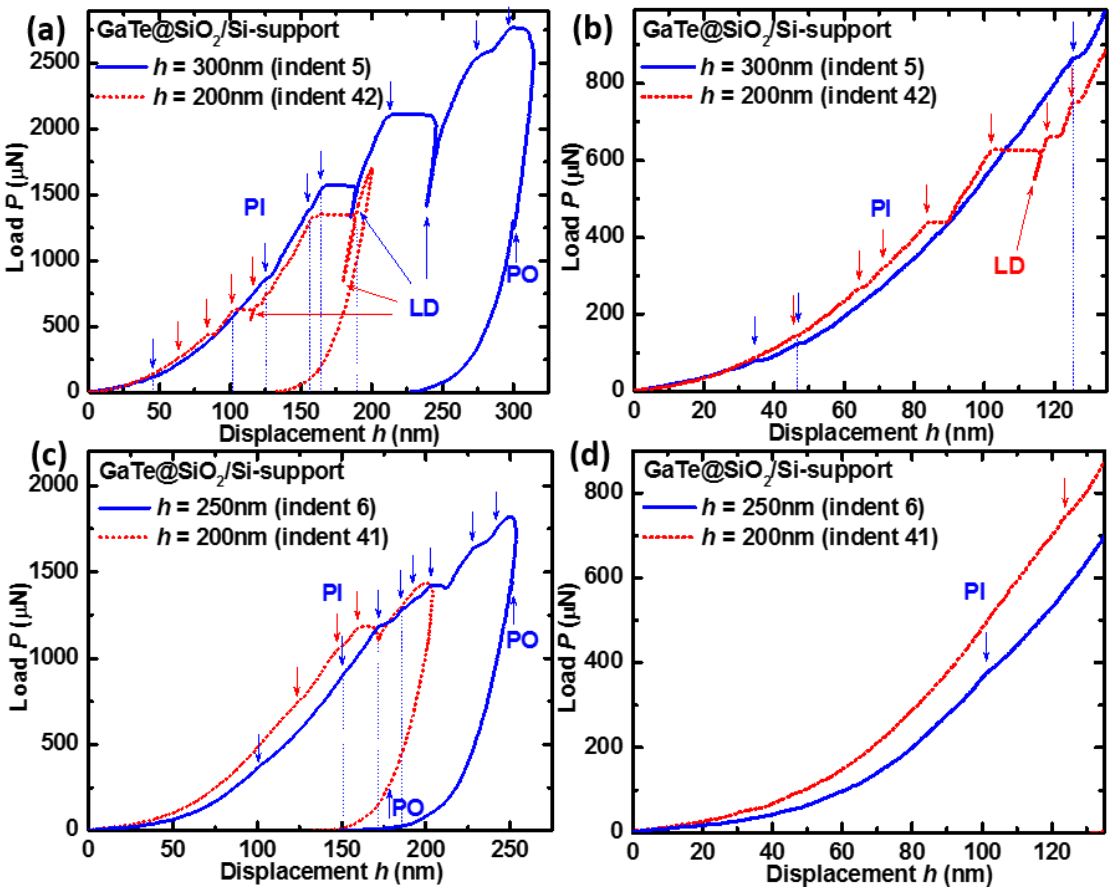


Figure 7.9. Comparison of *P-h* curves: (a) at indentation depth of *h*=300 nm vs. *h*=200 nm for Type III, which with almost the same layer thickness (see Table 7.1, only one layer difference, ~1.7 nm for each monolayer); (b) details of lower loading region (0-135 nm) of curves in (a); (c) at indentation depth of *h*=250 nm vs. *h*=200 nm for Type II, which with different layer thickness, and (d) details of lower loading region (0-135 nm) of curves in (c).

### 7.4.1.2 Morphology and microstructure analysis of nanoindentation

The morphology and microstructure of the indents were investigated by AFM and high-resolution SEM for further understanding of the *P-h* curves. As can be seen from Figure 7.10(a, b), only very small residual imprints are left after an indentation of 80 nm, and the size of the imprints increases with the indentation depth. At deeper indentation up to 250 nm (Figure 7.10(c, d)), pile-ups were observed; AFM measurements revealed that the heights of the pile-ups are around 150 nm, 125 nm and 100 nm, respectively, between the three sharp corners of the pyramidal indent. Moreover, three cracks emitted from the corners were observed with a similar length of ~2 μm; notably, one of these cracks were deflected and followed a weak path that is parallel or perpendicular to the other two cracks, indicating favoured crack paths existed. For the indent with a depth of 300 nm (Figure 7.10(e, f)), more severe fracture occurred with asymmetric pile-ups with the height of ~300 nm, 50 nm and 50

nm respectively. The direction perpendicular to the top-layer boundary (as marked in Figure 7.10(e)) is a favored crack path and the length of the cracks reached about 4 μm along this direction; note there is no crack in the direction parallel to the top-layer boundary. Between the two long cracks, the height of the pile-up reached a maximum of about 300 nm.

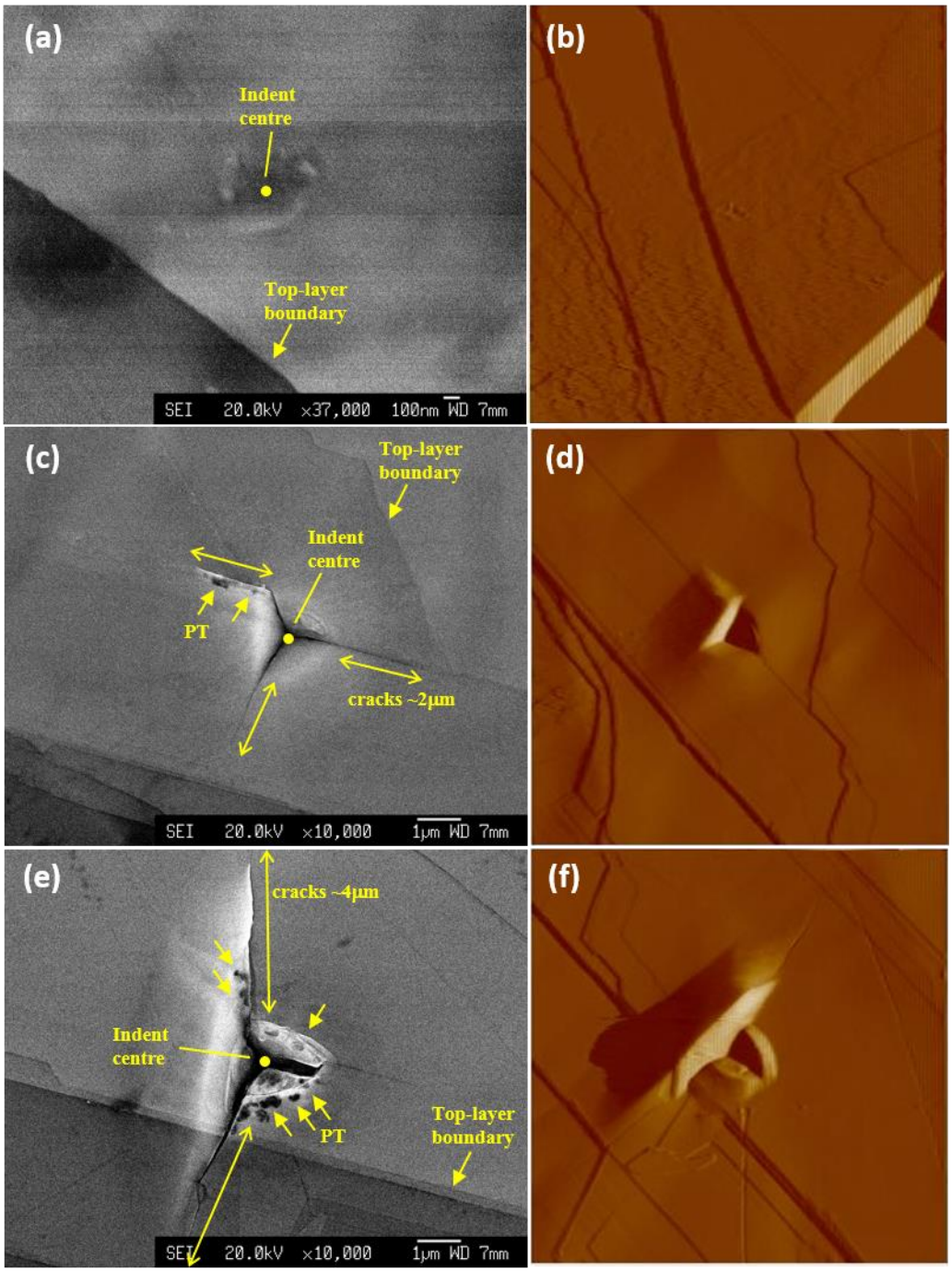


Figure 7.10. SEM and AFM images of the indent morphology for indentation depth of: (a, b) 80 nm; (c, d) 250 nm; (e, f) 300 nm, with the crack lengths, layer-boundaries, indent center and phase transformation (PT) like dark spots being labelled.

At the center of the indent imprint in Figure 7.10(e), some materials with lower SEM signal intensity (corresponds to higher resistivity), i.e. dark spots appeared (as marked by the arrows) which may indicate the possibility of a phase transformation into a higher resistivity phase. It is very likely considering the local high stress generated during the indentation. Similarly, in Figure 7.10(c), some 'darker' materials also appeared along the deflected crack (marked by the arrows). A higher resolution image of Figure 7.10(e) is shown in Figure 7.11. Some small spherical materials were clustered at the center and the right part of the indent imprint that along the parallel direction of the top-layer boundary, while absent along the two long cracks sides; this implies a stress-induced phase transformation may have taken place during the indentation process and may along a preferred crystal orientation. No further details of the indent morphology except the prolonged cracks can be observed for the sample under 250 nm depth indentation; also, no cracks and fracture around or within the small residual indent imprint can be seen for the sample under 80 nm depth indentation; these imply fracture as the possible origin of LDs.

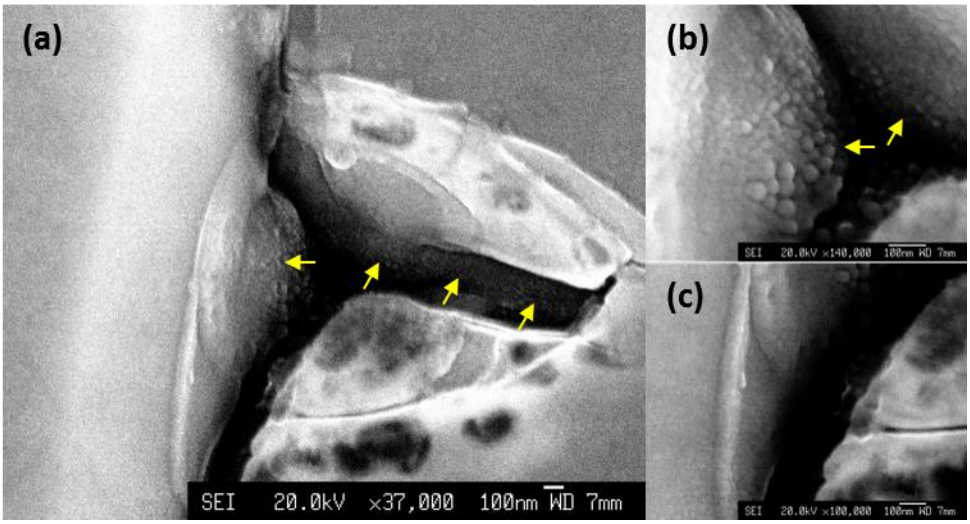


Figure 7.11. SEM images of the detailed morphology for (a) indent center and (b-c) magnified cracks details under the indentation depth of 300 nm, with the arrows indicating spherical materials.

Further SEM imaging of other indents under the same displacement load were analyzed and the results are shown in Figure 7.12. These images are grouped according to the order of the three types of *P-h* curves summarized in Figure 7.8. In Figure 7.12(a, d), three slightly asymmetric pile-ups around the pyramidal imprint were observed accompanied by three similar cracks with lengths of about 1.5 μm. For the indent 42 sample as shown in Figure 7.12(b, e), the pile up are more pronounced but no obvious formation of cracks. While

significant fracture and cracks of the total flakes in that exceptional sample of indent 43 were observed in Figure 7.12(c, f); this is different from all the above indent imprints probably due to a loose near edge part of the GaTe flake was indented. Note that the sample had been cracked away, i.e. slipping on the substrate (see the detailed crack morphology in Figure 7.12(c)) which is found can be well accounted for the much lower maximum load and the longer PI stage in the final loading region, as displayed in the *P-h* curve of Figure 7.8(c). It should also be noted that only in indent 42, some weak phase transformation like 'darker' materials as those in Figure 7.10 and Figure 7.11 and columnar fractural features were observed; besides, only this sample and the 80 nm depth sample do not present obvious cracks and PO, i.e., PO seems can be closely correlated to the formation of cracks. Based on the morphology features of Figure 7.10 and Figure 7.12 as well as the *P-h* curves shown in Figure 7.6 and Figure 7.8, the following correlation can be summarized: (i) pyramidal indent imprints without observable pile-ups, fracture and cracks result in the Type I *P-h* curve. The small PIs appeared at low indentation load (<500 μN) indicates that the deformation mechanism prior to fracture; (ii) pyramidal indent imprints with three similar pile-ups and crack lengths lead to the Type II *P-h* curve. Relative larger residue displacement (i.e., plastic deformation) and noticeable POs are normally accompanied with the formation of cracks; (iii) pyramidal indent imprints with fracture, asymmetric pile-ups and crack prolongations can be correlated to the Type III *P-h* curve. In this case, the events of larger PIs and significant LDs occurred at depths of ~120 nm, ~180 nm and ~240 nm with a step of ~60 nm, and accompanied with the formation of obvious fracture. Pronounced deformation and crack propagation along preferred orientations indicate the heterogeneous nature of the in-plane properties of the GaTe film. To further understand the mechanism for such response to indentation, the residual stresses in the GaTe film and potential phase transition are evaluated in the following section.

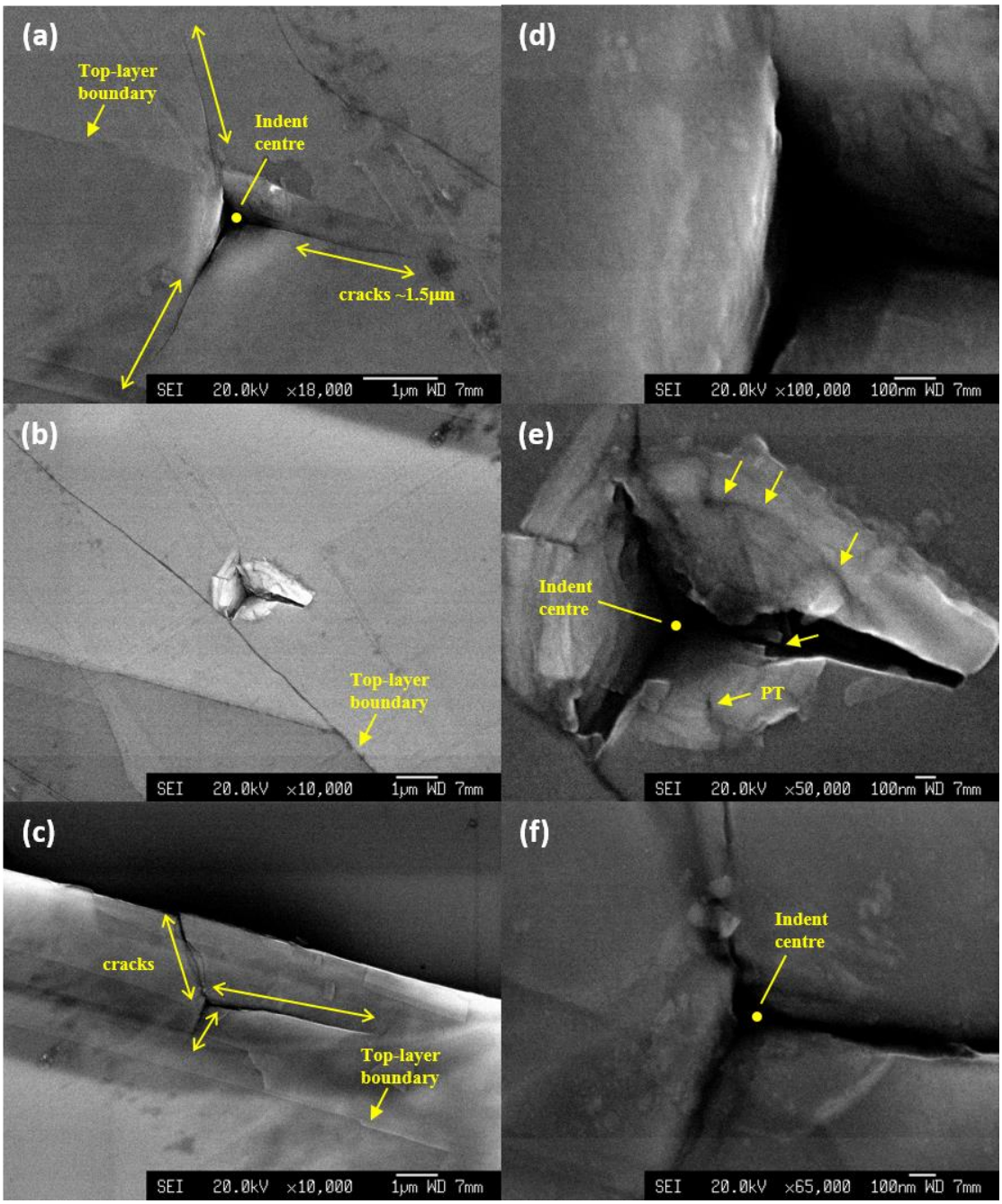


Figure 7.12. SEM images of residual indents under an indentation depth of 200 nm, with the cracks lengths, indent center, layer-boundaries, phase transformation (PT) and columnar features being labelled or indicated by arrows. Image pairs of (a, d), (b, e) and (c, f) correspond to the three type of *P-h* curves shown in Figure 7.7(a), (b) and (c), respectively.

### 7.4.1.3 Micro-Raman spectrum and stress analysis

Raman spectroscopy was used to evaluate the residual stress distribution around the indents and study the potential phase transformations at the residual imprints. The mapping area was 4×4 $\mu m^2$, with a step resolution of 0.5 μm for all samples (as indicated by the squares in Figure 7.13 and Figure 7.17).

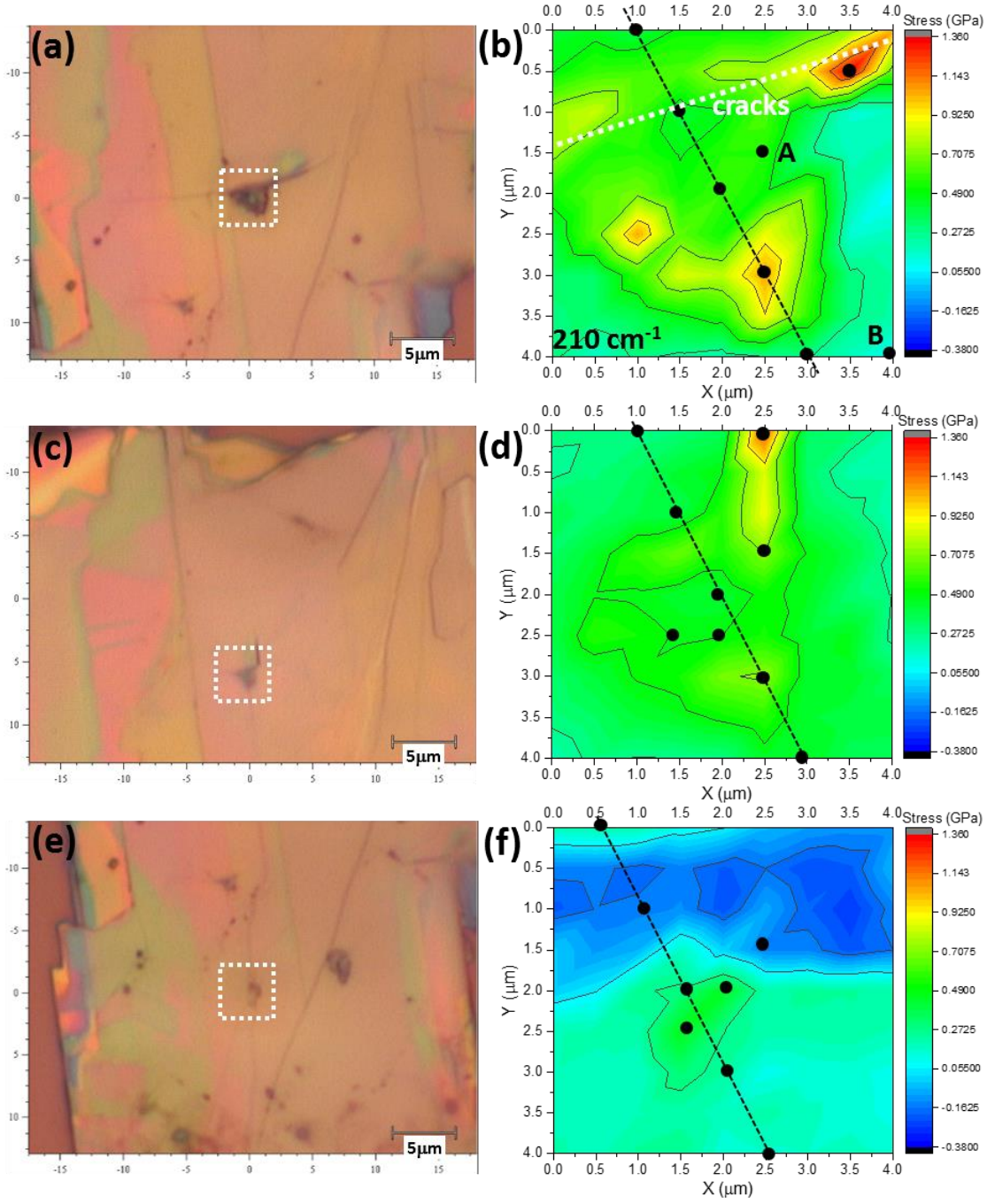


Figure 7.13. Optical microscopy image and mapping area (4×4 μm$^2$, as labelled in square) after: (a) 300 nm; (c) 250 nm; (e) 80 nm depth indentation. Stress evaluation mapping of the labelled area after: (b) 300 nm; (d) 250 nm; (f) 80 nm depth indentation. The black line is one of the axis of the pyramidal indent and the black dots are selected points for Raman spectra comparison.

From the indent imprint created at depth of 300 nm, 250 nm and 80 nm, the residual stress maps (see Figure 7.13) showed an average tensile stress of about 0.51±0.25 GPa, 0.42±0.16 GPa and 0.07±0.18 GPa, respectively (the error bar represents the homogeneity of

stress distribution). It is noticed that the tensile stress along the edges of indent imprints (or pile-up region) are much larger than those of around the indent center and the non-indent area. It is also noticed that, for the 300 nm depth sample, as shown in Figure 7.13(b), the tensile residue stress around the cracks (labelled by the white dot line) were significantly larger (~0.7 GPa) than that of the non-crack side (~0.1 GPa); also, the pile-up and cracks region (including the non-crack side) had induced larger tensile stress (~1.3 GPa) than that of the indent center (~0.5 GPa), and was much larger than that of the indent- and crack-free area (~0.1 GPa). In contrary, Figure 7.13(d) and (f) showed that more homogeneous tensile stress distribution around the indents were formed in the 250 nm and 80 nm depth samples; moreover, in the former, the largest tensile stress (~1.0 GPa) was formed along the crack whose prolongation direction had changed, as shown in Figure 7.13(d). To conclude, in areas away from the indent and cracks, a subtle tensile stress of ~0.1 GPa is left for all samples, this reflects the relaxed residue stress from the formation of cracks. Higher tension is normally caused in the more pronounced pile-up region and corners of the cracks.

Furthermore, Raman spectrum evolution along the black line (see Figure 7.13(b), one axis of the pyramidal indent) of the 300 nm depth sample was inspected, as shown in Figure 7.14. Significant difference was evident between the indent (A) and the neighbor non-indent area (B), where no sharp Raman peaks can be distinguished at the pile-up region (A is near the indent center); instead, amorphous/disorder-like broadened peaks appeared. Most importantly, several new peaks (e.g., 89, 118 $cm^{-1}$) appeared and other peaks either became less apparent due to the widening of peaks (109, 114.4, 126, 143, 209 and 282 $cm^{-1}$), or disappeared (74.8, 162, 176, 268 $cm^{-1}$). As discussed in Chapter 6, GaTe multilayer flakes had presented similar Raman spectrum due to the amorphous/disorder-like phase transformation after being hydrostatically compressed over ~20 GPa and decompressed to ambient pressure. All the above Raman spectrum changes imply the formation of amorphous/disorder-like structure or new phases, induced by the high local stress generated during indentation process. However, no significant amorphous-like broadened peaks appeared in the Raman spectrum of the 80 nm and 250 nm depth indented samples, but the new peaks around 90 and 99 $cm^{-1}$ were also apparent (see the insets in Figure 7.16). Therefore, these structure transformations probably can be correlated to the large PI and LD events appeared in the loading curve; and the ‘darker’ materials in Figure 7.11 probably originate from the amorphous-like phase. The PI event was also found and proved as an indicator of phase transformation in other semiconductors such as 4H-SiC,[335] GaAs.[336] Besides, it is shown in Figure 7.8(c) and Figure 7.12(c) that the flake sliding also results in significant PIs; note that even after 300 nm depth indentation, better quality Raman spectrum of GaTe is still obtained at the indent center, and the residual indent depth measured by AFM was much smaller (~150 nm) than the sample thickness (~375 nm), thus the small PIs are probably due to the interlayer sliding within the multilayered material.

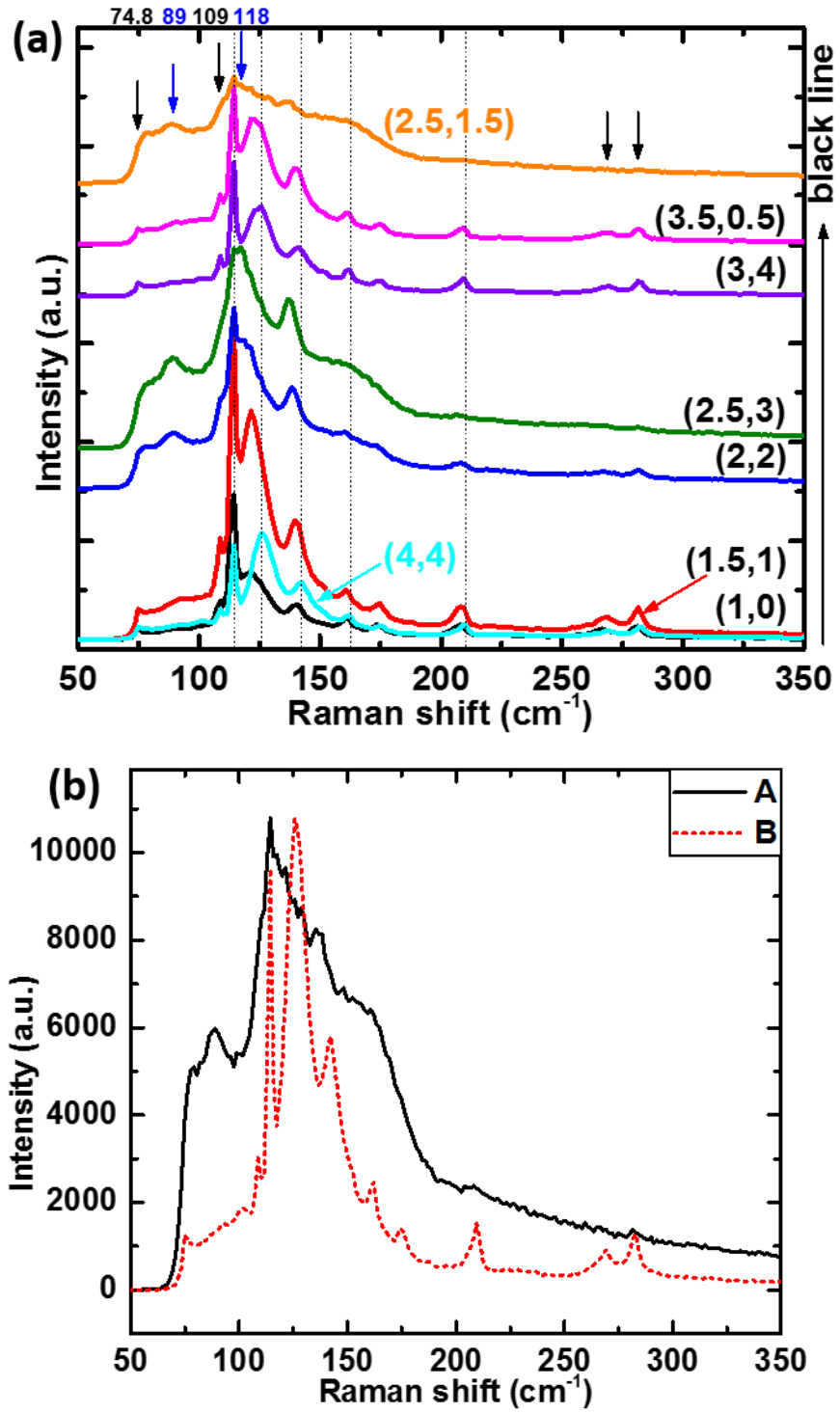


Figure 7.14. After 300 nm depth indentation: (a) micro-Raman spectrum evolution along the black line and selected abnormal points displayed in Figure 7.13(b); (b) detailed Raman spectrum comparison between the indent center and non-indent area, where A and B represent the selected points in Figure 7.13(b).

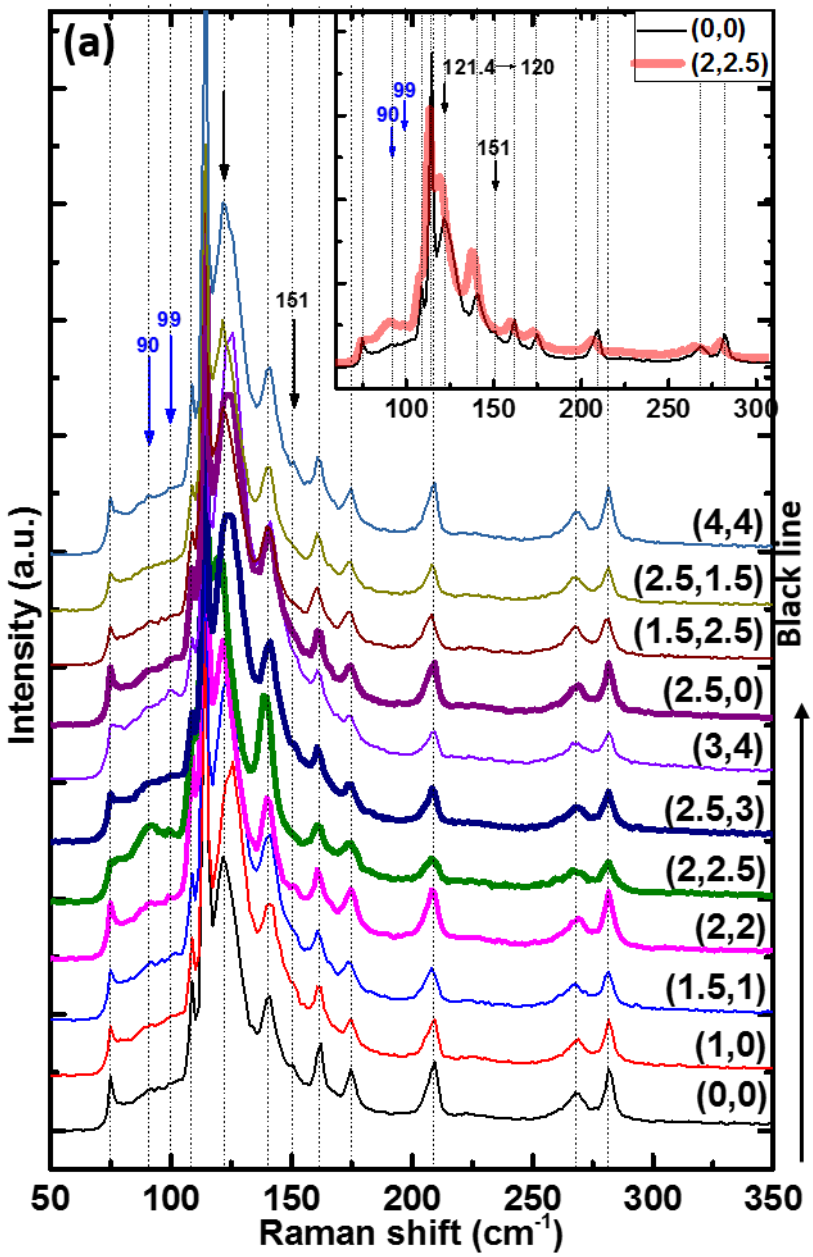


Figure 7.15(a). Micro-Raman spectrum evolution along the black line and selected abnormal points after 250 nm (corresponding to Figure 7. (d)) depth indentation; inset is the detailed Raman spectrum comparison between the indent center and non-indent area.

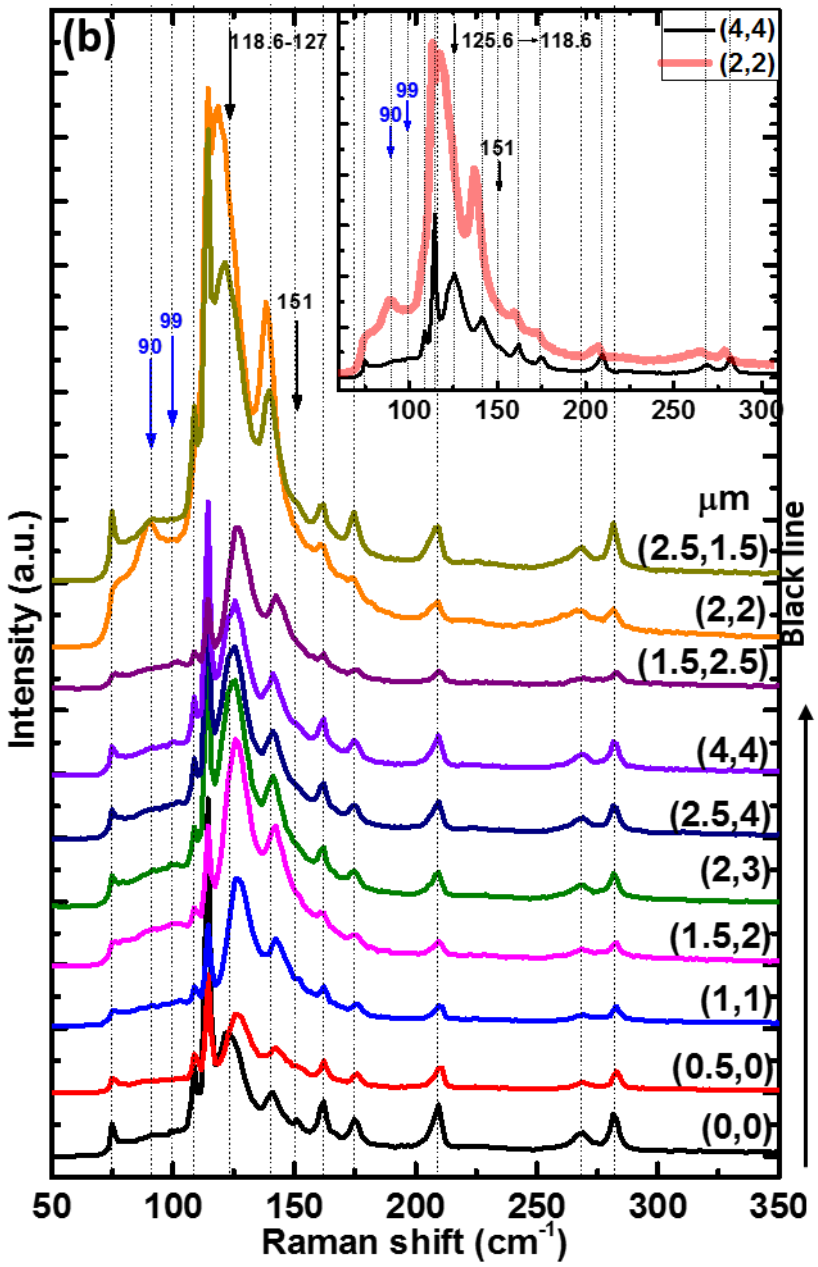


Figure 7.16(b). Micro-Raman spectrum evolution along the black line and selected abnormal points after 80 nm depth indentation (corresponding to Figure 7. (f)); inset is the detailed Raman spectrum comparison between the indent center and non-indent area.

In addition, residue stress of three indents under the same loading depth of 200 nm were compared. In corresponding to the marked (a, b, c) region in (d), Figure 7.17 shows an average stress of about -0.09±0.12 GPa (compressive), -0.07±0.13 GPa (compressive) and 0.057±0.18 GPa (tensile) were generated after the indentation, respectively (the error bar stands for the homogeneity of stress distribution). Note that sample (c) in Figure 7.17 is indented at the edge of the film causing stress relaxed, and its average residue stress is very close to that generated after 80 nm depth indentation, therefore, 0.057 GPa (tensile) can be used as a reference value as zero stress. It was also found that fracture tends to result in larger

tensile residue stress in the indent area, this was especially the case for the indent shown in Figure 7.17(c) and Figure 7.12(c) where large fracture and cracks were formed. Compressive stress tend to form around the indent to balance the tensile stress generated on the indent. Besides, a larger inhomogeneous stress was formed around the edges of the indent imprint in Figure 7.17(b), similar to the condition of 300 nm depth indent sample which has the same thickness; this is mainly due to the indent fracture with asymmetric or un-sharp crack prolongations resulting in an asymmetric stress accumulation.

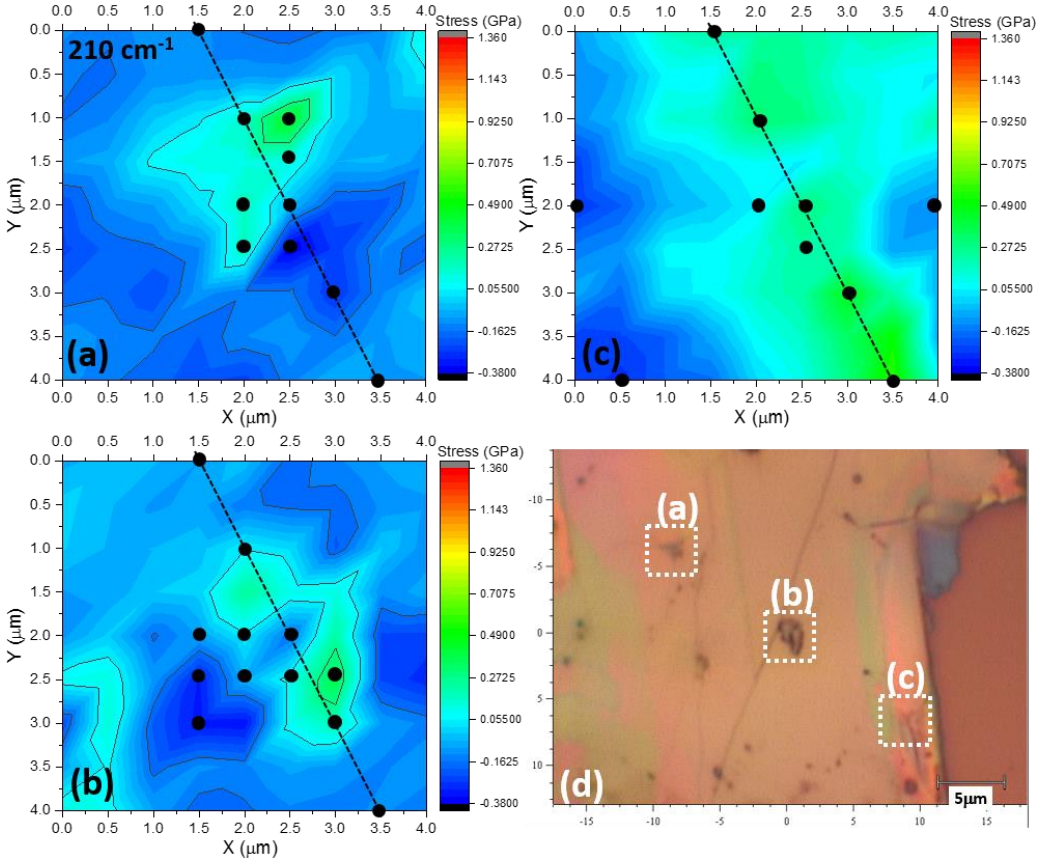


Figure 7.17. Stress mapping for (a-c) three different indents of 200 nm depth (corresponding to Figure 7.4-7(a-c)), and (d) microscopy images for indent imprints.

From the Raman spectra evolution along one of the axis of the indents (see the black line in Figure 7.17), no significant changes happened on the indent types shown in Figure 7.18(a) and Figure 7.18(c), while an amorphous like Raman spectrum similar to that of Figure 7.14 appeared in Figure 7.18(b), indicating a local phase transformation was induced.

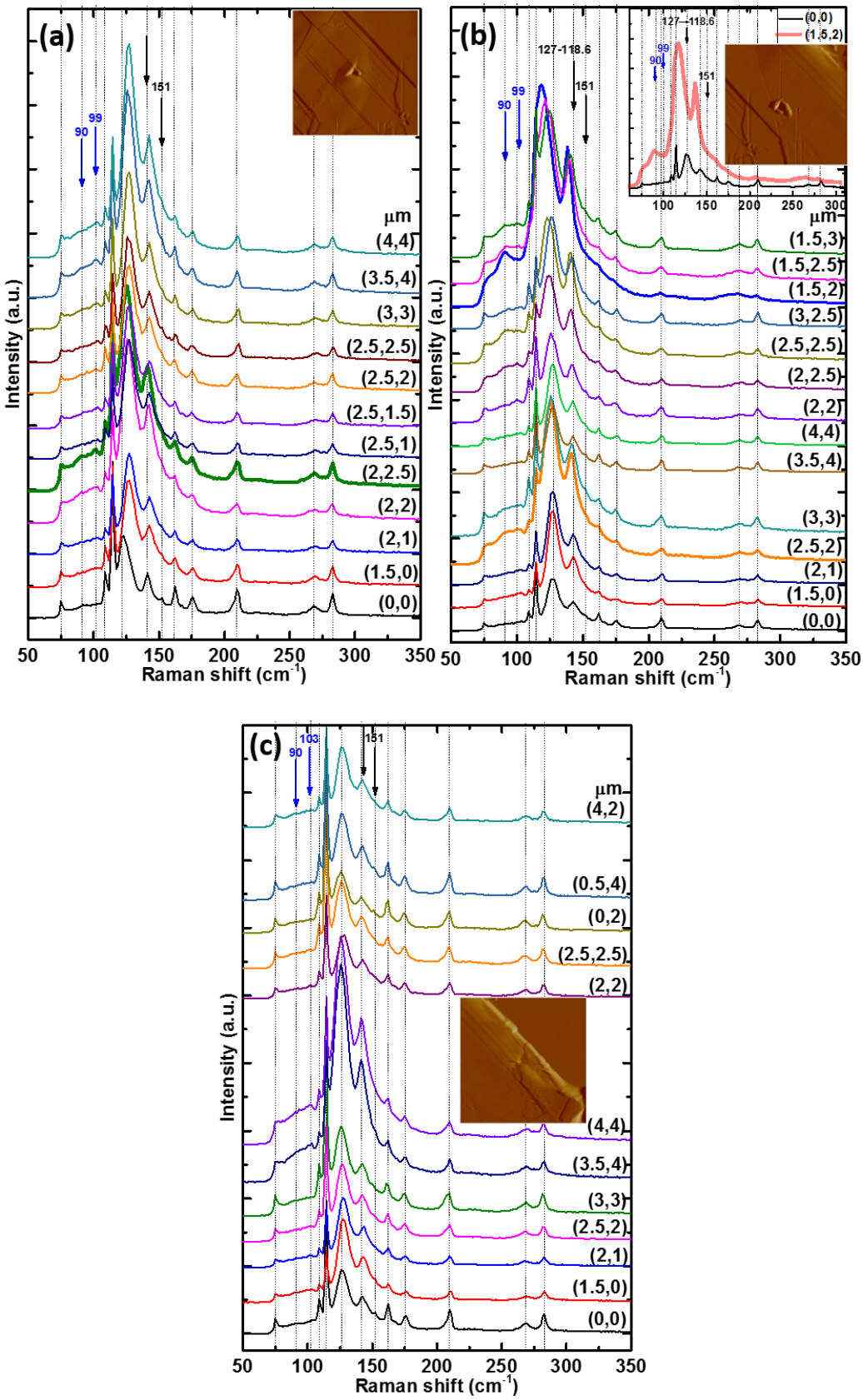


Figure 7.18. Raman spectrum evolution along the loading line in the corresponding (a-c) nanoindentation pits in Figure 7.17. Inset: AFM morphology image for each pit.

### 7.4.2 Mechanical properties of suspended GaTe multilayer flakes

#### 7.4.2.1 Nanoindentation characterization

In order to isolate the mechanical properties of GaTe multilayers from the complicated coupling effects of substrate, indents under different depth were performed on free-standing GaTe flakes which were transferred onto the "T-shape" membrane structure slits fabricated on the $SiO_2$/Si substrates (see detailed experiments in Section 7.2.1), these slits are indicated as the dash outline in Figure 7.19. The width of the slits was about 6 μm (larger than the cross-sectional tip radius at the indentation depth of 350 nm, which is ~500 nm calculated from $A=3\sqrt{3}\tan 65.3^2 h_p^2$) and the two slits are perpendicular to each other for sake of measuring the in-plane anisotropic mechanical properties simultaneously. Based on the $SiO_2$/Si substrates supported results shown in Section 7.4.1.1, the *P-h* curves of >200 nm depth indentation had similar characters as those under 200 nm depth indentation and the slits depth was ~300 nm, therefore only a loading range of 250 to 350 nm depth indentation was investigated here.

Unlike the *P-h* curves obtained under 250 nm depth indentation, when a ~779.7 nm thick GaTe flake was indented to 350 nm depth along the in-plane zigzag orientation ($90^o$ in Figure 7.19), significant PIs and LDs were presented at the depth of about (255 nm, 150 μN) and (315 nm, 225 μN) on the loading curve, with a significant push-out appeared at ~ (330 nm, 125 μN) on the unloading curve. Also, it is evident that multiple small PIs and LDs instead of smooth elastic behavior had presented especially during the 100-250(or 350) nm depth loading process for all tests. These multiple PIs events in *P-h* curves are similar to the behavior of dislocation mediated activity reported in single-crystal Pt[337] (a transition from elastic to plastic transformation due to the dislocation nucleated beneath the tip), or the so-called shear localization into "shear band" that observed in a Pd-based amorphous alloy;[338] in different, obvious multiple LDs in following of each PI are also presented here, including at depth of ~120 nm, ~180 nm and ~240 nm. This agrees well with those LDs events observed in supported GaTe samples. Generally, these LDs emerge at a step of 10-20 nm or 10-20 μN while the PIs at a step of 2-10 nm or 1-7 μN; the initial significant LD appears at ~50 nm and ~20 μN while the initial PI starts at ~15 nm and ~8 μN along the zigzag ($90^o$) orientation. Considering the weak interlayer vdW force that bonded along the normal direction of the exfoliated GaTe surface (see the XRD spectrum in Chapter 6), as well as the results obtained in the above supported GaTe flakes, these multiple small PIs and LDs can be ascribed to the interlayer sliding and cracks behaviors generated within the GaTe multilayers which is driven by the lateral force that is parallel to the layer surface and increases gradually with the indentation depth. Notably, after the initial period, the minimum force to drive the interlayer sliding is ~1 μN, comparable to that ~0.6 μN in bilayer graphene.[339] We notice a recently

investigated nanoindentation of nanostructured Ti/Al multilayers also presented multiple PIs but no LDs which was concluded to the formation of localized shear bands.[340]

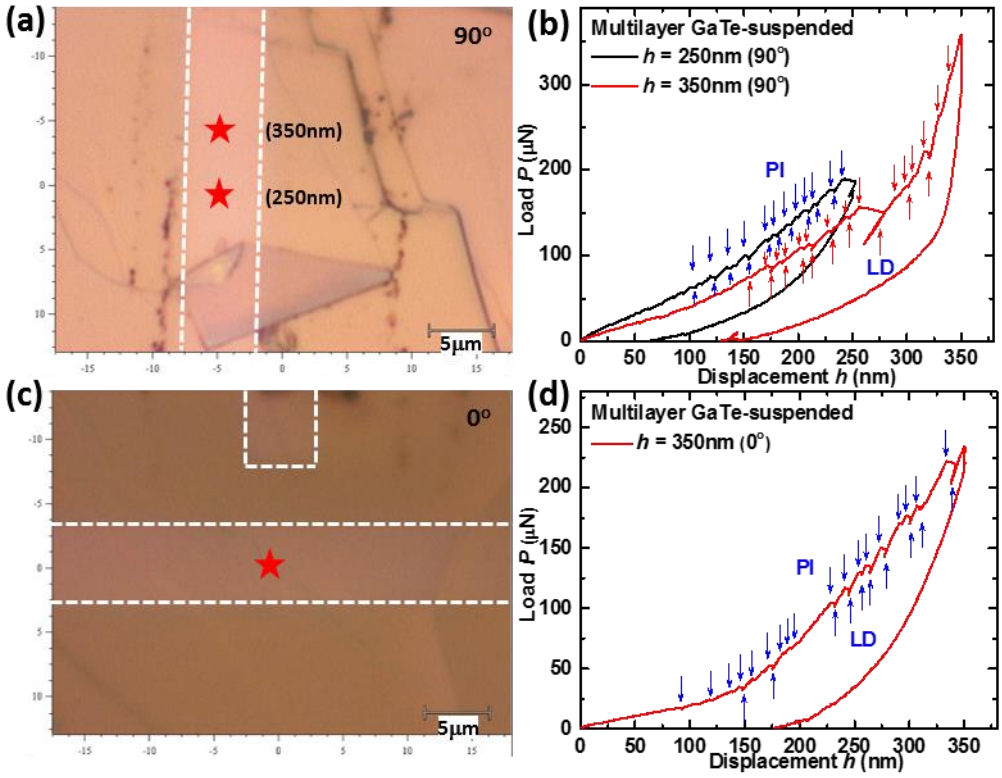


Figure 7.19. *P-h* curves under different indentation depth for free-standing GaTe flakes: (a) microscopy image for 90° orientation slits, (b) under 250 nm and 350 nm-90° depth indentation, and (c) microscopy image for 0° orientation slits, (d) under 350 nm-0° depth indentation, where 0° and 90° represented the armchair and zigzag in-plane crystal orientation. Marks in (a) and (c) represents where the indentation pit was performed. Up and Down arrows in (b) and (d) represent pop-in and load-drop appeared in the loading curve respectively, where they are recorded as different types of jumps by the indenter.

As the monoclinic GaTe crystal structure has displayed a high in-plane anisotropy, zigzag and armchair (0° in Figure 7.19) orientation of the single-crystal GaTe flake was directional suspended along the vertical and horizontal direction of the slits respectively, and in-plane anisotropic indentation was undertaken at both crystal orientations with the same depth of 350 nm. Interestingly, the *P-h* curve under 350 nm depth indentation along the 0° orientation slit is very similar to that under 250 nm depth indentation along the 90° orientation slit, both achieving a maximum load of ~200 μN. The residual displacement is larger along the 0° orientation slit indentation, indicating a larger plastic deformation resulted. The LDs are found emerged at a step of 6-30 nm or 3-20 μN while the PIs at a step of 2-13 nm or 1-7 μN,

similar to that of the 90$^{o}$ orientation; but, the initial significant PI and LD both appear at ~40 nm and ~9 μN, higher than those along the 90$^{o}$ orientation slit indentation. This comparison illustrates that different mechanical properties existed along the zigzag and armchair in-plane crystal orientations, and the zigzag (90$^{o}$) orientation is easier to drive the interlayer sliding than the armchair (0$^{o}$) orientation, i.e., the shear stress that parallel to the 2D layer is larger along the armchair orientation. Besides, the armchair orientation is found can suffer an 11% larger strain than the zigzag orientation based on present work. In addition, the reduced Young's modulus was calculated to be 1.96 GPa and 1.72 GPa along zigzag and armchair orientations, much smaller than that of monolayer graphene (~1 TPa) and few-layer GaTe (~25 GPa).[214,341] Therefore, the sudden increased load force and slope at ~(275 nm, 200 μN) of the loading curve for the indentation along the 90$^{o}$ orientation slit indicated that GaTe probably became harder due to the interlayer sliding, this probably also resulted in an increased elastic modulus when under larger deformation. Whether this is due to dislocation related behaviors or change in the material structure (phase transition) needs further investigation which is now not available in this thesis. Recently, a high strain of ~8%, similar to some metals, was just reported in 10 nm GaTe multilayer using AFM tip based nanoindentation without considering the anisotropy.[341] The anisotropic maximum strain along different in-plane crystal orientations of GaTe multilayers are still under further study in this work.

#### 7.4.2.2 Morphology and micro-Raman spectrum analysis for suspended GaTe flakes after nanoindentation

From the AFM tomography, by plotting the thickness profile across the indent region, a permanent concave imprint of ~50 nm in depth was left after the indentation, as illustrated by the AFM curve in the inset of Figure 7.20(a) and the AFM phase image in Figure 7.20(b). Notably, the asymmetric depth profile may be due to the indentation position not at the center of the rectangular slits (located at ~4.5 μm/6 μm of the slits). Besides, the larger PI and LD appeared at ~255 nm and ~275 nm imply invisible defects such as fracture, crack, or dislocation may have formed within the material.[334] This would be consistent with the permanent plastic deformation observed, i.e., the concave imprint left, after indentation.

By performing micro-Raman mapping, similar to those described in Section 7.4.1.3, the possible structural changes around the indentation imprints were analyzed. As shown in Figure 7.20(c) and (d), for the indentation performed on the 90$^{o}$ orientation slit, the Raman spectra evolution along the vertical and horizontal direction of the indent center (corresponding to the label 'V' and 'H' in the inset of Figure 7.20(b)) were investigated. Apparently, new peaks around 95 and 102 cm$^{-1}$ appeared while some other peaks either disappeared or became less apparent (indicated by the black arrow) in the indent region for

both directions; these Raman spectra changes were ascribed to the amorphous-like phase transition as in the previous analysis. Notably, the new peaks have shifted to relative higher frequencies compared to those results of $SiO_2$/Si substrates supported, likely being induced by a larger stress due to the larger depth indentation. No significant difference can be distinguished between the Raman spectra evolution along the cross-slit direction (H) and parallel-slit direction (V), indicating relative homogeneous stress was left. The significant changes of Raman spectra implies that the zigzag orientation (90°) probably was mainly deformed and stretched under the indentation on the 90° orientation slit. This agrees with the original design that the plastic deformation was expected to be mainly stretched by the 90° orientation slit and substrate along the zigzag orientation.

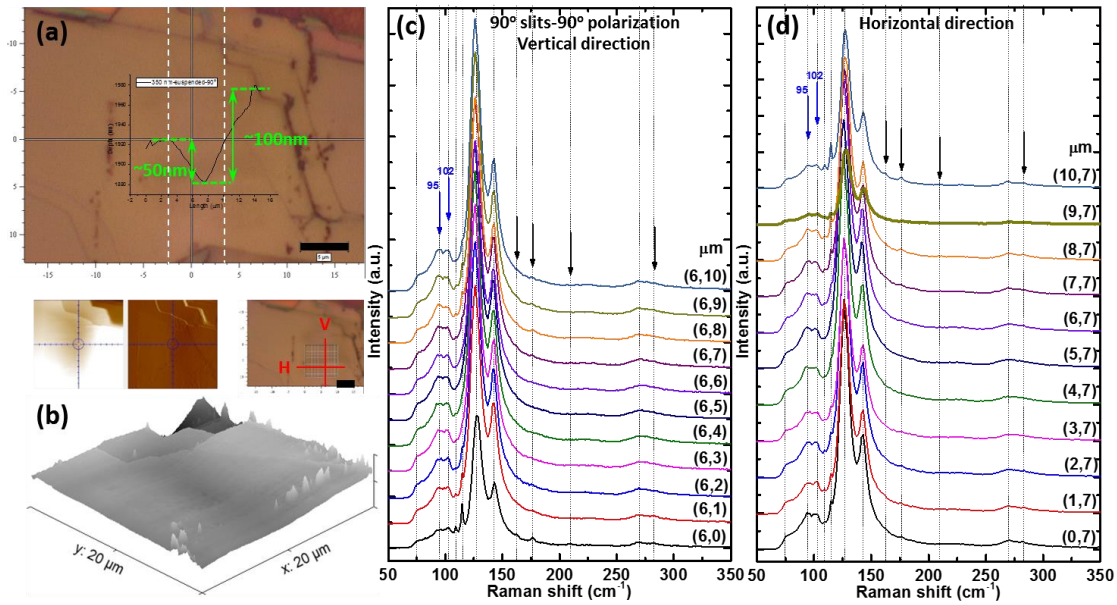


Figure 7.20. After 350 nm depth indentation on the 90° orientation slit and measuring along the zigzag (90°) crystal orientation: (a) optical microscopy image and mapping area (below the right bottom of (a), all labelled scale bars represent 5 μm), inset is the depth profile measured by AFM; (b) AFM images of the indent morphology: top are phase image and 2D morphology image of indent area respectively, bottom is the 3D morphology image of the indent area; Micro-Raman spectra evolution along (c) the vertical direction (V) and (d) horizontal direction (H) of the mapping area.

For the indentation performed on the 0° orientation slit, the Raman spectrum measured along the same zigzag orientation (90° polarization) as that in Figure 7.20 shows a much higher peak intensity and resolution, as displayed in Figure 7.21, indicating a higher quality of crystal structure along the zigzag orientation was left after the 0° orientation slit indentation than those after the 90° orientation slit indentation. Besides the new 95 and 102 $cm^{-1}$ peaks

with weaker intensity than those in Figure 7.20 the Raman spectrum evolution along both the vertical and horizontal direction of the indent center shows no other significant difference.

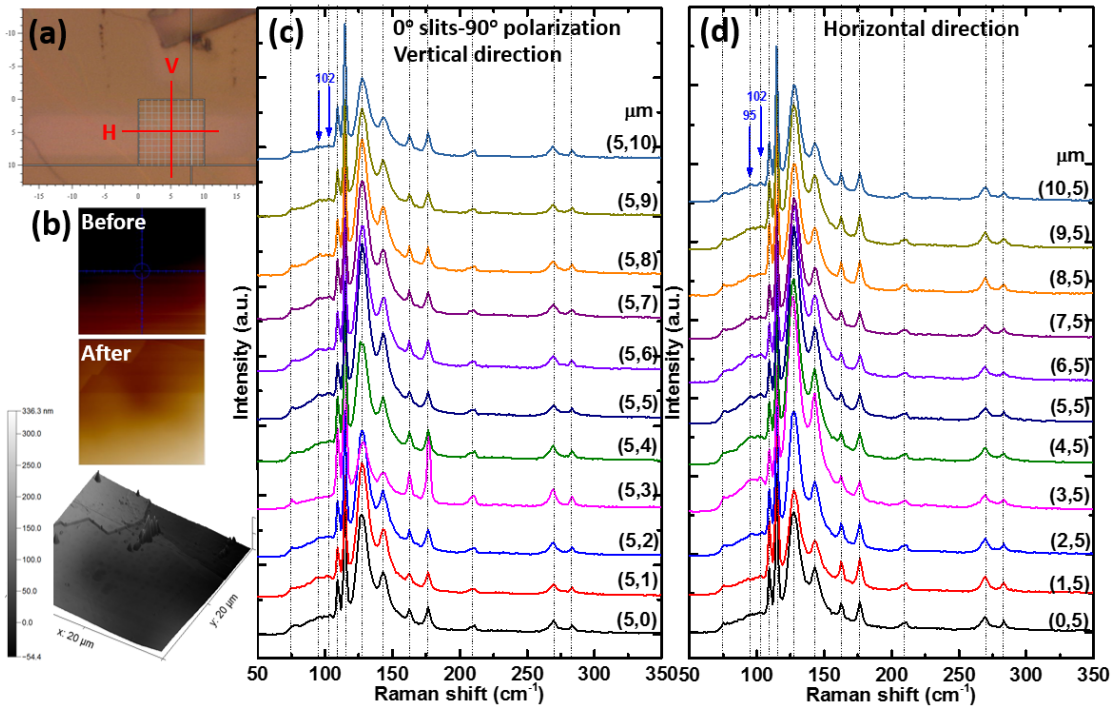


Figure 7.21. After 350 nm depth indentation on the 0° orientation slit and measuring along the zigzag (90°) crystal orientation: (a) optical microscopy image and mapping area, (b) AFM images of indent morphology: top are indent area phase images before and after the indent, bottom is the 3D morphology image of indent area; Micro-Raman spectra evolution along (c) the vertical direction (V) and (d) horizontal direction (H) of the mapping area.

Considering the above analysis, the Raman spectra mapping along the armchair orientation (0° polarization) was then measured, as plotted in Figure 7.22, where a much weaker peak intensity and even disappeared peaks than those measured in Section 7.4.1.3 was shown, indicating at least degraded crystal quality along the armchair orientation. Furthermore, appearance of a stronger new peak locating at 102 $cm^{-1}$ was apparent; this implies the 102 $cm^{-1}$ new peak mainly origins from the crystal structure distortion along the armchair orientation, where a phase transition is further induced. Comparison of Figure 7.21 and Figure 7.22 shows that the zigzag orientation has a better crystal quality while a worse one along the armchair orientation was left after indentation on the 0° orientation slit, this confirms that the deformation and stretching of GaTe film was mainly along the armchair orientation as designed under this condition. Moreover, such deformation and stretching probably results from the interlayer sliding, as the new peak at 102 $cm^{-1}$ appears for the indentations on both 90° and 0° orientation slits.

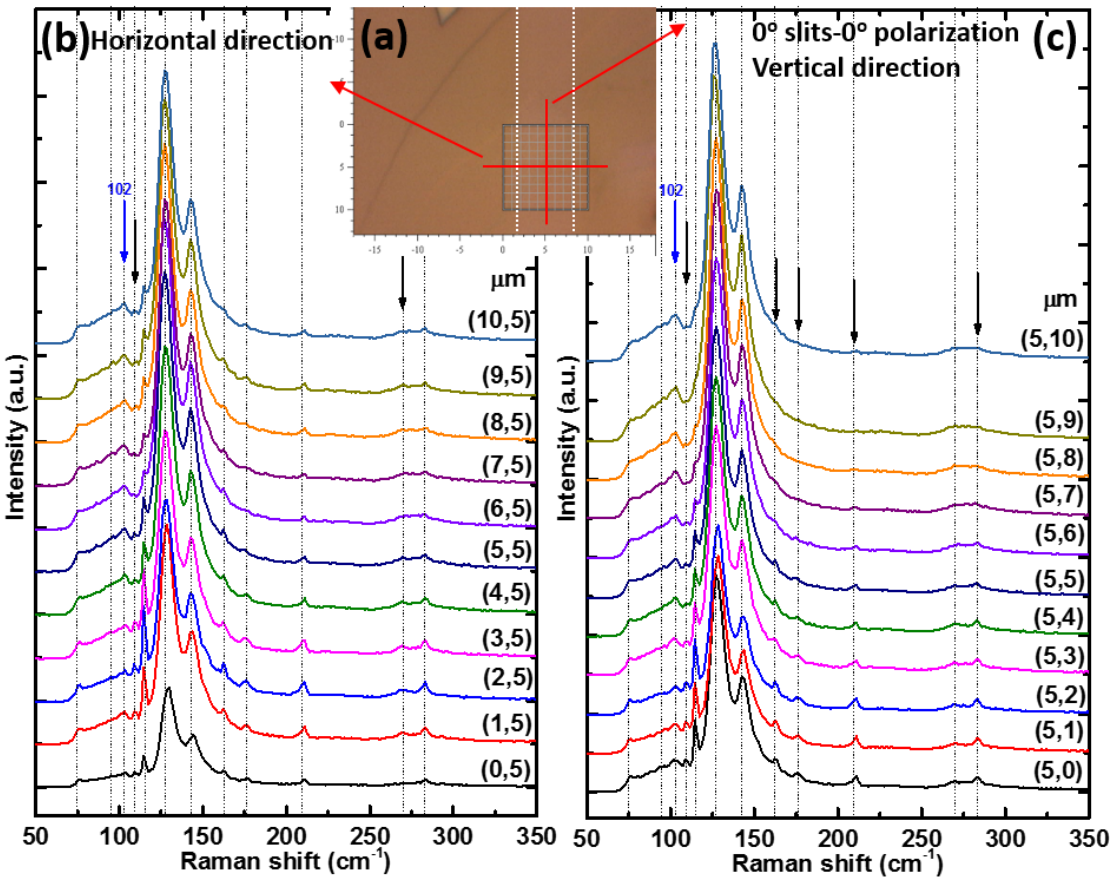


Figure 7.22. After 350 nm depth indentation on the 0° orientation slit and measuring along the armchair (0°) crystal orientation: (a) optical microscopy image and mapping area (labelled by square) of the indent; Micro-Raman spectrum evolution along (b) horizontal direction (H) and (c) vertical direction (V) of the mapping area.

## 7.5 Conclusions

The thermal properties of free-standing GaTe flakes were studied mainly by micro-Raman opto-thermography, and the thermal conductivities along the in-plane armchair and zigzag orientations of a ~150 nm-thick GaTe flake were measured to be: $\kappa_{zigzag}$ = 5±0.31 W/mK and $\kappa_{armchair}$ = 3±0.21 W/mK, respectively. The mechanical properties of both $SiO_2$/Si substrates supported and free-standing multilayered GaTe flakes were investigated through nanoindentation, AFM, SEM and stress mapping using micro-Raman spectrum. The vdW adhesion force between GaTe flakes and the substrates was found to be much stronger than that between GaTe interlayers, resulting in the easier fracture of materials within the GaTe multilayers instead of slippage on the substrate. Three different types of *P-h* curves with the corresponding indent morphology characters in supported GaTe multilayers were demonstrated: (i) only PI (in the loading curve), with only a small pyramidal indent pit without observable fracture, pile-ups and cracks formed; (ii) PI + PO (in the unloading curve),

featured by a pyramidal indent morphology with three similar pile-ups and crack prolongations; (iii) PI + LD (in the loading curve) + PO, where a pyramidal indent morphology with fracture and asymmetric pile-ups, crack prolongations are normally generated. Such PIs and LDs events were also observed on the free-standing GaTe flakes, without any observable facture or cracks even under slightly larger displacement loading than that of supported flakes. The PIs and LDs in the loading curve probably originate from the interlayer sliding, cracks and the induced phase transition within the GaTe multilayers during the indentation. The initial depth and force of the PIs (LDs) are ~15 nm and ~8 μN along the zigzag orientation while ~40 nm and ~9 μN along the armchair orientation, implying it is easier to drive the interlayer sliding at the zigzag orientation; after the initial period, the minimum force to drive the interlayer sliding is ~1 μN, comparable to that ~0.6 μN in bilayer graphene. An 11% larger strain along the armchair orientation than the zigzag orientation was also observed based on our present work. The detailed mechanism for these abnormal mechanical properties need further study.

# Chapter 8.

## Conclusions

In AlGaN/GaN devices based electronic applications, thermal management is extremely important. This is as devices are operated at high power density, which can result in high temperature rises within the devices, especially the device channel which leads to degradation and failure. To improve the device thermal management, thermal resistance from the channel to the heat sink must be reduced to a minimum as much as possible with efficient heat removal. This can be achieved by increasing the thermal conductivity of the substrate which accounts for the majority of the total thermal resistance or a topside heat spreader; effective thermal boundary resistances ($TBR_{eff}$) between materials also need to be minimized. Cost-effective CVD grown polycrystalline diamond is mainly investigated in this work as an important heat spreading strategy for next generation power devices as it can exhibit very high thermal conductivity, as high as ~2200 W/mK. However it is challenging to characterize these high thermal conductivity and the related TBRs. Furthermore, upon the requirements of increased data rates for communications and computing, future electronics is also required to be smaller with dimension scaling to even atomic scale. Incorporation of new two dimensional (2D) materials channels especially those with distinguished properties is considered to be a very promising solution to address these challenges. In this work, nanosecond time-domain thermoreflectance (TDTR) was used to investigate the thermal properties of polycrystalline diamond integrated with GaN devices. Multiple experimental techniques combined with theoretical calculations were employed to study the phase transition, thermal and mechanical properties of multilayered GaTe, a novel 2D material with low in-plane symmetry. The main conclusions about these work are summarized in the following.

### 8.1 Thermal properties of diamond integrated GaN HEMTs

To investigate how the barrier layer influences the thermal properties of GaN-on-diamond, polycrystalline diamond (PCD) films grown on GaN using a well controlled 5 nm thick amorphous SiN or AlN dielectric material as barrier layers as well as without barrier

layer were studied and systematically compared to gain insight into their thermal properties via nanosecond TDTR complemented by transmission electron microscopy (TEM) analysis. These diamond films were grown on the N-polar GaN surface under different recipes with methane concentrations in the feed gas controlled from 0.1% to 1% of the total gas flow including hydrogen and argon, and under different temperatures from 670 to 830 $^{o}$C. Results show that SiN barrier layers result in the lowest $TBR_{eff,\ Dia/GaN}$ for all of the growth temperatures studied. An average state-of-the-art low value of ~6.5 $m^2K/GW$ was achieved by using a 5 nm ultrathin SiN barrier layer, forming smooth interfaces, making it a good candidate for the seeding and growth of diamond onto GaN. This low $TBR_{eff,\ Dia/GaN}$ value is close to the predicted lower limit of 5.5 $m^2K/GW$, which includes contribution of the diffuse mismatch model (DMM) theory predicted values for both GaN/SiN and SiN/diamond interfaces as well as the SiN layer thermal resistance; the lowest TBR is predicted to be ~3 $m^2K/GW$ by DMM for only GaN/diamond interfaces. Materials with this low $TBR_{eff,\ Dia/GaN}$ will enable a ~45% reduction in device peak temperature with respect to GaN-on-SiC HEMTs. In contrast, direct seeding and growth of diamond onto GaN without barrier layer resulted in one to two orders of magnitude higher $TBR_{eff}$ than SiN due to rougher interfaces formed. AlN might be an alternative to SiN as barrier material to achieve low $TBR_{eff}$ but it introduced a large variation in interfacial roughness and therefore a larger $TBR_{eff}$ variation within the sample, which needs to be further optimized in the growth method such as seeding and nucleation to enable smoother interfaces achieved. $TBR_{eff,\ Dia/GaN}$ using the SiN barrier layer is not that dependent on the diamond growth temperature and growth recipe, correspondingly for samples using the AlN barrier layers and grown without barrier layers. The effective thermal conductivity of the first micrometer diamond was found to increase with higher growth temperature at above 750 °C while it is almost independent of growth temperature below 750 °C for the temperature range studied, regardless of the recipe and the barrier layer material. This paragraph conclusions has significant content reproduced from my published work as a first author (published in ACS Applied Materials & Interfaces 9(39), 34416-34422),[29] with permission from ACS ©2017.

To evaluate the topside heat spreading strategy, PCD heat spreader structures grown onto high-k dielectric $Si_3N_4$ passivated AlGaN/GaN HEMT structures were studied, with diamond film thicknesses varying from 155 to 1000 nm. Nanosecond TDTR characterizations were combined with device thermal simulations to investigate the heat spreading benefit of the PCD layer. The results show that the observed thermal conductivity ($\kappa_{Dia}$) of PCD films has a strong film thickness dependence, which can be attributed to the in-plane grain size evolution with film thickness, with the measured values of $320 \pm 150$ W/mK for 1 μm-thick PCD, which is nearly one order of magnitude lower than the bulk PCD value of ~2200 W/mK. Numerous disordered intragrain structures such as twins and stacking faults are observed using a high-resolution TEM, which can greatly increase the phonon scattering within the

diamond grains and account for its lower thermal conductivity. The PCD layers do not show a sizable temperature dependence of $\kappa_{Dia}$ in the measured range from 25 to 225 °C which is very different from bulk PCD where it is seen to decrease with temperature. The $TBR_{eff, Dia/GaN}$ is higher than that in recent reports, mainly attributed to the thicker $Si_3N_4$ used in the samples studied due electrical characteristics. No obvious temperature dependence on $TBR_{eff, Dia/GaN}$ can be concluded for all studied samples. Transistor thermal modeling using the experimental $\kappa_{Dia}$ and $TBR_{eff, Dia/GaN}$ values shows that growing the PCD film heat spreader in the source-drain opening of a passivated AlGaN/GaN-on-Si HEMT only reduces the peak temperature by a maximum of 15%. Without considering the $TBR_{eff, Dia/GaN}$, a further 10% temperature reduction was observed. There is limited thermal benefit when the PCD film thickness is increased beyond ~2 μm even considering the anisotropic thermal conductivity, unless both source-drain opening and metal contacts are overgrown by PCD to increase the area of the heat spreader which can achieve a 1.5× better thermal benefit. This paragraph conclusions has significant content reproduced from my published work as a first author (published in Applied Physics Letters 111(3), 041901),[37] with permission from AIP ©2017.

### 8.2 Structural, thermal and mechanical properties of GaTe multilayered materials:

Chalcogenide based materials that with layered structures recently have raised huge interests due to their potential in memory phase switching devices and their unique optoelectronic properties. To be able to exploit their full potential it is imperative to gain a detailed understanding on the pressure-dependent electronic, vibrational, optical and structural properties. In this work, we have systematically explored the pressure-dependent in-plane anisotropic properties of multilayered Gallium Tellurite (GaTe) flakes using multiple experimental techniques combined with first-principles calculations from ambient pressure up to 46 GPa. We have discerned salient phase transitions with a strong anisotropic and reversible peak splitting of two Raman modes while changes in compressibility for other Raman modes started at ~6.5 GPa using angle-resolved polarized micro-Raman spectroscopy. A following structural phase transition from monoclinic phase into cubic phase at ~15 GPa accompanied with an electronic transition from semiconducting to metallic phase was also observed from the vanished Raman modes in micro-Raman spectrum and the obvious changes in the diffraction pattern of synchrotron XRD spectrum. The experimental results are further confirmed by theoretical calculations, which allow to gain detailed physical insight into the nature of these phase transitions. The first phase transition at ~6.5 GPa is found to originate from a lattice distortion induced iso-structural phase transition which is mainly due to the enhanced interaction of adjacent layers Te-Te atoms over their van der Waals (vdW) gap induced changes in the in-plane bonding. The second phase transition at ~15 GPa is mainly triggered by the easier breaking of some Ga-Ga bonds that along parallel to the in-plane direction than those bonded along perpendicular direction to the layers under higher pressures.

The transformed iso-structural monoclinic phase was also found to co-exist with a cubic phase in a broad pressure range due to the inhomogeneous strain introduced by the disordered phase formed during pressure. These pressure-tuned properties of multilayered GaTe flakes provide new insights for manipulating strain-dependent anisotropic light-material interactions and the anisotropic coupling of solid-state properties for other low symmetry layered materials. Our findings also reveal new opportunities for these low in-plane symmetry materials in potential applications of phase-switch devices, memory devices and strain-modulated optoelectronics.

The temperature dependence and polarization dependence of the GaTe phonon frequency were used to probe its lattice thermal conductivity along the armchair and zigzag in-plane crystal orientations respectively. A very low thermal conductivity of ~3-5 W/mK was demonstrated for these GaTe flakes along the above in-plane orientations with an anisotropic ratio of ~1.67, and it also revealed that thermal conductivity along the armchair orientation is much lower than that along the zigzag orientations due to its relative larger unharmonicity from the atomic configuration.

The mechanical properties of multilayered GaTe flakes were investigated through nanoindentation, AFM, and stress mapping using micro-Raman spectroscopy. The vdW adhesion force between GaTe flakes and the substrates was found to be much stronger than that between GaTe interlayers, resulting in the easier fracture of materials within the GaTe multilayers instead of slippage on the substrate. Three different types of *P-h* curves with the corresponding indent morphology characters in supported GaTe multilayers were demonstrated: (i) only PI (in the loading curve), with only a small pyramidal indent pit without observable fracture, pile-ups and cracks formed; (ii) PI + PO (in the unloading curve), featured by a pyramidal indent morphology with three similar pile-ups and crack prolongations; (iii) PI + LD (in the loading curve) + PO, where a pyramidal indent morphology with fracture and asymmetric pile-ups, crack prolongations are normally generated. Such PIs and LDs events were also observed on the free-standing GaTe flakes, without any observable facture or cracks even under slightly larger displacement loading than that of supported flakes. The PIs and LDs in the loading curve probably originate from the interlayer sliding, cracks and the induced phase transition within the GaTe multilayers during the indentation. The initial depth and force of the PIs (LDs) are ~15 nm and ~8 μN along the zigzag orientation while ~40 nm and ~9 μN along the armchair orientation, implying it is easier to drive the interlayer sliding at the zigzag orientation; after the initial period, the minimum force to drive the interlayer sliding is ~1 μN, comparable to that ~0.6 μN in bilayer graphene. An 11% larger strain along the armchair orientation than the zigzag orientation was also observed based on our present work.

## 8.3 Suggestions for future work

Although direct growth of diamond onto GaN without any barrier layer had demonstrated much higher TBR or even delamination at interfaces, it is still very necessary to remove this barrier layer as it is typically amorphous and has very low thermal conductivity blocking the heat efficiently transport into the substrate. The present higher TBR of direct growth is mainly due to the weak bonding of diamond with GaN and the harsh growth environment. Therefore, exploiting appropriate new interlayer material and structure with lower thermal resistance as well as new growth technology are expected. Moreover, surface activated bonding technology can also be tried to directly bond single-crystalline diamond or high thermal conductivity low-cost CVD grown PCD with GaN epilayer which probably can form robust GaN/diamond interfaces with promising mechanical properties and further reduce the TBR as it can produce much thinner smooth interlayer and has advantage in large scale fabrication.

In further, for GaN-on-diamond devices by growing diamond onto the GaN epilayer, the conventional diamond growth temperature of about 750-850 $^{o}$C is still too high for GaN which can result in some degradation of GaN especially for those near the interfaces. Low temperature growth would be preferred for retaining the GaN quality however normally results in lower growth rate and smaller grain size evolution of diamond with respect to its thickness which means lower thermal conductivity. Also, the initial diamond nucleation layer is vital for the TBR and the average diamond thermal conductivity, which are mainly correlated to the interfacial microstructure and diamond grain size, respectively. As low temperature growth can provide relative bigger size of the initial grains for seeding due to the relative lower thermal stress, we can try to employ a hybrid temperature growth method to grow the polycrystalline diamond, i.e., a first-step low temperature growth for about 100 nm-thick of the initial diamond layer followed by a second-step continuous higher temperature growth (will be still lower than the conventional diamond growth temperature of about 750 $^{o}$C). This method probably can enhance the GaN quality than the present technology as well as increase the average diamond grain size therein the diamond thermal conductivity over 500 W/mK in the first micrometre (meanwhile, the TBR at the GaN-diamond interface will be kept at about 20 $m^2K/GW$ or decreased to lower) for the industry beneficial.

As to GaTe multilayers, thickness dependent high pressure induced phase transition and anisotropic thermal conductivity, mechanical properties of especially few-layers or even monolayer GaTe need to be further explored. Especially, new approaches of fabricating few-layers and monolayer GaTe 2D samples need to be firstly and intensively investigated. Besides, high pressure electrical measurements are also very necessary as it will experimentally provide insights into the changes in electric properties helping us to gain an

even deeper understanding of the mechanisms of phase transitions in GaTe multilayers and few-layers. According to the above unique properties investigated, potential nanoflexible and strain-modulated devices, high performance novel optoelectronics, phase-switch, memory and thermoelectric devices, and thermal diodes as well as functional vdW heterojunction devices based on GaTe and other similar low in-plane symmetry 2D materials are deserved a try.

# Reference


1 Bardeen, J. & Brattain, W. H. The transistor, a semi-conductor triode. *Phys. Rev.* **74**, 230 (1948).

2 Mimura, T., Hiyamizu, S., Fujii, T. & Nanbu, K. A new field-effect transistor with selectively doped GaAs/n-AlxGa1-xAs heterojunctions. *Jpn. J. Appl. Phys.* **19**, L225 (1980).

3 Maruska, H. á. & Tietjen, J. The preparation and properties of vapor‐deposited single‐crystal‐line GaN. *Appl. Phys. Lett.* **15**, 327-329 (1969).

4 Nakamura, S., Mukai, T. & Senoh, M. High-power GaN pn junction blue-light-emitting diodes. *Jpn. J. Appl. Phys.* **30**, L1998 (1991).

5 Akasaki, I., Amano, H., Kito, M. & Hiramatsu, K. Photoluminescence of Mg-doped p-type GaN and electroluminescence of GaN pn junction LED. *J. Lumin.* **48**, 666-670 (1991).

6 Asif Khan, M., Bhattarai, A., Kuznia, J. & Olson, D. High electron mobility transistor based on a GaN‐Al x Ga1− x N heterojunction. *Appl. Phys. Lett.* **63**, 1214-1215 (1993).

7 Palmour, J., Kong, H.-S., Waltz, D., Edmond, J. & Carter Jr, C. 6H-silicon carbide transistors for high temperature operation. *Trans. 1st Internat. High Temp. Elect. ConJ*, 229 (1991).

8 Binari, S., Redwing, J., Kelner, G. & Kruppa, W. AlGaN/GaN HEMTs grown on SiC substrates. *Electron. Lett* **33**, 242-243 (1997).

9 Chumbes, E. M. *et al.* AlGaN/GaN high electron mobility transistors on Si (111) substrates. *IEEE Trans. Electron Devices* **48**, 420-426 (2001).

10 Gaska, R., Osinsky, A., Yang, J. & Shur, M. S. Self-heating in high-power AlGaN-GaN HFETs. *IEEE Electron Device Lett.* **19**, 89-91 (1998).

11 Via, G. D. in *Proc. CS MANTECH Conf.*

12 Cheney, D. J. *et al.* Degradation mechanisms for GaN and GaAs high speed transistors. *Materials* **5**, 2498-2520 (2012).

13 Kuball, M. *et al.* Measurement of temperature in active high-power AlGaN/GaN HFETs using Raman spectroscopy. *IEEE Electron Device Lett.* **23**, 7-9 (2002).

14 Ostermeir, R., Brunner, K., Abstreiter, G. & Weber, W. Temperature distribution in Si-MOSFETs studied by micro-Raman Spectroscopy. *IEEE Trans. Electron Devices* **39**, 858-863 (1992).

15 Sarua, A. *et al.* Integrated micro-Raman/infrared thermography probe for monitoring of self-heating in AlGaN/GaN transistor structures. *Electron Devices, IEEE Transactions on* **53**, 2438-2447 (2006).

16 Kuball, M. *et al.* Time-resolved temperature measurement of AlGaN/GaN electronic

devices using micro-Raman spectroscopy. *IEEE Electron device lett.* **28**, 86-89 (2007).
17 Martin-Horcajo, S. *et al.* Transient thermoreflectance for gate temperature assessment in pulse operated GaN-based HEMTs. *IEEE Electron device lett.* **37**, 1197-1200 (2016).
18 Simon, R. B., Pomeroy, J. W. & Kuball, M. Diamond micro-Raman thermometers for accurate gate temperature measurements. *Appl. Phys. Lett.* **104**, 213503 (2014).
19 Anaya, J. *et al.* Thermal conductivity of ultrathin nano-crystalline diamond films determined by Raman thermography assisted by silicon nanowires. *Appl. Phys. Lett.* **106**, 223101 (2015).
20 Kuball, M. & Pomeroy, J. W. A review of raman thermography for electronic and opto-electronic device measurement with submicron spatial and nanosecond temporal resolution. *IEEE Transactions on Device and Materials Reliability* **16**, 667-684 (2016).
21 Lin, C.-H. *et al.* Nanoscale mapping of temperature and defect evolution inside operating AlGaN/GaN high electron mobility transistors. *Appl. Phys. Lett.* **95**, 033510 (2009).
22 Burzo, M. G., Komarov, P. L. & Raad, P. E. Noncontact transient temperature mapping of active electronic devices using the thermoreflectance method. *IEEE transactions on components and packaging technologies* **28**, 637-643 (2005).
23 Anaya, J. *et al.* Simultaneous determination of the lattice thermal conductivity and grain/grain thermal resistance in polycrystalline diamond. *Acta Mater.* **139**, 215-225 (2017).
24 Felbinger, J. G. *et al.* Comparison of GaN HEMTs on diamond and SiC substrates. *IEEE Electron Device Lett.* **28**, 948-950 (2007).
25 Anaya, J. *et al.* Control of the in-plane thermal conductivity of ultra-thin nanocrystalline diamond films through the grain and grain boundary properties. *Acta Mater.* **103**, 141-152 (2016).
26 Manoi, A., Pomeroy, J. W., Killat, N. & Kuball, M. Benchmarking of thermal boundary resistance in AlGaN/GaN HEMTs on SiC substrates: Implications of the nucleation layer microstructure. *IEEE Electron Device Lett.* **31**, 1395-1397 (2010).
27 Pomeroy, J. W., Bernardoni, M., Dumka, D., Fanning, D. & Kuball, M. Low thermal resistance GaN-on-diamond transistors characterized by three-dimensional Raman thermography mapping. *Appl. Phys. Lett.* **104**, 083513 (2014).
28 Sun, H. *et al.* Reducing GaN-on-diamond interfacial thermal resistance for high power transistor applications. *Appl. Phys. Lett.* **106**, 111906 (2015).
29 Zhou, Y. *et al.* Barrier-Layer Optimization for Enhanced GaN-on-Diamond Device Cooling. *ACS Appl. Mater. Interfaces* **9**, 34416-34422 (2017).
30 Cho, J., Bozorg-Grayeli, E., Altman, D. H., Asheghi, M. & Goodson, K. E. Low thermal resistances at GaN–SiC interfaces for HEMT technology. *IEEE Electron Device Lett.* **33**, 378-380 (2012).
31 Rossi, S. *Nanocrystalline diamond growth for top heat-spreading applications on GaN-based devices*, Universität Ulm, (2015).
32 Tadjer, M. J. *et al.* Nanocrystalline diamond capped AlGaN/GaN high electron mobility transistors via a sacrificial gate process. *physica status solidi (a)* **213**, 893-897 (2016).
33 Meyer, D. J. *et al.* Large-signal RF performance of nanocrystalline diamond coated AlGaN/GaN high electron mobility transistors. *IEEE Electron device lett.* **35**, 1013-1015 (2014).
34 Wang, A., Tadjer, M. & Calle, F. Simulation of thermal management in AlGaN/GaN HEMTs with integrated diamond heat spreaders. *Semicond. Sci. Technol.* **28**, 055010 (2013).

35 Anaya, J., Sun, H., Pomeroy, J. & Kuball, M. in *2016 15th IEEE Intersociety Conference on Thermal and Thermomechanical Phenomena in Electronic Systems (ITherm)*. 1558-1565.
36 Zhang, R., Zhao, W., Yin, W., Zhao, Z. & Zhou, H. Impacts of diamond heat spreader on the thermo-mechanical characteristics of high-power AlGaN/GaN HEMTs. *Diamond Relat. Mater.* **52**, 25-31 (2015).
37 Zhou, Y. *et al.* Thermal characterization of polycrystalline diamond thin film heat spreaders grown on GaN HEMTs. *Appl. Phys. Lett.* **111**, 041901 (2017).
38 Georgiou, T. *et al.* Vertical field-effect transistor based on graphene–WS 2 heterostructures for flexible and transparent electronics. *Nature nanotechnology* **8**, 100 (2013).
39 Jariwala, D., Marks, T. J. & Hersam, M. C. Mixed-dimensional van der Waals heterostructures. *Nature materials* **16**, 170 (2017).
40 Geim, A. K. & Novoselov, K. S. The rise of graphene. *Nature materials* **6**, 183 (2007).
41 Palacios, T., Hsu, A. & Wang, H. Applications of graphene devices in RF communications. *IEEE Communications Magazine* **48** (2010).
42 Ambacher, O. Growth and applications of group III-nitrides. *J. Phys. D: Appl. Phys.* **31**, 2653 (1998).
43 Leszczynski, M. *et al.* Lattice parameters of gallium nitride. *Appl. Phys. Lett.* **69**, 73-75 (1996).
44 Bernardini, F., Fiorentini, V. & Vanderbilt, D. Spontaneous polarization and piezoelectric constants of III-V nitrides. *Phys. Rev. B* **56**, R10024 (1997).
45 Morkoc, H. *Nitride semiconductors and devices*. Vol. 32 (Springer Science & Business Media, 2013).
46 Chen, G. *et al.* Fundamental optical transitions in GaN. *Appl. Phys. Lett.* **68**, 2784-2786 (1996).
47 Perlin, P. *et al.* Pressure studies of gallium nitride: crystal growth and fundamental electronic properties. *Phys. Rev. B* **45**, 13307 (1992).
48 Yu, P. Y. & Cardona, M. *Fundamentals of semiconductors: physics and materials properties*. (Springer, 1996).
49 Molloy, K. C. *Group theory for chemists: fundamental theory and applications*. (Elsevier, 2010).
50 Davydov, V. Y. *et al.* Phonon dispersion and Raman scattering in hexagonal GaN and AlN. *Phys. Rev. B* **58**, 12899 (1998).
51 Harima, H. Properties of GaN and related compounds studied by means of Raman scattering. *J. Phys.: Condens. Matter* **14**, R967 (2002).
52 Nipko, J., Loong, C.-K., Balkas, C. & Davis, R. Phonon density of states of bulk gallium nitride. *Appl. Phys. Lett.* **73**, 34-36 (1998).
53 Ruf, T. *et al.* Phonon dispersion curves in wurtzite-structure GaN determined by inelastic X-ray scattering. *Phys. Rev. Lett.* **86**, 906 (2001).
54 Bungaro, C., Rapcewicz, K. & Bernholc, J. Ab initio phonon dispersions of wurtzite AlN, GaN, and InN. *Phys. Rev. B* **61**, 6720 (2000).
55 Vandersande, J. & Wood, C. The thermal conductivity of insulators and semiconductors. *Contemporary Physics* **27**, 117-144 (1986).
56 Kaviany, M. *Heat transfer physics*. (Cambridge University Press, 2014).
57 Cho, J. *et al.* Phonon scattering in strained transition layers for GaN heteroepitaxy. *Phys. Rev. B* **89**, 115301 (2014).
58 Ma, J., Wang, X., Huang, B. & Luo, X. Effects of point defects and dislocations on spectral phonon transport properties of wurtzite GaN. *J. Appl. Phys.* **114**, 074311 (2013).

59 Florescu, D., Asnin, V., Pollak, F. H., Molnar, R. & Wood, C. High spatial resolution thermal conductivity and Raman spectroscopy investigation of hydride vapor phase epitaxy grown n-GaN/sapphire (0001): Doping dependence. *J. Appl. Phys.* **88**, 3295-3300 (2000).
60 Florescu, D. *et al.* Thermal conductivity of fully and partially coalesced lateral epitaxial overgrown GaN/sapphire (0001) by scanning thermal microscopy. *Appl. Phys. Lett.* **77**, 1464-1466 (2000).
61 Zou, J., Kotchetkov, D., Balandin, A., Florescu, D. & Pollak, F. H. Thermal conductivity of GaN films: Effects of impurities and dislocations. *J. Appl. Phys.* **92**, 2534-2539 (2002).
62 Lindsay, L., Broido, D. & Reinecke, T. Thermal conductivity and large isotope effect in GaN from first principles. *Phys. Rev. Lett.* **109**, 095901 (2012).
63 Witek, A. Some aspects of thermal conductivity of isotopically pure diamond—A comparison with nitrides. *Diamond Relat. Mater.* **7**, 962-964 (1998).
64 Luo, C.-Y., Marchand, H., Clarke, D. & DenBaars, S. Thermal conductivity of lateral epitaxial overgrown GaN films. *Appl. Phys. Lett.* **75**, 4151-4153 (1999).
65 Liu, W., Balandin, A. A., Lee, C. & Lee, H. Y. Increased thermal conductivity of free‐standing low‐dislocation‐density GaN films. *physica status solidi (a)* **202** (2005).
66 Peter, Y. & Cardona, M. *Fundamentals of semiconductors: physics and materials properties*. (Springer Science & Business Media, 2010).
67 Yang, Z., Li, L. & Wang, W. GaN grown by molecular beam epitaxy at high growth rates using ammonia as the nitrogen source. *Appl. Phys. Lett.* **67**, 1686-1688 (1995).
68 Hughes, W. *et al.* Molecular beam epitaxy growth and properties of GaN films on GaN/SiC substrates. *Journal of Vacuum Science & Technology B: Microelectronics and Nanometer Structures Processing, Measurement, and Phenomena* **13**, 1571-1577 (1995).
69 Dapkus, P. A critical comparison of MOCVD and MBE for heterojunction devices. *J. Cryst. Growth* **68**, 345-355 (1984).
70 Nakamura, S. GaN growth using GaN buffer layer. *Jpn. J. Appl. Phys.* **30**, L1705 (1991).
71 Al Balushi, Z. Y. & Redwing, J. M. In situ stress measurements during direct MOCVD growth of GaN on SiC. *J. Mater. Res.* **30**, 2900-2909 (2015).
72 Raghavan, S. & Redwing, J. M. Growth stresses and cracking in GaN films on (111) Si grown by metal-organic chemical-vapor deposition. I. AlN buffer layers. *J. Appl. Phys.* **98**, 023514 (2005).
73 Raghavan, S. & Redwing, J. Growth stresses and cracking in GaN films on (111) Si grown by metalorganic chemical vapor deposition. II. Graded AlGaN buffer layers. *J. Appl. Phys.* **98**, 023515 (2005).
74 Marchand, H. *et al.* Metalorganic chemical vapor deposition of GaN on Si (111): Stress control and application to field-effect transistors. *J. Appl. Phys.* **89**, 7846-7851 (2001).
75 Kim, M.-H., Do, Y.-G., Kang, H. C., Noh, D. Y. & Park, S.-J. Effects of step-graded Al x Ga 1− x N interlayer on properties of GaN grown on Si (111) using ultrahigh vacuum chemical vapor deposition. *Appl. Phys. Lett.* **79**, 2713-2715 (2001).
76 Liu, H. *et al.* Influence of stress on structural properties of AlGaN/GaN high electron mobility transistor layers grown on 150 mm diameter Si (111) substrate. *J. Appl. Phys.* **113**, 023510 (2013).
77 Mohan, N., Manikant, Soman, R. & Raghavan, S. Integrating AlGaN/GaN high electron mobility transistor with Si: A comparative study of integration schemes. *J. Appl. Phys.* **118**, 135302 (2015).

78 Gelmont, B., Kim, K. & Shur, M. Monte Carlo simulation of electron transport in gallium nitride. *J. Appl. Phys.* **74**, 1818-1821 (1993).
79 Mishra, U. K., Shen, L., Kazior, T. E. & Wu, Y.-F. GaN-based RF power devices and amplifiers. *Proc. IEEE* **96**, 287-305 (2008).
80 Ibbetson, J. P. *et al.* Polarization effects, surface states, and the source of electrons in AlGaN/GaN heterostructure field effect transistors. *Appl. Phys. Lett.* **77**, 250-252 (2000).
81 Ambacher, O. *et al.* Two dimensional electron gases induced by spontaneous and piezoelectric polarization in undoped and doped AlGaN/GaN heterostructures. *J. Appl. Phys.* **87**, 334-344 (2000).
82 Jang, H. W. *et al.* Mechanism of two-dimensional electron gas formation in Al x Ga 1− x N/GaN heterostructures. *Appl. Phys. Lett.* **81**, 1249-1251 (2002).
83 Lu, W., Kumar, V., Schwindt, R., Piner, E. & Adesida, I. A comparative study of surface passivation on AlGaN/GaN HEMTs. *Solid·State Electron.* **46**, 1441-1444 (2002).
84 Rajasingam, S. *et al.* Micro-Raman temperature measurements for electric field assessment in active AlGaN-GaN HFETs. *IEEE Electron device lett.* **25**, 456-458 (2004).
85 Sun, H., Bajo, M. M., Uren, M. J. & Kuball, M. Implications of gate-edge electric field in AlGaN/GaN high electron mobility transistors during OFF-state degradation. *Microelectronics Reliability* **54**, 2650-2655 (2014).
86 Wakejima, A. *et al.* Observation of cross-sectional electric field for GaN-based field effect transistor with field-modulating plate. *Appl. Phys. Lett.* **90**, 213504 (2007).
87 Ungersböck, S.-E. *Advanced modeling of strained CMOS technology*. (na, 2007).
88 Hemstreet Jr, L. A., Fong, C. & Cohen, M. L. Calculation of the band structure and optical constants of diamond using the nonlocal-pseudopotential method. *Phys. Rev. B* **2**, 2054 (1970).
89 Yamamoto, T., Janssens, S. D., Ohtani, R., Takeuchi, D. & Koizumi, S. Toward highly conductive n-type diamond: Incremental phosphorus-donor concentrations assisted by surface migration of admolecules. *Appl. Phys. Lett.* **109**, 182102 (2016).
90 Yan, B. *et al.* The effect of phosphorus and nitrogen co-doped on the synthesis of diamond at high pressure and high temperature. *Int. J. Refract. Met. Hard Mater.* **54**, 309-314 (2016).
91 Weber, W. Adiabatic bond charge model for the phonons in diamond, Si, Ge, and α− Sn. *Phys. Rev. B* **15**, 4789 (1977).
92 Coe, S. & Sussmann, R. Optical, thermal and mechanical properties of CVD diamond. *Diamond Relat. Mater.* **9**, 1726-1729 (2000).
93 Yates, L. *et al.* in *Compound Semiconductor Integrated Circuit Symposium (CSICS), 2016 IEEE.* 1-4 (IEEE).
94 Berman, R., Hudson, P. & Martinez, M. Nitrogen in diamond: evidence from thermal conductivity. *Journal of Physics C: Solid State Physics* **8**, L430 (1975).
95 Sukhadolau, A. *et al.* Thermal conductivity of CVD diamond at elevated temperatures. *Diamond Relat. Mater.* **14**, 589-593 (2005).
96 Wörner, E., Wild, C., Müller-Sebert, W., Locher, R. & Koidl, P. Thermal conductivity of CVD diamond films: high-precision, temperature-resolved measurements. *Diamond Relat. Mater.* **5**, 688-692 (1996).
97 Graebner, J., Mucha, J., Seibles, L. & Kammlott, G. The thermal conductivity of chemical‐vapor‐deposited diamond films on silicon. *J. Appl. Phys.* **71**, 3143-3146 (1992).
98 Gruen, D. M., Liu, S., Krauss, A. R. & Pan, X. Buckyball microwave plasmas:

Fragmentation and diamond‐film growth. *J. Appl. Phys.* **75**, 1758-1763 (1994).
99 Hartmann, J., Voigt, P. & Reichling, M. Measuring local thermal conductivity in polycrystalline diamond with a high resolution photothermal microscope. *J. Appl. Phys.* **81**, 2966-2972 (1997).
100 Reichling, M., Klotzbücher, T. & Hartmann, J. Local variation of room-temperature thermal conductivity in high-quality polycrystalline diamond. *Appl. Phys. Lett.* **73**, 756-758 (1998).
101 Philip, J. *et al.* Elastic, mechanical, and thermal properties of nanocrystalline diamond films. *J. Appl. Phys.* **93**, 2164-2171 (2003).
102 Angadi, M. A. *et al.* Thermal transport and grain boundary conductance in ultrananocrystalline diamond thin films. *J. Appl. Phys.* **99**, 114301 (2006).
103 Liu, W. *et al.* Thermal conduction in nanocrystalline diamond films: Effects of the grain boundary scattering and nitrogen doping. *Appl. Phys. Lett.* **89**, 171915-171915 (2006).
104 Shamsa, M. *et al.* Thermal conductivity of nitrogenated ultrananocrystalline diamond films on silicon. *J. Appl. Phys.* **103**, 083538 (2008).
105 Morelli, D. T., Perry, T. A. & Farmer, J. W. Phonon scattering in lightly neutron-irradiated diamond. *Phys. Rev. B* **47**, 131 (1993).
106 Smereka, P., Li, X., Russo, G. & Srolovitz, D. J. Simulation of faceted film growth in three dimensions: microstructure, morphology and texture. *Acta Mater.* **53**, 1191-1204 (2005).
107 Ophus, C., Ewalds, T., Luber, E. J. & Mitlin, D. The role of self-shadowing on growth and scaling laws of faceted polycrystalline thin films. *Acta Mater.* **58**, 5150-5159 (2010).
108 Liu, T., Raabe, D. & Mao, W.-M. A review of crystallographic textures in chemical vapor-deposited diamond films. *Frontiers of Materials Science in China* **4**, 1-16 (2010).
109 Dumka, D., Chou, T., Faili, F., Francis, D. & Ejeckam, F. AlGaN/GaN HEMTs on diamond substrate with over 7W/mm output power density at 10 GHz. *Electron. Lett* **49**, 1298-1299 (2013).
110 Francis, D. *et al.* Formation and characterization of 4-inch GaN-on-diamond substrates. *Diamond Relat. Mater.* **19**, 229-233 (2010).
111 Jessen, G. *et al.* in *2006 IEEE Compound Semiconductor Integrated Circuit Symposium.* 271-274 (IEEE).
112 Cho, J. *et al.* Improved thermal interfaces of GaN–diamond composite substrates for HEMT applications. *IEEE Trans. Compon. Packag. Manuf. Technol.* **3**, 79-85 (2013).
113 Chabak, K. D. *et al.* Full-wafer characterization of AlGaN/GaN HEMTs on free-standing CVD diamond substrates. *IEEE Electron device lett.* **31**, 99-101 (2010).
114 May, P. W. Diamond thin films: a 21st-century material. *Philosophical Transactions of the Royal Society of London A: Mathematical, Physical and Engineering Sciences* **358**, 473-495 (2000).
115 Goodwin, D. & Butler, J. Theory of diamond chemical vapor deposition. *Handbook of industrial diamonds and diamond films*, 527-581 (1997).
116 Butler, J. E. & Woodin, R. L. Thin film diamond growth mechanisms. *Phil. Trans. R. Soc. Lond. A* **342**, 209-224 (1993).
117 Yan, C.-s., Vohra, Y. K., Mao, H.-k. & Hemley, R. J. Very high growth rate chemical vapor deposition of single-crystal diamond. *Proceedings of the National Academy of Sciences* **99**, 12523-12525 (2002).
118 Wild, C. *et al.* Chemical vapour deposition and characterization of smooth {100}-faceted diamond films. *Diamond Relat. Mater.* **2**, 158-168 (1993).

119 Yang, S., He, Z., Li, Q., Zhu, D. & Gong, J. Diamond films with preferred< 110> texture by hot filament CVD at low pressure. *Diamond Relat. Mater.* **17**, 2075-2079 (2008).
120 Wild, C., Kohl, R., Herres, N., Müller-Sebert, W. & Koidl, P. Oriented CVD diamond films: twin formation, structure and morphology. *Diamond Relat. Mater.* **3**, 373-381 (1994).
121 Won, Y., Cho, J., Agonafer, D., Asheghi, M. & Goodson, K. E. Fundamental Cooling Limits for High Power Density Gallium Nitride Electronics. *IEEE Trans. Compon. Packag. Manuf. Technol.* **5**, 737-744 (2015).
122 Cahill, D. G. *et al.* Nanoscale thermal transport. *J. Appl. Phys.* **93**, 793-818 (2003).
123 Cahill, D. G. *et al.* Nanoscale thermal transport. II. 2003–2012. *Applied Physics Reviews* **1**, 011305 (2014).
124 Little, W. The transport of heat between dissimilar solids at low temperatures. *Can. J. Phys.* **37**, 334-349 (1959).
125 Swartz, E. & Pohl, R. Thermal resistance at interfaces. *Appl. Phys. Lett.* **51**, 2200-2202 (1987).
126 Swartz, E. T. & Pohl, R. O. Thermal boundary resistance. *Rev. Mod. Phys.* **61**, 605 (1989).
127 Stoner, R. & Maris, H. Kapitza conductance and heat flow between solids at temperatures from 50 to 300 K. *Phys. Rev. B* **48**, 16373 (1993).
128 Stevens, R. J., Smith, A. N. & Norris, P. M. Measurement of thermal boundary conductance of a series of metal-dielectric interfaces by the transient thermoreflectance technique. *J. Heat Transfer* **127**, 315-322 (2005).
129 Snyder, N. Heat transport through helium II: Kapitza conductance. *Cryogenics* **10**, 89-95 (1970).
130 Lyeo, H.-K. & Cahill, D. G. Thermal conductance of interfaces between highly dissimilar materials. *Phys. Rev. B* **73**, 144301 (2006).
131 Hopkins, P. E., Norris, P. M. & Stevens, R. J. Influence of inelastic scattering at metal-dielectric interfaces. *J. Heat Transfer* **130**, 022401 (2008).
132 Stevens, R. J., Zhigilei, L. V. & Norris, P. M. Effects of temperature and disorder on thermal boundary conductance at solid–solid interfaces: Nonequilibrium molecular dynamics simulations. *Int. J. Heat Mass Transfer* **50**, 3977-3989 (2007).
133 Butler, S. Z. *et al.* Progress, challenges, and opportunities in two-dimensional materials beyond graphene. *ACS nano* **7**, 2898-2926 (2013).
134 Xia, F., Wang, H. & Jia, Y. Rediscovering black phosphorus as an anisotropic layered material for optoelectronics and electronics. *Nature communications* **5**, 4458 (2014).
135 Wang, X. *et al.* Highly anisotropic and robust excitons in monolayer black phosphorus. *Nature nanotechnology* **10**, 517-521 (2015).
136 Ling, X. *et al.* Anisotropic Electron-Photon and Electron-Phonon Interactions in Black Phosphorus. *Nano Lett.* **16**, 2260-2267 (2016).
137 Huang, S. *et al.* In-plane optical anisotropy of layered gallium telluride. *ACS nano* **10**, 8964-8972 (2016).
138 Chenet, D. A. *et al.* In-plane anisotropy in mono-and few-layer ReS2 probed by Raman spectroscopy and scanning transmission electron microscopy. *Nano Lett.* **15**, 5667-5672 (2015).
139 Zhao, L.-D. *et al.* Ultrahigh power factor and thermoelectric performance in hole-doped single-crystal SnSe. *Science*, aad3749 (2015).
140 Zhang, S. *et al.* Anomalous Polarized Raman Scattering and Large Circular Intensity Differential in Layered Triclinic ReS2. *ACS nano* **11**, 10366-10372 (2017).
141 Wang, J. *et al.* Determination of Crystal Axes in Semimetallic T′ - MoTe2 by

Polarized Raman Spectroscopy. *Adv. Funct. Mater.* **27** (2017).
142 Fei, R. *et al.* Enhanced thermoelectric efficiency via orthogonal electrical and thermal conductances in phosphorene. *Nano Lett.* **14**, 6393-6399 (2014).
143 Radisavljevic, B., Radenovic, A., Brivio, J., Giacometti, V. & Kis, A. Single-layer MoS2 transistors. *Nature nanotechnology* **6**, 147-150 (2011).
144 Liu, F. *et al.* High-sensitivity photodetectors based on multilayer GaTe flakes. *ACS nano* **8**, 752-760 (2014).
145 Sun, D. *et al.* Ultrafast hot-carrier-dominated photocurrent in graphene. *Nature nanotechnology* **7**, 114 (2012).
146 Ling, X., Wang, H., Huang, S., Xia, F. & Dresselhaus, M. S. The renaissance of black phosphorus. *Proceedings of the National Academy of Sciences* **112**, 4523-4530 (2015).
147 Zhou, L. *et al.* A Sensitive Phonon-Based Probe for Structure Identification of 1T'MoTe2. *J. Am. Chem. Soc.* (2017).
148 Taube, A., Łapińska, A., Judek, J. & Zdrojek, M. Temperature dependence of Raman shifts in layered ReSe2 and SnSe2 semiconductor nanosheets. *Appl. Phys. Lett.* **107**, 013105 (2015).
149 Luo, Z. *et al.* Anisotropic in-plane thermal conductivity observed in few-layer black phosphorus. *Nature communications* **6** (2015).
150 Lee, S. *et al.* Anisotropic in-plane thermal conductivity of black phosphorus nanoribbons at temperatures higher than 100 [thinsp] K. *Nature communications* **6** (2015).
151 Yang, S. *et al.* Highly-anisotropic optical and electrical properties in layered SnSe. *Nano Research*, 1-11 (2017).
152 Lee, S. *et al.* Anisotropic in-plane thermal conductivity of black phosphorus nanoribbons at temperatures higher than 100 K. *Nature communications* **6**, 8573 (2015).
153 Dresselhaus, M. S., Jorio, A., Hofmann, M., Dresselhaus, G. & Saito, R. Perspectives on carbon nanotubes and graphene Raman spectroscopy. *Nano Lett.* **10**, 751-758 (2010).
154 Dresselhaus, M., Jorio, A. & Saito, R. Characterizing graphene, graphite, and carbon nanotubes by Raman spectroscopy. *Annu. Rev. Condens. Matter Phys.* **1**, 89-108 (2010).
155 Cong, C. *et al.* Raman characterization of ABA-and ABC-stacked trilayer graphene. *ACS nano* **5**, 8760-8768 (2011).
156 Pimenta, M. *et al.* Studying disorder in graphite-based systems by Raman spectroscopy. *PCCP* **9**, 1276-1290 (2007).
157 Mak, K. F. *et al.* Tightly bound trions in monolayer MoS2. *Nature materials* **12**, 207-211 (2013).
158 Souza Filho, A. *et al.* Stokes and anti-Stokes Raman spectra of small-diameter isolated carbon nanotubes. *Phys. Rev. B* **69**, 115428 (2004).
159 Roldán, R., Castellanos-Gomez, A., Cappelluti, E. & Guinea, F. Strain engineering in semiconducting two-dimensional crystals. *J. Phys.: Condens. Matter* **27**, 313201 (2015).
160 Zhang, J. *et al.* High thermoelectric performance can be achieved in black phosphorus. *Journal of Materials Chemistry C* **4**, 991-998 (2016).
161 Fei, Z. *et al.* Edge conduction in monolayer WTe 2. *Nature Physics* **13**, 677 (2017).
162 Xi, X. *et al.* Ising pairing in superconducting NbSe 2 atomic layers. *Nature Physics* **12**, 139 (2016).
163 Huang, B. *et al.* Layer-dependent ferromagnetism in a van der Waals crystal down to the monolayer limit. *Nature* **546**, 270 (2017).

164 Sun, Z., Martinez, A. & Wang, F. Optical modulators with 2D layered materials. *Nature Photonics* **10**, nphoton. 2016.2015 (2016).
165 Chen, J. *et al.* Optical nano-imaging of gate-tunable graphene plasmons. *Nature* **487**, 77 (2012).
166 Withers, F. *et al.* Light-emitting diodes by band-structure engineering in van der Waals heterostructures. *Nature materials* **14**, 301 (2015).
167 Koppens, F. *et al.* Photodetectors based on graphene, other two-dimensional materials and hybrid systems. *Nature nanotechnology* **9**, 780 (2014).
168 Xia, F., Wang, H., Xiao, D., Dubey, M. & Ramasubramaniam, A. Two-dimensional material nanophotonics. *Nature Photonics* **8**, 899 (2014).
169 Mak, K. F. & Shan, J. Photonics and optoelectronics of 2D semiconductor transition metal dichalcogenides. *Nature Photonics* **10**, 216-226 (2016).
170 Bao, Q. & Loh, K. P. Graphene photonics, plasmonics, and broadband optoelectronic devices. *ACS nano* **6**, 3677-3694 (2012).
171 Wang, Q. H., Kalantar-Zadeh, K., Kis, A., Coleman, J. N. & Strano, M. S. Electronics and optoelectronics of two-dimensional transition metal dichalcogenides. *Nature nanotechnology* **7**, 699-712 (2012).
172 Lee, H. S. *et al.* MoS2 nanosheet phototransistors with thickness-modulated optical energy gap. *Nano Lett.* **12**, 3695-3700 (2012).
173 Xiao, D., Liu, G.-B., Feng, W., Xu, X. & Yao, W. Coupled spin and valley physics in monolayers of MoS 2 and other group-VI dichalcogenides. *Phys. Rev. Lett.* **108**, 196802 (2012).
174 Mak, K. F., He, K., Shan, J. & Heinz, T. F. Control of valley polarization in monolayer MoS2 by optical helicity. *Nature nanotechnology* **7**, 494-498 (2012).
175 Cao, T. *et al.* Valley-selective circular dichroism of monolayer molybdenum disulphide. *Nature communications* **3**, 887 (2012).
176 Zeng, H., Dai, J., Yao, W., Xiao, D. & Cui, X. Valley polarization in MoS2 monolayers by optical pumping. *Nature nanotechnology* **7**, 490-493 (2012).
177 Fontana, M. *et al.* Electron-hole transport and photovoltaic effect in gated MoS2 Schottky junctions. *Scientific reports* **3** (2013).
178 Sachs, B. *et al.* Doping mechanisms in graphene-MoS2 hybrids. *Appl. Phys. Lett.* **103**, 251607 (2013).
179 Radisavljevic, B. & Kis, A. Mobility engineering and a metal–insulator transition in monolayer MoS2. *Nature materials* **12**, 815-820 (2013).
180 Ye, J. *et al.* Superconducting dome in a gate-tuned band insulator. *Science* **338**, 1193-1196 (2012).
181 Tongay, S. *et al.* Thermally driven crossover from indirect toward direct bandgap in 2D semiconductors: MoSe2 versus MoS2. *Nano Lett.* **12**, 5576-5580 (2012).
182 Johari, P. & Shenoy, V. B. Tuning the electronic properties of semiconducting transition metal dichalcogenides by applying mechanical strains. *ACS nano* **6**, 5449-5456 (2012).
183 Nayak, A. P. *et al.* Pressure-induced semiconducting to metallic transition in multilayered molybdenum disulphide. *Nature communications* **5**, 3731 (2014).
184 Nayak, A. P. *et al.* Pressure-dependent optical and vibrational properties of monolayer molybdenum disulfide. *Nano Lett.* **15**, 346-353 (2014).
185 Nayak, A. P. *et al.* Pressure-modulated conductivity, carrier density, and mobility of multilayered tungsten disulfide. *ACS nano* **9**, 9117-9123 (2015).
186 Chi, Z.-H. *et al.* Pressure-induced metallization of molybdenum disulfide. *Phys. Rev. Lett.* **113**, 036802 (2014).
187 Zhao, Z. *et al.* Pressure induced metallization with absence of structural transition in

layered molybdenum diselenide. *Nature communications* **6** (2015).
188 Wang, X. *et al.* Pressure-induced iso-structural phase transition and metallization in WSe2. *Scientific Reports* **7** (2017).
189 Ataca, C. & Ciraci, S. Functionalization of single-layer MoS2 honeycomb structures. *The Journal of Physical Chemistry C* **115**, 13303-13311 (2011).
190 Jo, S., Costanzo, D., Berger, H. & Morpurgo, A. F. Electrostatically induced superconductivity at the surface of WS2. *Nano Lett.* **15**, 1197-1202 (2015).
191 Fu, L. *et al.* K-Λ crossover transition in the conduction band of monolayer MoS2 under hydrostatic pressure. *Science advances* **3**, e1700162 (2017).
192 Zhao, Q. *et al.* Thickness-induced structural phase transformation of layered gallium telluride. *PCCP* **18**, 18719-18726 (2016).
193 Schwarz, U., Syassen, K. & Kniep, R. Structural phase transition of GaTe at high pressure. *J. Alloys Compd.* **224**, 212-216 (1995).
194 Pellicer-Porres, J., Segura, A., Munoz, V. & San Miguel, A. High-pressure x-ray absorption study of GaTe including polarization. *Phys. Rev. B* **61**, 125 (2000).
195 Schwarz, U., Olguin, D., Cantarero, A., Hanfland, M. & Syassen, K. Effect of pressure on the structural properties and electronic band structure of GaSe. *physica status solidi (b)* **244**, 244-255 (2007).
196 Keum, D. H. *et al.* Bandgap opening in few-layered monoclinic MoTe2. *Nature Physics* **11**, 482-486 (2015).
197 Kappera, R. *et al.* Phase-engineered low-resistance contacts for ultrathin MoS2 transistors. *Nature materials* **13**, 1128-1134 (2014).
198 Wang, Y. *et al.* Structural phase transition in monolayer MoTe 2 driven by electrostatic doping. *Nature* **550**, 487 (2017).
199 Giorgianni, F. *et al.* Subcycle insulator-to-metal transition in vanadium dioxide by terahertz-field-driven tunneling. *arXiv preprint arXiv:1706.00616* (2017).
200 Zhu, J. *et al.* Temperature-gated thermal rectifier for active heat flow control. *Nano Lett.* **14**, 4867-4872 (2014).
201 Chen, Y. *et al.* Pressure–Temperature Phase Diagram of Vanadium Dioxide. *Nano Lett.* **17**, 2512-2516 (2017).
202 Raoux, S. *et al.* Phase-change random access memory: A scalable technology. *IBM J. Res. Dev.* **52**, 465-479 (2008).
203 Yamada, N., Ohno, E., Nishiuchi, K., Akahira, N. & Takao, M. Rapid‐phase transitions of GeTe‐Sb2Te3 pseudobinary amorphous thin films for an optical disk memory. *J. Appl. Phys.* **69**, 2849-2856 (1991).
204 Tominaga, J., Kikukawa, T., Takahashi, M. & Phillips, R. Structure of the optical phase change memory alloy, Ag–V–In–Sb–Te, determined by optical spectroscopy and electron diffraction. *J. Appl. Phys.* **82**, 3214-3218 (1997).
205 Kolobov, A. V. *et al.* Understanding the phase-change mechanism of rewritable optical media. *Nature materials* **3**, 703 (2004).
206 Hudgens, S. & Johnson, B. Overview of phase-change chalcogenide nonvolatile memory technology. *MRS Bull.* **29**, 829-832 (2004).
207 Wang, Z. *et al.* Role of Ga vacancy on a multilayer GaTe phototransistor. *ACS nano* **8**, 4859-4865 (2014).
208 Hu, P. *et al.* Highly sensitive phototransistors based on two-dimensional GaTe nanosheets with direct bandgap. *Nano Research* **7**, 694 (2014).
209 Mandal, K. C. *et al.* Layered GaTe crystals for radiation detectors. *IEEE Trans. Nucl. Sci.* **58**, 1981-1986 (2011).
210 Susoma, J. *et al.* Second and third harmonic generation in few-layer gallium telluride characterized by multiphoton microscopy. *Appl. Phys. Lett.* **108**, 073103 (2016).

211 Pal, S. & Bose, D. Growth, characterisation and electrical anisotropy in layered chalcogenides GaTe and InTe. *Solid State Commun.* **97**, 725-729 (1996).
212 Reshmi, P., Kunjomana, A., Chandrasekharan, K., Meena, M. & Mahadevan, C. Structural, electrical and mechanical properties of GaTe for radiation detector applications. *International Journal of Soft Computing Engineering* **1**, 228-232 (2011).
213 Akinwande, D. *et al.* A review on mechanics and mechanical properties of 2D materials—Graphene and beyond. *Extreme Mechanics Letters* **13**, 42-77 (2017).
214 Lee, C., Wei, X., Kysar, J. W. & Hone, J. Measurement of the elastic properties and intrinsic strength of monolayer graphene. *Science* **321**, 385-388 (2008).
215 Cooper, R. C. *et al.* Nonlinear elastic behavior of two-dimensional molybdenum disulfide. *Phys. Rev. B* **87**, 035423 (2013).
216 Bertolazzi, S., Brivio, J. & Kis, A. Stretching and breaking of ultrathin MoS2. *ACS nano* **5**, 9703-9709 (2011).
217 Song, L. *et al.* Large scale growth and characterization of atomic hexagonal boron nitride layers. *Nano Lett.* **10**, 3209-3215 (2010).
218 López-Polín, G. *et al.* Increasing the elastic modulus of graphene by controlled defect creation. *Nature Physics* **11**, 26 (2015).
219 Min, K. & Aluru, N. Mechanical properties of graphene under shear deformation. *Appl. Phys. Lett.* **98**, 013113 (2011).
220 Song, Z., Artyukhov, V. I., Wu, J., Yakobson, B. I. & Xu, Z. Defect-detriment to graphene strength is concealed by local probe: the topological and geometrical effects. *ACS nano* **9**, 401-408 (2014).
221 Pereira, V. M. & Neto, A. C. Strain engineering of graphene's electronic structure. *Phys. Rev. Lett.* **103**, 046801 (2009).
222 Duerloo, K.-A. N., Li, Y. & Reed, E. J. Structural phase transitions in two-dimensional Mo-and W-dichalcogenide monolayers. *Nature communications* **5**, 4214 (2014).
223 Li, Y., Duerloo, K.-A. N., Wauson, K. & Reed, E. J. Structural semiconductor-to-semimetal phase transition in two-dimensional materials induced by electrostatic gating. *Nature communications* **7**, 10671 (2016).
224 Koenig, S. P., Boddeti, N. G., Dunn, M. L. & Bunch, J. S. Ultrastrong adhesion of graphene membranes. *Nature nanotechnology* **6**, 543 (2011).
225 Boddeti, N. G. *et al.* Mechanics of adhered, pressurized graphene blisters. *Journal of Applied Mechanics* **80**, 040909 (2013).
226 Boddeti, N. G. *et al.* Graphene blisters with switchable shapes controlled by pressure and adhesion. *Nano Lett.* **13**, 6216-6221 (2013).
227 Carpick, R. W. & Batteas, J. D. in *Springer Handbook of Nanotechnology* 605-629 (Springer, 2004).
228 Butt, H.-J., Cappella, B. & Kappl, M. Force measurements with the atomic force microscope: Technique, interpretation and applications. *Surf. Sci. Rep.* **59**, 1-152 (2005).
229 Burnham, N. A., Dominguez, D. D., Mowery, R. L. & Colton, R. J. Probing the surface forces of monolayer films with an atomic-force microscope. *Phys. Rev. Lett.* **64**, 1931 (1990).
230 Johnson, K., Kendall, K. & Roberts, A. Surface energy and the contact of elastic solids. *Proc. R. Soc. Lond. A* **324**, 301-313 (1971).
231 Derjaguin, B. V., Muller, V. M. & Toporov, Y. P. Effect of contact deformations on the adhesion of particles. *J. Colloid Interface Sci.* **53**, 314-326 (1975).
232 Maugis, D. Adhesion of spheres: the JKR-DMT transition using a Dugdale model. *J. Colloid Interface Sci.* **150**, 243-269 (1992).
233 Aghababaei, R., Warner, D. H. & Molinari, J.-F. Critical length scale controls adhesive

wear mechanisms. *Nature communications* **7**, 11816 (2016).
234 Fan, X., Zheng, W., Chihaia, V., Shen, Z. & Kuo, J.-L. Interaction between graphene and the surface of SiO2. *J. Phys.: Condens. Matter* **24**, 305004 (2012).
235 Gao, W., Xiao, P., Henkelman, G., Liechti, K. M. & Huang, R. Interfacial adhesion between graphene and silicon dioxide by density functional theory with van der Waals corrections. *J. Phys. D: Appl. Phys.* **47**, 255301 (2014).
236 Wang, P., Gao, W. & Huang, R. Entropic effects of thermal rippling on van der Waals interactions between monolayer graphene and a rigid substrate. *J. Appl. Phys.* **119**, 074305 (2016).
237 Kitt, A. L. *et al.* How graphene slides: Measurement and theory of strain-dependent frictional forces between graphene and sio2. *Nano Lett.* **13**, 2605-2610 (2013).
238 Wang, L. *et al.* One-dimensional electrical contact to a two-dimensional material. *Science* **342**, 614-617 (2013).
239 Loudon, R. The Raman effect in crystals. *Adv. Phys.* **13**, 423-482 (1964).
240 Batten, T., Pomeroy, J., Uren, M., Martin, T. & Kuball, M. Simultaneous measurement of temperature and thermal stress in AlGaN/GaN high electron mobility transistors using Raman scattering spectroscopy. *J. Appl. Phys.* **106**, 094509 (2009).
241 Cui, J., Amtmann, K., Ristein, J. & Ley, L. Noncontact temperature measurements of diamond by Raman scattering spectroscopy. *J. Appl. Phys.* **83**, 7929-7933 (1998).
242 Cahill, D. G. Analysis of heat flow in layered structures for time-domain thermoreflectance. *Rev. Sci. Instrum.* **75**, 5119-5122 (2004).
243 Beran, A. The reflectance behaviour of gold at temperatures up to 500° C. *Tschermaks mineralogische und petrographische Mitteilungen* **34**, 211-215 (1985).
244 Robinson, I. & Tweet, D. Surface X-ray diffraction. *Rep. Prog. Phys.* **55**, 599 (1992).
245 Birkholz, M. *Thin film analysis by X-ray scattering*. (John Wiley & Sons, 2006).
246 Ersoy, O. K. *Diffraction, Fourier optics and imaging*. (Wiley Online Library, 2007).
247 Hohenberg, P. & Kohn, W. Inhomogeneous electron gas. *Phys. Rev.* **136**, B864 (1964).
248 Green, M. A. Self-consistent optical parameters of intrinsic silicon at 300 K including temperature coefficients. *Sol. Energy Mater. Sol. Cells* **92**, 1305-1310 (2008).
249 Keller, H. E. in *Handbook of biological confocal microscopy* 145-161 (Springer, 2006).
250 Power, M. Characterisation of temperature and mechanical stress in AlGaN/GaN devices designed for power electronic applications. *PhD Thesis*.
251 Temple, P. A. & Hathaway, C. Multiphonon Raman spectrum of silicon. *Phys. Rev. B* **7**, 3685 (1973).
252 Bormett, R. W. *et al.* Ultraviolet Raman spectroscopy characterizes chemical vapor deposition diamond film growth and oxidation. *J. Appl. Phys.* **77**, 5916-5923 (1995).
253 Burton, J. *et al.* Spatial characterization of doped SiC wafers by Raman spectroscopy. *J. Appl. Phys.* **84**, 6268-6273 (1998).
254 Cai, H. *et al.* Synthesis of Highly Anisotropic Semiconducting GaTe Nanomaterials and Emerging Properties Enabled by Epitaxy. *Adv. Mater.* **29** (2017).
255 Kong, W. *et al.* Angle resolved vibrational properties of anisotropic transition metal trichalcogenide nanosheets. *Nanoscale* **9**, 4175-4182 (2017).
256 Loebich, O. The optical properties of gold. *Gold bulletin* **5**, 2-10 (1972).
257 Komarov, P. L., Burzo, M. G. & Raad, P. E. in *Semiconductor Thermal Measurement and Management Symposium, 2006 IEEE Twenty-Second Annual IEEE.* 199-203 (IEEE).
258 Chen, G. & Hui, P. Pulsed photothermal modeling of composite samples based on transmission-line theory of heat conduction. *Thin Solid Films* **339**, 58-67 (1999).
259 Hui, P. & Tan, H. A transmission-line theory for heat conduction in multilayer thin

films. *IEEE Trans. Compon. Packag. Manuf. Technol.: Part B* **17**, 426-434 (1994).
260 Kuhlman, K. L. Review of inverse Laplace transform algorithms for Laplace-space numerical approaches. *Numerical Algorithms* **63**, 339-355 (2013).
261 Novoselov, K. S. *et al.* Electric field effect in atomically thin carbon films. *Science* **306**, 666-669 (2004).
262 Meitl, M. A. *et al.* Transfer printing by kinetic control of adhesion to an elastomeric stamp. *Nature materials* **5**, 33 (2006).
263 Castellanos-Gomez, A. *et al.* Deterministic transfer of two-dimensional materials by all-dry viscoelastic stamping. *2D Materials* **1**, 011002 (2014).
264 Van Dreumel, G. *et al.* Comparison of GaN and AlN nucleation layers for the oriented growth of GaN on diamond substrates. *Diamond Relat. Mater.* **19**, 437-440 (2010).
265 Tao, L., Theruvakkattil Sreenivasan, S. & Shahsavari, R. Interlaced, Nanostructured Interface with Graphene Buffer Layer Reduces Thermal Boundary Resistance in Nano/Microelectronic Systems. *ACS Appl. Mater. Interfaces* **9**, 989-998 (2016).
266 Rajan, S., Chini, A., Wong, M. H., Speck, J. S. & Mishra, U. K. N-polar Ga N ／ Al Ga N ／ Ga N high electron mobility transistors. *J. Appl. Phys.* **102**, 044501 (2007).
267 Pomeroy, J. W. *et al.* Contactless Thermal Boundary Resistance Measurement of GaN-on-Diamond Wafers. *IEEE Electron Device Lett.* **35**, 1007-1009 (2014).
268 Simon, R. B., Anaya, J. & Kuball, M. Thermal conductivity of bulk GaN—Effects of oxygen, magnesium doping, and strain field compensation. *Appl. Phys. Lett.* **105**, 202105 (2014).
269 Ziade, E. *et al.* Thickness dependent thermal conductivity of gallium nitride. *Appl. Phys. Lett.* **110**, 031903 (2017).
270 Cho, J., Francis, D., Altman, D. H., Asheghi, M. & Goodson, K. E. Phonon conduction in GaN-diamond composite substrates. *J. Appl. Phys.* **121**, 055105 (2017).
271 Ziade, E. *et al.* Thermal transport through GaN–SiC interfaces from 300 to 600 K. *Appl. Phys. Lett.* **107**, 091605 (2015).
272 Glassbrenner, C. & Slack, G. A. Thermal conductivity of silicon and germanium from 3 K to the melting point. *Phys. Rev.* **134**, A1058 (1964).
273 Touloukian, Y. (Plenum, New York, 1970).
274 Victor, A. C. Heat capacity of diamond at high temperatures. *J. Chem. Phys.* **36**, 1903-1911 (1962).
275 Moelle, C. *et al.* Specific heat of single-, poly-and nanocrystalline diamond. *Diamond Relat. Mater.* **7**, 499-503 (1998).
276 Levinshtein, M. E., Rumyantsev, S. L. & Shur, M. S. *Properties of Advanced Semiconductor Materials: GaN, AIN, InN, BN, SiC, SiGe*. (John Wiley & Sons, 2001).
277 Cho, J. *et al.* in *Thermal and Thermomechanical Phenomena in Electronic Systems (ITherm), 2014 IEEE Intersociety Conference on.* 1186-1191 (IEEE).
278 Bai, S., Tang, Z., Huang, Z. & Yu, J. Thermal Characterization of Thin Films Using Transient Thermoreflectance Technique. *IEEE Trans. Ind. Electron.* **56**, 3238-3243 (2009).
279 Yimin, Z. *et al.* Pulsed photothermal reflectance measurement of the thermal conductivity of sputtered aluminum nitride thin films. *J. Appl. Phys.* **96** (2004).
280 Choi, S. R., Kim, D., Choa, S.-H., Lee, S.-H. & Kim, J.-K. Thermal conductivity of AlN and SiC thin films. *Int. J. Thermophys.* **27**, 896-905 (2006).
281 Beechem, T., Graham, S., Hopkins, P. & Norris, P. Role of interface disorder on thermal boundary conductance using a virtual crystal approach. *Appl. Phys. Lett.* **90**, 054104 (2007).
282 Mandal, S., Thomas, E. L., Jenny, T. A. & Williams, O. A. Chemical Nucleation of Diamond Films. *ACS Appl. Mater. Interfaces* **8**, 26220-26225 (2016).

283 Bozorg-Grayeli, E. *et al.* Thermal conduction inhomogeneity of nanocrystalline diamond films by dual-side thermoreflectance. *Appl. Phys. Lett.* **102**, 111907 (2013).
284 Verhoeven, H. *et al.* Influence of the microstructure on the thermal properties of thin polycrystalline diamond films. *Appl. Phys. Lett.* **71**, 1329-1331 (1997).
285 Sood, A. *et al.* in *Thermal and Thermomechanical Phenomena in Electronic Systems (ITherm), 2014 IEEE Intersociety Conference on.* 1192-1198 (IEEE).
286 Ono, A., Baba, T., Funamoto, H. & Nishikawa, A. Thermal conductivity of diamond films synthesized by microwave plasma CVD. *Jpn. J. Appl. Phys.* **25**, L808 (1986).
287 Trew, R. J., Green, D. S. & Shealy, J. B. AlGaN/GaN HFET reliability. *IEEE Microw. Mag.* **10**, 116-127 (2009).
288 Won, Y., Cho, J., Agonafer, D., Asheghi, M. & Goodson, K. E. in *Compound Semiconductor Integrated Circuit Symposium (CSICS), 2013 IEEE.* 1-5 (IEEE).
289 Goyal, V., Sumant, A. V., Teweldebrhan, D. & Balandin, A. A. Direct Low‐Temperature Integration of Nanocrystalline Diamond with GaN Substrates for Improved Thermal Management of High‐Power Electronics. *Adv. Funct. Mater.* **22**, 1525-1530 (2012).
290 Alomari, M. *et al.* Diamond overgrown InAlN/GaN HEMT. *Diamond Relat. Mater.* **20**, 604-608 (2011).
291 Dumka, D. *et al.* in *Compound Semiconductor Integrated Circuit Symposium (CSICS), 2013 IEEE.* 1-4 (IEEE).
292 Sun, H. R. *et al.* Temperature-Dependent Thermal Resistance of GaN-on-Diamond HEMT Wafers. *IEEE Electron device lett.* **37**, 621-624, doi:10.1109/Led.2016.2537835 (2016).
293 Tadjer, M. J. *et al.* Reduced self-heating in AlGaN/GaN HEMTs using nanocrystalline diamond heat-spreading films. *IEEE Electron Device Lett.* **33**, 23-25 (2012).
294 Anderson, T. J. *et al.* Nanocrystalline Diamond-Gated AlGaN/GaN HEMT. *IEEE Electron Device Lett.* **34**, 1382-1384 (2013).
295 Pobedinskas, P. *et al.* Surface plasma pretreatment for enhanced diamond nucleation on AlN. *Appl. Phys. Lett.* **102**, 201609 (2013).
296 Williams, O. A. *et al.* Growth, electronic properties and applications of nanodiamond. *Diamond Relat. Mater.* **17**, 1080-1088 (2008).
297 Pomeroy, J. W., Uren, M. J., Lambert, B. & Kuball, M. Operating channel temperature in GaN HEMTs: DC versus RF accelerated life testing. *Microelectronics Reliability* **55**, 2505-2510 (2015).
298 Abrams, H. Grain size measurement by the intercept method. *Metallography* **4**, 59-78 (1971).
299 Liu, W. & Balandin, A. A. Thermal conduction in AlxGa1-xN alloys and thin films. *J. Appl. Phys.* **97**, 73710-73710 (2005).
300 Bogner, M., Hofer, A., Benstetter, G., Gruber, H. & Fu, R. Y. Differential 3ω method for measuring thermal conductivity of AlN and Si 3 N 4 thin films. *Thin Solid Films* **591**, 267-270 (2015).
301 Okhotin, A., Pushkarskij, A. & Gorbachev, V. Thermophysical properties of semiconductors. (1972).
302 Balandin, A. A. Thermal properties of graphene and nanostructured carbon materials. *Nature materials* **10**, 569-581 (2011).
303 Mohr, M. *et al.* Influence of grain boundaries on elasticity and thermal conductivity of nanocrystalline diamond films. *Acta Mater.* **122**, 92-98 (2017).
304 Cahill, D. G. & Pohl, R. Heat flow and lattice vibrations in glasses. *Solid State Commun.* **70**, 927-930 (1989).
305 Lee, S. M. & Cahill, D. G. Heat transport in thin dielectric films. *J. Appl. Phys.* **81**,

2590-2595 (1997).
306 Kuzmik, J. *et al.* Thermal characterization of MBE-grown GaN/AlGaN/GaN device on single crystalline diamond. *J. Appl. Phys.* **109**, 086106 (2011).
307 Verhoeven, H., Boettger, E., Flöter, A., Reiss, H. & Zachai, R. Thermal resistance and electrical insulation of thin low-temperature-deposited diamond films. *Diamond Relat. Mater.* **6**, 298-302 (1997).
308 Shamsa, M. *et al.* Thermal conductivity of diamond-like carbon films. *Appl. Phys. Lett.* **89**, 161921-161921 (2006).
309 Xiaohua, L., Wanqi, J. & Yaohe, Z. Numerical analysis of Cd1− xZnxTe crystal growth by the vertical Bridgman method using the accelerated crucible rotation technique. *J. Cryst. Growth* **219**, 22-31 (2000).
310 Von Dreele, R. & Larson, A. General structure analysis system. *Regents of the University of California*, 210-213 (2001).
311 Oganov, A. R. & Glass, C. W. Crystal structure prediction using ab initio evolutionary techniques: Principles and applications. *J. Chem. Phys.* **124**, 244704 (2006).
312 Oganov, A. R., Ma, Y., Lyakhov, A. O., Valle, M. & Gatti, C. Evolutionary crystal structure prediction as a method for the discovery of minerals and materials. *Reviews in Mineralogy and Geochemistry* **71**, 271-298 (2010).
313 Oganov, A. R., Lyakhov, A. O. & Valle, M. How Evolutionary Crystal Structure Prediction Works · and Why. *Acc. Chem. Res.* **44**, 227-237 (2011).
314 Kresse, G. & Furthmüller, J. Efficient iterative schemes for ab initio total-energy calculations using a plane-wave basis set. *Phys. Rev. B* **54**, 11169 (1996).
315 Kresse, G. & Furthmüller, J. Efficiency of ab-initio total energy calculations for metals and semiconductors using a plane-wave basis set. *Computational materials science* **6**, 15-50 (1996).
316 Lyakhov, A. O., Oganov, A. R., Stokes, H. T. & Zhu, Q. New developments in evolutionary structure prediction algorithm USPEX. *Comput. Phys. Commun.* **184**, 1172-1182 (2013).
317 Gonze, X. & Lee, C. Dynamical matrices, Born effective charges, dielectric permittivity tensors, and interatomic force constants from density-functional perturbation theory. *Phys. Rev. B* **55**, 10355 (1997).
318 Togo, A., Oba, F. & Tanaka, I. First-principles calculations of the ferroelastic transition between rutile-type and CaCl 2-type SiO 2 at high pressures. *Phys. Rev. B* **78**, 134106 (2008).
319 Perdew, J. P., Burke, K. & Ernzerhof, M. Generalized gradient approximation made simple. *Phys. Rev. Lett.* **77**, 3865 (1996).
320 Monkhorst, H. J. & Pack, J. D. Special points for Brillouin-zone integrations. *Phys. Rev. B* **13**, 5188 (1976).
321 Fonseca, J. J. *et al.* Bandgap Restructuring of the Layered Semiconductor Gallium Telluride in Air. *Adv. Mater.* (2016).
322 Susoma, J., Lahtinen, J., Kim, M., Riikonen, J. & Lipsanen, H. Crystal quality of two-dimensional gallium telluride and gallium selenide using Raman fingerprint. *AIP Advances* **7**, 015014 (2017).
323 Anzellini, S., Dewaele, A., Occelli, F., Loubeyre, P. & Mezouar, M. Equation of state of rhenium and application for ultra high pressure calibration. *J. Appl. Phys.* **115**, 043511 (2014).
324 Dewaele, A., Datchi, F., Loubeyre, P. & Mezouar, M. High pressure–high temperature equations of state of neon and diamond. *Phys. Rev. B* **77**, 094106 (2008).
325 Sánchez-Royo, J. *et al.* Angle-resolved photoemission study and first-principles calculation of the electronic structure of GaTe. *Phys. Rev. B* **65**, 115201 (2002).

326 Yamamoto, A. *et al.* Excitons and band structure of highly anisotropic GaTe single crystals. *Phys. Rev. B* **64**, 035210 (2001).
327 Low, T. *et al.* Tunable optical properties of multilayer black phosphorus thin films. *Phys. Rev. B* **90**, 075434 (2014).
328 Lam, K.-T., Dong, Z. & Guo, J. Performance limits projection of black phosphorous field-effect transistors. *IEEE Electron device lett.* **35**, 963-965 (2014).
329 Zeier, W. G. *et al.* Thinking Like a Chemist: Intuition in Thermoelectric Materials. *Angew. Chem. Int. Ed.*, n/a-n/a, doi:10.1002/anie.201508381 (2016).
330 Snyder, G. J. & Toberer, E. S. Complex thermoelectric materials. *Nature materials* **7**, 105 (2008).
331 Lin, S. *et al.* High Thermoelectric Performance of Ag9GaSe6 Enabled by Low Cutoff Frequency of Acoustic Phonons. *Joule* **1**, 816-830 (2017).
332 Li, W. *et al.* Crystal Structure Induced Ultralow Lattice Thermal Conductivity in Thermoelectric Ag9AlSe6. *Advanced Energy Materials* (2018).
333 Huang, M., Pascal, T. A., Kim, H., Goddard III, W. A. & Greer, J. R. Electronic− mechanical coupling in graphene from in situ nanoindentation experiments and multiscale atomistic simulations. *Nano Lett.* **11**, 1241-1246 (2011).
334 Chrobak, D. *et al.* Deconfinement leads to changes in the nanoscale plasticity of silicon. *Nature nanotechnology* **6**, 480 (2011).
335 Matsumoto, M., Huang, H., Harada, H., Kakimoto, K. & Yan, J. On the phase transformation of single-crystal 4H–SiC during nanoindentation. *J. Phys. D: Appl. Phys.* **50**, 265303 (2017).
336 Chrobak, D., Nordlund, K. & Nowak, R. Nondislocation origin of GaAs nanoindentation pop-in event. *Phys. Rev. Lett.* **98**, 045502 (2007).
337 Lund, A. C., Hodge, A. M. & Schuh, C. A. Incipient plasticity during nanoindentation at elevated temperatures. *Appl. Phys. Lett.* **85**, 1362-1364 (2004).
338 Schuh, C. & Nieh, T. A nanoindentation study of serrated flow in bulk metallic glasses. *Acta Mater.* **51**, 87-99 (2003).
339 Wei, X. *et al.* Recoverable slippage mechanism in multilayer graphene leads to repeatable energy dissipation. *ACS nano* **10**, 1820-1828 (2016).
340 Fu, K. *et al.* Ultra-high specific strength and deformation behavior of nanostructured Ti/Al multilayers. *J. Phys. D: Appl. Phys.* **50**, 365302 (2017).
341 Chitara, B. & Ya'akobovitz, A. Elastic Properties and Breaking Strengths of GaS, GaSe and GaTe Nanosheets. *Nanoscale* (2018).